UAB
Universitat Autònoma de Barcelona

# High-Throughput Methodologies for Binary and Ternary Organic Solar Cells

**Albert Harillo Baños**

**ADVERTIMENT.** L'accés als continguts d'aquesta tesi queda condicionat a l'acceptació de les condicions d'ús establertes per la següent llicència Creative Commons: https://creativecommons.org/licenses/?lang=ca

**ADVERTENCIA.** El acceso a los contenidos de esta tesis queda condicionado a la aceptación de las condiciones de uso establecidas por la siguiente licencia Creative Commons: https://creativecommons.org/licenses/?lang=es

**WARNING.** The access to the contents of this doctoral thesis it is limited to the acceptance of the use conditions set by the following Creative Commons license: https://creativecommons.org/licenses/?lang=en

UAB
Universitat Autònoma
de Barcelona

# High-Throughput Methodologies for Binary and Ternary Organic Solar Cells

*Albert Harillo Baños*

*PhD Thesis*

Nanostructured Materials for Optoelectronics and Energy Harvesting Group (Nanopto)

Institut de Ciència de Materials de Barcelona (ICMAB-CSIC)

Supervisor: *Mariano Campoy Quiles*

Director*: Gemma Garcia Alonso*

PhD Program in Materials Science, Department of Physics

Universitat Autònoma de Barcelona (UAB)

Bellaterra (Barcelona), 2023

# Acknowledgements

No se me da muy bien escribir emociones… ¡Pero hay mucho que quiero agradecer, aunque sea breve!

Primero, a mi familia. A mi madre, **Maria** y a **Enric**, que siempre me han cuidado con toda su alma, y me han apoyado en todo lo que he querido hacer en la vida. A mi padre, **Jordi**, por siempre estar ahí, por ayudarme en absolutamente todo lo que haga falta. A mi hermano, **Isaac** y a **Ondine**, porque siempre me has motivado a ser una mejor versión de mí mismo, aunque me tuvieras que arrastrar en mi contra. Y por supuesto, a la peque, a **Olivia**, que, con solo mirarla, hace que quieras hacer el mundo un poquito mejor para ella. Y aunque ya no estén, no me olvidare nunca de mis abuelos, **Juana, Salvador, Montse**, que me cuidaron con todo su amor de pequeño, y de no tan pequeño.

También agradecer a mis amigos, esos con los que puedes volver a ser un niño, reír, imaginar y olvidarte de todo estrés. A toda **La Ley del Metal**, y especialmente a **Víctor, Bigotes, Edu, Alba, Armand, Gerard, Didi,** por siempre estar ahí para lo importante, y para lo que no importa, pero es risas, ¡aunque haya que insistir un poco a veces! Gracias por tantos años de roles y *Drachens*.

Y como no, agradecer a los que han estado trabajando a mi lado toda esta tesis, todos los compañeros del ICMAB que han estado en más cerca que nadie ayudando en el laboratorio: **Xabier, Martí, Sergi, Alfonsina, Bernhard, Osnat, Miquel, Arianna, Alex...** Y, sobre todo, a un gran mentor y arquitecto de esta tesis, **Mariano**. ¡Con un grupo como este, trabajar en el laboratorio es un gusto!

# Index

Index ..... 1
1. Abstract ..... 3
2. List of Publications ..... 5
3. Introduction ..... 6
3.1. Photovoltaic effect and Solar Cells ..... 7
3.2. Organic semiconductors ..... 11
3.3. Organic Solar Cells ..... 12
3.4. Ternary OPV ..... 19
3.5. Parametric Landscape ..... 21
3.6. High-throughput experimentation ..... 26
4. Results ..... 28
4.1. Global Summary and objectives ..... 28
4.2. High-throughput exploration of processing parameters ..... 30
4.2.1. Fabrication of thickness gradient devices ..... 30
4.2.2. Paper I: Polymer:Polymer Solar Cells ..... 31
4.2.3. High-throughput exploration of composition ..... 36
4.2.4. Characterization of composition gradient samples ..... 39
4.2.5. Paper II: Novel material optimization: P3HT:NIPb3T-Rd ..... 40
4.3. Paper III: Exploring the composition space in ternary solar cells ..... 43
4.3.1. Materials ..... 46
4.3.2. Characterization of ternary composition gradients ..... 49
4.3.3. Ternary Diagrams ..... 52
4.3.4. Normalization of photocurrent ..... 55
4.4. Paper IV: Correlating microstructure and composition in ternary blends ..... 57
5. Conclusions ..... 59
6. Future work ..... 60
7. References ..... 65
8. Annexes ..... 70
8.1. Annex 1: Summary of the complete methodology for optimization of ternary OPV systems ..... 70
8.2. Annex 2: Lamp Comparison for WBIC ..... 73
PAPER I ..... 77
PAPER II ..... 99
PAPER III ..... 175

PAPER IV…….203

# 1. Abstract

Organic Solar Cells are complex devices capable of converting light into electricity through the photovoltaic effect using organic semiconductors. They have garnered considerable interest due to their several advantages when compared to other Solar Cell technologies, such as Silicon. These properties include light-weight and flexible devices, tunability of optical properties such as color and semitransparency, solution processability with exceptional industrial scale-up capabilities, and higher efficiency in in-door light conditions.

The photovoltaic effect takes place in the active layer, which is formed by two or more organic semiconductors. The active layer must contain semiconductors with different electronic character, at least one electron donor material and one electron acceptor material. Donors are most commonly polymers, while acceptors usually are fullerenes or small molecules. These materials are deposited together from solution, forming a bulk heterojunction active layer, creating donor-acceptor interfaces capable of splitting the excitons formed by light absorption. However, Organic Solar Cells require multiple additional layers for contact selectivity, and their properties depend strongly on thickness, donor:acceptor ratio and microstructure of the active layer.

This results in a complex and multi-dimensional parametric landscape affecting the final Power Conversion Efficiency of Organic Solar Cell devices. Typically, an Edisonian approach, based in intense prototyping while exploring discreetly each parameter individually, has been taken for these kinds of research. However, this approach is efficient in terms of time and resources, and limits the growth of Organic Solar Cell technology.

In this thesis we design and explore new high-throughput methodologies designed to allow the screening of Organic Solar Cells performance variations in multiple parameters, speeding the optimization process. These methodologies are based on the manufacturing of gradients in the parameters of interest, and aim to change the prototyping-intensive approach of Organic Solar Cell research to a measuring-intensive approach.

For this purpose, we use techniques already in use within our research group, as well as improving them and designing new ones. First, in Paper I, we use active layer thickness gradients and statistical analysis of the measured parameters to rapidly optimize a novel Polymer:Polymer system with a fraction of the materials needed with a standard fabrication approach. In this process, the most crucial fabrication parameters are discovered, in this case, solvent selection, and a new visualization of Power conversion efficiency in the Hansen solubility space is created, allowing for predictions of solvent-dependent performance.

Afterwards, in Paper II, we use composition gradients to optimize another novel system. These gradients coupled with hyperspectral imaging allow for a composition ratio optimization in a single sample, generating large libraries of compositions. The deposition method is based on two-drop depositions, while the hyperspectral imaging comprises Raman spectroscopy for composition retrieval, LBIC and WBIC for photocurrent characterization. White Beam Induced Photocurrent (WBIC) measuring was first used during this thesis, allowing for a more accurate photocurrent measurement than single wavelength LBIC.

Next, in Paper III, the composition gradient methodology was then expanded to be applicable to Ternary Organic Solar Cells. This included the design of new deposition techniques based on sequential depositions, allowing for the creation of ternary composition libraries of more than

10000 data points per sample. The resulting methodology is applied to multiple ternary systems, proving its adaptability. Moreover, different areas of the ternary composition space can be covered with only slight modifications during the depositions. Multiple maxima in performance are located within the same ternary composition space, and the results corroborated with discrete sampling.

In Paper IV, we further refined this methodology, increasing the yield of the data obtained. Some of the improvements allow us to gain an insight in microstructure of the active layer using PL, without complicating the methodology. The methodology is applied to a new high efficiency ternary system. A new photocurrent normalization is added to the methodology to compensate the photocurrent differences between devices due to the appearance of defects and pinholes in some layers.

# 2. List of Publications

1. Albert Harillo-Baños, Qunping Fan, Sergi Riera-Galindo, Ergang Wang, Olle Inganäs, and Mariano Campoy-Quiles. **High-Throughput Screening of Blade-Coated Polymer:Polymer Solar Cells: Solvent Determines Achievable Performance**. *ChemSusChem* **202101888**, 1–11 (2021).

**Contribution**: Fabrication and characterization (Electrical, Microscopy, Hansen, PL, Raman) of the solar cells with thickness gradients. Statistical analysis of the data, representation of data. Paper writing.

2. Matías J. Alonso-Navarroa, Alexandra Harbuzaru, Paula de Echegaraya, Iratxe Arrechea-Marcos, Albert-Harillo-Baños, Alejandro de la Peña, M. Mar Ramos, J. Teodomiro López Navarrete, Mariano Campoy-Quiles, Rocío Ponce Ortiz, José L. Segura. **Effective interplay of donor and acceptor groups for tuning optoelectronic properties in oligothiophene-naphthalimide assemblies**. *Journal of Material Chemistry C* **8**, 15277–15289 (2020).

**Contribution**: Fabrication and characterization of the solar cells, both with composition gradients and with thickness gradients. Characterization of nk coefficients, Raman spectra and Raman Cross-section of NIPb3T-Rd. Writing of the "Organic photovoltaic proof of concept" section of the paper.

3. Harillo-Baños, A., Rodríguez-Martínez, X. & Campoy-Quiles, M. **Efficient Exploration of the Composition Space in Ternary Organic Solar Cells by Combining High-Throughput Material Libraries and Hyperspectral Imaging**. *Advanced Energy Materials,* **1902417**, 1–12 (2019).

**Contribution**: Investigation and design of the ternary composition gradient devices. Design of the WBIC technique. Fabrication and characterization of the solar cells. Data curation and visualization. Paper writing.

4. Sandra Hultmark, Sri Harish Kumar Paleti, Albert Harillo, Sara Marina, Ferry Anggoro Ardy Nugroho, Yanfeng Liu, Leif K. E. Ericsson, Ruipeng Li, Jaime Martín, Jonas Bergqvist, Christoph Langhammer, Fengling Zhang, Liyang Yu, Mariano Campoy-Quiles, Ellen Moons, Derya Baran, and Christian Müller. **Suppressing Co-Crystallization of Halogenated Non-Fullerene Acceptors for Thermally Stable Ternary Solar Cells**. *Advanced Functional Materials,* **30**, 1–10 (2020).

**Contribution**: Fabrication and characterization of the ternary composition gradient solar cells.

# 3. Introduction

The world's energetic demand has been growing continuously, and will continue to increase for the foreseeable future. However, fossil fuels are still the main energy source worldwide, with the huge environmental consequences that this entails. The scientific community has been warning and advising about these consequences, as the Earth is drawing closer to a threshold where the effects of climate change will be irreversible. This makes the research of new, environmentally-conscious and renewable sources of energy not a commodity but a "must" in the near future.

Among these renewable and cleaner sources of energy, solar energy appears as one of the main options with tremendous growing potential. As of 2022, Solar Energy covered around 4.5% of the total global energy demand, increasing from a 3.7% in 2021.[1] It is the second-largest growing renewable source, surpassed only by Wind power. Solar is expected to keep expanding until it becomes a major contributor.

The primary method of harnessing solar energy for power generation is through the use of photovoltaics (PV). In 2022, global energy consumption amounted to ~24400 TWh. Meanwhile, 23000 TW of solar energy reaches Earth annually. By covering only a ~0.57% of the land area of the Earth with photovoltaics (solar cells, SC), the world's energy needs could be met.

## 3.1. Photovoltaic effect and Solar Cells

A Solar Cell is a solid-state electronic device capable of converting the power of incident light directly into electricity. It is formed by one or more semiconducting materials between two electrodes, of which at least the one on the illuminated side has to be transparent.

Silicon Solar Cells, Organic photovoltaics (OPVs) and all other PV technologies are based on the photovoltaic effect. This effect was initially demonstrated by Edmond Becquerel in 1839 when he observed the generation of current and voltage under illumination using an electrochemical cell with platinum electrodes.[2] It took several years before the creation of the first Solar Cell. In 1884, Charles Fritts coated Selenium with a thin layer of gold, creating the first Solid State Solar Cell. Although these cells had efficiency of only about 1% and a very high cost, they served as a proof of concept for energy harvesting using the photovoltaic effect. In the same year, Fritts' solar cell was installed for the first time on a rooftop in New York City.

The physics of the photovoltaic effect are now well understood (see Figure 1 for an example in organic Solar Cells): A semiconductor material can absorb incoming photons with energy above its Band Gap. This absorption promotes an electron in the valence band of the material to an excited state in the conduction band, leaving a hole in the valence band. This electron-hole pair is referred to as an *exciton*. Subsequently, the exciton can undergo *dissociation*, when it separates into an electron and a hole at an offset in the conduction and valence bands. This dissociation can occur at a p-n junction, where an effective electron donor material interfaces with an electron acceptor material, or by temperature like in silicon. These charges then travel to their corresponding electrodes, generating an electrical current. If the excitons were unable to dissociate, they will decay by the electron falling back into the hole, resulting in radiative recombination (light, PL) or non-radiative recombination (heat or Auger recombination).

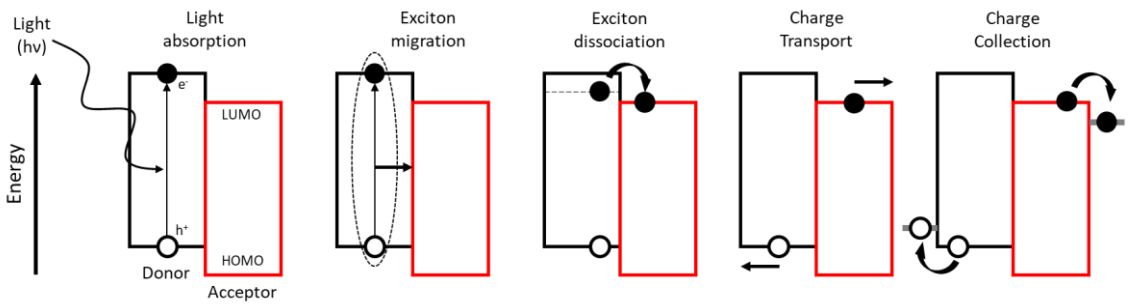


**Figure 1.** Sketch of the energy diagram in a photovoltaic process for an excitonic solar cell. It comprises the next sequential processes: (1) Light absorption and formation of an exciton; (2) Exciton migration towards donor-acceptor interface; (3) Dissociation of exciton via charge transfer states; (4) Transport of free charges; (5) collection of charges at the corresponding electrodes.

At a macroscopic level, Solar Cells are characterized by their JV curve, which represents the photocurrent density extracted from the cell when sweeping the applied voltage. In absence of illumination, solar cells act as diodes, and their JV curve is the same as that of a diode. However, when illuminated, the JV curve shifts to a quadrant where energy can be extracted. From the JV curve, several parameters can be extracted to characterize the Solar Cell. These parameters include open circuit voltage ($V_{oc}$), Short circuit current ($J_{sc}$), Fill Factor (FF) and power conversion efficiency (PCE). An example of a JV curve can be seen in Figure 2, with each parameter explained below.

Open circuit Voltage, or $V_{oc}$, is the maximum voltage attainable from a cell, obtained when the current flowing through is zero. $V_{oc}$ is primarily determined by the band gap of the photo active material(s). However, it can be also influenced by various other factors, such as light intensity, temperature, microstructure of the materials in the active layer and the work function of the electrodes. It also can suffer losses. Charger carrier recombination, for instance, can decrease the $V_{oc}$. In the case of OPV (similar to Amorphous silicon), disorder within the materials can lead to the presence of gap tail states. These states allow the carriers to relax, bringing the electron quasi-Fermi level down, and the hole quasi-Fermi level up, decreasing $V_{oc}$.[3]

Short Circuit Photocurrent, or $J_{sc}$, is the current flowing through the Cell when it is short-circuited, as in zero voltage. It is a result of the generation and extraction of photogenerated charge carriers. For an ideal Solar Cell, $J_{sc}$ represents the maximum photocurrent that can be extracted from the cell. The magnitude of $J_{sc}$ is intricately linked to processes such as absorption, exciton generation, dissociation, transport, and collection of charges. Factors that affect these processes, including changes in illumination, alterations in microstructure, or variations in active layer thickness, can impact $J_{sc}$.[4]

While $V_{oc}$ and $J_{sc}$ signify the maximum attainable voltage and current from the solar cell, respectively, it's important to note that power output at these operation points is zero. The Fill Factor, or FF, quantifies the ratio of the maximum power obtainable from the cell to the product of $V_{oc}$ and $J_{sc}$. It can also be conceptualized as the "squareness" of the JV curve, where an ideal Solar Cell would have an FF of 100%, forming a perfect square. In simpler terms, FF is the area of the square delineated by the optimal voltage and current point, divided by the area defined by $V_{oc}$ and $J_{sc}$. FF is influenced by a complex interplay of interconnected factors, making its complete comprehension challenging.[5]

The final primary parameter is the Power Conversion Efficiency, or PCE. PCE quantifies the proportion of electrical power at the maximum power point in relation to the incident light power, typically under the AM 1.5G spectrum with 1 Sun intensity.

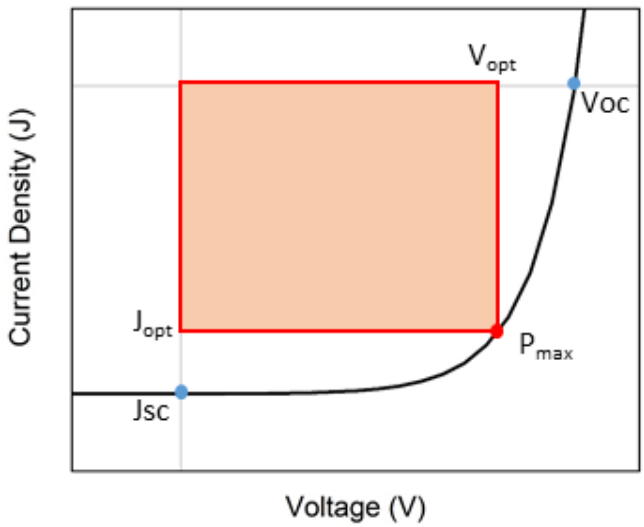


**Figure 2.** Example of a JV curve for an illuminated Solar Cell. Main parameters of the curve are plotted, with the red square delimiting the generated power.

$$FF = \frac{J_{opt} * V_{opt}}{Jsc * Voc} = \frac{P_{max}}{Jsc * Voc}$$

$$PCE = \frac{FF * Jsc * Voc}{P_{in}}$$ where $P_{in}$ = 1000W/m$^2$ under 1 Sun intensity.

Moreover, the design of new solar cells needs to consider several additional parameters, particularly when exploring potential industrial scalability and real-world applications. Among these factors are the long-term stability of the cell, both during illumination and in shelf life; mechanical attributes and durability; and sustainability aspects, such as abundance of materials, toxicity, environmental compatibility, energy consumption during manufacturing, and recyclability.

Photovoltaic technologies have been historically divided into three generations. The most common and widely used is the first generation, crystalline silicon (c-Si), accounting for over 90% of commercial SCs.[6] In the initial stages of solar energy research and implementation, c-Si offered several advantages, both in research and in commercial applications. One key advantage is its large dielectric constant ($\varepsilon_r$ ~ 10-15), which promotes the screening of Coulomb interactions between the generated charges. This results in a large exciton radius, exceeding the lattice spacing. Combined with the low effective mass of the charges in silicon, exciton dissociation becomes spontaneous even at room temperature, as the binding energies ($E_b$) are below 25 meV ($K_bT$ at room temperature). These loosely bonded excitons, named *Mott-Wannier excitons,* can be dissociated solely through the thermal fluctuations of the system. These dissociated charges can then be collected by selective electrodes, or a p-n junction capable of acting as selective electrodes. This characteristic allows for the production of bulky Solar Cells, which were easier to manufacture during the early stages of commercial use.

From a commercial standpoint, c-Si cells have become highly attractive for everyday use due to the abundance of silicon, the second most abundant element in Earth's crust, long lifespan (20-30 years), and high efficiencies (achieving a record of 26.7% power conversion efficiency, PCE).[7] Consequently, crystalline silicon has dominated the photovoltaic technology field.

However, Silicon Solar Cells have several limitations and drawbacks, reducing the scope of their implementation in the long term. These drawbacks stem from the rigidity and weight associated with thick silicon cells and the glass structure required to maximize efficiency and protect the cell respectively, as well as the complex and energy-consuming fabrication process. As silicon is an indirect semiconductor, its absorption is rather poor, needing thick active layers to absorb light. Furthermore, the poor aesthetics and mechanical properties of these cells pose another challenge when integrating them, as they are completely opaque and mechanically fragile. Consequently, the integration of silicon PV is constrained, and despite its high efficiency, it is limited to solar farms, roofs, and rigid bulky electronics. There are numerous other potential applications that have been left unfilled by silicon PV. For instance, indoor solar cells (SCs) for Internet of Things (IoT) devices, building integrated photovoltaics (BIPV), portable and wearable devices, as well as specialty locations like underwater and agrovoltaics.

The search for new technologies that could fulfill these applications has led to the development of the second generation PV, which incorporates technologies such as Gallium Arsenide (GaAs), amorphous silicon (a-Si:H), Cadmium Telluride (CdTe), and copper indium gallium (di)selenide

(CIGS). The main focus of the second generation was to create thinner photoactive layers, as these materials solve the absorption problem by being direct semiconductors. Thinner layers are beneficial in industrial use as they inherently reduce material usage during manufacturing. Second-generation PV managed to decrease the core device thickness from the 50-200 µm seen in c-Si to 1-50 µm while maintaining similar efficiency and even surpassing the record efficiency for single junction devices, which is now held by GaAs at 28.8% under 1 Sun illumination.[8]

Despite these improvements, second-generation PV technologies often remain rigid and brittle. They also contain scarce and/or highly toxic materials (such as Arsenic, Cadmium, and Tellurium) and typically require manufacturing via vacuum deposition methods. Consequently, second-generation PV is not very industrial-friendly, leading to a higher cost-to-energy generated ratio and limiting its widespread use to rather niche applications.

Then, Third Generation PV emerged, where we will find OPV. This third generation consists of flexible, lightweight, solution processed materials, with the thinnest photoactive layers until now, well below 1µm, in the nanoscale. Apart from OPV, this generation also includes Dye-sensitized (DSSCs), perovskites and quantum dot (QDSCs) solar Cells. All these cells share a few features that make them very promising: flexibility and lightweight, thinner architecture, very low energy payback time, solution processing with potential for low-cost industrial manufacturing. However, they also share a more limited maximum PCE (except Perovskites SCs) and a shorter lifetime. These emerging PV technologies might be able to cover all those applications outside of the scope of Silicon PV.

This thesis deals with Organic Solar Cells, arguably the most sustainable of the PV technologies, as will be explained later. However, before diving into OPV we need to talk about their active materials.

The events needed for the creation of Third generation PV were first observed in 1958 when David Kearns and Melvin Calvin observed the photovoltaic effect in laminated organic systems.[9] However, almost 30 years would have to pass before the world saw the first bilayer organic photovoltaic solar cell, by Ching W. Tang in 1986.[10] Although having a very modest 1% PCE, it served as a first step in OPV research. A few years later, a key milestone was introduced in two publications by A.J. Heeger[11] and A.B. Holmes.[12] These publications substituted the evaporated bi-layer engineered by Tang for a solution processed Bulk Heterojunction (BHJ), enhancing photogeneration and efficiency in OPV and opening the future of the OPV field.

## 3.2. Organic semiconductors

In chemistry, an organic compound is defined as a compound where carbon is covalently bonded to other elements, most commonly hydrogen, nitrogen and oxygen.

Certain organic materials exhibit semiconducting properties due to the nature of their conjugated bonds. These bonds form when the molecules contain alternating simple and double (or triple) bonds. The presence of these conjugated bonds gives rise to delocalization of electrons in the π-orbitals both above and below the σ plane. This facilitates the easy movement of charges along and between nearby molecules through intra and intermolecular hopping. Furthermore, these π-conjugated systems promote molecular backbones to crystallize via π-π stacking and π-π van der Waals interactions.

The formation of π bonds gives place to two distinct molecular orbital: bonding (π) and antibonding (π*). Analogous to inorganic crystalline semiconductors and their valence and conduction bands, organic semiconductors display a band gap resulting from the π and π* molecular orbitals. Due to the lack of long-range periodicity in organic semiconductors, these molecular orbitals replace the valence and conduction bands present in inorganic crystalline semiconductors. As a result, the highest occupied molecular orbital (HOMO) is the substituent of the valence band, while the lowest unoccupied molecular orbital (LUMO) substitutes the conduction band.

The HOMO-LUMO band gap in most organic semiconductors is of the order of visible light (400-900 nm). Coupled with the substantial extinction coefficients of the π clouds, this results in narrow yet highly absorbent bands in the spectrum of solar irradiance. Organic dyes and some biological compounds, such as eye pigments, lay in absorption bands.

Furthermore, the introduction of electron-donating groups in the conjugated backbone increases the HOMO energy level, while electron-withdrawing groups mainly decrease the LUMO energy level. This property grants organic semiconductors the unique feature to exhibit tunable optical and electronic characteristics, allowing adjustment of their energy levels and band gap to meet specific needs.

On a macroscopic scale, organic semiconductors are soft, flexible and lightweight solids. This opens up multiple avenues for novel applications that rigid crystalline inorganic semiconductors are unable to fulfill. Additionally, organic semiconductors feature added side chains, often included to enhance solubility. This enables the processing of organic semiconductors directly from solution using more industrially available techniques.

While some of the applications of these materials are already commercial, such as Organic Light-Emitting Diodes (OLEDs), now present in screen displays globally, others remain under research or industrial development. These include Organic Field Effect Transistors (OFET) for flexible electronics, Organic Lasers, Organic photodetectors,[13] Organic Thermoelectrics, Artificial Skin,[14] Bioelectronics and Biocompatible Probes[15] for medical applications, and, of course, Organic Solar Cells - the main focus of this thesis.

## 3.3. Organic Solar Cells

Organic Solar Cells, OPVs, use organic semiconductors as their active layer materials. As discussed in the section about organic semiconductors, these materials exhibit several properties that translate into advantages for OPV. Noteworthy among these attributes is the ability to tune the optical properties, thereby enabling color adjustment or achieving semi transparency. Moreover, OPV is compatible with flexible substrates, conferring them exceptional versatility.

Organic semiconductors exhibit lower refractive indices, resulting in reduced angular dependence on incident light and diminished reflection losses. Moreover, OPVs are able to effectively capture low-intensity light due to their thinner, and therefore lower electrical resistance, active layers. Additionally, OPV are composed of abundant and non-toxic materials, aligning with sustainability objectives. Furthermore, their processing occurs through solution-based methods at low temperatures, contributing to their eco-friendliness.

Although OPV has not reached the high PCE values of c-Si cells, their efficiency has been rapidly increasing over the last few years, recently reaching a PCE record of 19.31% at 1 Sun illumination.[16] And despite this lower PCE than c-Si cells, there are multiple other applications where OPV could fulfill than silicon cells could not.

Due to the thin and flexible nature of OPV, its ability to efficiently capture indoor light with less angular dependence than silicon and a better spectral match between OPV and artificial lightning, OPV could be implemented in the next generation of electronic devices, specifically powering Internet of Things electronics (IoT). These devices strive to be omnipresent yet invisible to us, requiring energy for their operation. Electrically connecting all IoT devices would be impossible, and battery replacement too expensive, but OPV can provide the autonomy and freedom they need.[17–19]

The band gap tunability of materials in OPV offers significant advantages for creating cells with specific functions. These include implementation in indoor light environments and achieving color and transparency tunability for architectural integration (BIPV).[20,21] Additionally, this tunability plays a crucial role in underwater applications, where OPV can efficiently harvest light for power generation.

Furthermore, the semi-transparency of OPV devices makes them suitable for integration into windows and agrovoltaics systems. In such applications, the cells not only generate power but also act as filters for solar light, allowing the passage of optimal illumination for people and plants, respectively.[22]

The light-weight and flexible nature of OPV opens up possibilities for their use in portable and wearable devices. Moreover, the light-weight nature of OPV makes them suitable for space applications, where ease of transport and a lower cross-section for radiation exposure are essential considerations.[23]

Table 1 provides a summary of the potential applications of OPV and the specific characteristics that make their implementation in these applications feasible.

**Table 1.** Potential applications and characteristics of OPV.

| Application | What can OPV bring? |
|---|---|
| In-door, Internet-of-things (IoT) | Gap tunability, low angular dependence, good PCE with low illumination |
| Windows | Semitransparency, color tunability, low angular dependence |
| Portable, Wearable | Light-weight, flexibility |
| Building integrated (BIPV) | Light-weight, color tunability, low angular dependence |
| Agrovoltaics | Gap tunability, low angular dependence |
| Underwater | Gap tunability |
| Space | Gap tunability, light-weight, low cross section for radiation |

The fabrication process of OPVs is relatively simple and very scalable for industrial production. While Silicon SCs require high temperatures for manufacturing, OPV can be manufactured from solution using roll-to-roll (R2R) processes, which are very industry-friendly techniques. Also, the manufacturing process requires more moderate temperatures, usually ranging from 40 to 120 °C instead of the 700°C and above needed for c-Si. Moreover, OPV also uses very abundant and non-toxic materials. These characteristics result in a very low energy payback time.[*]

However, OPVs also have drawbacks that prevent them from completely surpassing Silicon. The two main limitations are lower stability and overall efficiency. Silicon cells tend to maintain good efficiency for 20 to 30 years, while OPVs have a lifespan that is halved or even less, lasting around 5 to 10 years.[24–26] In terms of efficiency, silicon cells still hold their record at 26.81%,[27] while OPV has recently reached above 19%.[16] Nevertheless, the extensive research in OPV has rapidly narrowed this efficiency gap in recent years.

These factors present us with two different paths of integrating the same photovoltaic effect to our world and energy production. Both Silicon SCs and OPVs can be utilized in various applications, and a symbiotic relationship between both can lead to a full integration of Solar Energy in our cities and everyday life.

At a microscopic level, OPVs function with some distinctions compared to c-Si cells. OPVs rely on charge transfer between two distinct materials: an electron donor and an electron acceptor, which have different electronegativities.

[*] Time needed for a Solar Cell to generate the energy invested in its manufacturing.

The process of electrical energy production in OPV starts with the absorption of light within the active layer. This light can be absorbed by either of the two materials, inducing an electron transition from the HOMO band to the LUMO band of said material, forming an exciton. However, these excitons differ from the Mott-Wannier excitons formed in c-Si cells. The lower dielectric constant of the organic semiconductors results in strongly bound excitons. Referred to as *Frenkel* excitons, they cannot be dissociated by temperature alone and have a shorter diffusion length. Instead, exciton dissociation has to take place at the interface of the donor and acceptor material. After dissociation, charge carriers have to be transported by their respective materials to the electrodes, as in holes for the donor and electrons for the acceptor. Therefore, both materials should be good conductors of their respective carriers.

Given that the exciton's diffusion length within the active layer is approximately 20nm, the layer's architecture must facilitate the transport of an exciton, formed in any part of the layer, to reach a donor:acceptor (D:A) interface within that 20nm span. The initial and straightforward concept involved a bilayer structure, wherein each layer consists of one pure material and maintains a thickness of around 20nm, for a total active layer thickness of 40nm. However, this approach falls short in terms of photocurrent generation, as less thickness significantly restricts the light absorption capacity. Ideally, active layers should be of at least 100nm to maximize absorption. However, this greatly exceeds the exciton diffusion length of the organic semiconductors, necessitating a different approach to solve this compromise.

The solution to the trade-off between absorption and exciton diffusion was to transition from a bilayer structure to a bulk heterojunction (BHJ). In a BHJ the donor and acceptor materials (as well as any others in the active layer) are blended together and deposited from the same solution. Once deposited, the materials undergo phase separation, yielding random dispersed throughout the layer. This new microstructure has a profound influence in efficiency, but has to be treated carefully. It is crucial that the domain size is around the exciton diffusion length. Furthermore, the BHJ should have enough channels for the charge carrier to reach their corresponding electrodes. Yet, provided that the domain size is apt and charge carriers can access the electrodes, the heterojunction facilitates an increase in layer thickness beyond 100nm. The aim is to ensure that all excitons ideally encounter an interface within their diffusion length. For visual clarity, Figure 3 presents a schematic illustration of diverse layer architectures.

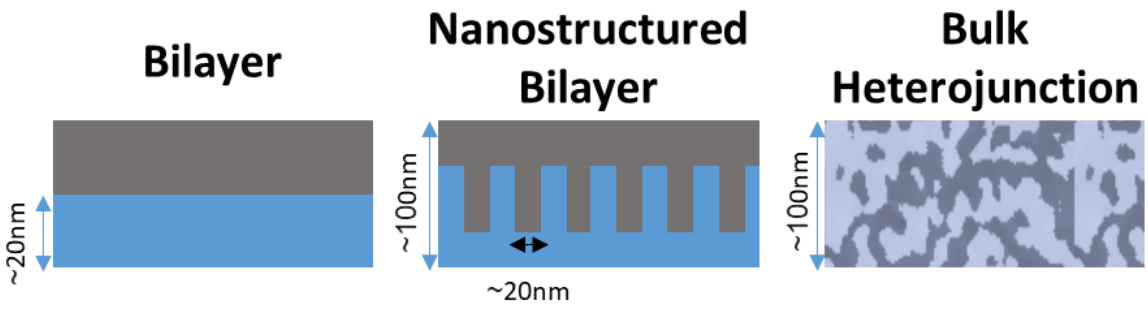


**Figure 3**. Examples of active layer architectures.

The materials employed as organic semiconductors in OPVs have continuously evolved since the inception of the research field, with a focus on enhancing absorption, charge carrier mobility, stability, and reducing synthetic complexity. Generally, donor materials are polymer semiconductors, while acceptors are fullerenes or small molecules. Nonetheless, there exist instances of acceptor polymers and donor small molecules, allowing polymer:polymer and Small molecule:Small molecule OPV devices.

Among the early and extensively researched donor polymers is P3HT, which has served as a workhorse material in OPV. P3HT boasts a relatively simple synthesis, resulting in high cost-effectiveness. Consequently, P3HT remained a standard in OPV research for numerous years until quite recently. However, P3HT-based devices encounter challenges in achieving high PCEs, with the highest around 6%, and an average of approximately 4% even with highly optimized systems.[28]

To enhance PCE, researchers have developed a variety of new polymers as substitutes for P3HT, leading to a consistent increase in PCEs over recent years. These emerging polymers frequently belong to the category of low band gap polymers, characterized by a band gap below 2eV. This facilitates absorption of wavelengths higher than 620nm, broadening the coverage of the solar spectrum by OPV devices. Notable instances of such low band gap polymers include PM6 and PTQ10.[29]

As for the acceptor materials, initial choices centered on fullerenes like PC60BM and PC70BM. Fullerenes, due to their straightforward synthesis and high electron mobility, were deemed ideal for OPVs. However, limited absorption capability restricted the final PCE of the devices, since all photocurrent generation depended on the donor material.

In response, non-fullerene acceptors, or NFAs, were developed to address this concern. These NFA are small conjugated molecules, usually containing electron-rich and electron-poor moieties to achieve a lower band gap and broader absorption. The electron-rich groups are shielded by side-chains, enabling interaction only between the electron-deficient groups and the donor material. This results in increased photocurrents and higher voltages compared to fullerenes.[30]

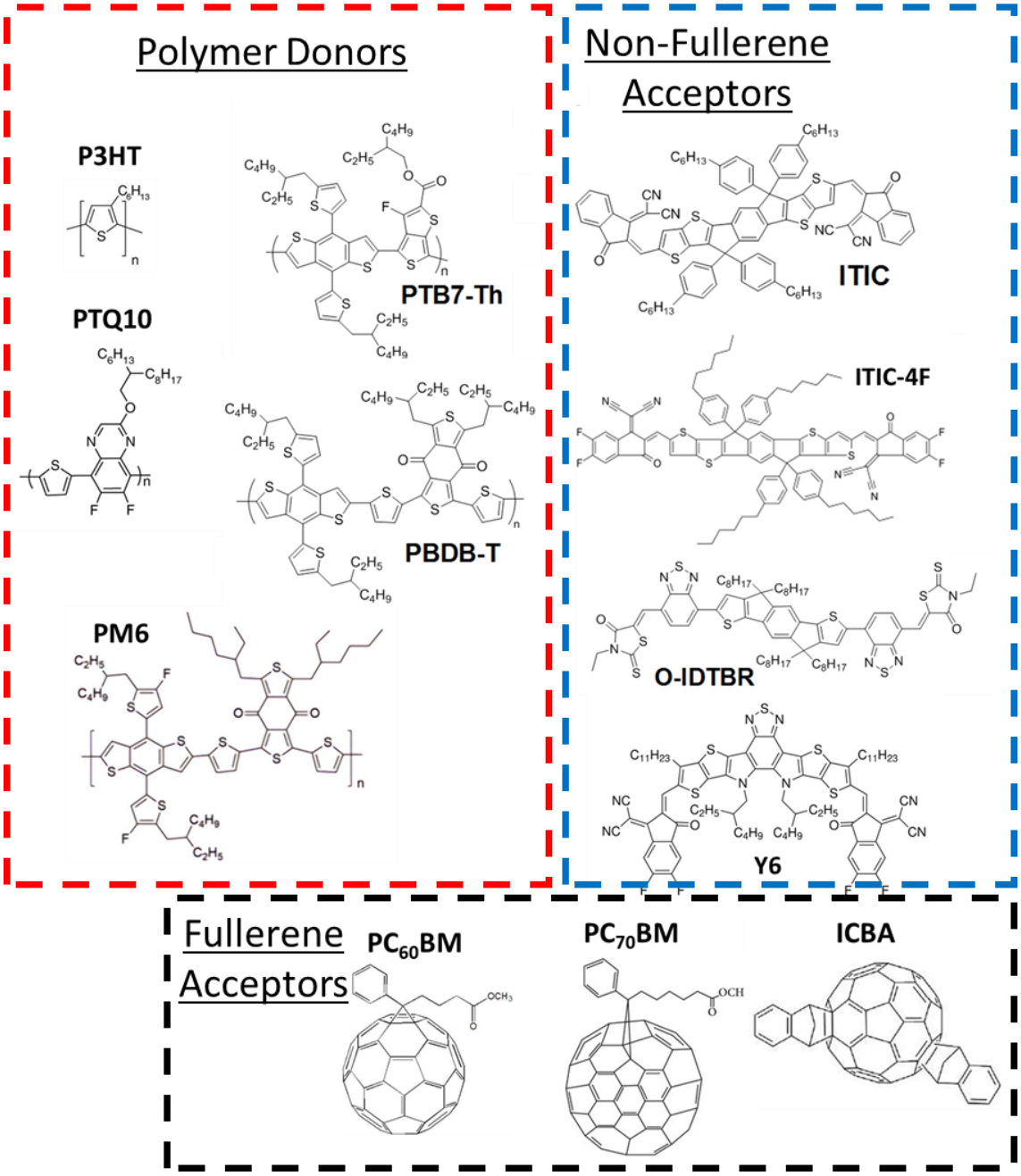


**Figure 4.** Examples of molecular structures for materials commonly used in OPV devices.

The architecture of the organic solar cell plays a crucial role in its performance and efficiency. A typical OPV consists of multiple thin film layers between the two electrodes. Depending on the polarity of these two contacts, the cell will have a conventional or an inverted architecture (Figure 5). A typical OPV comprise a total of 6 layers, in order starting from Sun side:

- Substrate: Transparent, possibly flexible
- Front electrode: Transparent
- Front charge transport layer
- Active Layer (AL)
- Back charge transport layer
- Back electrode: metallic

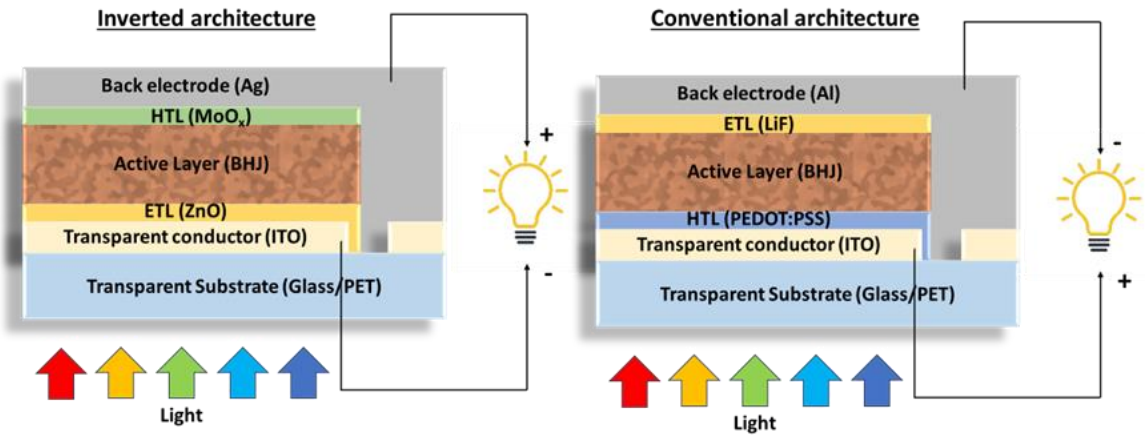


**Figure 5.** OPV device layer architectures. Between parenthesis in each layer is an example of common materials used (except for Active Layer, where it's mentioned the most common structure: bulk heterojunction).

In research settings, the most common substrate choice is Indium Tin Oxide (ITO) sputtered on glass. ITO serves as the transparent conductor necessary for the front electrode. However, ITO is the most expensive material in OPV, as it contains Indium, a scarce rare earth, and is deposited through sputtering, a relatively expensive technique.[31] Nevertheless, extensive research is being conducted to find more cost-effective and solution processable alternatives, such as graphene or silver nanowires.[32] For industrial applications, the glass substrate could be replaced with transparent flexible plastic, such as PET, keeping the flexibility of OPVs.

In lab-scale experimentation, a metal electrode is typically deposited by evaporation to serve as a back electrode. In industrial environments, the electrodes are typically manufactured with roll-to-roll (R2R) compatible techniques such as screen printing. Aluminum is the most frequently used metal for back electrodes in the normal architecture, while silver is preferred for the inverted architecture. The inverted architecture becomes more appealing from an industrial perspective due to silver's superior resistance to oxidation compared to aluminum, enhancing stability. Moreover, silver can be printed from paste or nanoparticle solution, increasing compatibility with R2R manufacturing.

The charge transport layers, also known as interlayers or hole and electron transport layers, are deposited between the active layer and the electrodes to enhance contact selectivity and charge extraction. The need for these interlayers arises due to the bulk heterojunction (BHJ) structure of the active layer, as it cannot ensure that the contacts are isolated from the opposite material. Therefore, to prevent recombination and losses, the presence of selective interlayers is needed.

The selection of materials for these interlayers depends on their energy level alignment with respect to the work function of the contacting electrode, as well as the donor's HOMO and acceptor's LUMO. In the inverted architecture, common interlayers include ZnO (ETL, electron transport layer) and MoO3 (HTL, hole transport layer), while the conventional architecture often utilizes PEDOT:PSS (HTL) and LiF (ETL). In lab-scale experiments, the first transport layer is usually deposited from solution before the AL, while the second transport layer is deposited by evaporation prior to the evaporation of the metallic back electrode.

Arguably, the most crucial part of the solar cell is the active layer (AL), which consists of at least two different organic semiconductor materials: a p-type (electron donor) material, and a n-type or (electron accepting) material. The selection of materials for the OSC aims to broaden the absorption band by using complementary absorbing materials and to maximize exciton dissociation through proper alignment of HOMO-LUMO energy levels. Other considerations include microstructure compatibility and solubilities.

## 3.4. Ternary OPV

Multicomponent OPV, and specifically ternary OPV, has garnered significant interest due to its potential to exhibit improved performance compared to binary OPV systems.[33–35] A multicomponent OPV refers to any OPV that incorporates more than two materials in its active layer. In the case of ternary OPV, the active layer comprises three materials: either 1 donor and 2 acceptors or 2 donors and 1 acceptor.

Ternary blends can present higher performance in one or more photovoltaic parameters when compared to the corresponding binaries, resulting in higher PCE. [36,37] Moreover, even in cases where the overall performance is not improved, ternaries can still be beneficial. For example, instead of a PCE increase, the addition of a third material with lower synthetic complexity can lead to a reduced manufacturing cost while maintaining performance. Similarly, a third material could be added to change the physical appearance of the device (e.g. color).

There is still not a full understanding of ternaries, but some mechanisms have been found to contribute to the improvement. These include complementary absorption of the materials, that broaden the absorption spectrum and therefore the light harvesting; Cascade energy levels that improve exciton dissociation, charge carrier transport and reduce recombination in the interfaces;[38] Enhanced open circuit voltage due to alloying-like effects;[39] Improved stability and photocurrent due to lock-in microstructure,[40] better phase separation and suppression of aggregation.[35]

Importantly, some ternary systems have been reported amongst the best performing OPVs reported to date. For instance, Zhan et al. showed that the ternary system PM6:Y6:BTP-M obtained a PCE of 17.03%, about 1.42% higher than the best of the corresponding binaries.[41] Another example by Cui et al. recently reported a 19% PCE ternary system with a PBQx-TF:eC9-2Cl:F-BTA3 active layer, increasing a 1.3% from the PBQx-TF:eC9-2Cl binary.[42] Several reviews have thoroughly explored the use of ternary systems and concluded the ternary approach a strong approach at increasing the efficiency of OPV.[30,43–45]

The most conventional protocol for optimization of ternary systems requires the exploration of a 2D composition phase space. This increases exponentially the number of samples required to tens or hundreds of samples, when compared to corresponding binaries. Therefore, it's extremely resource consuming, both in materials and time, or even non-possible.[46]

To circumvent this, the vast majority of studies regarding ternary OSCs, explore the composition phase space in ternary systems only partially. The most common strategy is locking the D:A ratio (usually to 1:1) and only varying the relative composition of the two materials with the same electronic character. As an example, $D:A1_x:A2_{(1-x)}$ or $D1_x:D2_{(1-x)}:A$. [36,47,48] Another approach often used is to fix the total D:A ratio of the best binary, and replace part of the main acceptor by the secondary acceptor.

However, there is no fundamental principle nor evidence that the optimal composition ratio is in the 1:1 trajectory in the phase space (or in any other phase space line for that matter).[40] In fact, a lot of binary systems (especially ones where transport and/or optical properties are unbalanced) show optimums far from the 1:1 ratio. Similar results can be found in ternaries as well.[36,40,49] In other words, the optimum composition can, in practice, be found anywhere in the phase space. The lack of a theory or predicting model that helps to identify the optimum composition implies that an experimental approach of exploration ought to be carried out for each new multicomponent system. In Figure 6 we show the composition and PCE of the

optimized devices obtained from 6 different papers and reviews for 1 donor and 2 acceptor ternary systems.

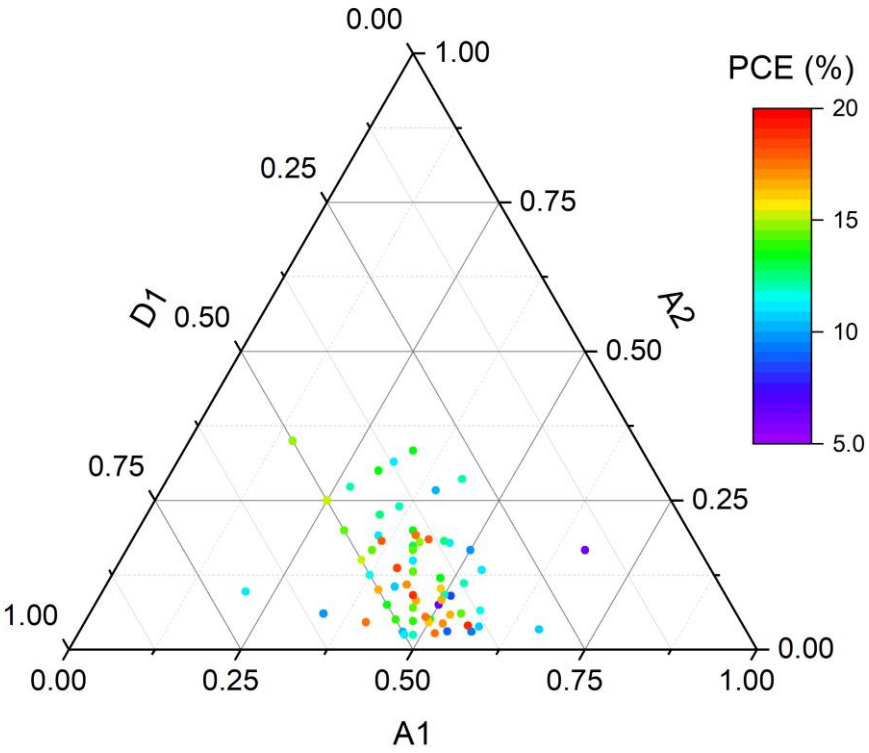


**Figure 6.** Review of the composition of the highest PCE of ternary system devices extracted from bibliography.[36,39,50–53]

It's noteworthy that outside the cluster of data seen in the Figure 6 was not explored in almost any of the papers, so it's impossible to know if any other optimized devices could be found there.

With the usual optimization process for ternaries, the maximum of performance might still be unknown, due to the limitations of the optimization process. This leaves room for even a greater improvement with respect to those initially reported. There may even be multiple maxima of performance in the same system. Therefore, methods that help to explore the phase space of ternary systems in a time-effective, material-effective and in more complete fashion are strongly needed.

## 3.5. Parametric Landscape

One of the main challenges in the research of Organic Solar Cells is the complexity of the parametric landscape, which ultimately determines the performance of the final device. Parameters such as layer thickness and composition, solvent selection, deposition parameters (e.g. temperature), and the resulting microstructure all play crucial roles. Moreover, these parameters must be optimized for each blend of Donor:Acceptor, of which there are dozens available commercially as of today, as well as for each layer of the device, which typically consists of a minimum of five layers and the substrate. The combination of these factors creates a complex, multi-parametric and highly correlated landscape that requires extensive research to optimize OPV and its major parameters like $V_{oc}$, $J_{sc}$ and FF.

Figure 7 shows a diagram depicting various parameters, their sources, whether they affect thickness, composition and microstructure, and how in turn these affect final $V_{oc}$, $J_{sc}$ and FF. Some of these effects will be further discussed below.

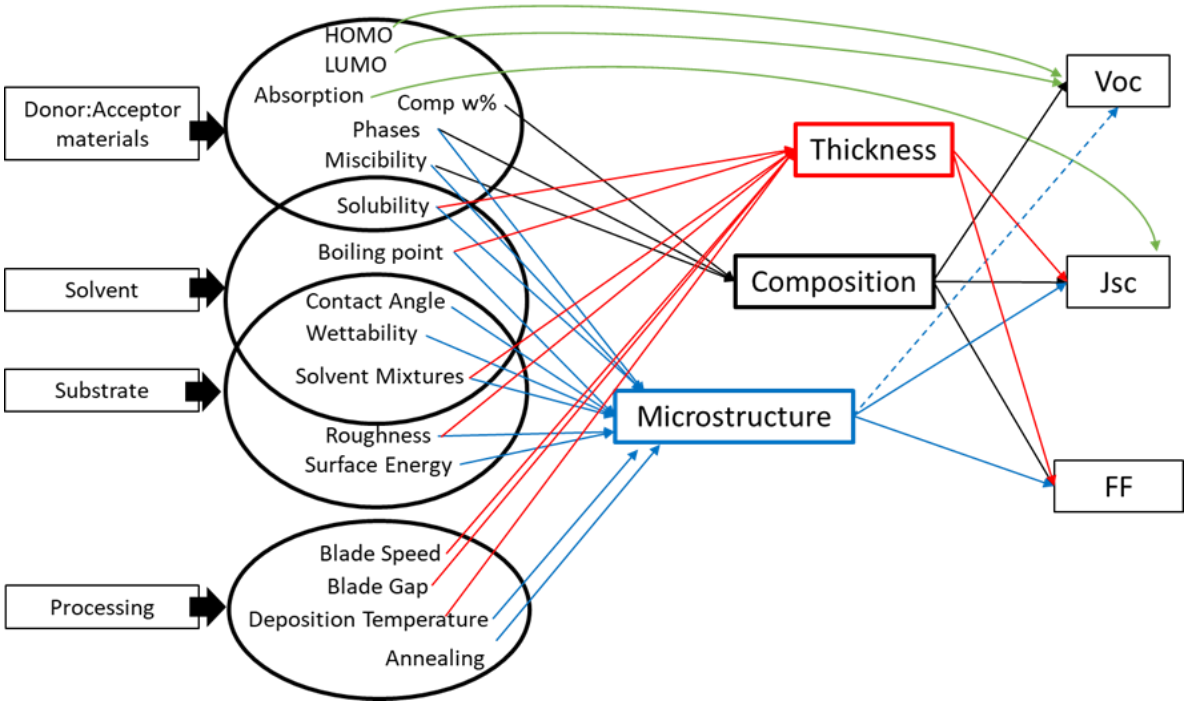


**Figure 7.** Interaction diagram of the parametric landscape in OPV. Note: this is not an exhaustive diagram, more parameters might have an effect in final performance.

As explained in Section 3.1, $V_{oc}$ mainly depends on the energy levels of the materials used (provided appropriate electrode choice). However, energy levels depend mildly on the microstructure and crystallinity of the materials.[35] Furthermore, this microstructure also influences the recombination of excitons, which in turn affects the $V_{oc}$ again. It also depends on the photocurrent (diode equation) but logarithmically saturates rapidly with light intensity.

Photocurrent depends mainly on light absorption and charge transport. In turn, absorption depends on the spectral overlap of the solar spectrum and the absorption coefficient of the active materials, along with the thickness of the layer. Interference patterns can appear in the

devices as the layer thicknesses are of the same order as light wavelength. Additionally, microstructure can influence both absorption and transport. The absorption coefficient and refractive index depend on the D:A composition ratio and the degree of order of the materials, such as whether they are crystalline or amorphous. On the other hand, transport also depends on the degree of order of the materials and the D:A ratio, especially when there exists an imbalance in hole and electron mobilities between the donor and acceptor materials.

Finally, FF depends mainly on charge transport. Several factors affect this transport process, such the charge carrier mobility of the active materials, the series resistance of the interlayers and electrodes, the selectivity of the transport layers and contacts, as well as any potential defects such as parasitic resistances or pinholes. Similar to photocurrent, the charge carrier mobility experiences considerable variation with microstructure.[54] Active layer thickness also influences FF, as thicker layers restrict charge transport, consequently leading to a decrease in FF with increasing thickness.

Hence, to optimize $V_{oc}$, $J_{sc}$ and FF we need to improve the associated parameters. Some of these, like energy levels, absorption coefficients and charge mobilities depend on the active materials and their microstructure. Conversely, parameters such as thickness and composition ratios are dependent on the manufacturing process. We need to know how to control microstructure, thickness and composition by using variables within the manufacturing process.

Without modifying the materials, there are three points of manipulation to alter microstructure, thickness and composition: The material solution, the depositing technique and its parameters, and post-processing.

First and foremost, given that OPV are solution-processed, modifications to the initial solution can influence the final device. Adjusting the concentration of the materials in solution can serve to regulate thickness, with higher concentrations yielding thicker layers. On the other hand, the solvent system also plays a significant role. Choices in solvent selection, co-solvent systems and additives have the potential to alter the final layer during deposition. Alterations in the solubilities of the materials and variations in boiling point of the solution lead to changes in the drying kinetics of the deposition. Consequently, this leads to changes in microstructure, as a faster drying “freezes” the BHJ in a thermodynamically out-of-equilibrium state. Conversely, slower drying permits the materials sufficient time for self-arrangement into a thermodynamic equilibrium. It's noteworthy that neither of those microstructures’ states can be guaranteed to be superior nor optimal, as the optimal microstructure is inherently determined by the materials themselves, including factors such as their crystallinity and tendency to aggregate.

The second avenue for influencing the final layer is the deposition technique and its associated parameters. There are several different deposition techniques, each offering distinct deposition kinetics. Examples include spin coating, slot die coating, spray coating, dip coating and blade coating.

In the elaboration of this thesis, the technique employed was Blade Coating, also called Doctor Blading or Knife Coating. This technique consists in positioning a sharp blade at a fixed distance from the substrate. The solution is then placed in front of the blade, spreading beneath it due to surface tension. Subsequently, the blade is moved at a fixed speed across the substrate. During this movement, part of the solution remains behind the blade, resulting in the creation of a wet film. Once film dries, the coating process is complete. Figure 8 illustrates a schematic of the blade coating process.

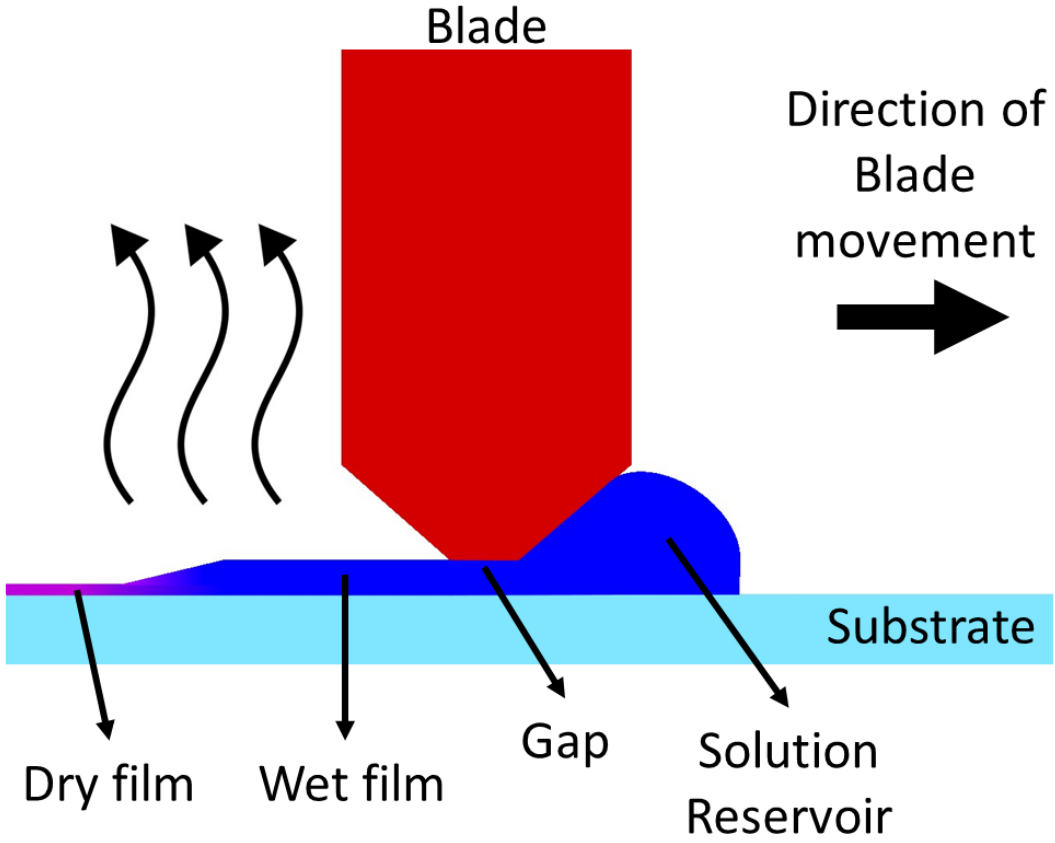


**Figure 8.** Schematic representation of blade coating technique.

Blade coating has several variable parameters that can be adjusted to change the final layer of the OPV device. Firstly, there is the blade gap, which refers to the distance between the blade and the substrate. Typically falling within the range of 50 to 300 µm, this gap can be modified to achieve varying outcomes. Larger gaps yield greater solution retention in the wet film, leading to the formation of thicker films.

The next adjustable parameter is the movement speed of the blade, usually in the order of tens of mm/s. Control over this speed can be exercised through the hardware of the blade coater setup. Higher speeds result in thicker films due to increased shearing forces that leave more solution in the wet film as the blade's speed rises.

Finally, temperature is very commonly applied in blade coating, to heat the substrate and/or solution. Temperature during deposition influences the drying kinetics of the wet film. Alongside the boiling point of the solvent, higher temperatures or lower boiling points cause rapid drying and the “freezing” of the microstructure. In contrast, lower temperature or higher boiling point lead to slower drying and the attainment of thermodynamic equilibrium within the microstructure.

Moreover, post-processing techniques offer further means to manipulate the resulting film. Vapor and thermal annealing are examples of such methods. Vapor annealing involves subjecting the device to an atmosphere saturated with vaporized solvent, while thermal annealing requires subjecting the device to elevated temperatures. Both approaches allow the movement and reorganization of materials within the layer, leading to microstructural changes that align more closely with thermodynamic equilibrium. However, the precise control of

parameters such as temperature, solvent selection, and duration is crucial in order to achieve the optimal microstructure and prevent excessive phase separation of the material.

Having explored the avenues for influencing thickness, microstructure, and composition, we now delve into the challenges inherent in optimizing these parameters.

Optimizing the thickness of the active layer is not a straightforward task due to a trade-off problem. Thicker active layers maximize light absorption, while thinner ones maximize charge extraction. This dilemma arises because the charge transport in organic semiconductors is lower compared to silicon.[55] Typically, $J_{sc}$ increases linearly with active layer thickness for thin layers (0-50 nm), has mild oscillations for moderate thicknesses (50-150 nm), and steadily decreases for thicker films (above 200 nm). This decrease in thick layers is due to the limited charge transport of the materials.

Another critical factor to optimize is the donor:acceptor blend ratio. Different blending ratios will affect both absorption and the microstructure of the active layer. Organic semiconductor donors and acceptors are often partially miscible, allowing their mixtures to be represented in phase diagrams. The blending ratio and deposition parameters, such as temperature, solvent, additives and deposition technique influence the thermodynamic phases present in the final dry film. This final solid-state mixture is referred to as the film morphology. Optimizing this morphology is a complex challenge, as both the acceptor and donor phases need to be blended in the scale of 10-20nm, which corresponds to exciton diffusion length. Additionally, they must form continuous percolating networks to enable charge transportation to the electrodes with minimal recombination.

Moreover, there is no known fundamental reason for the optimum blend of any given Donor:Acceptor to have any particular composition or even be close to 1:1 ratios. As a result, all new blends must be thoroughly optimized in their composition, covering a wide range of blending ratios with little more than an educated guess as a starting point. For instance, consider the blend of the semi-crystalline donor polymer P3HT with the fullerene acceptor PC70BM, which has an optimum blending ratio of 1:0.7 D:A.[56] In contrast, a somewhat similar blend with the same PC70BM acceptor and a more amorphous polymer, PCDTBT, has a rather extreme optimum blending ratio of 1:4.[57] Furthermore, when switching to non-fullerene small molecules acceptors, the acceptor's contribution to the absorption of the OPV increases, leading to changes in the optimum blending ratios. For example, in the case of polymer donor PM6 and NFA acceptor Y6, the optimum composition is 1:1.2.[58] Unfortunately, there is still no unified model capable of explaining the differences in optimum blending ratios. Therefore, researchers have to estimate the optimal ratio based on material features such as complementary absorptions, unbalanced charge carrier mobilities, oscillator strength, and miscibility.[59] However, confirming (or disproving) the initial estimate empirically necessitates the exploration of a large number of composition ratios, spanning as far as from 1:4 to 4:1.

Another method to control the film morphology is by influencing the drying mechanism of the blend solution, which can lead to changes in the final film morphology. Several factors can be adjusted to control drying, including deposition temperature, solvent choice and solvent additives. Additionally, post-deposition treatments, with thermal annealing being the most common, can also be employed. Thermal annealing can be used to "reset" the microstructure formed during processing and attempt to drive dissimilar morphologies into a more optimal configuration. However, this process is not without its challenges. It can result in excessive phase

separation in certain cases, such as when mixing materials with a low entropy of mixing (e.g., polymer:polymer blends) or materials that have a tendency to crystallize into large domains. Similarly, if starting from a "frozen," kinetically-trapped, or out-of-equilibrium morphology, sufficient energy during annealing can cause large phase separation, even reaching the limit of miscibility.

Typically, increasing temperature results in higher molecular mobility, which may lead to diffusion in the case of the small molecule (often the acceptor).[60] Even when annealing temperatures are kept below the glass transition temperature ($T_g$) of the polymer (the matrix), the small molecules can diffuse and form large acceptor domains. This process is clearly accelerated when $T>T_g$(matrix).[61] However, this might result in excessively large phase separation, even leading to device failure. As a result, fine-tuning of annealing temperatures and times is necessary to enhance the microstructure and, consequently, the final PCE. In some cases, the performance can increase up to 40% compared to the same unannealed device (e.g. PCDTBT:PC70BM blend).[62] On the other hand, some blends might perform better with no annealing at all.

Furthermore, changing the deposition technique can also alter the obtained microstructure. For instance, some blends that require annealing when manufactured by spin coating might experience a decrease in PCE with the same annealing when manufactured by blade coating, due to the different drying kinetics. Hence, the choice of deposition method must also be considered in optimizing the film morphology and device performance.

In situations where researchers lack the foundational principles and the predictive capability to decipher the behavior of complex systems, such as in the realm of OPVs, resorting to Edisonian experimentation—trial and error—becomes a prevailing approach. This method relies on extensive prototyping, entailing a step-by-step exploration of individual parameter combinations, often on a sample-by-sample basis. However, in the field of OPV this process is so tedious, and significantly expensive, both in man-hours and resources. This expense is compounded by the fact that crucial resources, like substrates and the active materials, are primarily designed for experimentation and come at considerable costs.

Given these constraints, many researchers find themselves compelled to restrict their exploration of the parameter space to certain "common" values, such as near 1:1 donor-to-acceptor composition ratios, active layer thicknesses around 100 nm, the use of single-solvent solutions, or standard deposition parameters. Unfortunately, narrowing the parametric landscape might lead to erroneous or incomplete conclusions in the screenings. Furthermore, researching Ternary OPV blends increases exponentially the size of the parametric landscape, turning the already challenging Edisonian approach almost insurmountable.

Hence, the pressing need emerges to formulate novel high-throughput strategies that would enable a more comprehensive exploration of the intricate OPV parameter landscape.

## 3.6. High-throughput experimentation

As explained in the previous section, the parametric landscape for OPV is vast and highly correlated. The sheer number of required samples and data points to determine a material's viability for OPV, optimal processing conditions, and device parameters is overwhelming. Consequently, researchers must develop novel experimental approaches that transcend the traditional Edisonian sample-by-sample method.[63]

Edisonian experimentation refers to an experimental methodology in which only one parameter is screened at a time, in search for its maxima or minima in a specific figure of merit. For example, the composition ratio of a certain OPV system is explored to discover its maximum PCE. Once located, the composition is fixed and we move on to screening the active layer thickness searching for its optimum. Nevertheless, screening one-dimensional parameters independently in the context of a multiparametric and highly correlated system such as OPV might lead to overlooking absolute performance maxima.

Combinatorial experimentation, in contrast, involves simultaneous screening of multiple parameters, realized by combining material properties or manufacturing variables. This means that combinatorial experimentation screens more than one parameter at a time, in search of the absolute maxima. Combinatorial studies can be categorized into fabrication-intensive and measurement-intensive methodologies. The former employs discrete samples with expedited manufacturing techniques, while the latter employs samples with parameter gradients, coupled with fast and intensive measurement techniques.

On the other hand, high-throughput methods deal with systematically changing a parameter at faster speeds, unattainable by the sample-by-sample Edisonian approach. High-throughput methodologies are inherently faster and resource effective than Edisonian approaches, allowing for the exploration of several parameters or systems in the same amount of time and same resource usage. This can be achieved through rapid manufacturing techniques, such as machine-automated production, or through the use of gradients, such as active layer thickness gradients.[59,64,65]

Lastly, Design of Experiments (DoE) represent experimentation strategies aiming to extract maximum information with minimal experimental effort. DoE strives to discover the performance maximums by strategically sampling the parameter space. In complex parameter spaces such as for OPV, the rationale for these strategies may prove too complex for researchers to develop. Nonetheless, data-driven software can be devised to generate DoE strategies. Artificial intelligence (AI), specifically Machine Learning (ML) is able to extract trends and correlations from extensive experimental data, predicting future trends in the parametric landscape. Genetic Algorithms represent another avenue, guiding experiments towards optimums and consequently reducing the number of samples needed. [59,66]

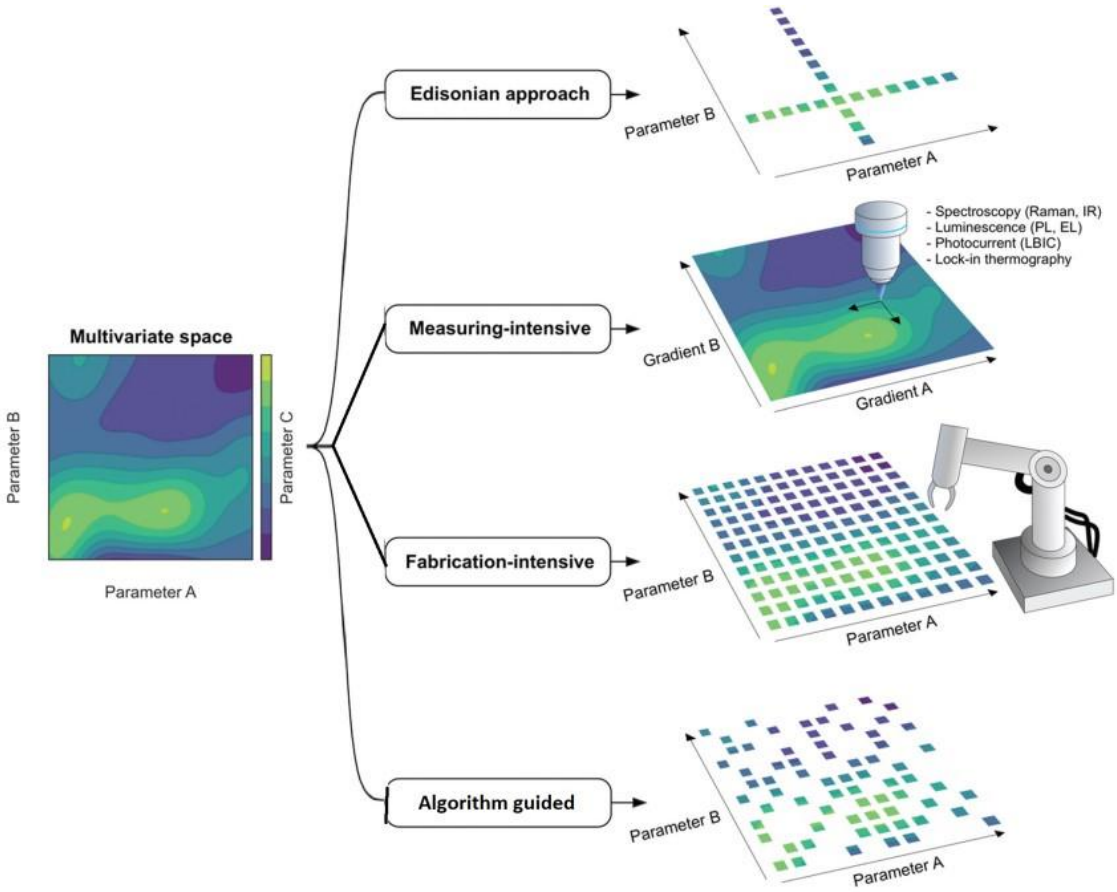


**Figure 9.** Example of the different experimental approaches to a multiparametric space exploration. This case can be compared to a typical case in OPV where A and B parameters are composition and thickness of the active layer, respectively, and C is PCE. Figure adapted from *Rodríguez et al.*[63]

Each of these experimental approaches boasts its own benefits, challenges, and associated costs.

# 4. Results

## 4.1. Global Summary and objectives

The main objective of this thesis is the development and application of new high-throughput methodologies for the fabrication and characterization of Organic Solar Cells in order to effectively and quickly optimize novel systems, for both binary and ternary OPVs. This goal is achieved by applying and improving methods already used within the research group, such as thickness and composition gradients, as well as designing new techniques to expand said methods for their use in ternary systems, and enhance the accuracy and reproducibility of the methodologies.

The pursuit of these objectives has led to the publication of four articles that have been peer-reviewed and published in high impact factor academic journals. While a brief overview of each of these articles is provided in this section, a more comprehensive discussion can be found in their respective sections. Furthermore, the complete articles have been attached at the end of this thesis for your reference.

In **Paper I**, published in *ChemSusChem*, we explored the use of a novel polymer acceptor, derived from the NFA Y5. This polymer acceptor, named PF5-Y5, was paired with the well-established and commercially available polymer donor PBDB-T, forming a promising new Polymer:Polymer system that required optimization with no previous information. However, due to the limited availability of PF5-Y5, this optimization required high-throughput techniques capable of generating maximal data with minimal material usage. For that purpose, we applied techniques already in use in our laboratory, being the main one for this study the use of thickness gradient in all fabricated samples, allowing for an intrinsic optimization of thickness in every individual sample, and therefore for every other parameter changed. Furthermore, the data collected underwent rigorous analysis, including statistical methods like ANOVA, which revealed solvent selection as the most critical parameter within this Polymer:Polymer system. Based on these insights, we devised a graphical representation to illustrate and even predict PCE with a representation of PCE in the Hansen solubility parameter space, avoiding the need to obtain the Hansen parameters for the materials.

In **Paper II**, published in *Journal of Materials Chemistry C*, we aimed to optimize yet another system, this time using a novel NFA, NIPb3T-Rd. The acceptor was paired with one of the most extensively studied materials in OPV, the donor polymer P3HT. Like in Paper I, the availability of the acceptor was limited, and therefore we needed to apply high-throughput techniques already in use within our group. This time, the selected foundational technique used for the study was the fabrication of composition gradients. These gradients allow the creation of large composition libraries, from where D:A composition ratios can be optimized in a single sample. However, for this approach to work, we needed some essential data from the novel NIPb3T-Rd, specifically nk coefficients, Raman spectra and Raman Cross-section. Once this data was obtained, a sample featuring a composition gradient was fabricated to identify the optimal composition. Subsequently, five discrete thickness gradient samples were produced to validate these results and optimize for thickness. Despite achieving modest performance results, this novel system was successfully optimized using only six samples.

In **Paper III**, published in *Advanced Energy Materials* and featured in the cover of the journal issue, we addressed one of the major challenges in Ternary OPV screenings: the increase in

dimensionality of the composition parametric landscape. This increase in the variables for Ternary OPV leads to a high-throughput methodology being even more essential than for binary systems. For that purpose, we expanded our high-throughput optimization methodology to be applicable to Ternary systems, specifically for one polymer Donor and two molecular Acceptors. We designed the fabrication procedure to be experimentally simple, reproducible and easily adaptable to explore different compositions within the ternary composition diagram. This approach is based on sequential deposition of pristine materials in a continuous device, generating large libraries of compositions within a single sample. These samples were subsequently characterized using Raman spectroscopy and photocurrent measurements. Notably, we enhanced our previous photocurrent characterization technique by incorporating a white excitation light source instead of a single-wavelength laser, significantly boosting measurement accuracy. Through this innovative methodology, we successfully optimized three distinct ternary systems, achieving this outcome with minimal sample utilization. Our results were further validated using discrete samples.

In **Paper IV**, published in *Advanced Functional Materials*, we further developed and fine tuned our ternary optimization methodology with a novel system. We developed a new normalization technique for extracted photocurrent data from composition gradient samples, enabling more accurate comparisons of photocurrents across different samples, even in the presence of defects that might otherwise skew results. Additionally, we explored new methods to increase the yield of the information extracted during the characterization, including how to correlate PL quenching, and therefore microstructure, with photocurrent generation. These enhancements significantly improved the reliability and utility of our ternary optimization methodology.

In the subsequent sections, I will provide a comprehensive review of each paper's key findings and discuss any related work that, while not directly addressed in the papers themselves, plays an equally essential role in this thesis.

## 4.2. High-throughput exploration of processing parameters

### *4.2.1. Fabrication of thickness gradient devices*

Active layer thickness is one of the most relevant parameters in OPV, and arguably one that requires extensive work as many (ca 10) separate samples are normally needed to find the optimum thickness. In order to accelerate this optimization and be able to do efficient thickness screenings, our group adopted a high-throughput technique based on creating thickness gradients over a single substrate,[67] and then evaporating an array of pixels on top. This allows for a complete screening in a single sample, covering the optimum thickness. As two arrays of 12 pixels are evaporated on both sides of the substrate, reproducibility is also checked with this geometry.

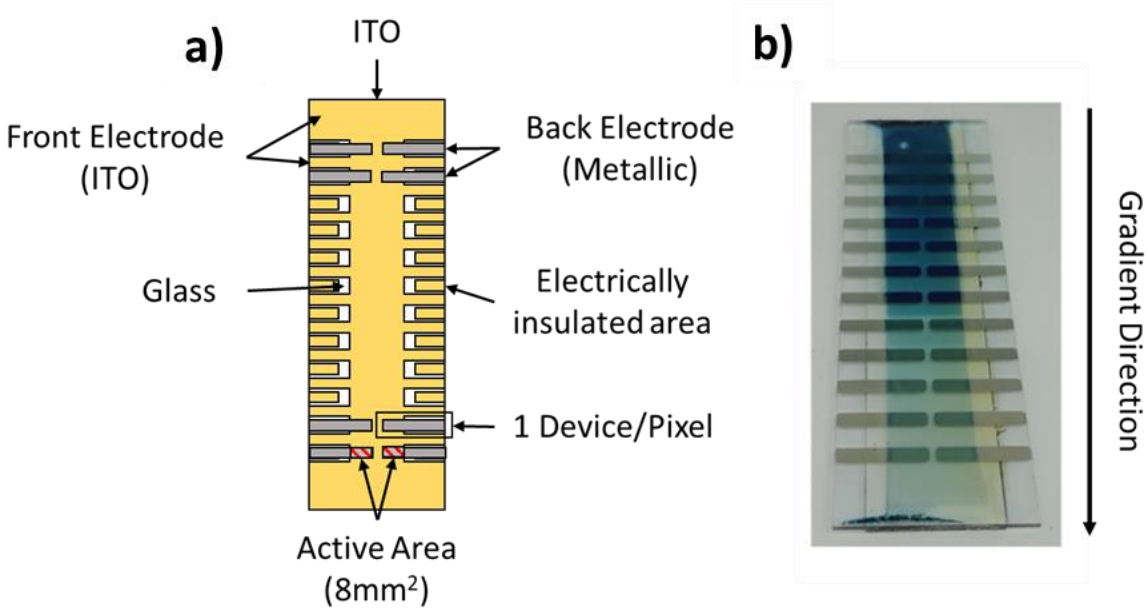


**Figure 10.** a) Schematic of a sample used for thickness gradient OPV devices b) Image of a completed thickness gradient sample, with 24 devices, 12 different thicknesses.

In blade coating, the thickness of the resulting film can be controlled by several factors: the speed of the blade, deposition temperature, blade-substrate gap, concentration of the solution, and volume of solution used.

For the manufacturing of thickness gradients in our laboratory, a commercial blade coater (Zehntner ZAA 2300) was modified by Dr. Bernhard Dörling, who coupled a speed controller allowing for a linear change in the speed of the blade (range from 99 to 1mm/s) during blading. By varying the speed linearly an approximately linear change in the final thickness of the deposited thin film is created. When manufacturing OPV with our typical materials (polymer:small molecule) with a speed range from 90 to 10 mm/s, a solution concentration around 20mg/mL and the substrate temperature selected for the solvent (Chlorobenzene ~90 °C, Chloroform ~40 °C), the resulting gradient ranges from around 200nm to 30nm within a 75mm long substrate. The exact values depend on the materials deposited and the other

deposition parameters mentioned previously, as well as if the blade is accelerating or decelerating during deposition (Figure 11).

Although multiple parameters can affect the final thickness, it is important to note that the results have been proved to be reproducible in multiple studies within our group.[68]

This variable speed approach can be used for all the solution-processed layers, but during this Thesis, it was only used for the optimization of the Active Layer (AL). Once the gradient in the active layer is introduced, the top electrode is evaporated in the form of 12 independent and consecutive pixels, so the specific thickness of the active layer is slightly different for each pixel, but quite homogeneous within one pixel (~170 nm gradient along 75mm gives around 2nm per mm, so <10nm difference typically within a pixel).

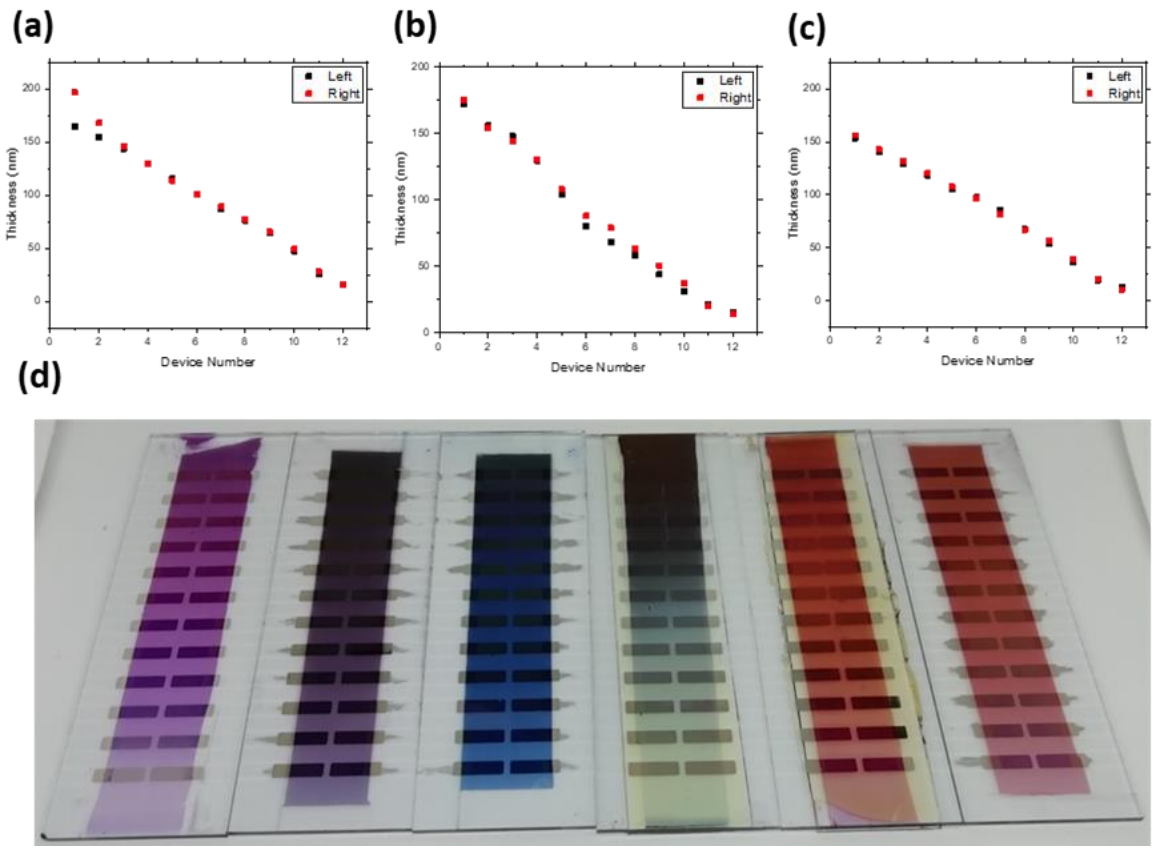


**Figure 11.** Example of devices fabricated with a standard thickness gradient technique. Thickness plotted against device number, where device 1 is the thicker (highest blading speed at 90mm/s) and device 12 is the thinnest (lowest blading speed at 10mm/s). Thickness measured with Profilometry. The 3 measured samples are active layers of a) PM6:Y6 b) PM6:ITIC-4F c) PM6:$PC_{70}BM$. d) Image of multiple samples with thickness gradient from thick on top to thin on bottom. **Note**: these samples are not the ones measured in a-c plots, but were selected just by physical appearance.

### *4.2.2. Paper I: Polymer:Polymer Solar Cells*

All-Polymer Solar Cells (All-PSCs) have attracted interest in the OPV community due to their potential advantages over conventional Polymer Donor:Small molecule acceptor OPVs. These include enhanced stability, both thermal and mechanical, and greater processing versatility, a critical factor in efficient industrial upscaling.[69–71] However, it's important to note that while all-

PSCs exhibit slightly lower overall Power Conversion Efficiencies (PCEs) compared to Polymer:Small molecule OPVs, this performance gap is progressively narrowing.[71–73] One of the factors for this lower performance is the formation of non-optimal film morphologies which, sometimes is related to lower absorption and electron mobilities in comparison to some of the most efficient small molecule acceptors. The lower electron mobility has been addressed by designing new polymers, like N2200. [73–75]

With these properties and the morphology issue in consideration, we set out to optimize a new Polymer:Polymer system using a novel polymer acceptor. The materials used for this study were PBDB-T as donor material and PF5-Y5 as acceptor material. PBDB-T is commercially available and was purchased from Brilliant matters, PF5-Y5 was synthesized by Prof. Wang group as reported in their study.[76] Importantly, due to the synthesis intricacies of the acceptor, a mere 24mg was at our disposal. This quantity would have been inadequate for a comprehensive screening utilizing conventional optimization techniques. Consequently, an approach leveraging high throughput methodologies became imperative.

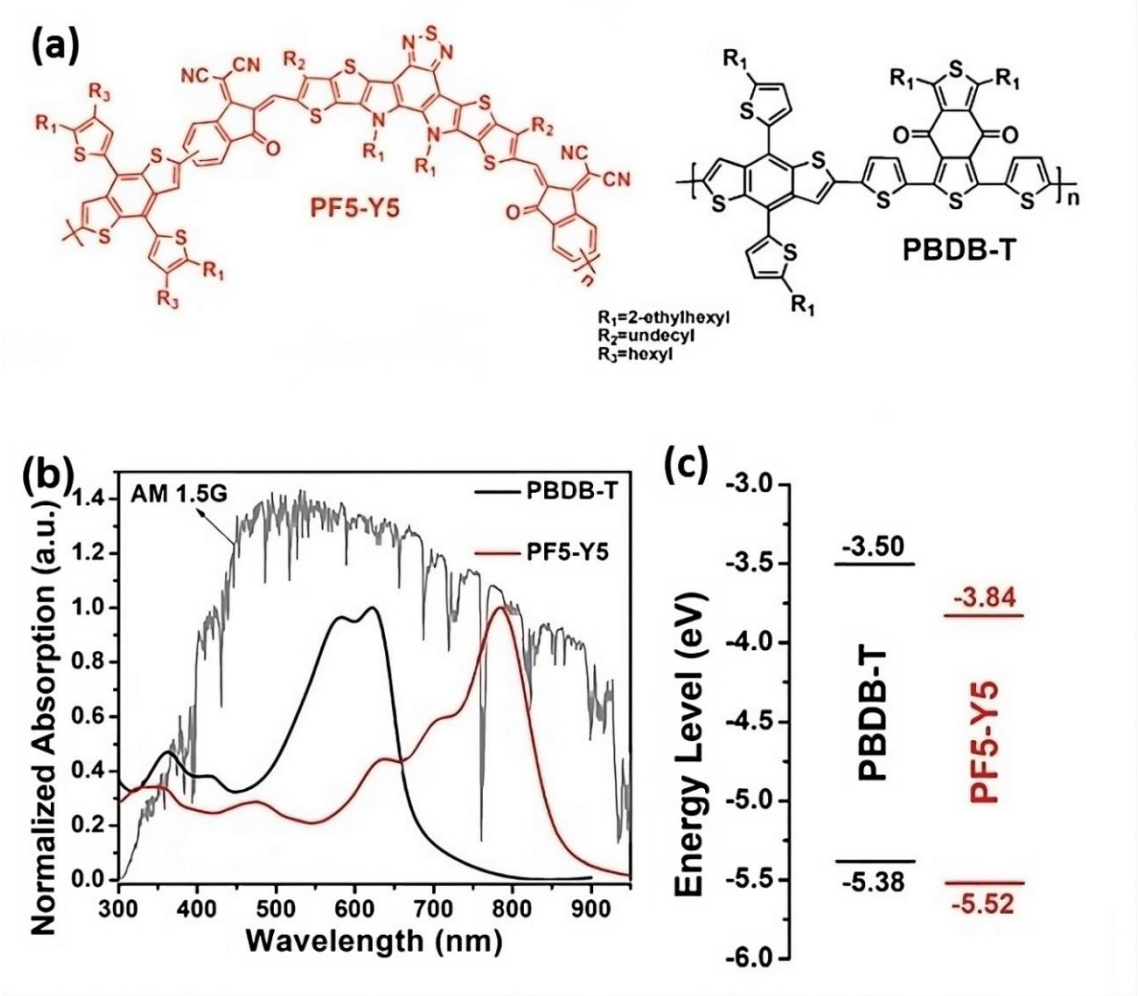


**Figure 12.** a) Molecular structure of polymer acceptor PF5-Y5 (left) and of polymer donor PBDB-T (right). b) Normalized absorption of both materials in neat films. c) Molecular energy levels measured from neat films using cyclic voltammetry.[76]

Thickness gradients were applied in every manufactured device, reducing drastically the amount of samples needed for a wide exploration of the parametric landscape. These thickness gradients for every sample freed up our ability to explore other critical parameters with the material that otherwise would have been used to explore thickness dependence. In total, we successfully manufactured 648 devices using only 22mg of donor and 24mg of acceptor, exploring up to 26 different processing conditions. These conditions encompassed a spectrum of factors, including the aforementioned thickness gradient, deposition temperature, solvent utilization, composition ratios, and sequential coatings

To put this into perspective, a comparable study conducted via spin coating would necessitate approximately 1.2mg of material per data point, ultimately amounting to a staggering 330mg for each material.[59] In our study, a mere 22mg of PBDB-T donor material and 24mg of PF5-Y5 acceptor material were utilized, averaging a mere 0.07mg per data point.

Figure 13 illustrates an instance of the measured parameters for a single sample from the PBDB-T:PF5-Y5 system's thickness gradient.

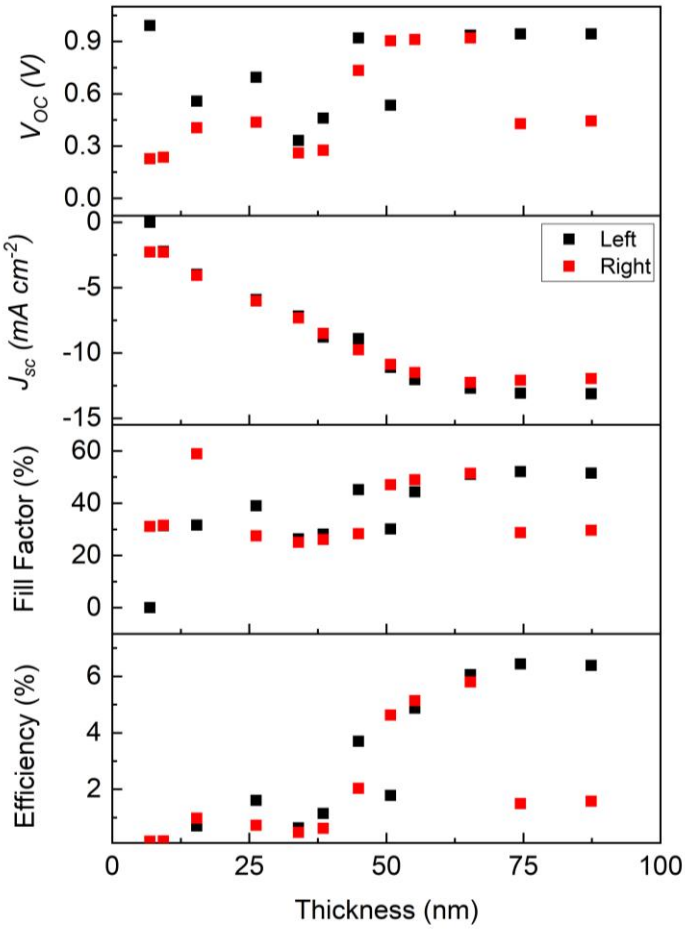


**Figure 13**. $J_{sc}$, $V_{oc}$, FF, and PCE as a function of active layer thickness for each pixel for one of the best solvents (CB/DCB). Each substrate contains 24 pixels, 12 on either side (labeled left and right). The thickness gradient is expected to be along the long axis of the substrate, leaving two nominal duplicates per thickness.

To determine which of the explored parameters have a larger impact in the final PCE, we performed a One-Way Analysis of Variance (ANOVA) on the main parameters of the fabricated devices.[77–79] This analysis yields the F factor, a quantification of the extent to which a given parameter alteration (such as thickness or solvent) influences a target parameter's variation (in this case, PCE). Therefore, the F factor serves as a gauge of the magnitude of a parameter's effect on the ultimate PCE outcome.

The results in the ANOVA study indicated that within the explored parameter space, solvent selection is the most critical factor, surpassing even thickness and D:A ratio. With these results we aimed to analyze the role of polymer solubility using Hansen solubility parameters. However, determining these solubility parameters for polymers is very material demanding, requiring in the order of tens to hundreds of milligrams for each of the materials. Since our study was based on obtaining the most information with the least amount of material, we opted to utilize PCE as a substitute for polymer solubility. Moreover, using directly the obtained PCE might be more informative in the optimization process, as it delivers direct information of performance vs solvent, while material solubility doesn't assure a direct relation to performance.

For each solvent system, we mapped the corresponding best PCE in the Hansen solubility space. To do that, we assigned the Hansen parameters of the solvent (or mixture) that was used for its active layer deposition to the color-coded value of the corresponding PCE. This results in a 3D image, whose 2D projections are shown in Figure 14. In this representation we obtain a continuous landscape with two maxima and a valley between them. This might be due to the difference in solubility of each material, the interaction between solvent and the possibility of some of the solvent/s promoting aggregation. It is noteworthy that the maximum in this representation does not represent the maximum in solubility but the optimum solubility of the PBDB-T:PF5-Y5 system for OPV.

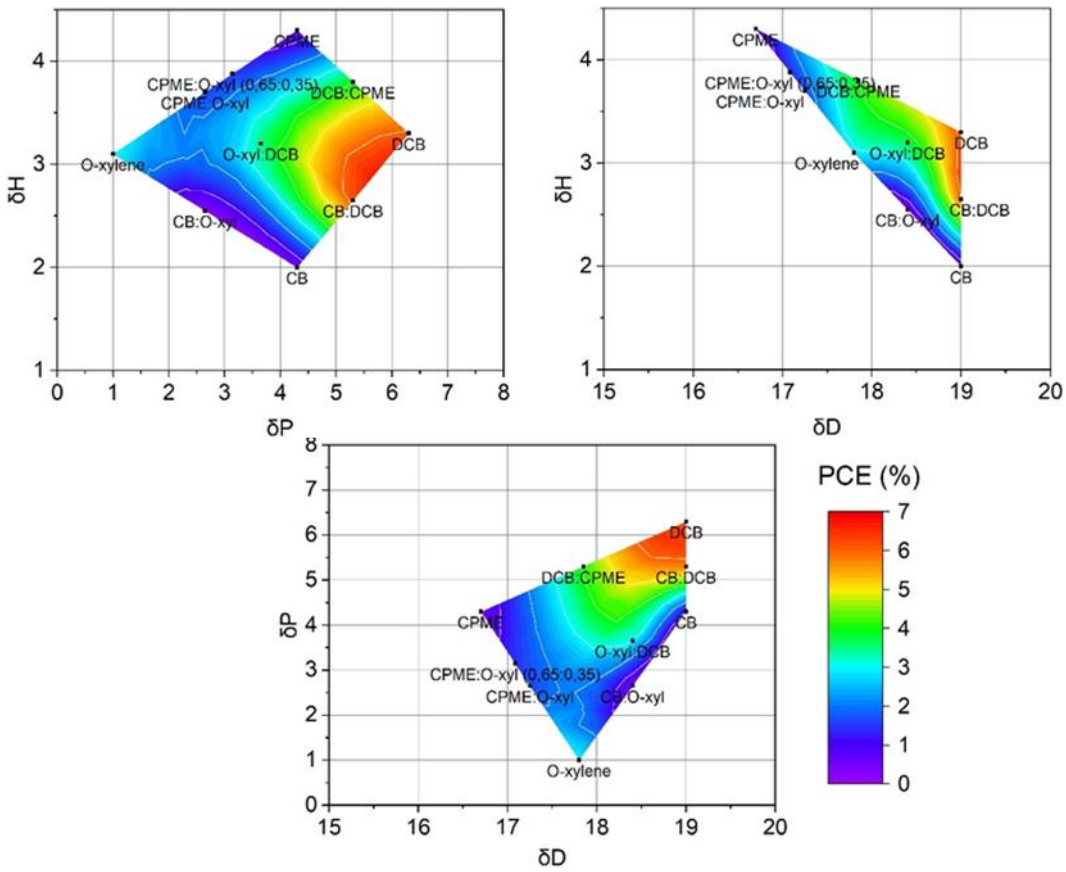


**Figure 14.** Performance landscape of polymer:polymer solar cells represented on the Hansen solubility space.

It should be pointed out that the original set of data only contained about 80% of the points showcased in Figure 14. After the first version of this representation was created, we decided to assess the prediction ability of this Hansen approach. As a result, we fabricated devices with two more solvent mixtures, and found out the results perfectly fitted into the surface. A complete study of the predicting ability of this approach would require a larger set of data points, and therefore much more material and solvent mixtures, which was beyond the scope of the study for Paper I. However, these results strongly suggest that this representation can be useful for solvent optimization in all-PSCs

### *4.2.3. High-throughput exploration of composition*

Another critical parameter for OPV manufacturing, besides active layer thickness, is the composition ratio, known as D:A ratio. Similarly to thickness studies, composition studies necessitate one sample per data point, as a distinct solution must be prepared for each composition. Following the same principle of obtaining more data points per sample and leveraging the use of gradients, we developed a method to manufacture devices with composition gradients.[80]

To obtain a composition gradient, both materials are individually dissolved in pristine solutions and then co-deposited side-by-side through a multi-nozzle pipette. When the rheology and deposition parameters are correct, during the blade coating these two solutions will mix, generating a composition gradient approximately orthogonal to the deposition direction.

Previous studies within our research group explored the processing parameters that allowed for this mixing. Specifically, optimal mixing is achieved through intermediate blading speeds (20-70 mm/s) and deposition temperatures (80-105 $^{o}$C). Exceedingly high speeds and/or temperatures may induce complete separation of the materials, colloquially referred to as “bacon effect” due to the resultant appearance of the layer. Conversely, slower speeds and lower temperatures may yield a fully homogenized layer.

Another important parameter is the miscibility of the materials and the viscosity of the solution. High viscosity solutions like Polymer:polymer prove more challenging to blend with this technique, whereas Polymer:NFA or Polymer:fullerene mix easier.[81] To mitigate the challenges posed by poor miscibility, a potential workaround involves introducing a small proportion (5-10%) of one of the materials into the solution of the other, and vice versa. This tactic serves to harmonize the viscosity of each solution, augmenting the miscibility of the solutions and consequently promoting enhanced mixing during deposition. Although this means that the pure materials will not be available in the device, that is not normally a major problem, as pure materials do not usually present a high OPV performance.

These composition gradients can be combined with thickness gradients, thus yielding 2D gradients, thickness following blading direction and composition more or less perpendicular to it. An example of a 2D gradient sample can be seen in Figure 15.

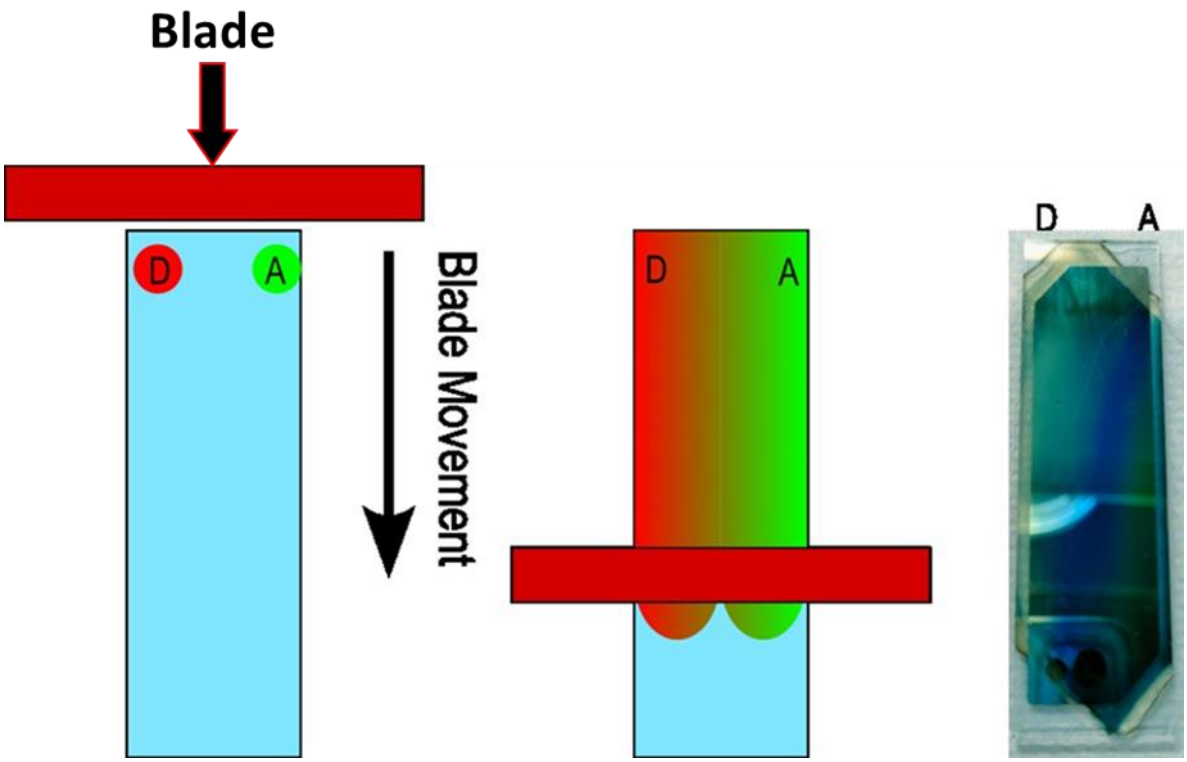


**Figure 15.** Sketch of composition gradient Active Layers, from left to right: Depositing two different solutions of pristine materials (Donor and Acceptor). Blade coating and mixing, gradient generation. Image of final result where the light blue areas (left) correspond to the donor, the dark green (right) to the acceptor, and deep blue (center) to the mixed region. **Note**: Colors in the final image have been digitally enhanced for a better contrast.

Due to the 2D-gradient nature of these devices, conventional methods of characterization are not directly applicable. Two options are conceivable: First one consists of homogeneously illuminating a sample that exhibits a 2D array of electrodes and measuring this sequentially using complex multiplexing detection. While this is advantageous in terms of the information it yields, enabling the acquisition of the full JV curve, its implementation proves complex. Moreover, the spatial resolution and number of data points would be limited by manufacturing constraints and the local composition would need to be checked independently.

The second option involves using a single pixel (continuous electrode) configuration and locally probing the performance through local illumination, which produces photocurrent only within the specific region of illumination. This approach is simpler, restrained only by the spot size of the illumination source. However, from a device point of view, it only provides $J_{sc}$ values, not $V_{oc}$ or FF measurements. Nevertheless, as will be elaborated upon later, this configuration allows us to concurrently measure the photocurrent and the local composition through spectroscopic tools.

In our pursuit of maximizing data points while adhering to a simplified manufacturing approach, we opted for the second alternative and transitioned to continuous electrode devices. This transition implies that each substrate will act as a singular OPV device, instead of the 24 devices of the non-composition gradient samples. To achieve this, the manufacturing process necessitates a slight modification. An additional chemical etching step is introduced, and adjustments are made to the cleaning and evaporation stages.

Considering our utilization of fully covered ITO substrates, we need to manually isolate the top electrode, and that is achieved by chemically etching the ITO in two strips at the corners, using solid Zn and diluted HCl in water, creating the two isolated electrodes. The cleaning and evaporation steps are modified to match the new shape of the electrodes. Figure 16 shows a schematic of the processing of the devices.

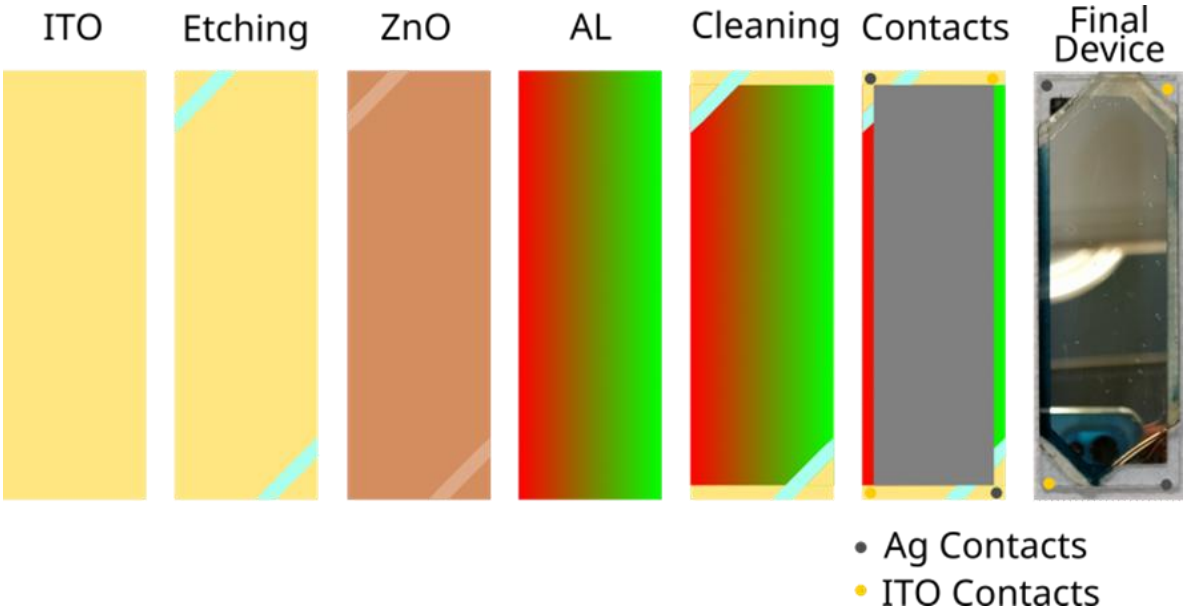


**Figure 16.** Schematic of the manufacturing protocol of composition gradient devices. Starting from left, ITO substrate (75mm X 25mm); Etching of ITO with ZnO and HCl to isolate 2 electrodes; Deposition of ZnO; Deposition of composition gradient; Cleaning of electrodes; Contact evaporation; Image of final device.

### *4.2.4. Characterization of composition gradient samples*

As explained in the previous section, the use of 2D composition gradient and single electrode, necessitates the development of a methodology to locally illuminate and measure photocurrent, as well as to deduce the local composition of the sample.

For the purpose of measuring the local photocurrent of each point of the device, we employed a variation of Laser Beam Induced Current technique, LBIC for short. In LBIC, a laser is focused on the device while this is electrically connected to measure its photocurrent. The laser scans the device, generating a photocurrent map across the device. However, a laser emitting a single wavelength is insufficiently accurate to characterize OPV, as it does not resemble the Solar Spectrum. The diverse absorptions of the plethora of materials used for OPV would result in the laser disproportionately promoting some materials with high absorption in its specific wavelength, potentially leading to skewed outcomes and the visualization of erroneous optimum compositions.

To address this limitation, we introduced a modification to LBIC, that we called WhiteBIC or WBIC. In this variation, the laser is replaced with a broadband light source, ideally a Solar Simulator light source. This adjustment permits a more equitable evaluation of the contribution of all constituent materials, and the resultant optimal compositions more closely align with those obtained through discrete sampling. However, a loss in spatial resolution is produced when using broadband light. In our setup, monochromatic light has a spot size of ~20µm in diameter, while for white light is ~150µm. Nonetheless, this spatial resolution is usually enough to characterize the devices and distinguish any significant detail, while being less prone to errors and scattering generated by defects.

Having established WBIC for the measurement of local photocurrent in devices, we only require a way to co-locally measure the composition. Previous studies within our research group demonstrated the power of Raman for mapping film features as composition and thickness. This approach remains applicable to operational devices, as it accounts for the complex refractive indices and interlayer thicknesses in its transfer matrix modeling. Furthermore, as Raman is measured using laser light (wavelength 488 nm in our case) it yields extra data, as LBIC can be measured simultaneously.

However, Raman characterization requires preparation and previous work for each new material. In short: The thin film cross-section has to be determined for multiple layer thicknesses, usually by manufacturing a thickness gradient sample. The Raman spectra of the pure material in thin film is also obtained. Additionally, refractive index (**n**) and extinction coefficient (**k**) coefficients are required, usually obtained through ellipsometry from the same gradient sample. A more in-depth explanation on how to extract composition from Raman spectra can be found in prior works of the research group.[80,82,83]

Given the concurrent measurement feasibility of Raman and WBIC, in our configuration involving the same setup, both the photocurrent under Solar Simulator light and the local composition can be obtained and mapped. This facilitates obtaining detailed images of both. An example in a working OPV device can be seen in the next section (Figure 18).

### 4.2.5. Paper II: Novel material optimization: P3HT:NIPb3T-Rd

With the complete binary system optimization method implemented, we decided to apply it to novel materials coming from a collaboration with Prof. Jose L. Segura and Dr. Matías J. Alonso-Navarro (Universidad Complutense de Madrid), who had recently developed a series of promising small molecules. These molecules are naphthalimide fused thienopyrazine derivatives, and exhibited potential to act as NFAs. After a short preliminary study, we decided to focus our optimization process in just one of the molecules, named NIPb3T-Rd.

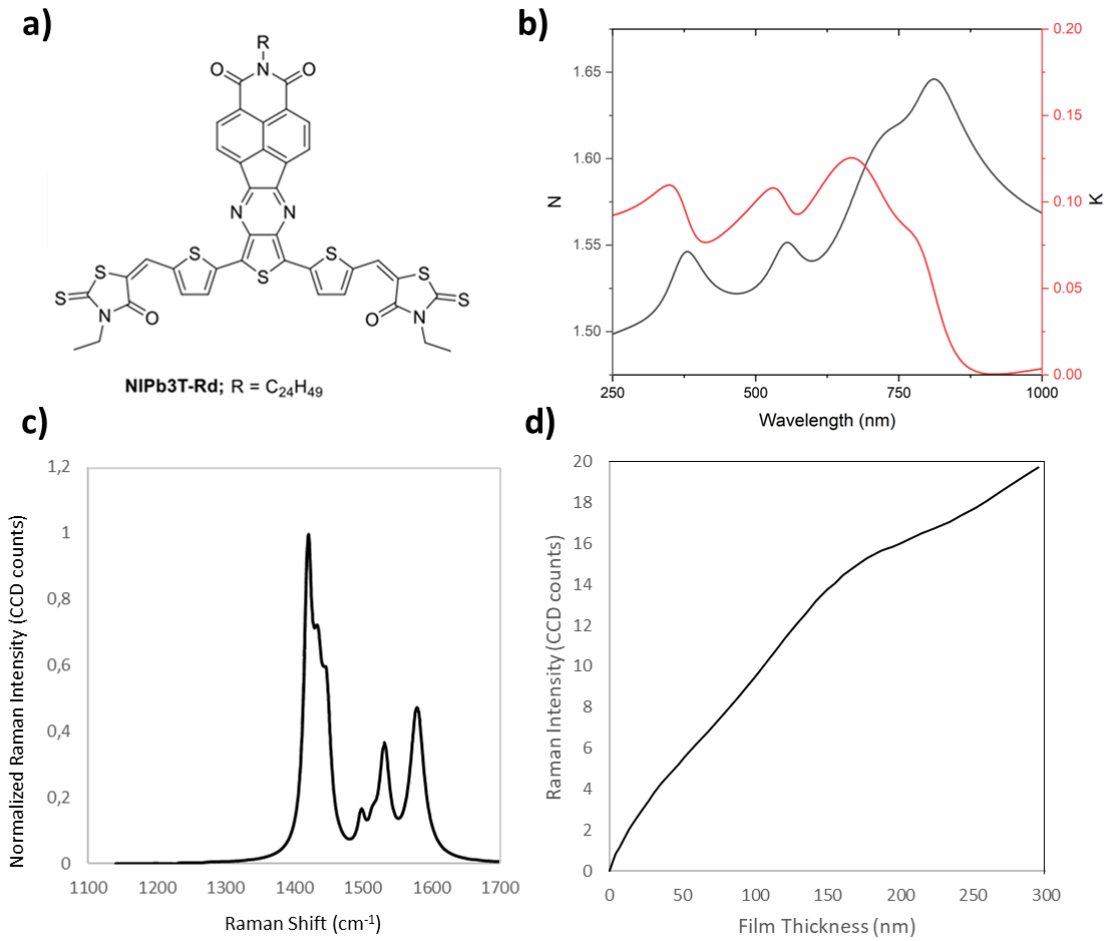


**Figure 17.** a) Molecular Structure of NIPb3T-Rd. b) n and k coefficients obtained with Ellipsometry c) Normalized Raman spectra of NIPb3T-Rd in thin film (488 nm excitation laser, averaged from different thicknesses) d) Raman intensity vs Film thickness.

This molecule could be a good candidate for OPV, combined with P3HT, a readily available and commercial donor polymer that, while offering moderate performance, boasts an exceptionally low cost. Moreover, the low band gap of NIPb3T-Rd leads to a complementary absorption with P3HT, thereby facilitating the absorption of a broader range of solar spectrum wavelengths. Unfortunately, the limited availability of NIPb3T-Rd imposed certain constraints on the study, as only a small quantity of the acceptor material was at our disposal.

In preparation for the subsequent Raman Characterization, we needed to obtain essential data for NIPb3T-Rd, specifically nk coefficients, Raman spectra and Raman Cross-section. To achieve this, we blade coated a film of pure NIPb3T-Rd onto a glass substrate, applying a partial thickness gradient, resulting in homogeneous thick and thin layers on opposite sides of the substrate, with a gradient in between. Then, nk coefficients were obtained through ellipsometry, measuring the

thick and thin layers separately. The Raman spectra and Cross-section were collected using Raman spectrometry with a 488 nm laser excitation, scanning across the thickness gradient in the film. The results of these measurements are summarized in a previous figure, Figure 17. Notably, the values obtained at a wavelength of 488 nm were especially critical, as subsequent Raman characterizations would be conducted at this specific wavelength. The obtained values for n at 488 nm were 1.52, and for k, they were 0.096. For Raman Cross-Section, opting for simplicity and data consistency, we normalize all cross-sections to the values obtained for PC70BM, obtaining a ratio for each material. In the case of NIPb3T-Rd, the normalized cross-section was determined to be 0.15±0.02 for its Raman band at 1421 $cm^{-1}$ and 0.07±0.01 for the band at 1580 $cm^{-1}$.

With all the necessary parameters, and using the available materials, we proceed to fabricate a composition gradient sample using the two-drop method, and analyzed it via Raman spectroscopy (with 488nm LBIC) and WBIC, effectively mapping both the composition and photocurrent. Figure 18 presents the outcomes of these three maps, with the WBIC map representing the entire device, while the other two offer a closer view of a particularly interesting area

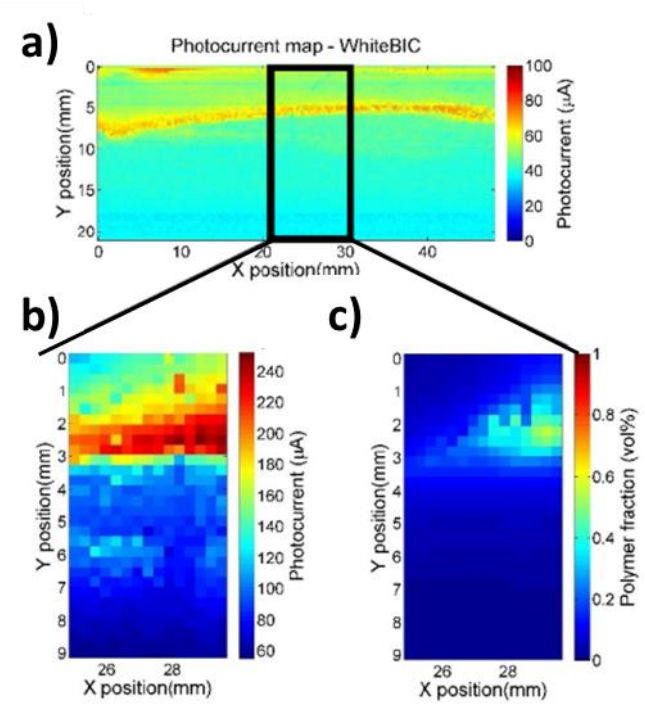


**Figure 18.** a) Local photocurrent under white light mapping (WBIC) of a P3HT:NIPb3T-Rd OPV device with a composition gradient. b) Local photocurrent under 488nm laser illumination, zoomed in c) P3HT fraction map, zoomed in.

Through the examination of this single sample, preliminary insights into performance were gleaned. Our deductions indicated that the most favorable efficiencies occurred within polymer-rich compositions. To gauge the accuracy of the composition gradient method, we crafted five discrete samples characterized by thickness gradients and varying P3HT:NIPb3T-Rd composition ratios encompassing the optimal range identified by the continuous sample. Each of these five discrete samples comprised 24 separate cells, allowing for the determination of essential electrical parameters such as $J_{sc}$, $V_{oc}$, FF, and ultimately, the overall PCE. Moreover, the thickness gradient facilitated a rapid optimization of layer thickness, as it generated 12 distinct thicknesses, each with two corresponding devices, culminating in a total of 24 data points per composition. The outcomes are depicted in Figure 19.

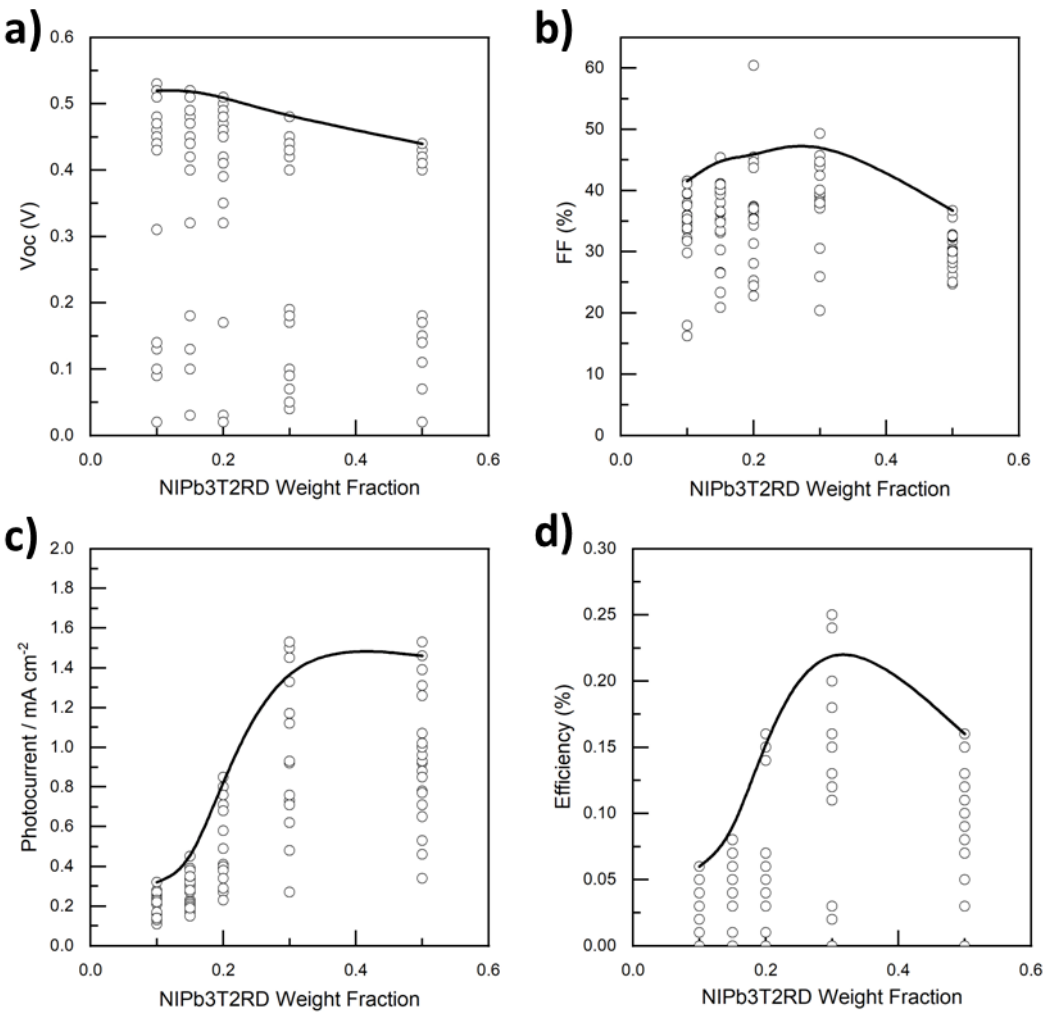


**Figure 19**. Electrical parameters of discrete OPV devices with a thickness gradient, for 5 different P3HT:NIPb3T-Rd composition ratios a) Open circuit voltage. b) Fill Factor c) Short circuit current d) Efficiency.

Despite the very modest PCEs, the final results indicate an optimal composition of 0.7:0.3 D:A ratio, aligning well with the results obtained from the 2D composition gradient method. Consequently, we established that the high-throughput approach proved dependable, robust, and capable of optimizing a novel system with as few as 6 samples.

## 4.3. Paper III: Exploring the composition space in ternary solar cells

As explained in Section 3.4, Ternary Solar Cells are promising due to their enhanced performance and array of advantages. However, the optimization process for ternary systems is too complex, demanding substantial resources and time. This often results in optimization efforts that are partially incomplete or confined within narrow scopes.

The primary challenge in the optimization of ternary systems stems from the inherent 2D composition space. This complexity necessitates the creation of numerous samples with varying compositions to comprehensively explore the parameter landscape. In light of this, we sought out on designing an innovative methodology aimed at exploring the ternary composition space more efficiently with reduced time investment, resource consumption and material usage.

We based our approach on adapting the 2D composition gradient method employed for optimization of binary systems explained in Section 4.2.4 (Paper II), aiming to expand the methodology to ternary systems. However, this expansion was not straightforward, as more complex gradient deposition and characterization techniques needed to be developed during this thesis in order to expand from binaries to ternaries.

Therefore, we explored a range of processing strategies, including multi-drop depositions and sequential depositions. Among these variations, we found that a layer-by-layer (sequential) deposition method offered the most advantageous balance of reproducibility, comprehensiveness, and adaptability for generating ternary composition libraries. As a result, we focused on developing this layer-by-layer approach.

In this selected processing technique, the ternary libraries are generated by depositing sequentially the active materials (D, A1 and A2) from separate pristine solutions, while maintaining the other deposition parameters the same (Solvent, deposition temperature). This sequential deposition using non-orthogonal solvents doesn't lead to the "washing" or detachment of the layers below. Instead it generates vertical intermixing and, in some cases, to a gradual vertical segregation. This layer-by-layer approach has been used to optimize vertical phase segregation in some binary Polymer:NFA devices.[84,85]

In the case of ternaries with 1 Donor (polymer) and 2 Acceptor (FA or NFA), our study underscores the significance of the deposition order in shaping the resulting ternary libraries. The process starts with the deposition of the polymer (donor) layer, followed by the sequential deposition of the two acceptors. Our experimental findings indicate that initiating the process with the deposition of small molecule acceptors does not yield functional devices. Our current hypothesis is that viscosity of the polymeric solution is critical when depositing it as second or third layer. In such instances, the comparatively lower molecular mobility of the polymer impedes complete mixing with the acceptor layers below. This results in a more discrete stacking of layers rather than the desired vertically mixed gradient. In contrast, when the polymer is deposited first, the small molecule acceptors exhibit greater mobility, enabling the creation of a well-mixed layer arrangement. Furthermore, the polymer layer typically adheres more effectively to the substrate, preventing detachment during subsequent layer depositions. When initiating the process with a small molecule acceptor layer, the likelihood of partial washout of that layer increases, yielding a more limited ternary library.

The full fabrication process starts by depositing the polymer in a large area substrate (75x25mm), either as a homogenous layer or a thickness gradient layer. Following a few seconds pause to reset the blade and ensure the complete drying of the first layer, the second layer deposition is initiated from a corner of the substrate rather than the edge, while maintaining a

fixed blade speed. This generates a rather controllable thickness gradient, achieved by the change in the wetting front, as this front travels through the substrate. For the third layer, we simply rotate the substrate again along the long axis, and start the deposition from the corner on the other side of the long axis of the substrate. A schematic representation of the process and the results expected can be seen in Figure 20.

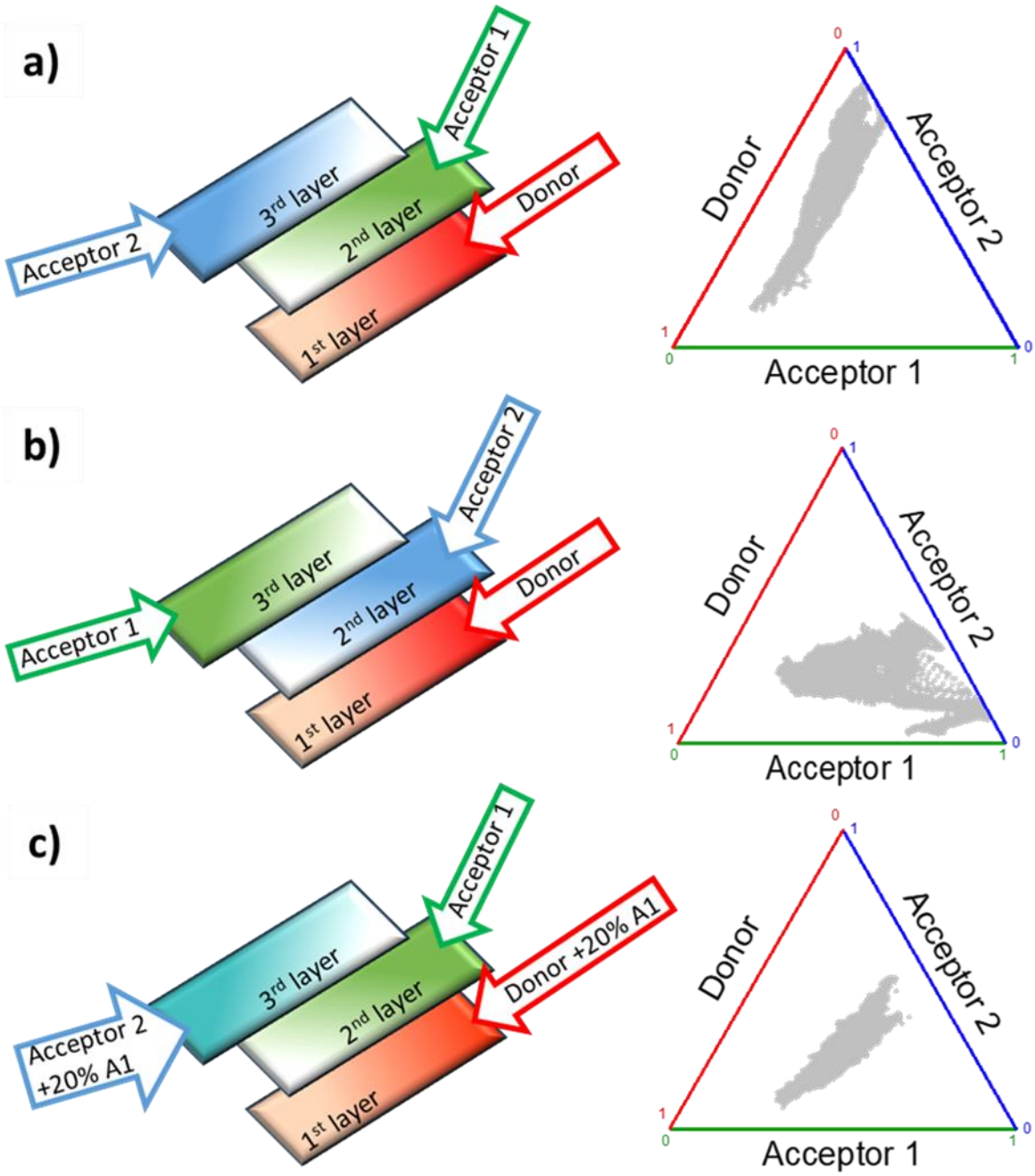


**Figure 20.** Sketches of the sequential blade coating deposition steps used to explore ternary blend composition diagrams for a) Gradient first donor layer with sequential Acceptor 1 as 2nd layer and Acceptor 2 as 3rd layer; b) Changing the order of the two acceptor layers; c) Adding 20 w% of Acceptor 1

to the solutions of Donor and Acceptor 2, same deposition order as the first sample. The dots correspond to experimental data obtained for a PTB7-Th:ITIC-4Cl:ITIC-4F ternary.

From an experimental standpoint, this processing approach remains notably simple. The only alteration to the conventional deposition process is the two rotations of $45^{O}$ of the substrate and doing three coatings instead of one. No modifications are needed to the coating set-up, the substrate or any other layer.

Furthermore, the exploration range within the ternary diagram can be finely tuned by implementing a range of simple modifications to the processing methodology. We have explored extensively, and among the most impactful variations is the alteration of material order within the 2nd and 3rd layers. This leads to substantial differences in the relative loading of the two acceptor materials in the layer, allowing covering very separate zones on the ternary diagram. This becomes especially advantageous for the initial development of devices in a new system. By generating a ternary data library that spans a broader region of the ternary diagram, we establish a foundational platform for subsequent experiments.

Another approach to fine-tune the covered region involves the addition of a percentage of one material to the solution of the others (and consequently the other layers). This strategic adjustment enables a finer degree of control over the covered zone. Notably beneficial for targeting new zones previously beyond reach in initial system experiments, this technique accentuates the adaptability of the method.

These modifications, designed with simplicity and adaptability in mind, resonate with the overarching philosophy of maintaining an uncomplicated experimental process.

It is worth noting that other adjustments, such as altering the blade speed for one of the top layers or modifying the concentration of one of the pristine solutions, were also explored. However, these alterations yielded a less predictable exploration of ternary space in some instances, and in certain cases, complications during deposition rendered the samples unusable.

We conducted evaluations to detect excessive vertical segregation within the active layer—a potential consequence of insufficient mixing in the layer-by-layer deposition process, potentially leading to a layered structure. It's noteworthy to point out that the majority of devices manufactured with this methodology have an inverted architecture. With a layered structure of the active layer, the donor material would be contacting the ETL, which is the opposite transport layer, a configuration that would render the devices non-functional. Contrary to this scenario, our findings indicate that devices with different architectures (normal and inverted) fabricated with identical deposition parameters and materials yield very similar photocurrent values.

### *4.3.1. Materials*

Our investigation has been directed towards three different D:A1:A2 blends: PTB7-Th:ITIC:PC70BM, PBDB-T:ITIC:PC70BM, and P3HT:O-IDFBR:O-IDTBR. The first two combinations are expected to maximize the absorption by pairing a low bandgap polymer (PTB7-Th or PBDB-T), the low bandgap and highly absorbing ITIC and the UV-absorbing PC70BM. This blend not only facilitates the harvesting of shorter wavelength photons but also contributes to the refinement of film morphology.[44,86] In contrast, the ternary blend P3HT:O-IDFBR:O-IDTBR represents a paradigmatic example of complementary absorption that has demonstrated to yield PCEs as high as 7.7%. This promising performance is notable due to the economical nature of mass-producing these active layer materials.[48]

The determination of the local composition of inhomogeneous blend films by means of Raman spectroscopy underpins our high-throughput methodology.[80,82,83] This technique enables the use of gradients produced from solution with moderate spatial control. However, it imposes certain restrictions on the materials to be tested, which we need to pre-evaluate for the selected ternaries. Specifically, all materials should be clearly distinguishable in terms of their vibrational fingerprint. The inherent heterogeneity of the conjugated backbones in organic semiconductors translates into peak-rich and characteristic vibrational spectra, mainly in the spectral window associated with C=C and C-C stretching modes (≈1200–1600 cm−1).[83] Figure 21 depicts the vibrational Raman spectra of three different donor materials, namely PBDB-T (aka PCE12), PTB7-Th (aka PCE10), and the workhorse p-type polymer RR-P3HT. Figure 21 illustrates the Raman vibrational fingerprint of four different conjugated small molecules used as electron transporting materials: a fullerene acceptor, PC70BM; and three NFAs, ITIC, O-IDTBR, and O-IDFBR.

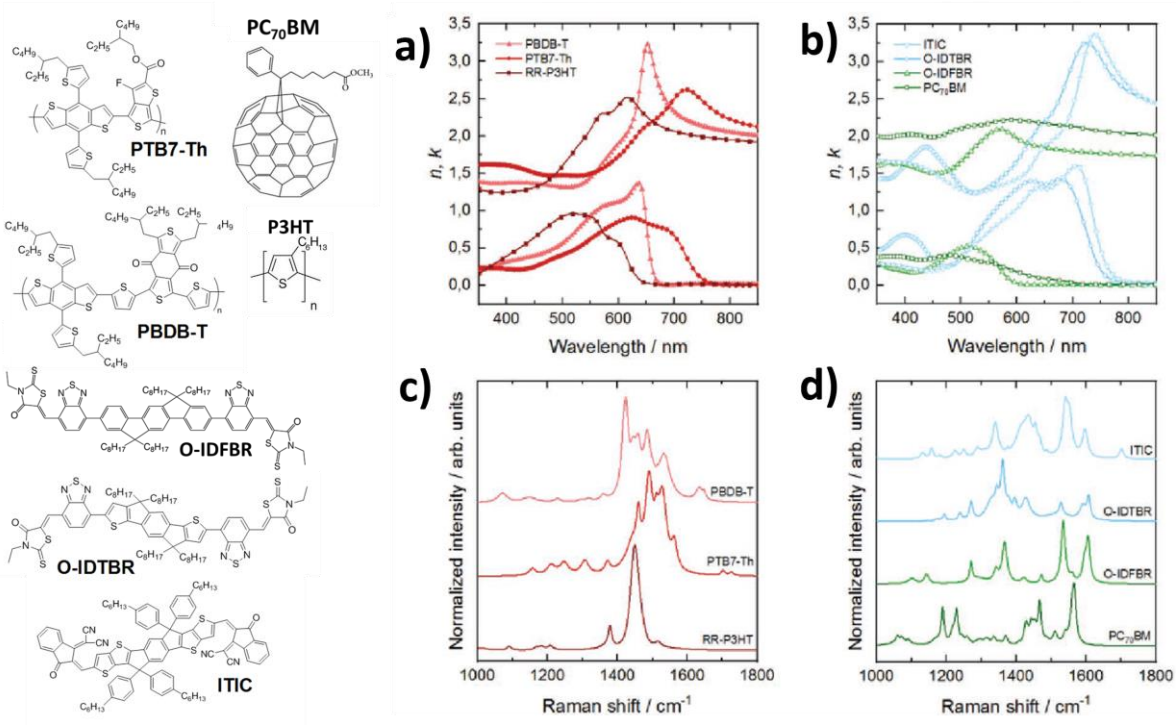


**Figure 21**. (Left) Chemical structures of the organic conjugated donor and acceptor materials used in this work. (Right) a) Refractive indices measured by means of variable-angle spectroscopic ellipsometry (VASE) of organic donors and b) organic acceptors. c) Normalized Raman spectra of donors and d) acceptors at 488 nm excitation.

A comprehensive analysis of this vibrational database indicates that all potential ternary combinations should, in principle, be readily distinguishable. The Raman fingerprinting capability does not, hence, represent an important restriction in this sense (see also Ref.71). Additionally, a successful analysis of ternary blend films requires the Raman cross-section of the materials to be similar enough to properly deconvolute the spectra and enable an accurate quantification of the composition of the film. Otherwise, a large Raman intensity ratio between dissimilar materials might hinder or even impede a proper deconvolution.[82,83] Table 2 summarizes our experimentally deduced Raman cross-section for the seven materials employed, a determination that requires previous knowledge of the complex refractive index of each material (see Figure 21) and the measurement of the thickness-dependent Raman signal using a sample with a thickness wedge. Following our previous accuracy estimates, only those blends including RR-P3HT as donor and either ITIC or PC70BM as acceptor(s) would be problematic due to their cross-section ratio being larger than 30. Note that the Raman cross-sections and refractive indices only need to be measured once per material, and can be also taken from literature.[83]

**Table 2.** Raman Cross-sections as ratios of PC70BM Cross-section. All measured at 488 nm excitation wavelength. The Raman band used for each Cross-section is also included.

| Material | Cross-Section | Raman Band ($cm^{-1}$) |
|---|---|---|
| RR-P3HT | 57±11 | 1450 |
| PTB7-Th | 2.4±0.3 | 1490 |
| PBDB-T | 5±1 | 1424 |
| O-IDFBR | 9±1 | 1535 |
| O-IDTBR | 4±1 | 1361 |
| ITIC | 1.2±0.3 | 1540 |
| PC70BM | 1 | 1557 |

### *4.3.2. Characterization of ternary composition gradients*

This section focuses on the characterization of the ternary gradient samples explained in the previous section. The method is a quite straightforward evolution of the binary composition gradient characterization method explained in Section 4.2.3.

As explained in Section 4.2.3, we need a way to retrieve the local composition for every point in the sample. This is accomplished using Raman Spectroscopy. In Figure 22 we show several Raman spectra for a Ternary system, including the reference spectra obtained for the three materials and three spectra obtained from a blended sample at different points with different composition ratios. It can be observed how the spectra changes depending on the local composition, and therefore, knowing the reference spectra of the pristine material, the composition for each measured spectra of the composition gradient sample can be recovered.

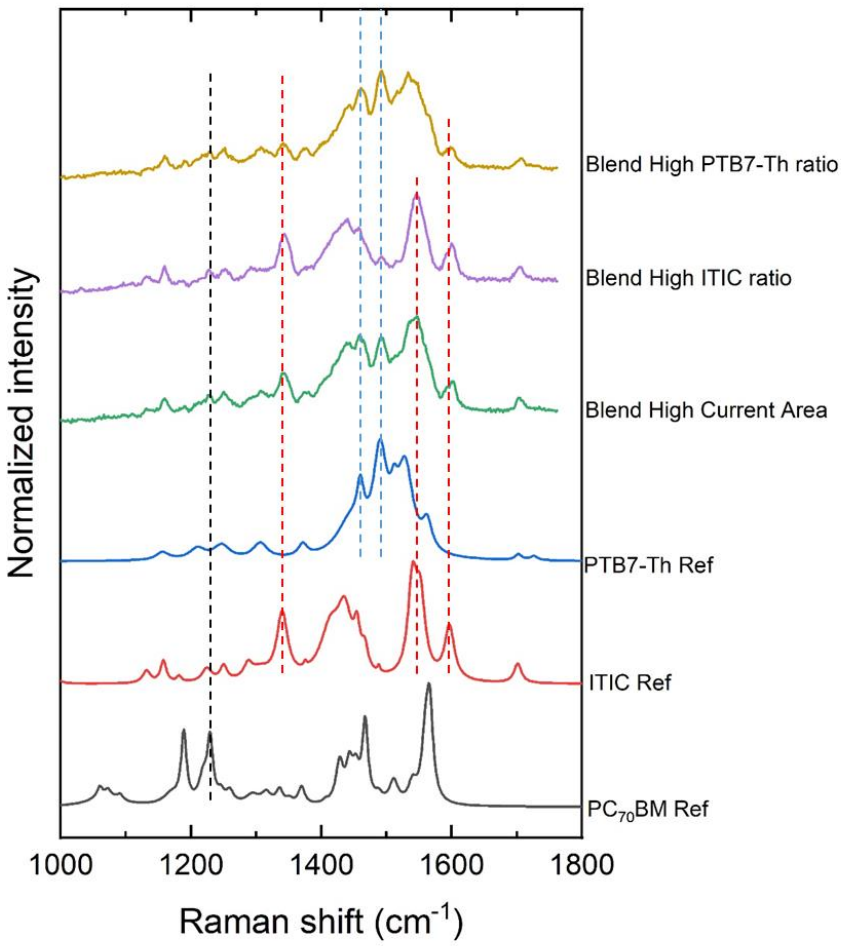


**Figure 22.** Raman spectra for pristine PTB7-Th, ITIC and PC70BM and for blended PTB7-Th:ITIC:PC70BM composition gradient device, at different locations of the sample. Dashed lines are a help to the eye, indicating identifiable peaks. **Note**: Blend spectra extracted from same sample as maps in Figure 23, for comparison purposes.

Additionally, measuring the generated photocurrent co-locally to Raman is necessary, for which we use WBIC. Nevertheless, the latter technique underwent several refinements and improvements to establish a WBIC technique versatile enough for all types of solar cells and

materials. With this hyperspectral imaging characterization we are able to obtain ~10000 data points per sample.

The initial iteration of the local photocurrent technique was done using LBIC, using the same laser (488 nm) as to obtain the Raman spectra. While this enabled the fastest characterization, requiring only a single scan for both Raman and LBIC, this technique has limited validity as a proxy for efficiency. It relies solely on a single wavelength for photocurrent measurement and is more susceptible to scattering effects at imperfections, which can couple light into the active layer and yield artifacts.

The second iteration involved adding a subsequent co-local scan after the Raman scan. This second scan was done using the built-in white LED lamp of the WiTEC set-up. Although this is slower than measuring only the LBIC, the difference is not twofold, largely due to the more rapid data acquisition enabled by the significantly greater signal intensity. Implementation of this improvement was simple, as it merely required the lamp already used for sample illumination and imaging. The lamp boasts a broad spectrum, making it a better proxy for the ultimate device efficiency by simulating a white light source more effectively. Moreover, it enables collection of reflected light during the experiment. In the case of opaque samples, a single experiment can provide both the local photocurrent under white light and the sample absorption (1-R, being R reflected light) at the same location. This light source is not, however, a perfect Solar Simulator, leaning towards the blue side of the spectrum and lacking IR. This limitation might be significant when studying low band-gap materials (e.g., Y6) since the light source might not excite the main absorption band of such materials, leading to inaccurate results for the optimum composition.

Third and final iteration involved substituting the built-in lamp by a Xenon Lamp, thereby broadening the spectrum and increasing the similarity to the Solar Spectrum. This represents the costliest option, as it necessitates a Solar Simulator lamp compatible with the Raman setup. However, it also offers the most accurate representation, both in terms of spectrum and illumination power density. It's important to note that the distinct sharp peaks exhibited by Xenon lamps could introduce challenges when measuring absorption, as the complex spectrum often proves difficult to normalize accurately.

Figure 23 shows a complete set of the maps obtained through this characterization methodology for a single device, including WBIC, LBIC, Raman, PL and Absorption.

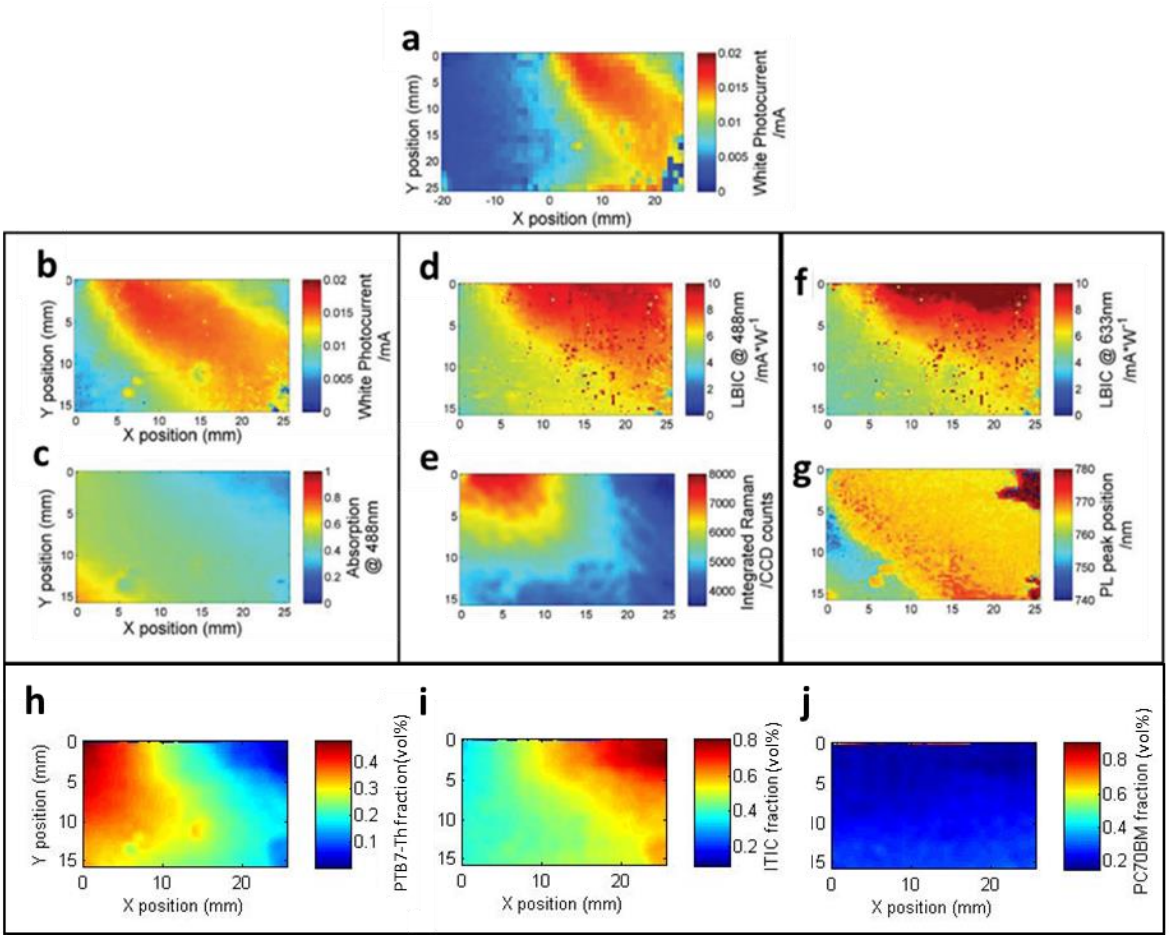


**Figure 23**. Full set of optical characterization maps performed in a sequentially deposited sample of PTB7-Th:PC70BM:ITIC, following the deposition procedure of Figure 20b. Each box corresponds to a separate measurement. a) Coarse photocurrent map obtained with white light; b) higher resolution white light photocurrent map centered at the region of better performance; c) absorption at 488 nm excitation wavelength d) photocurrent map acquired at 488 nm excitation (LBIC); e) integrated Raman scattered intensity from 1100 to 1600 cm−1 at 488 nm excitation; f) photocurrent map acquired at 633 nm excitation (LBIC); g) wavelength of the main PL peak measured at 633 nm excitation; h) extracted composition (vol%) for PTB7-Th; i) for ITIC; j) for PC70BM. **Note:** Maps from the same sample of the spectra in Figure 22, for comparison purposes.

### 4.3.3. Ternary Diagrams

Dealing with more than 10.000 data points per sample for each of the several scanned parameters, can pose a challenge when trying to compare and draw conclusions. To enhance data comprehensibility, employing graphical representations is the optimal approach.

Given that all data is collected co-locally, we can eliminate spatial dependencies, resulting in a ternary diagram that is decoupled from the physical position or the specific cell where each data point originated. This diagram is a 2D representation of all the possible compositions for the ternary system, so all data points can be represented only by their composition ratio. Moreover, this diagram can be extended into a 3D representation by incorporating a color scale reflecting any other pertinent parameter, such as photocurrent, serving as a surrogate for final efficiency.

These ternary diagrams also allow to represent all the samples in the same diagram and order all data to show the higher photocurrents on top while keeping all others (that might arise from differences in thickness or microstructure) hidden below. This conjoined diagram shows all the data obtained, and specially the topography of the upper crust in which, as we will show, all maxima of photocurrent can be immediately found. An example of a resulting ternary diagram for the P3HT:O-IDFBR:O-IDTBR system can be seen in Figure 24.

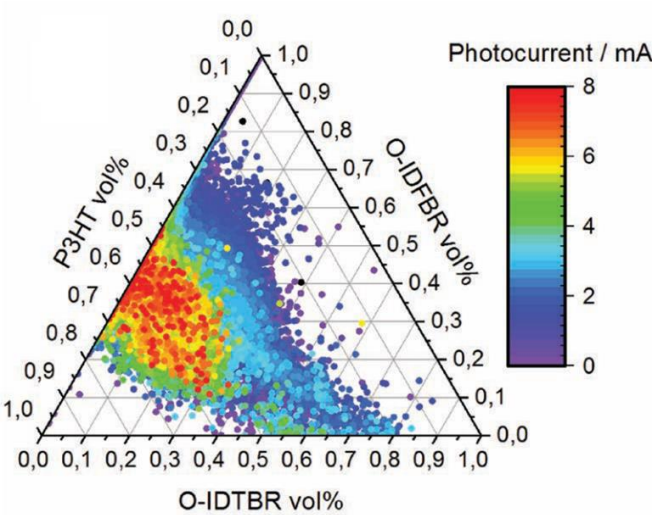


**Figure 24**. Ternary composition diagram corresponding to seven different RR-P3HT:O-IDFBR:O-IDTBR devices, with color corresponding to LBIC at 488nm.

As seen in Figure 24, these ternary diagrams are better at representing the results obtained with the ternary optimization methodology. We can also discern the motive behind the change from LBIC to WBIC measurements. The RR-P3HT:O-IDFBR:O-IDTBR was the first system manufactured as a proof of concept through this methodology, and was measured using LBIC at 488nm. In this system we can clearly see an optimum in photocurrent centered around 0.55:0.35:0.1 composition ratio. However, in the literature the reported optimum is at 0.5:0.15:0.35, where our diagram shows a slight decrease in photocurrent. This change, however, might be due to the low absorption of O-IDTBR at the laser's wavelength, 488nm, in conjunction with both P3HT and O-IDFBR having their maximum absorption peak at 488nm. This results in a disparity in the generated photocurrent and in a disproportional promotion of the contribution of O-IDFBR, thereby shifting the optimum composition ratio to higher loadings of O-IDFBR. To avoid this

single wavelength problem, we substituted the laser excitation (LBIC) for white light excitation (WBIC), and proceeded to other ternary systems, like the ones shown in Figure 25.

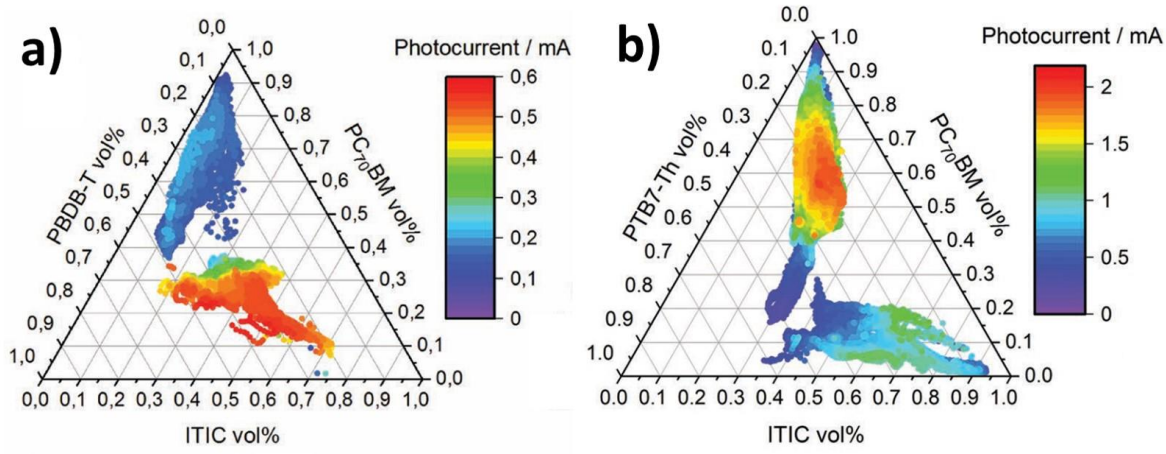


**Figure 25**. Ternary composition diagram corresponding to a) two PBDB-T:ITIC:PC70BM devices processed changing the coating order of the acceptor materials with color corresponding to WBIC b) two PTB7-Th:ITIC:PC70BM devices processed changing the coating order of the acceptor materials, with color corresponding to WBIC.

In the case of PTB7-Th:ITIC:PC70BM the two samples cover separate zones of the ternary diagram, with three maxima and a deep minimum. These maximums in photocurrent are located at volumetric composition ratios 0.35:0.60:0.05, 0.2:0.6:0.2 for one sample, and the third and markedly higher at 0.2:0.2:0.6, while the deep minimum sits at 0.5:0.3:0.2, observed in both samples. Interestingly, such minimum lies on the usual blending ratio scheme followed in the literature, i.e., keeping the donor loading fixed at 50%, while varying the ratio of both acceptors.

In order to check the existence of the multiple photocurrent maxima in the PTB7-Th:ITIC:PC70BM system we fabricated discrete devices with fixed stoichiometry and thickness gradients, keeping the loading of PTB7-Th donor at 25% to following the trajectory of two of the photocurrent maxima. The results are depicted in Figure 26, where an acute drop in photocurrent occurs at composition ratio 0.25:0.35:0.45 (w:w:w), resulting in two photocurrent maxima matching the ones found in the composition gradient devices.

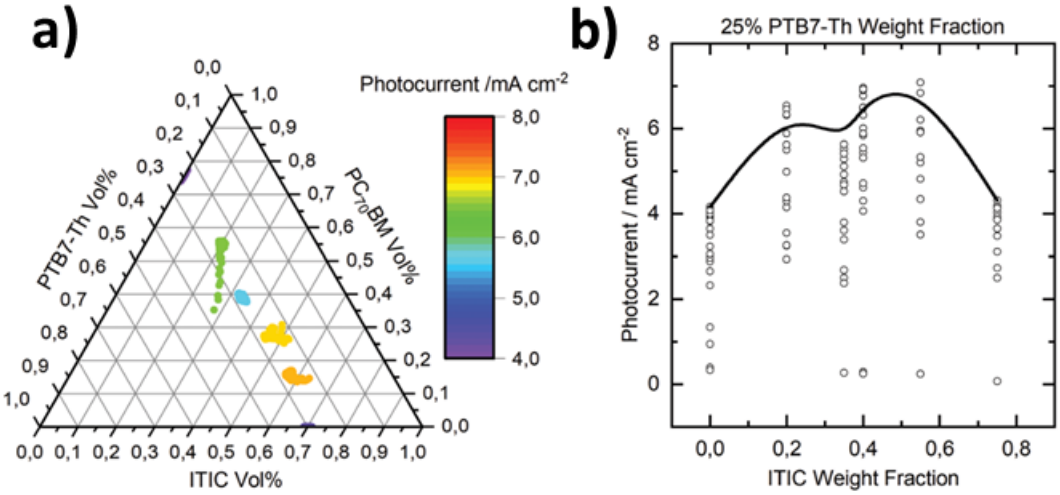


**Figure 26.** a) Ternary composition diagram of six different samples (24 devices each, thickness gradient and fixed composition), with the highest photocurrent obtained in the sample as color scale. b) Photocurrent dispersion obtained for all thickness gradient samples (fixed PTB7-Th loading at 25 wt%) as a function of ITIC wt%. The black line is a guide to the eye.

However, the relative value of the two photocurrent maxima is inverse as the one obtained in the ternary diagram, as the highest values in the discrete samples align with the lower maxima in the ternary diagram. This might be due to differences in thickness of the composition gradient samples, or a discrepancy in the absolute values of photocurrent of the two samples, maybe due to defects such as pinholes.

### *4.3.4. Normalization of photocurrent*

Typically, each studied system needs at least 4 samples to cover >60% of the ternary diagram. Given the large area of the samples, the multiple layers, varied depositions, and diverse materials, reproducibility tends to manifest in terms of trends rather than absolute photocurrent values. This is due to defects like pinholes, aggregates or dust that can create localized shortcuts impacting photocurrent. However, the majority of these defects exhibit a linear influence on photocurrent. Hence, a normalization process can be applied to standardize all samples to a similar level.

Yet, this normalization process cannot be achieved merely by aligning all samples with the best-performing one. Such an approach would render the study inconclusive, as different samples cover distinct portions of the ternary diagram. Instead, we make use of the idea that an equivalent composition ratio should yield approximately equal photocurrent across all samples.

The normalization procedure commences from the highest performing cell and extends to other cells. It involves finding overlapping composition ratios between the best performing cell and the one being normalized. Subsequently, data points from both samples within a 5% composition ratio range in the overlapping region are selected. To account for the unmeasured variations in thickness, only the superior data points ("Upper Crust") are considered. Within this overlapping dataset the top 10% photocurrent data points for each sample are selected. These selected data points should average to a very similar photocurrent, as both share the same composition ratio and thickness optimization. By averaging the Upper Crust values for each sample, a multiplication factor is determined. This factor is then applied to the entire set of data for the cell to derive a new normalized photocurrent. This normalization procedure is subsequently extended to other cells in need of normalization.

Sometimes, not all the cells will overlap with the best performing cell. In such instances, a “chaining” approach can be utilized, where normalization proceeds by normalizing an overlapping cell and then using this normalized cell as a reference for normalizing other overlapping cells. In very few cases completely isolated samples are found. In these scenarios, an approximate factor can be estimated (albeit with low accuracy), or additional samples can be manufactured to bridge the gap. While the latter option demands more effort, it guarantees accurate values through additional samples and data.

An example of the ternary diagram representation before and after normalization can be seen in Figure 27.

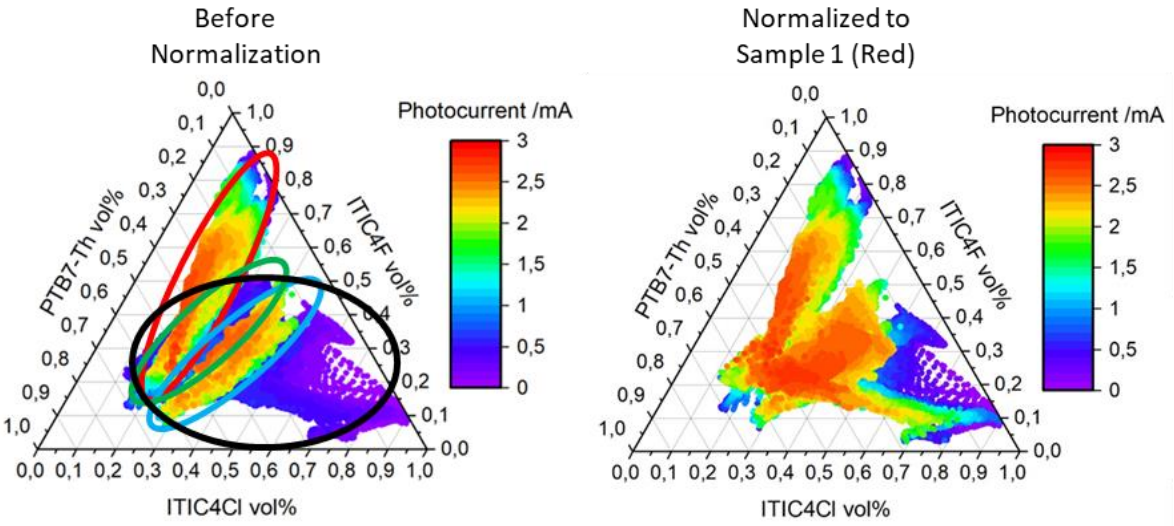


**Figure 27.** Example of the data obtained for a system before and after normalization. Before normalization (left) and after normalization (right). Each circle on the left diagram represents a different sample manufactured with different small modifications of the ternary gradient method.

As can be seen in Figure 27, the green and black circle samples overlap with the red circle sample (best performing), while the blue doesn't. A region was selected in the overlapping of red and green devices, as well as in the overlapping of red and black devices. Following the process explained before, both black and green data were normalized to the values of the red device. Subsequently, the blue device's data was normalized against the normalized values of the green device, given their overlapping.

This normalization process yields a more refined and coherent ternary diagram encompassing all the normalized data. Moreover, the diagram illuminates previously undiscovered areas of interest. The PTB7-Th:ITIC-4F:ITIC-4Cl ternary system shows two optimums in photocurrent with similar values, at 0.45:0.2:0.35 and at 0.4:0.45:0.15.

In conclusion, for this section on the methodology for Ternary optimization we developed a method to fabricate composition gradients in ternary systems, and co-locally characterize them by Raman spectroscopy, PL and photocurrent generation. Furthermore, the technique for photocurrent characterization was improved from a single wavelength laser excitation, to white light illumination, to Solar Simulator illumination, increasing the accuracy of the methodology. Then we applied the methodology to a total of 4 different ternary systems, finding multiple maxima in photocurrent that were later validated with the manufacturing of standard discrete devices.

## 4.4. Paper IV: Correlating microstructure and composition in ternary blends

Having completed the ternary optimization methodology, our focus shifted towards leveraging the extensive dataset produced by the methodology to gain deeper insights into OPV devices beyond just photocurrent. This led to a collaboration study centered around a previously unexplored ternary system, PTB7-Th:ITIC-4F:ITIC-4Cl (see Paper IV for details).

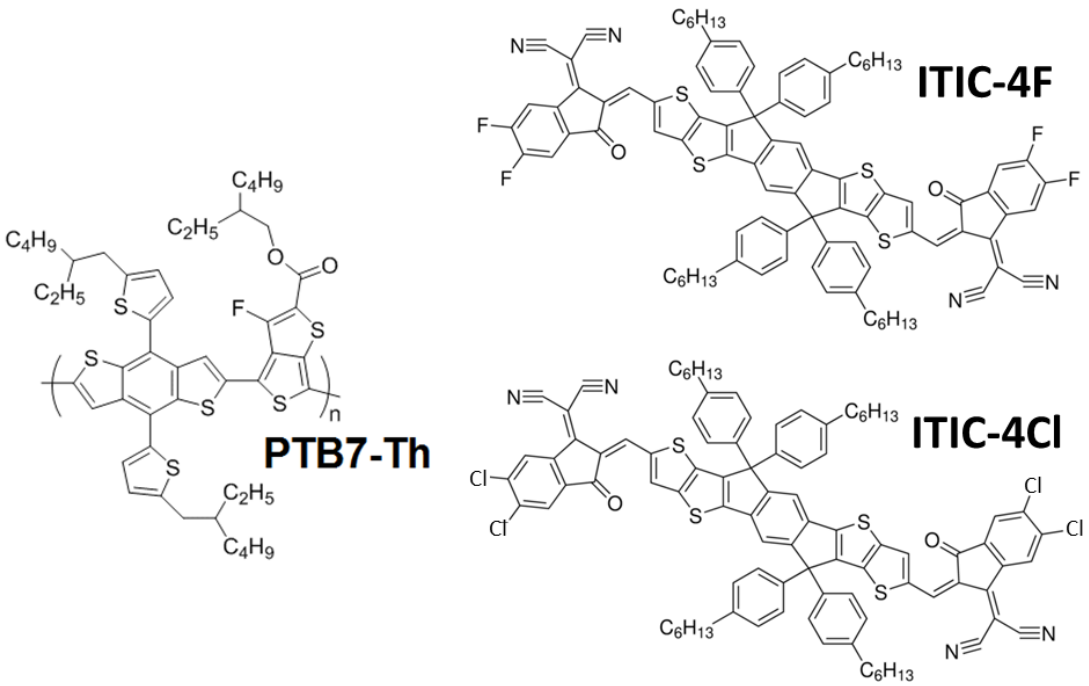


**Figure 28**. Chemical structures of ITIC-4Cl, ITIC-4F and PTB7-Th.

The study involved the fabrication and characterization of 4 ternary composition gradient samples, which were characterized via Raman, WBIC and PL techniques. These 4 samples effectively covered around 65% of the phase diagram, enabling us to discern local composition through Raman spectroscopy, evaluate local photocurrent via WBIC, and map PL intensity. The finalized ternary diagrams illustrating photocurrent and PL intensity for the four samples within this ternary system are depicted in Figure 29.

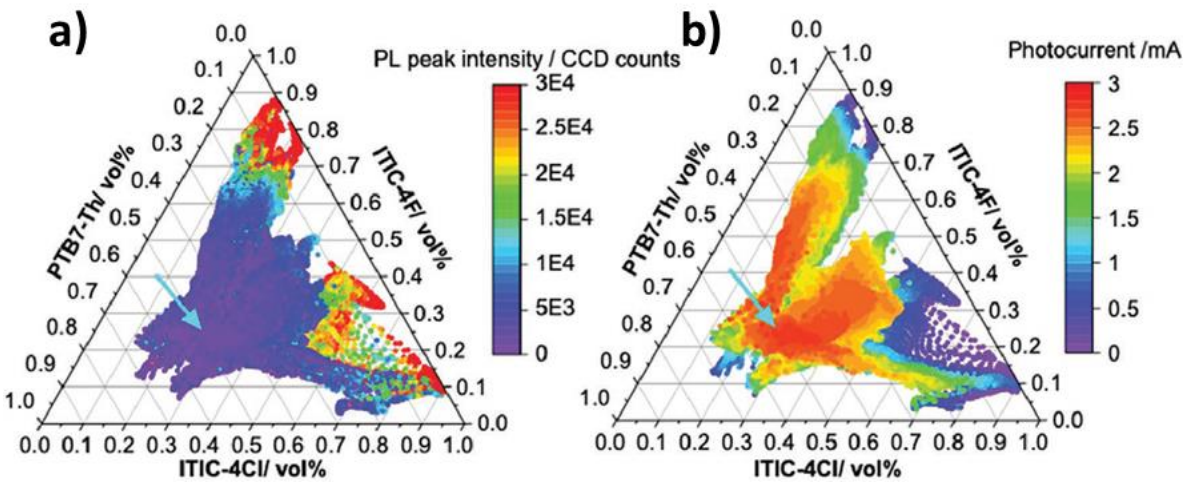

**Figure 29**. Ternary composition diagrams showing a) the photoluminescence intensity, PL; and b) the photocurrent obtained with white light for different compositions of PTB7-Th:ITIC-4F:ITIC-4Cl. The ternary 1:0.5:0.5 PTB7-Th:ITIC-4F:ITIC-4Cl is marked with arrows.

The observed results unveiled a correlation between PL and photocurrent trends. Specifically, higher photocurrents associated with compositions featuring substantial loading of all three materials aligned with enhanced PL quenching. This phenomenon was attributed to a heightened degree of intermixing between the donor polymer, PTB7-Th, and the two acceptors, ITIC-4F and ITIC-4Cl, in these compositions. The intricate interplay of these materials resulted in decreased PL intensity. Notably, this observation was corroborated by an AFM-IR analysis carried out by our collaborators, as detailed in Figure 5 of Paper IV.

Furthermore, an additional set of 6 discrete samples was fabricated, changing the relative composition of the two acceptors while maintaining a 1:1 Donor to acceptors ratio. The results from the discrete sample analysis corroborated the optimums found with the composition gradient study. The results were in agreement with the photocurrent map, as the highest performing device was 1:0.5:0.5 ratio, with a PCE of 8.3%.

Moreover, these discrete samples were used in a thermal stability study, comparing the ternary and its corresponding binary systems. This thermal stability study was performed by annealing the devices at several high temperatures for brief periods (10 minutes) or to lower temperatures for extended durations (205 hours). In both scenarios, ternary systems within the low PL intensity area demonstrated higher stability. This phenomenon stemmed from the pronounced degree of intermixing among the three materials, effectively inhibiting temperature-induced crystallization. Consequently, assessing PL quenching might be a potent tool for evaluating microstructure and intermixing degree.

# 5. Conclusions

The conclusions of this thesis are summarized as follows, with one bullet point for each of the published papers comprising this compendium of works:

- Thickness gradients have proven to be valuable for the rapid and cost-efficient optimization of Polymer:Polymer OPV systems. This approach requires only a fraction of the materials typically consumed by standard screening methodologies. Furthermore, data derived from extensive parametric screening can be subjected to statistical analysis, such as ANOVA, to identify critical optimization parameters. In the case of the PBDB-T:PF5-Y5 system, solvent selection emerged as the most crucial parameter. By utilizing the Hansen solubility parameters of the solvents, we developed a novel method to represent device PCE in the Hansen solubility space. This approach directly correlates with device performance, even allowing for PCE predictions with alternative solvents. Notably, it eliminates the need for acquiring the Hansen parameters of the materials.
- The methodology for optimization of binary systems was successfully applied for the novel P3HT:NIPb3T-Rd system, optimizing composition and thickness in as few as six samples. Leveraging composition gradients, Raman spectroscopy, and WBIC, we demonstrated that binary system composition can be optimized within a single sample. Subsequently, we validated these results using standard discrete devices.
- A novel methodology was designed to efficiently screen the complex, multi-dimensional parametric landscape of Ternary OPV systems. This methodology relies on sequential (layer-by-layer) blade coating depositions coupled with hyperspectral imaging through photocurrent measurements and spectroscopic techniques. The emergence of multiple maxima for a single Ternary system is demonstrated, the results validated with standard discrete samples, and its versatility proved by applying the methods for multiple different ternary systems.
- The ternary screening methodology was refined and successfully applied to a new ternary system. We significantly enhanced the yield of data obtained from this methodology by establishing correlations between photoluminescence (PL) quenching and microstructure. Additionally, we introduced a photocurrent normalization technique to the photocurrent measurements, enhancing reliability and facilitating more precise sample comparisons.

# 6. Future work

After the research conducted for this doctoral thesis, several avenues for further improvement and expansion of high-throughput methodologies for screening OPV systems have been identified.

Manufacturing techniques for composition gradient samples, such as layer-by-layer and two-drop methods, could benefit from refinements to avoid the appearance of pinholes and defects. Throughout our investigations, significant differences in photocurrent measurements have been observed between samples of the same system, which appear to result from linear losses due to pinholes in the large area sample. Fine tuning the techniques to eliminate the generation of these pinholes would lead to better sample comparisons, potentially reducing the need for photocurrent normalization.

In the final part of Section 4.4 (Paper IV), we briefly mentioned that some measurements from hyperspectral imaging in the ternary composition methodology could be correlated to thermal stability. It would be interesting to further explore this capability for studying device stability, one of the major challenges of current OPV, using composition gradient samples. This exploration could be paired with the design of new high-throughput methods for exploring stability, such as degradation gradients. These gradients could include thermal gradients, illumination time gradients or exposure to oxygen and water degradation tests. This opens up the possibility of investigating stability with respect to different parameters of the active layer, including thickness, composition, and microstructure.

Another avenue for expanding high-throughput screenings involves maximizing the use of the collected data. Similarly to the previous point, PL intensity could be related to microstructure and even stability. Furthermore, the positions of PL peaks could be analyzed and correlated to gain further insight into the behavior of the active layer. Additionally, comparing the blend Raman spectra to the Raman spectra of each pristine material and measuring shifts could serve as a proxy for crystallinity. Figure 30 illustrates the ternary composition diagrams for comprehensive characterization of a ternary system, representing the data that can be obtained without complicating the methodology.

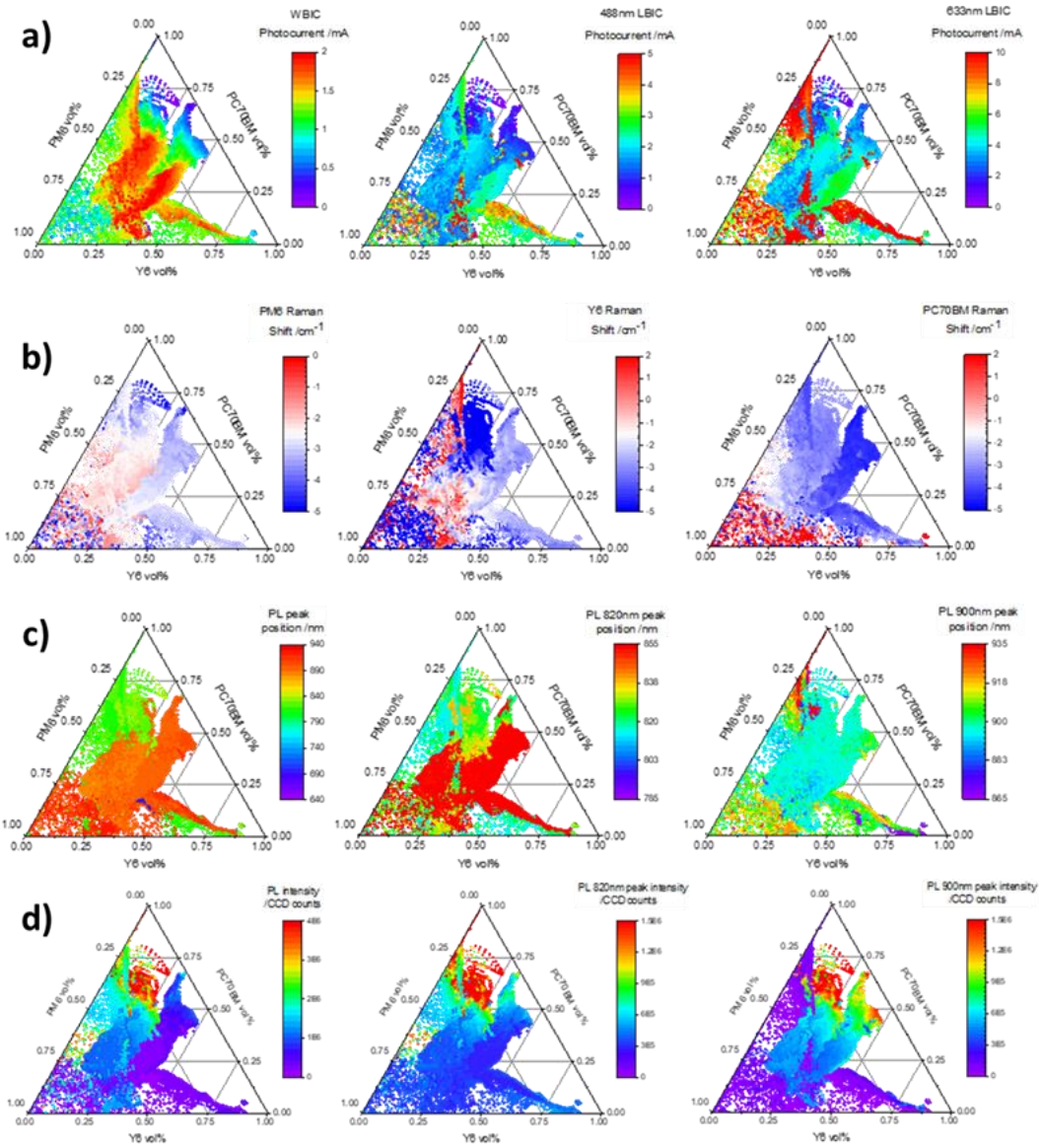


**Figure 30.** Full Ternary characterization of 4 samples of PM6:Y6:PC70BM ternary OPV. From left to right a) WBIC; LBIC at 488 nm excitation and LBIC at 633 nm excitation; b) Raman Shift in respect to the Raman spectra reference of pristine material in thin layer of PM6 Y6 and PC70BM; c) Position of the absolute peak of PL; of the peak centered at 820 nm; of the peak centered at 900 nm; d) PL intensity of the full spectrum; of the of the peak centered at 820 nm; of the peak centered at 900 nm.

The substantial amount of generated data through our high-throughput methodology presents the opportunity to delve deeper into the relationships between ternary systems and their corresponding binary systems. Uncovering these relationships would enable the prediction of ternary system behavior based on the performance of their binary counterparts, and vice versa. This would speed up the selection process for efficient ternary systems, as well as their exploration. In an still unpublished study we found a possible relation of the photocurrent vs composition behavior by manufacturing ternary and their corresponding binary composition gradient samples. The photocurrent mappings were compared by projecting the 2D composition space of the ternary system onto each of the 1D composition spaces of the binary systems, effectively 'hiding' one of the materials. The resulting photocurrent plot shape for each

projection exhibited a remarkable resemblance to the shape of the binary samples, as depicted in Figure 31 and Figure 32.

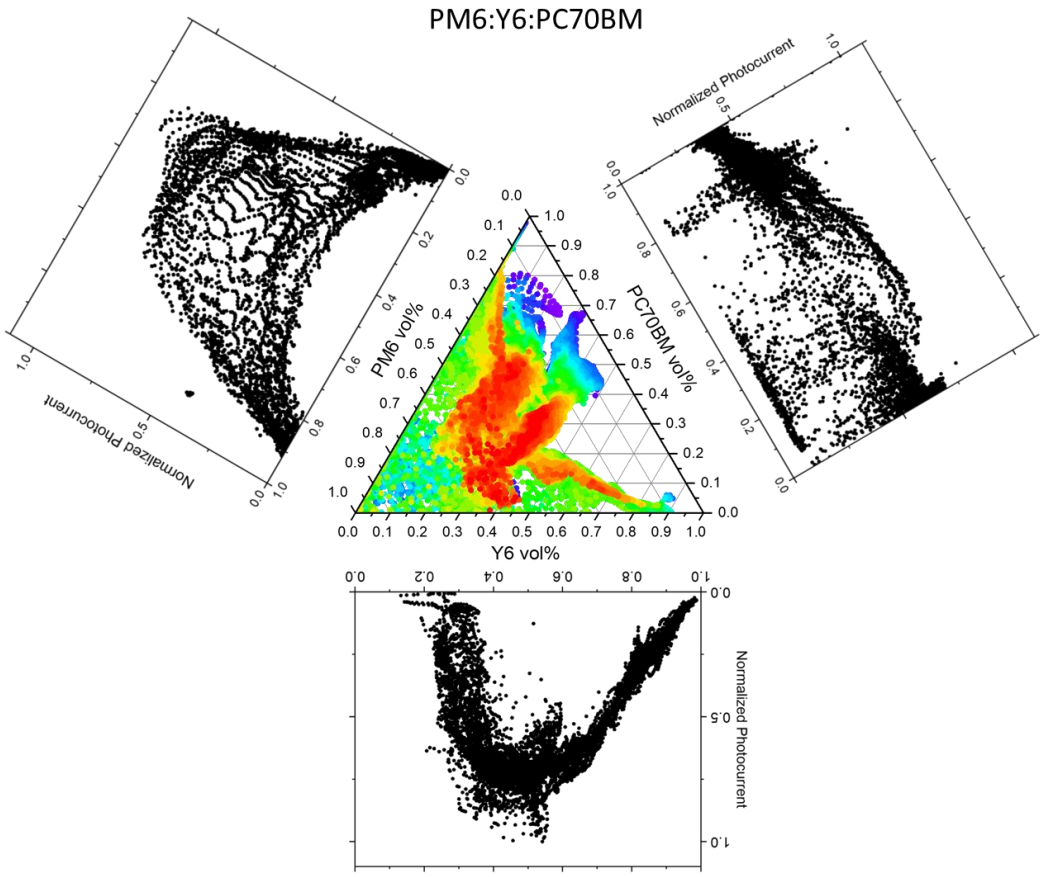


**Figure 31.** (center) Normalized Photocurrent in the ternary composition space, (exterior) with normalized photocurrent of each corresponding binary.

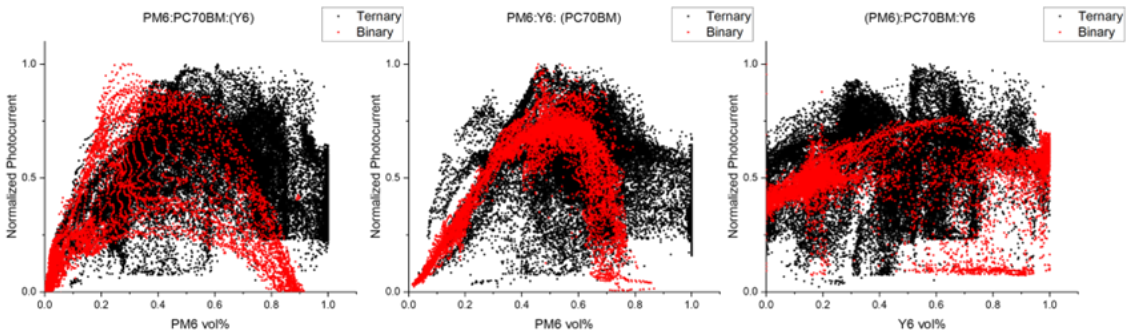


**Figure 32.** Comparison of Ternary projections and Binary photocurrents.

Once a working methodology for the fast and efficient optimization of ternary systems is established, attention could shift toward the other challenge in ternary OPV improvement: Material Selection. There are already dozens of commercially available materials, with more being synthesized continuously, even with high-throughput methodologies, analyzing every possible ternary system, or even binary, proves to be unattainable. Therefore, new strategies

for focusing our experiments on promising systems are essential. This could be accomplished through means like Artificial Intelligence (AI) training or Genetic Algorithms (GA).

An ongoing, though still unpublished, effort has been made involving a Genetic Algorithm approach, initially for binaries, and later for ternaries. The Genetic Algorithm relies on an initial matrix of PCE for different systems, with probabilities assigned to each material depending on their PCE. Subsequently, a new generation of systems is randomly selected using these probabilities, manufactured, measured and their PCE values added to the matrix if improvements have been achieved compared to previous iterations. This process can be repeated for as many generations as desired, with the probabilities of selection for better performing materials increasing as their PCE values rise.

The GA can also be extended to ternary systems by using the same matrix as the binary systems and adding two additional matrices. The first addition is a matrix to select composition from the PCE each composition has reached for any ternary system, information derived from an extensive literature review. The second matrix is employed to select the third material, accounting for the obtained increase in PCE of the ternary system compared to the initial binary system. Figure 33 and Tables 3-5 depict the diagram of the Genetic Algorithm and the corresponding PCE matrices, with the review of ternary compositions illustrated in Figure 6.

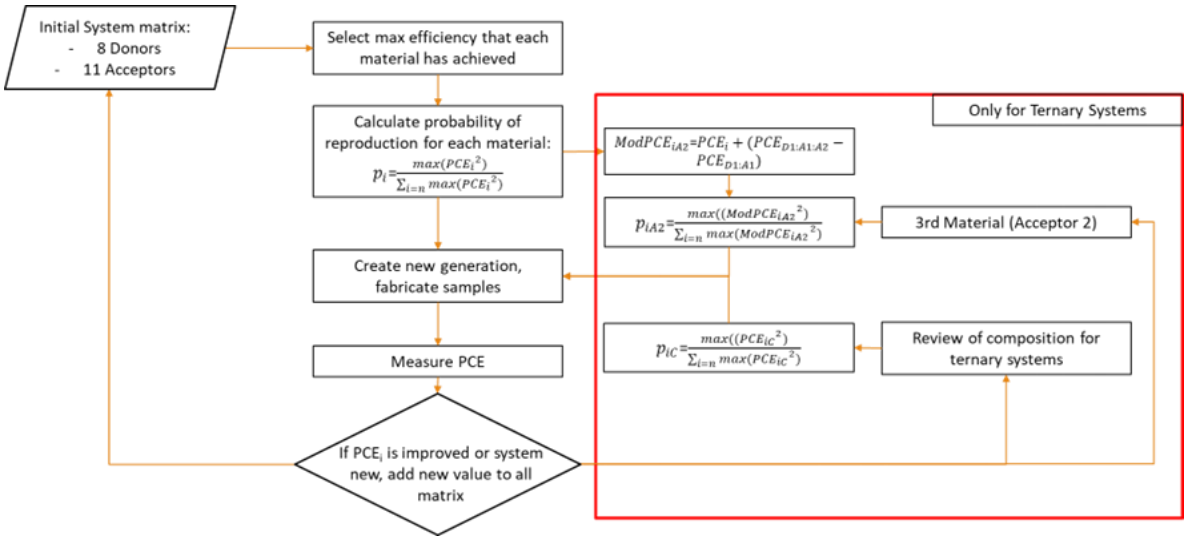


**Figure 33.** Diagram of the Genetic Algorithm.

**Tables 3-5.** Evolution of the PCE Matrix for the Genetic Algorithm, from initial to 3rd generation, to 6th generation. Ternaries were included only after the 3rd generation of binaries. Black circles indicate new records in the matrix or enhanced PCE for the same system.

## Initial Matrix

| | | Donors | | | | | | | |
|---|---|---|---|---|---|---|---|---|---|
| | | PBDB-T-2F | PBDB-T-2Cl | PBDB-T | PTB7-Th | P3HT | PTQ10 | PCDTBT | D18 |
| Acceptors | ITIC-4F | 9.95 | 9.6 | 6.2 | | | | | |
| | ITIC | 6.66 | 5.64 | 7.7 | 4.32 | 1.35 | 9 | | |
| | ITIC-M | | | 7.2 | | 2.31 | | | |
| | O-IDTBR | | | | | 5.61 | | | |
| | O-IDFBR | | | 2.28 | | 4.23 | | | |
| | EH-IDTBR | | | 6.5 | | 3.31 | | | |
| | PC60BM | | | | | 3.81 | 7.5 | | |
| | PC70BM | | | 4.08 | 8.31 | 1.16 | | 5.04 | |
| | ICBA | | | 3.63 | | 3.72 | | | |
| | Y12 | 9.45 | | | | | 10.71 | | 11.02 |
| | Y6 | | 4.27 | 8.6 | | | 11.36 | | 9.68 |

3rd generation (18 binary samples)

| | | Donors | | | | | | | |
|---|---|---|---|---|---|---|---|---|---|
| | | PBDB-T-2F | PBDB-T-2Cl | PBDB-T | PTB7-Th | P3HT | PTQ10 | PCDTBT | D18 |
| Acceptors | ITIC-4F | 9.95 | 9.6 | 6.2 | | 0.04 | 12.82 | | |
| | ITIC | 6.66 | 5.64 | 7.7 | 4.32 | 1.35 | ~~9.28~~ | | |
| | ITIC-M | | 7.04 | 7.2 | | 2.31 | | | |
| | O-IDTBR | | | 5.19 | 6.88 | 5.61 | | 0.52 | |
| | O-IDFBR | | | 2.28 | 2.71 | 4.23 | | | |
| | EH-IDTBR | 5.36 | | 6.5 | | 3.31 | | | |
| | PC60BM | | | | | 3.81 | 7.5 | | |
| | PC70BM | | 4.71 | 4.08 | 8.31 | 1.16 | | 5.04 | |
| | ICBA | | | ~~3.63~~ | | 3.72 | | | |
| | Y12 | 9.45 | | 10.36 | 5.96 | | 10.71 | | 11.02 |
| | Y6 | 8.98 | 4.27 | ~~8.6~~ | 5.53 | | 11.36 | | 9.68 |

6th generation (30 ternary samples)

| | | Donors | | | | | | | |
|---|---|---|---|---|---|---|---|---|---|
| | | PBDB-T-2F | PBDB-T-2Cl | PBDB-T | PTB7-Th | P3HT | PTQ10 | PCDTBT | D18 |
| Acceptors | ITIC-4F | 9.95 | 9.6 | 6.52 | 7.96 | 0.04 | 12.82 | | 7.26 |
| | ITIC | 7.18 | 5.64 | 7.7 | 4.32 | 1.35 | 9.28 | | |
| | ITIC-M | | 7.04 | 7.2 | | 2.31 | | 0.85 | 7.26 |
| | O-IDTBR | | | 5.19 | 6.88 | 5.61 | | 0.52 | |
| | O-IDFBR | | | 2.28 | 2.71 | 4.23 | | | |
| | EH-IDTBR | 5.36 | 1.2 | 6.5 | | 3.31 | | | |
| | PC60BM | | | | | 3.81 | 7.5 | | |
| | PC70BM | | 4.71 | 5.55 | 8.31 | 1.16 | | 5.04 | |
| | ICBA | | | 3.63 | | 3.72 | | | |
| | Y12 | 11.06 | 4.69 | 10.36 | 5.96 | | 12.55 | | 11.02 |
| | Y6 | ~~8.98~~ | 4.27 | 8.6 | 8.29 | | ~~11.36~~ | 0.85 | 9.68 |

While the Genetic Algorithm has proven valuable for exploring material matrices, it requires further fine-tuning to enhance efficiency and integration with other high-throughput methodologies.

# 7. References


1. Jones, D. Global Electricity Review 2022. 2003–2005 (2022). Available at: https://ember-climate.org/insights/research/global-electricity-review-2022/.

2. Becquerel, E. Report on the electrical effects produced under the influence of solar rays. *Comptes Rendus de 'l' Academie Sciences Paris*, Vol. 9, 1839, p. 561 (1839).

3. Qi, B. & Wang, J. Open-circuit voltage in organic solar cells. *J. Mater. Chem.* **22**, 24315 (2012).

4. Lu, N., Li, L., Sun, P. & Liu, M. Short-circuit current model of organic solar cells. *Chem. Phys. Lett.* **614**, 27–30 (2014).

5. Qi, B. & Wang, J. Fill factor in organic solar cells. *Phys. Chem. Chem. Phys.* **15**, 8972 (2013).

6. Benda, V. & Černá, L. PV cells and modules – State of the art, limits and trends. *Heliyon* **6**, e05666 (2020).

7. Lin, H. *et al.* 26.7% Efficiency Silicon Heterojunction Solar Cells Achieved By Electrically Optimized Nanocrystalline-Silicon Hole Contact Layers. *Nat. Portf.* 1–23 (2023).

8. Polman, A., Knight, M., Garnett, E. C., Ehrler, B. & Sinke, W. C. Photovoltaic materials: Present efficiencies and future challenges. *Science (80-. ).* **352**, (2016).

9. Kearns, D. & Calvin, M. Photovoltaic Effect and Photoconductivity in Laminated Organic Systems. *J. Chem. Phys.* **29**, 950–951 (1958).

10. Tang, C. W. Two-layer organic photovoltaic cell. *Appl. Phys. Lett.* **48**, 183–185 (1986).

11. Yu, G., Gao, J., Hummelen, J. C., Wudl, F. & Heeger, A. J. Polymer photovoltaic cells: Enhanced efficiencies via a network of internal donor-acceptor heterojunctions. *Science (80-. ).* **270**, 1789 (1995).

12. Halls, J. J. M. *et al.* Efficient photodiodes from interpenetrating polymer networks. *Nature* **376**, 498–500 (1995).

13. Ren, H., Chen, J. De, Li, Y. Q. & Tang, J. X. Recent Progress in Organic Photodetectors and their Applications. *Adv. Sci.* **8**, 1–23 (2021).

14. Someya, T. *et al.* A large-area, flexible pressure sensor matrix with organic field-effect transistors for artificial skin applications. *Proc. Natl. Acad. Sci.* **101**, 9966–9970 (2004).

15. Feron, K. *et al.* Organic Bioelectronics: Materials and Biocompatibility. *Int. J. Mol. Sci.* **19**, 2382 (2018).

16. Fu, J. *et al.* 19.31% Binary Organic Solar Cell and Low Non-Radiative Recombination Enabled By Non-Monotonic Intermediate State Transition. *Nat. Commun.* **14**, 1760 (2023).

17. Wu, Q. *et al.* High-performance organic photovoltaic modules using eco-friendly solvents for various indoor application scenarios. *Joule* **6**, 2138–2151 (2022).

18. Suthar, R., Dahiya, H., Karak, S. & Sharma, G. D. Indoor Organic Solar Cell for Low-power IoT Devices: Recent Progress, Challenges, and Application. *J. Mater. Chem. C* (2023). doi:10.1039/D3TC02570E

19. Jahandar, M., Kim, S. & Lim, D. C. Indoor Organic Photovoltaics for Self-Sustaining IoT Devices: Progress, Challenges and Practicalization. *ChemSusChem* **14**, 3449–3474 (2021).

20. Brus, V. V. *et al.* Solution-Processed Semitransparent Organic Photovoltaics: From Molecular Design to Device Performance. *Adv. Mater.* **31**, 1900904 (2019).

21. Li, Y., Huang, X., Sheriff, H. K. M. & Forrest, S. R. Semitransparent organic photovoltaics for building-integrated photovoltaic applications. *Nat. Rev. Mater.* **8**, 186–201 (2022).

22. Safat Dipta, S., Schoenlaub, J., Habibur Rahaman, M. & Uddin, A. Estimating the potential for semitransparent organic solar cells in agrophotovoltaic greenhouses. *Appl. Energy* **328**, 120208 (2022).

23. Cardinaletti, I. *et al.* Organic and perovskite solar cells for space applications. *Sol. Energy Mater. Sol. Cells* **182**, 121–127 (2018).

24. Torimtubun, A. A. A. *et al.* Shelf lifetime analysis of organic solar cells combining frequency and time resolved techniques. *Sustain. Energy Fuels* **5**, 6498–6508 (2021).

25. Du, X. *et al.* Efficient Polymer Solar Cells Based on Non-fullerene Acceptors with Potential Device Lifetime Approaching 10 Years. *Joule* **3**, 215–226 (2019).

26. Zhang, Y., Samuel, I. D. W., Wang, T. & Lidzey, D. G. Current Status of Outdoor Lifetime Testing of Organic Photovoltaics. *Adv. Sci.* **5**, 1800434 (2018).

27. Lin, H. *et al.* Silicon heterojunction solar cells with up to 26.81% efficiency achieved by electrically optimized nanocrystalline-silicon hole contact layers. *Nat. Energy* **8**, 789–799 (2023).

28. Kleinschmidt, A. T., Root, S. E. & Lipomi, D. J. Poly(3-hexylthiophene) (P3HT): Fruit fly or outlier in organic solar cell research? *J. Mater. Chem. A* **5**, 11396–11400 (2017).

29. Wen, Z. C., Yin, H. & Hao, X. T. Recent progress of PM6:Y6-based high efficiency organic solar cells. *Surfaces and Interfaces* **23**, 100921 (2021).

30. Li, Y. *et al.* Recent Progress in Organic Solar Cells: A Review on Materials from Acceptor to Donor. *Molecules* **27**, 1800 (2022).

31. Lippens, P. & Muehlfeld, U. Indium Tin Oxide (ITO): Sputter Deposition Processes. in *Handbook of Visual Display Technology* 779–794 (Springer Berlin Heidelberg, 2012). doi:10.1007/978-3-540-79567-4_54

32. Zeng, G. *et al.* Realizing 17.5% Efficiency Flexible Organic Solar Cells via Atomic-Level Chemical Welding of Silver Nanowire Electrodes. *J. Am. Chem. Soc.* **144**, 8658–8668 (2022).

33. Ameri, T., Khoram, P., Min, J. & Brabec, C. J. Organic ternary solar cells: A review. *Adv. Mater.* **25**, 4245–4266 (2013).

34. Xu, Y. *et al.* Simultaneously Improved Efficiency and Stability in All-Polymer Solar Cells by a P-i-N Architecture. *ACS Energy Lett.* **4**, 2277–2286 (2019).

35. Campoy-Quiles, M., Kanai, Y., El-Basaty, A., Sakai, H. & Murata, H. Ternary mixing: A simple method to tailor the morphology of organic solar cells. *Org. Electron. physics, Mater. Appl.* **10**, 1120–1132 (2009).

36. Sun, Y. *et al.* Simultaneous enhancement of short-circuit current density, open circuit voltage and fill factor in ternary organic solar cells based on PTB7-Th:IT-M:PC 71 BM. *Sol. Energy Mater. Sol. Cells* **182**, 45–51 (2018).

37. An, Q. *et al.* Efficient small molecular ternary solar cells by synergistically optimized photon harvesting and phase separation. *J. Mater. Chem. A* **3**, 16653–16662 (2015).

38. Cheng, P. *et al.* Unique Energy Alignments of a Ternary Material System toward High-Performance Organic Photovoltaics. *Adv. Mater.* **30**, 1801501 (2018).

39. Chen, Y. *et al.* Tuning $V_{oc}$ for high performance organic ternary solar cells with non-fullerene acceptor alloys. *J. Mater. Chem. A* **5**, 19697–19702 (2017).

40. de Zerio, A. D. & Müller, C. Glass Forming Acceptor Alloys for Highly Efficient and Thermally Stable Ternary Organic Solar Cells. *Adv. Energy Mater.* **8**, 1702741 (2018).

41. Zhan, L. *et al.* Over 17% efficiency ternary organic solar cells enabled by two non-fullerene acceptors working in an alloy-like model. *Energy Environ. Sci.* **13**, 635–645 (2020).

42. Cui, Y. *et al.* Single-Junction Organic Photovoltaic Cell with 19% Efficiency. *Adv. Mater.* **33**, 2102420 (2021).

43. Mohamed El Amine, B. *et al.* Latest Updates of Single-Junction Organic Solar Cells up to 20% Efficiency. *Energies* **16**, 3895 (2023).

44. Wang, B. *et al.* Insight Into the Role of PC71BM on Enhancing the Photovoltaic Performance of Ternary Organic Solar Cells. *Front. Chem.* **6**, 1–8 (2018).

45. Liu, X., Yan, Y., Yao, Y. & Liang, Z. Ternary Blend Strategy for Achieving High-Efficiency Organic Solar Cells with Nonfullerene Acceptors Involved. *Adv. Funct. Mater.* **28**, 1802004 (2018).

46. Angmo, D., Bjerring, M., Nielsen, N. C., Thompson, B. C. & Krebs, F. C. Fullerene alloy formation and the benefits for efficient printing of ternary blend organic solar cells. *J. Mater. Chem. C* **3**, 5541–5548 (2015).

47. Sun, X. *et al.* Air-processed high performance ternary blend solar cell based on PTB7-Th:PCDTBT:PC70BM. *Org. Electron. physics, Mater. Appl.* **37**, 222–227 (2016).

48. Baran, D. *et al.* Reducing the efficiency-stability-cost gap of organic photovoltaics with highly efficient and stable small molecule acceptor ternary solar cells. *Nat. Mater.* **16**, 363–369 (2017).

49. Xiao, Z., Jia, X. & Ding, L. Ternary organic solar cells offer 14% power conversion efficiency. *Sci. Bull.* **62**, 1562–1564 (2017).

50. Zhao, W., Li, S., Zhang, S., Liu, X. & Hou, J. Ternary Polymer Solar Cells based on Two Acceptors and One Donor for Achieving 12.2% Efficiency. *Adv. Mater.* **29**, 1604059 (2017).

51. Chang, L., Sheng, M., Duan, L. & Uddin, A. Ternary organic solar cells based on non-fullerene acceptors: A review. *Org. Electron.* **90**, 106063 (2021).

52. Doumon, N. Y., Yang, L. & Rosei, F. Ternary organic solar cells: A review of the role of the third element. *Nano Energy* **94**, 106915 (2022).

53. Zhao, C. *et al.* Recent advances, challenges and prospects in ternary organic solar cells. *Nanoscale* **13**, 2181–2208 (2021).

54. Rivnay, J. *et al.* Large modulation of carrier transport by grain-boundary molecular packing and microstructure in organic thin films. *Nat. Mater.* **8**, 952–958 (2009).

55. Coropceanu, V. *et al.* Charge Transport in Organic Semiconductors. *Chem. Rev.* **107**, 926–952 (2007).

56. Kim, J. Y. *et al.* Efficient Tandem Polymer Solar Cells Fabricated by All-Solution Processing. *Science (80-. ).* **317**, 222–225 (2007).

57. Beiley, Z. M. *et al.* Morphology-dependent trap formation in high performance polymer bulk heterojunction solar cells. *Adv. Energy Mater.* **1**, 954–962 (2011).

58. Yuan, J. *et al.* Single-Junction Organic Solar Cell with over 15% Efficiency Using Fused-Ring Acceptor with Electron-Deficient Core. *Joule* **3**, 1140–1151 (2019).

59. Rodríguez-Martínez, X. *et al.* Predicting the photocurrent–composition dependence in organic solar cells. *Energy Environ. Sci.* (2021). doi:10.1039/d0ee02958k

60. Watts, B., Belcher, W. J., Thomsen, L., Ade, H. & Dastoor, P. C. A Quantitative Study of PCBM Diffusion during Annealing of P3HT:PCBM Blend Films. *Macromolecules* **42**, 8392–8397 (2009).

61. Leman, D. *et al.* In Situ Characterization of Polymer–Fullerene Bilayer Stability. *Macromolecules* **48**, 383–392 (2015).

62. Liu, J. *et al.* Constructing the nanointerpenetrating structure of PCDTBT:PC70BM bulk heterojunction solar cells induced by aggregation of PC70BM via mixed-solvent vapor annealing. *J. Mater. Chem. A* **1**, 6216 (2013).

63. Rodríguez-Martínez, X., Pascual-San-José, E. & Campoy-Quiles, M. Accelerating organic solar cell material's discovery: high-throughput screening andbig data. *Energy Environ. Sci.* **14**, 3301–3322 (2021).

64. Langner, S. *et al.* Beyond Ternary OPV: High-Throughput Experimentation and Self-Driving Laboratories Optimize Multicomponent Systems. *Adv. Mater.* **32**, 1907801 (2020).

65. Du, X. *et al.* Elucidating the Full Potential of OPV Materials Utilizing a High-Throughput Robot-Based Platform and Machine Learning. *Joule* **5**, 495–506 (2021).

66. Cao, B. *et al.* How To Optimize Materials and Devices via Design of Experiments and Machine Learning: Demonstration Using Organic Photovoltaics. *ACS Nano* **12**, 7434–7444 (2018).

67. Nickel, F. *et al.* Spatial mapping of photocurrents in organic solar cells comprising wedge-shaped absorber layers for an efficient material screening. *Sol. Energy Mater. Sol. Cells* **104**, 18–22 (2012).

68. Pascual-San-José, E. *et al.* Blade coated P3HT:non-fullerene acceptor solar cells: A high-throughput parameter study with a focus on up-scalability. *J. Mater. Chem. A* **7**, 20369–20382 (2019).

69. Fan, B. *et al.* Surpassing the 10% efficiency milestone for 1-cm2 all-polymer solar cells. *Nat. Commun.* **10**, 4100 (2019).

70. Liu, X. *et al.* Ternary All-Polymer Solar Cells With 8.5% Power Conversion Efficiency and Excellent Thermal Stability. *Front. Chem.* **8**, 302 (2020).

71. Liu, T. *et al.* 16% Efficiency All-Polymer Organic Solar Cells Enabled By a Finely Tuned Morphology Via the Design of Ternary Blend. *Joule* **5**, 914–930 (2021).

72. Lee, C., Lee, S., Kim, G. U., Lee, W. & Kim, B. J. Recent Advances, Design Guidelines, and Prospects of All-Polymer Solar Cells. *Chem. Rev.* **119**, 8028–8086 (2019).

73. Fu, H. *et al.* High efficiency (15.8%) all-polymer solar cells enabled by a regioregular narrow bandgap polymer acceptor. *J. Am. Chem. Soc.* **143**, 2665–2670 (2021).

74. Yan, Y., Liu, Y., Zhang, Q. & Han, Y. Increasing N2200 Charge Transport Mobility to Improve Performance of All Polymer Solar Cells by Forming a Percolation Network Structure. *Front. Chem.* **8**, 394 (2020).

75. Gao, L. *et al.* All-Polymer Solar Cells Based on Absorption-Complementary Polymer Donor and Acceptor with High Power Conversion Efficiency of 8.27%. *Adv. Mater.* **28**, 1884–1890 (2016).

76. Fan, Q. *et al.* Over 14% efficiency all-polymer solar cells enabled by a low bandgap polymer acceptor with low energy loss and efficient charge separation. *Energy Environ. Sci.* **13**, 5017–5027 (2020).

77. Acton, C. *et al.* Analysis of Variance (ANOVA). *SPSS Soc. Sci.* **6**, 183–198 (2009).

78. Ostertagová, E. & Ostertag, O. Methodology and Application of Oneway ANOVA. *Am. J. Mech. Eng.* **1**, 256–261 (2013).

79. Archer, G. E. B., Saltelli, A. & Sobol, I. M. Sensitivity measures, anova-like techniques and the use of bootstrap. *J. Stat. Comput. Simul.* **58**, 99–120 (1997).

80. Sánchez-Díaz, A., Rodríguez-Martínez, X., Córcoles-Guija, L., Mora-Martín, G. & Campoy-Quiles, M. High-Throughput Multiparametric Screening of Solution Processed Bulk Heterojunction Solar Cells. *Adv. Electron. Mater.* **1700477**, 1700477 (2018).

81. Rodríguez-Martínez, X. *et al.* Microfluidic-Assisted Blade Coating of Compositional Libraries for Combinatorial Applications: The Case of Organic Photovoltaics. *Adv. Energy Mater.* **10**, 2001308 (2020).

82. Rodríguez-Martínez, X. *et al.* Combinatorial optimization of evaporated bilayer small molecule organic solar cells through orthogonal thickness gradients. *Org. Electron. physics, Mater. Appl.* **59**, 288–292 (2018).

83. Rodríguez-Martínez, X. *et al.* Quantifying local thickness and composition in thin films of organic photovoltaic blends by Raman scattering. *J. Mater. Chem. C* **5**, 7270–7282 (2017).

84. Sun, R. *et al.* A universal layer-by-layer solution-processing approach for efficient non-fullerene organic solar cells. *Energy Environ. Sci.* **12**, 384–395 (2019).

85. Granström, M. *et al.* Laminated fabrication of polymeric photovoltaic diodes. *Nature* **395**, 257–260 (1998).

86. Zhang, S. *et al.* Efficient Ternary Organic Solar Cells With Small Aggregation Phases and Low Bimolecular Recombination Using ICBA: ITIC Double Electron Acceptors. *IEEE Journal of Photovoltaics* **8**, 171-176 (2018).

# 8. Annexes

## 8.1. Annex 1: Summary of the complete methodology for optimization of ternary OPV systems

In this section we include an as concise as possible point-by-point summary of the complete methodology for the fabrication, characterization and optimization of composition for ternary OPV systems. We want to include this section for the benefit of other researchers wanting to replicate the methodology, as it does not appear as completely nor concisely in any of the presented papers in this thesis.

1. Preparing the solutions of pristine materials. Typical concentration is 15mg/mL, but can range from 10 to 20 mg/mL. We use 60mL per layer, so as a rule of thumb prepare 80-100mL of each solution per sample where it will be used. This gives enough margin for errors.

    a. Additionally, prepare more solutions with mixtures of different ratios of materials, to change the explored area of the ternary diagram for each of the samples.

    b. We mostly used chlorobenzene as solvent. But as long as the same solvent is used for all solutions, and said solvent works well with the system, the gradient technique should work properly.

2. Preparing the substrates.

    a. Substrates must be continuous ITO substrates.

    b. Etching to create 4 electrodes (Section 4.2.3, figure 16).

    c. Cleaning the substrates.

3. Depositing first transport layer.

4. Depositing the polymer (Donor) layer as a thickness gradient obtained by decelerating the blade (Section 4.2.1).

5. Rotating the substrate 45$^{o}$, in order to start the deposition from one of the corners. Deposit the second layer (Acceptor 1) with constant speed (usually 30mm/s) (Section 4.3).

6. Rotate the substrate further (until a total of 135$^{o}$ with respect to the first deposition), to start the deposition from the corner on the same long side but opposite short side of the substrate. Deposit the third layer (Acceptor 2), with the same parameters as the second. (Section 4.3).

7. Repeat 3 to 7 for all the samples needed. Apply variations to the processing to increase the coverage of the ternary diagram. Examples:

    a. Change order of 2$^{nd}$ and 3$^{rd}$ layers (Section 4.3, Figure 20)

b. Use solutions with one of the materials added to the other layers (e.g. 90:10) (Section 4.3, Figure 20).

8. Clean the electrodes of all the substrates (Section 4.2.3, figure 16).

9. Evaporation of the second transport layer and metal electrode (Section 4.2.3, figure 16).

10. Encapsulation.

11. Electrically connect them to the measuring set-up (WiTec) and prepare for measuring (Paper III).

12. Raman Spectrosopy of the sample. We use a 488nm laser, perform a continuous scan with each point being 300x300 µm and the sample 48x21mm, for a total of 11200 data points. (Paper III and Sections 4.2.3 and 4.3.2).

a. This measurement is also used to obtain simultaneously LBIC at 488nm in the same locations.

b. This takes 2 to 3 hours depending on integration time of measurement.

13. WBIC measurement. Measure the obtained photocurrent with white light, using the same locations and point size as in the Raman measurement. This will allow for a perfect spatial matching of Raman and WBIC. (Paper III and Sections 4.2.3 and 4.3.2).

a. WBIC can be measured with any white light source, but for accuracy, a Solar Simulator type of source is the best option.

b. Additionally, during this measurement the reflection of the sample can be recorded. From that, if the sample is opaque (no transmission) one can determine the local absorption.

c. This takes around 45 minutes.

14. Perform any additional measurements, for example PL or LBIC at different wavelengths. (Paper III and Paper IV).

a. Each extra measurement usually takes around 45 minutes (Raman is often the slowest due to the small cross section compared to PL or simple reflection).

15. Only after all needed measurements are done the sample can be removed from the Set-up. Note that special 3D holders can be used and secured with magnets in order to fix the sample always in the same position.

16. Cleaning and preparing the data obtained (Paper III).

a. Calculate normalized absorption trough reflection measurement.

b. Clean Raman spectra (CRR, background removal and spatial smoothing).

17. For each sample, pass all the data through the software to recover the composition for each of the points measured (Paper III). When the materials have not been used before in gradient methodologies, one would need to first determine the index of refraction of each pure material, as well as the Raman thin film cross section. (Section 4.2.4 and 4.2.5).

18. Generate all images and representations needed (Section 4.3.2).

19. (Optional) Normalize the photocurrent values of each sample (Section 4.3.4).

20. Merge all data, remove spatial dependence, and represent in ternary diagram (Section 4.3.3). Locate the best performing composition/s.

21. (Optional) Manufacture more devices to cover unexplored compositions.

22. (Optional) Manufacture discrete devices with fixed composition and thickness gradient of the interesting compositions, for a further and complete characterization of the system.

23. (Optional) Measure the discrete devices with known fixed composition in %weight (%w) using the Raman characterization technique, to obtain the %volume (%vol) composition of each device. Knowing the measured %vol and the real %w allows for the approximation the density of each material in the layer, and therefore the ternary gradient composition diagrams can be changed to %w for enhanced accuracy.

## 8.2. Annex 2: Lamp Comparison for WBIC

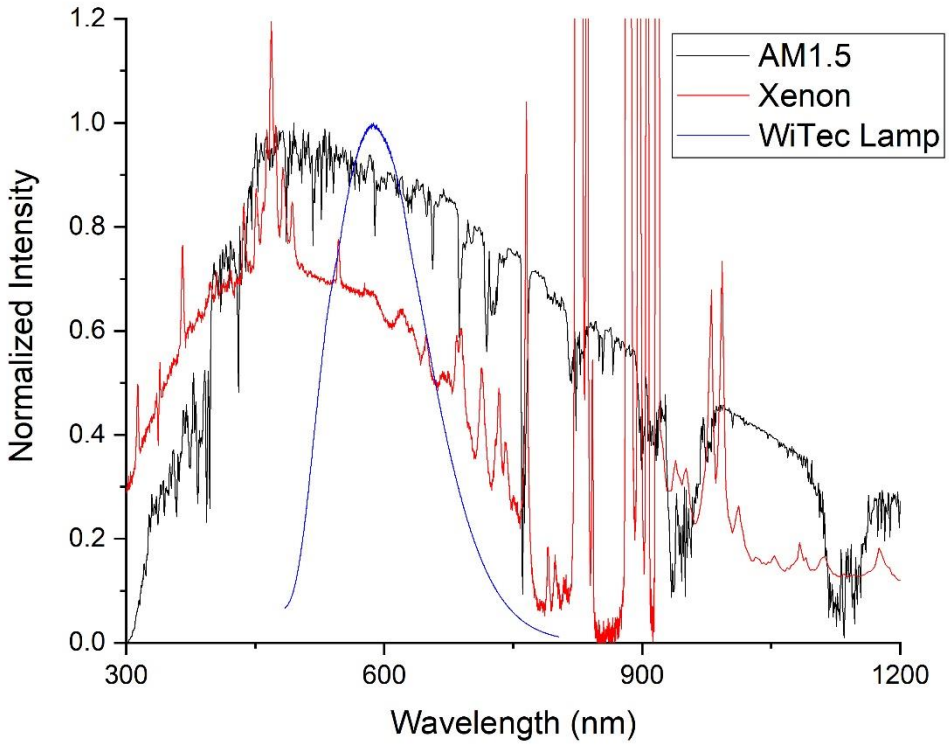


**Figure 35.** Comparison of lamps used for WBIC with Solar Spectrum (AM1.5): In-built light for the WiTec set-up (LED light) and Xenon lamp. **Note:** Not included single wavelength 488nm laser used for the firsts iterations of the methodology.

# PAPER I

## High-Throughput Screening of Blade-Coated Polymer:Polymer Solar Cells: Solvent Determines Achievable Performance

Albert Harillo-Baños, Qunping Fan, Sergi Riera-Galindo, Ergang Wang, Olle Inganäs, and Mariano Campoy-Quiles. *ChemSusChem* 202101888, 1–11 (2021).

ChemSusChem

Full Papers
doi.org/10.1002/cssc.202101888

Chemistry Europe
European Chemical Societies Publishing

www.chemsuschem.org

# High-Throughput Screening of Blade-Coated Polymer: Polymer Solar Cells: Solvent Determines Achievable Performance

Albert Harillo-Baños,[a] Qunping Fan,[b] Sergi Riera-Galindo,[c] Ergang Wang,[b] Olle Inganäs,*[c] and Mariano Campoy-Quiles*[a]

Optimization of a new system for organic solar cells is a multiparametric analysis problem that requires substantial efforts in terms of time and resources. The strong microstructure-dependent performance of polymer:polymer cells makes them particularly difficult to optimize, or to translate previous knowledge from spin coating into more scalable techniques. In this work, the photovoltaic performance of blade-coated devices was studied based on the promising polymer:polymer system PBDB-T and PF5-Y5 as donor and acceptor, respectively. Using the recently developed high-throughput methodology, the system was optimized for multiple variables, including solvent system, active layer composition, ratio, and thickness, among others, by fabricating more than 500 devices with less than 24 mg of each component. As a result, the power conversion efficiency of the blade-coated devices varied from 0.08 to 6.43% in the best device. The performed statistical analysis of the large experimental data obtained showed that solvent selection had the major impact on the final device performance due to its influence on the active layer microstructure. As a conclusion, the use of the plot of the device efficiency in the Hansen space was proposed as a powerful tool to guide solvent selection in organic photovoltaics.

## Introduction

In recent years, solution-processed organic photovoltaic (OPV) performance has improved significantly, surpassing power conversion efficiencies (PCEs) of 18%.[1,2] All-polymer solar cells (all-PSCs) have attracted increasing attention in the OPV field, as they exhibit several advantages with respect to polymer donor:small molecular acceptor solar cells, such as better thermal and mechanical stability, as well as improved processing versatility for up-scaling.[3–6] All-PSCs currently exhibit, however, overall slightly lower PCEs than their polymer:small molecule counterparts, although the gap is rapidly diminishing.[5,7,8] For many combinations, the lower performance is mainly due to the formation of non-optimal film morphologies, and in some cases, lower absorption coefficients than state-of-the-art molecular acceptors, such as O-IDTBR ((5Z,5′Z)-5,5′-((7,7′-(4,4,9,9-tetraoctyl-4,9-dihydro-s-indaceno[1,2-b:5,6-b′]-dithiophene-2,7-diyl)bis(benzo[c][1,2,5]thiadiazole-7,4-diyl))bis-(methanylylidene))bis(3-ethyl-2-thioxothiazolidin-4-one)) or ITIC (3,9-bis(2-methylene-(3-(1,1-dicyanomethylene)-indanone))-5,5,11,11-tetrakis(4-hexylphenyl)-dithieno[2,3-d:2′,3′-d′]-s-indaceno[1,2-b:5,6-b′]dithiophene),[9] and to lower charge carrier mobilities (electrons especially).[7,10]

The lower electron mobility issue has been addressed by designing polymer acceptors based on naphthalene diimide (NDI) like P(NDI2OD-T2) (commercially known as N2200)(Poly {[N,N′-bis(2-octyldodecyl)naphthalene-1,4,5,8-bis-(dicarboximide)-2,6-diyl]-alt-5,5′-(2,2′-bithiophene)),[7,10,11] or perylene diimide (PDI),[12,13] and lately on novel non-fullerene acceptor (NFA) molecules,[8,14,15] like the polymer used in this work, PF5-Y5 (see Figure 1 for the structure).[16] The electron mobility of the latter has been reported to be $3.18\times10^{-3}$ $cm^2 V^{-1} s^{-1}$, very close to the mobility of Y5 small-molecule acceptor ($3.82\times10^{-3}$ $cm^2 V^{-1} s^{-1}$), which acts as the electron-deficient unit for PF5-Y5, and higher than ITIC ($3.58\times10^{-4}$ $cm^2 V^{-1} s^{-1}$), one of the more widely used NFAs.[17] Moreover, PF5-Y5 displays an improved absorption coefficient compared to its small-molecule acceptor counterpart Y5.[16]

On the other hand, the film morphology issue is very intrinsic of polymer mixtures as it arises from the low entropy of mixing found in large-molecular-weight systems. Following Flory–Huggins theory, the very limited degrees of freedom

[a] A. Harillo-Baños, Dr. M. Campoy-Quiles
Institut de Ciència de Materials de Barcelona (ICMAB-CSIC)
Carrer dels Til·lers s/n Campus UAB
Bellaterra 08193 (Spain)
E-mail: mcampoy@icmab.es

[b] Dr. Q. Fan, Prof. E. Wang
Department of Chemistry and Chemical Engineering
Chalmers University of Technology
Göteborg, 412 96 (Sweden)

[c] Dr. S. Riera-Galindo, Prof. O. Inganäs
Biomolecular and Organic Electronics
Department of Physics, Chemistry and Biology (IFM)
Linköping University
Linköping, 581 83 (Sweden)
E-mail: olle.inganas@liu.se

Supporting information for this article is available on the WWW under https://doi.org/10.1002/cssc.202101888

*This publication is part of a collection of invited contributions focusing on "Advanced Organic Solar Cells". Please visit chemsuschem.org/collections to view all contributions.*

*© 2021 The Authors. ChemSusChem published by Wiley-VCH GmbH. This is an open access article under the terms of the Creative Commons Attribution License, which permits use, distribution and reproduction in any medium, provided the original work is properly cited.*


© 2021 The Authors. ChemSusChem published by Wiley-VCH GmbH

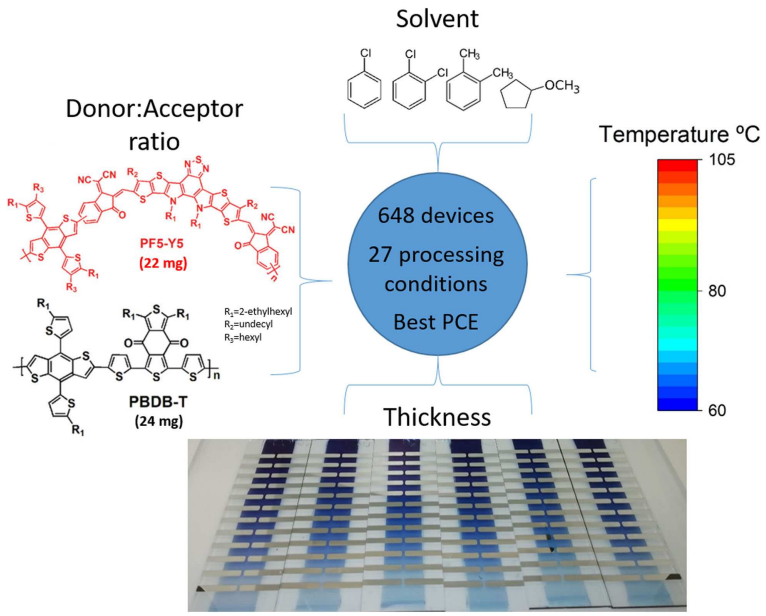


**Figure 1.** Schematic of the processing conditions for high-throughput screening of polymer:polymer solar cells.

accessible to most atoms in the covalently bonded polymer make the entropy of mixing small, and thus the tendency to demix pronounced.[18,19] A stronger π-orbital overlap at the donor/acceptor (D/A) interfaces is formed when the polymer donor and the polymer acceptor are aligned face-to-face, thereby reducing the exciton binding energy and promoting the formation of free charge carriers in all-PSCs.[20,21] Many efforts have been addressed to improve the morphology of all-PSCs by modifying the polymer structure, like side-chain engineering of the polymer backbone,[22,23] developing random copolymers,[24,25] or optimizing the molecular weight of the polymers.[26] Moreover, from a practical point of view, there are many examples of controlling the film morphology of all-PSCs blends by optimizing the deposition parameters; some examples include the use of different additives and solvents,[16,17,27,28] thermal and solvent annealing,[29,30] sequentially depositing the polymers (layer-by-layer),[31–33] mixed-flow microfluidic,[34] and even ternary systems.[4,5,35]

In most cases, spin coating with rapidly evaporating solvents is used to freeze the solution microstructure and thus prevent large-scale phase separation. With polymer:polymer blends in solution, the higher viscosity due to polymers will restrict diffusion and tend to retain the solution glassy-like blend structure. This approach cannot be readily transferred to other more scalable methods, such as blade coating, where slower rates of evaporation are found, and the drying period is often extended over many seconds. Also, the parameter space for optimization is very large, and large amounts of material are required to scan the different processing avenues. Besides, there may be fundamental limitations regarding how fast the solvent can be removed in a process such as blade coating, compared to spin coating. This, together with the lack of rationales for morphology control, has prevented all-PSCs from moving beyond lab scale. We note, however, the recent appearance of highly efficient all-PSCs over 1 $cm^2$ areas, albeit depositing the active layer again by spin coating.[36]

In this work, we investigate the importance of different deposition parameters, including solvent selection and solubility, in the final efficiency of devices based on PBDB-T:PF5-Y5 D/A blends. The corresponding chemical structures are shown in Figure 1. This system has resulted in one of the highest polymer:polymer efficiencies thus far, reaching 14% when optimized and processed by spin coating.[16] We have employed our high-throughput methodology recently developed to screen blade-coating conditions for all-PSCs.[37] Similar high-throughput methodology has been also reported recently to optimize the composition of ternary blends.[38] Using only 22 mg of D and 24 mg of A, we have produced more than 500 devices and scanned 27 different processing conditions (Figure 1). Statistical analysis based on ANOVA[39] shows that the parameters related to the solvent characteristics (boiling point and Hansen solubility parameters) are the most important factors correlating to efficiency. Additional spectroscopic measurements on the devices provide further insights into the morphology and its correlation with performance. Moreover, we propose to plot efficiency in the Hansen space (without the need to actually measure the Hansen parameters of the materials) as a tool to find appropriate solvents, that is, solvents that produce microstructures that optimize device performance.

## Results and Discussion

The corresponding chemical structures are shown in Figure 1. PF5-Y5 was synthesized following previous reports.[16] The polymers present complementary absorption spectra and their


© 2021 The Authors. ChemSusChem published by Wiley-VCH GmbH

energy levels allow to obtain high open-circuit voltage (see Figure S1 in the Supporting Information). In total, we have fabricated 648 devices by blade coating, with 26 different processing conditions, including 10 solvent systems, 6 D/A composition ratios (1:0.5, 1:0.75, 1:0.9, 1:1, 0.75:1, 0.5:1, 0.25:1, 0.11:1), 3 deposition temperatures (60, 80, and 105 °C), and sequential depositions. Additionally, all samples were fabricated with active layer thickness gradients by means of variable speed blade during deposition, in order to deepen the exploration of the parameter space at minimum material cost.[40] These thickness gradients were fabricated by linearly decelerating the blade during deposition from 90 to 10 mm $s^{-1}$, within the 7.5 cm length of substrate (each divided in 24 devices). Higher speeds produce thicker films, so by decelerating we obtain a gradient from a thicker to a thinner layer because we are working in viscous drag regime (also called Landau–Levich regime). Moreover, the thickness also depends on the amount of solution left in front of the blade, becoming thinner as the solution runs out; we minimized the thickness differences from batch to batch by depositing the same amount of solution in each deposition. The combination of these two effects increases the gradient slope. Typically we have obtained thicknesses from 100 to 30 nm in a single substrate (see Figure S2).[37] The entire study was done using only 22 mg of PBDB-T and 24 mg of PF5-Y5, averaging to 0.07 mg of total material per pixel, where each pixel has an area of 8 $mm^2$. This 0.07 mg average takes into account all the losses of the manufacturing, like excess solution and removed or non-contacted active layer. For comparison purposes, an equivalent study but without high-throughput methodology, which used spin coating, would have required around 1.2 mg per data point, or a total of 330 mg of each material.[41] The optimal composition ratio was found to be 1:0.75 D/A, but, as mentioned, more ratios were explored for completeness.[16]

The solvents used for this study were some of the most widely used solvents in OPV processing, namely *o*-xylene (O-XY), chlorobenzene (CB), and dichlorobenzene (DCB), as well as cyclopentyl methyl ether (CPME), a promising green solvent.[42,43] Some relevant properties of these solvents, such as boiling point and Hansen parameters,[44] are displayed in Table 1. Devices were fabricated with active layers that use these four solvents and binary mixtures thereof, usually by mixing a 1:1 volume ratio. Figure 2a shows representative current density–voltage (*J*–*V*) curves for different solvents, and Figure 2b gives an example of the use of thickness gradients to determine optimum thickness for the solvent system, which leads to a higher performance. Additionally, thickness-dependent data for other systems can be found in the Supporting Information (Figures S2, S4–S8). Even though in organic solar cells the optimized active layer thickness is generally over 100 nm, using blade coating of PBDB-T and PF5-Y5, the optimum thickness is below 100 nm. Probably, this may be because the microstructure of the polymers limits the charge transport, resulting in optimum efficiency for thinner active layers.[45]

Table 2 shows the D/A ratio, deposition temperature, and blade speed that led to highest performance for each solvent system, as well as the number of devices and the analyzed processing conditions (Notes). The final PCEs of the devices vary greatly depending on the deposition parameters with PCE values ranging from 0.08 to 6.4 %. Moreover, the photovoltaic parameters obtained for the same solvent system are different when comparing spin coating and blade coating, as the two techniques can lead to different film morphologies due to their

**Table 1.** Solvent properties.

| Short name | Boiling point [°C] | δ*D* | δ*P* | δ*H* | Structure |
|---|---|---|---|---|---|
| CPME | 106 | 16.7 | 4.3 | 4.3 | 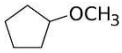 |
| O-XY | 144 | 17.8 | 1.0 | 3.1 | 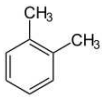 |
| CB | 132 | 19 | 4.3 | 2.0 | |
| DCB | 180 | 19 | 6.3 | 3.3 | |

**Table 2.** Conditions that led to the highest efficiency for each solvent, and corresponding device data.[a]

| Solvent system | D/A | *T* [°C] | Blade speed [mm $s^{-1}$] | $V_{oc}$ [V] | $J_{sc}$ [mA $cm^{-2}$] | FF [%] | PCE [%] | Number of devices per solvent system | Notes |
|---|---|---|---|---|---|---|---|---|---|
| CPME | 1:0.9 | 60, 80, 105 | 90 | 0.77 | −1.25 | 37.1 | 0.36 | 72 | thickness, *T* |
| CPME/O-XY (0.65:0.35) | 0.75:1 | 80 | 83 | 0.69 | −4.20 | 33.6 | 0.97 | 48 | thickness |
| CPME/O-XY (1:1) | 1:0.5 | 80 | 90 | 0.77 | −4.24 | 48.4 | 1.57 | 120 | thickness, D/A ratio |
| O-XY | 1:0.9 | 80 | 90 | 0.75 | −7.61 | 35.8 | 3.17 | 144 | thickness, D/A ratio |
| O-XY | 1:0.9 | 80 | 61 | 0.91 | −10.76 | 53.0 | 5.20 | 24 | thickness, 2 layers[b] |
| CB | 1:0.5 | 80 | 25 | 0.44 | −2.33 | 28.5 | 0.30 | 24 | thickness |
| DCB | 1:0.75 | 105 | 61 | 0.94 | −12.41 | 51.8 | 6.02 | 96 | thickness, D/A ratio |
| CB/DCB (1:1) | 1:1 | 105 | 83 | 0.94 | −13.09 | 52.1 | 6.43 | 24 | thickness |
| DCB/O-XY (1:1) | 0.5:1 | 105 | 32 | 0.88 | −8.26 | 49.3 | 3.59 | 48 | thickness, D/A ratio |
| CB/O-XY (1:1) | 1:0.75 | 80 | 10 | 0.38 | −0.67 | 30.7 | 0.08 | 24 | thickness |
| DCB/CPME (1:1) | 1:0.75 | 105 | 54 | 0.57 | −20.02 | 35.7 | 4.04 | 24 | thickness |

[a] $V_{oc}$: open-circuit voltage; $J_{sc}$: short-circuit current density; FF: fill factor. Notes indicates the screened fabrication parameters [b] The active layer was deposited twice in a sequential deposition, keeping the thickness gradient in both layers.


© 2021 The Authors. ChemSusChem published by Wiley-VCH GmbH

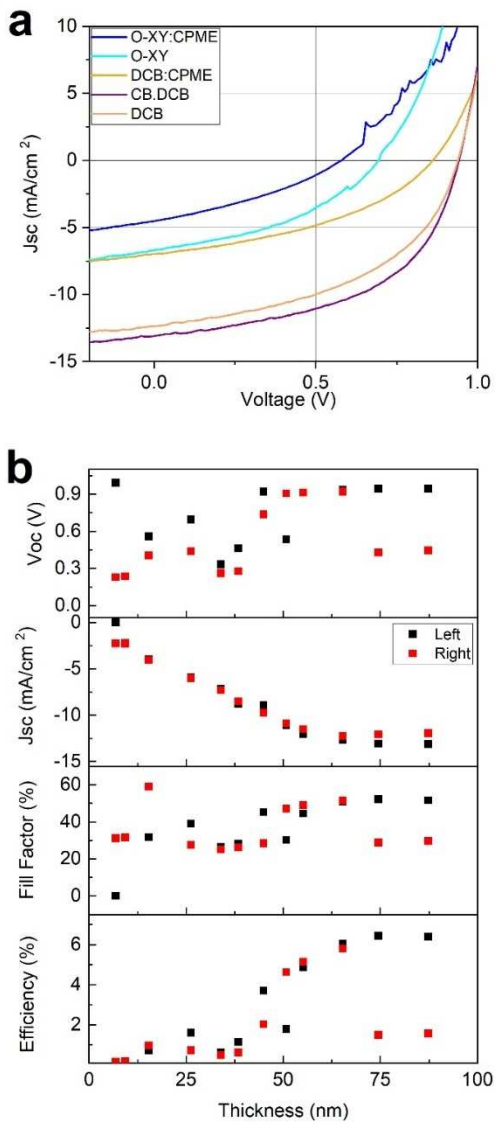


**Figure 2.** (a) *J–V* curves for one of the best cells for each of the five best solvent systems (O-XY, DCB, CB:DCB, CPME/O-XY, and DCB/CPME) (b) $J_{sc}$, $V_{oc}$, FF, and PCE as a function of active layer thickness for each pixel for one of the best solvents (CB/DCB). Each substrate contains 24 pixels, 12 on either side (labelled left and right). The thickness gradient is expected to be along the long axis of the substrate, leaving two nominal duplicates per thickness.

different drying mechanisms and times.[46] The devices with higher performance were those that used DCB as part of the solvent system. In Figure S10, the external quantum efficiencies (EQEs) of PBDB-T:PF5-Y5 at 1:1, 1:4, and 1:8 D/A ratio using DCB are shown. Devices with D/A ratio 1:1 have better performance, showing a deep valley at 700 nm in the EQE for thinner active layers; this effect decreases as the thickness of the active layer increases. Interestingly, at D/A ratio 1:4, devices with thicker active layer show higher EQE in the donor region than the acceptor region. Finally, devices with D/A ratio 1:8 have a poor performance, showing an EQE peak at 800 nm. On the other hand, employing CB as the only solvent resulted in very low PCE values. Interestingly, when using the mixed CB/DCB system, we obtained the highest PCE. Similarly, the devices were significantly improved when using DCB/CPME instead of just CPME. This might lead to the conclusion that, in solvent mixtures, the solvent with highest boiling point lasts longer during the deposition and, thus, is the one that has the greatest impact on the final morphology and the concomitant PSC performance. This is a similar mechanism to what is observed in some cases when additives are used.[47]

Other factors, such as pre-aggregation of the polymers in solution, will strongly depend on the solvent and solvent mixture and could have strong effects on the final micro-structure and concomitant photovoltaic performance.[48] From the above discussion, it seems clear that predicting which deposition conditions (including choice of solvent) are required for obtaining high efficiencies is not straightforward.

To determine which of the deposition parameters affects more strongly the final PCE, we performed a One-Way ANOVA analysis for several parameters of all of the fabricated devices.[49,50] This analysis results in a parameter, namely F factor, which quantifies how much the target magnitude (PCE in this case) varies when the given parameter is scanned. In other words, it is a statistical measure of the importance of a given parameter in the final efficiency. We analyzed the importance of the D/A ratio, the used blade speed for each pixel (as a proxy for active layer thickness), the boiling point, and Hansen solubility parameters to characterize each solvent. Deposition temperature was not analyzed in detail as different temperatures for the same system (CPME) resulted in negligible changes in performance. Results are shown in Table 3, where, as mentioned, larger F factors mean larger impact in the final PCE. The ANOVA analysis indicates that, within the relatively large parameter space explored, solvent selection is the parameter that has the largest impact on final PCE of the devices, even compared to thickness of the active layer and D/A composition ratio. A note of caution should be given here, as the ANOVA analysis only considers the existing data, and we have not fabricated cells with extreme thickness (e.g., μm) or composition values (e.g., 1:0), but rather typical (but relatively wide) range of values that result in efficient cells as described in the experimental section and in Figures 2b and S3–S7.

As solvent appears to be the most important of the explored parameters, we represented in a box plot the PCE of all the devices fabricated for each different solvent and mixture. In Figure 3, the solvent systems used in this work are ordered

**Table 3.** ANOVA analysis of the parameters varied during the solar cell fabrication.

| Property | F |
|---|---|
| blade speed | 6 |
| D/A ratio | 14 |
| $\delta D$ | 45 |
| $\delta P$ | 68 |
| $\delta H$ | 46 |
| boiling point[a] | 46 |
| boiling point[b] | 110 |

[a] For mixtures, average value between solvents. [b] For mixtures, value of the highest boiling point amongst components.


© 2021 The Authors. ChemSusChem published by Wiley-VCH GmbH

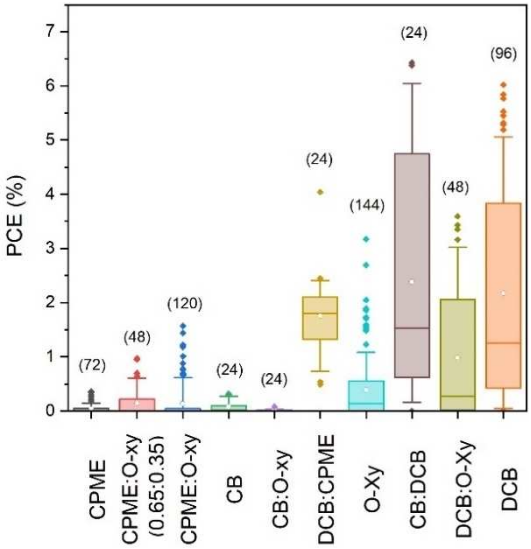


**Figure 3.** Statistical representation of all samples fabricated as a function of solvent (with increasing solvent boiling point). In parentheses is the number of devices fabricated per solvent. Each box contains 25th to 75th percentile of all the PCE for a solvent or mixture, while whiskers cover 10th to 90th. White dots inside the boxes are the mean PCE of the solvent, and colored dots outside the boxes are outliers above 90th or below 10th percentile.

from lower to higher boiling point on the *x*-axis. The observed trend between higher boiling point and higher PCE could be related with the slower evaporation rates in blade coating depositions, which would allow a morphological reorganization of the polymer:polymer system.

In light of the results of the ANOVA analysis (see Table 3), we decided to analyze the role of the solubility by plotting the PCE in the Hansen parameter space, assigning to each PCE value the Hansen coordinates of the corresponding solvent used for the preparation of the active layer of the device. The corresponding 2D projections of the 3D Hansen space are plotted in Figure 4.

In this representation, we obtain a continuous landscape with two PCE maxima and a deep valley in between. This double maximum in PCE might be due to different reasons, such as a difference in solubility of the two materials, the interaction between solvents, or the possibility of specific solvents promoting aggregation in solution. It is noteworthy to mention than we did not calculate the Hansen solubility parameters of both materials, and therefore we did not need the large quantities of materials that this kind of study requires. Instead, we find clear tendencies when plotting directly PCE. Also, in this representation, the maximum does not represent the maximum solubility, but rather the optimum solubility of the blend for solar cells, which has a more direct application in device fabrication and optimization. We would like to explain that our original data set included 80% of the data points

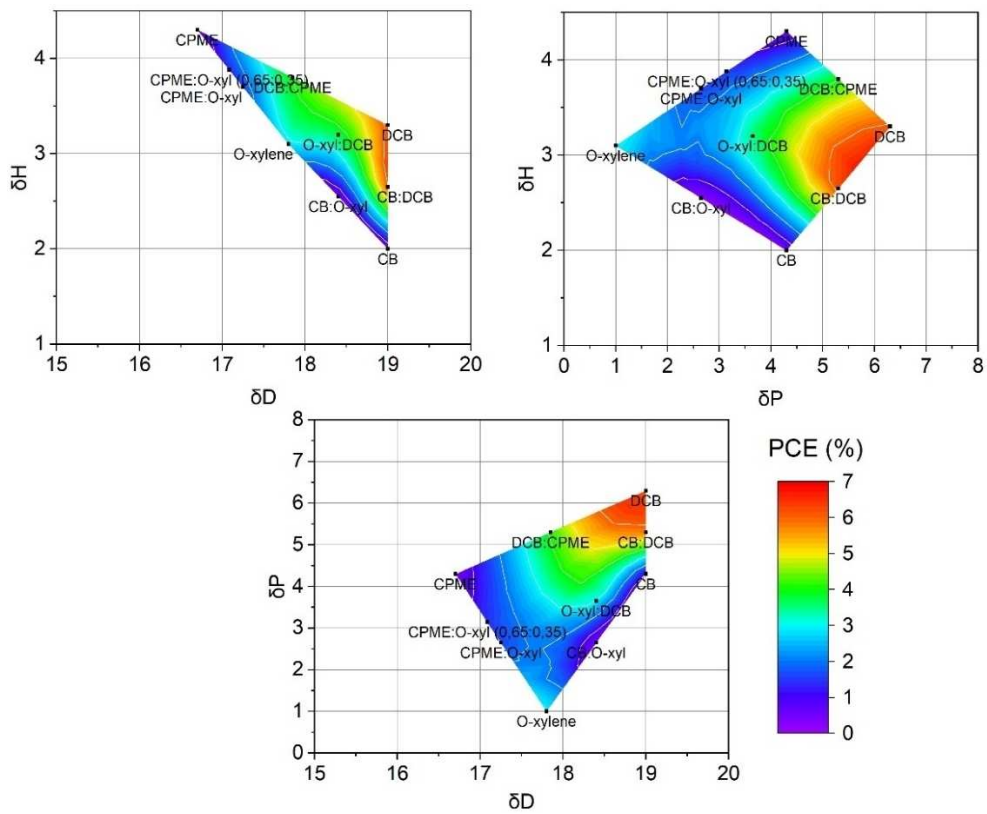


**Figure 4.** Performance landscape of polymer:polymer solar cells represented on the Hansen solubility space.


© 2021 The Authors. ChemSusChem published by Wiley-VCH GmbH

currently shown in Figure 4. After seen the initial version of the plotted data, we decided to make an initial evaluation of the predicting capability of the Hansen efficiency surface by fabricating cells using two additional solvent mixtures. We prepared CB/O-XY- and DCB/CPME-based devices, included in Figure 4, and found that they fitted into the surface. While a full evaluation of the predicting capability of this approach would require a larger subset of solvents and solvent mixtures, these results strongly suggest that this representation can be useful to identify good solvents in all-PSCs.

In order to understand the differences in performance of the devices fabricated based on different solvents, we evaluated the same device samples using a variety of microscopic and spectroscopic tools. Since our target was to perform the study minimizing the raw material employed, we performed this study on full devices, only using films of the pristine materials as reference. Figure 5 shows obtained optical microscopy and photoluminescence (PL) images taken on pixels with highest performance for five of the solvents used. The PL images show position-dependent integrated intensity for two PL bands, one

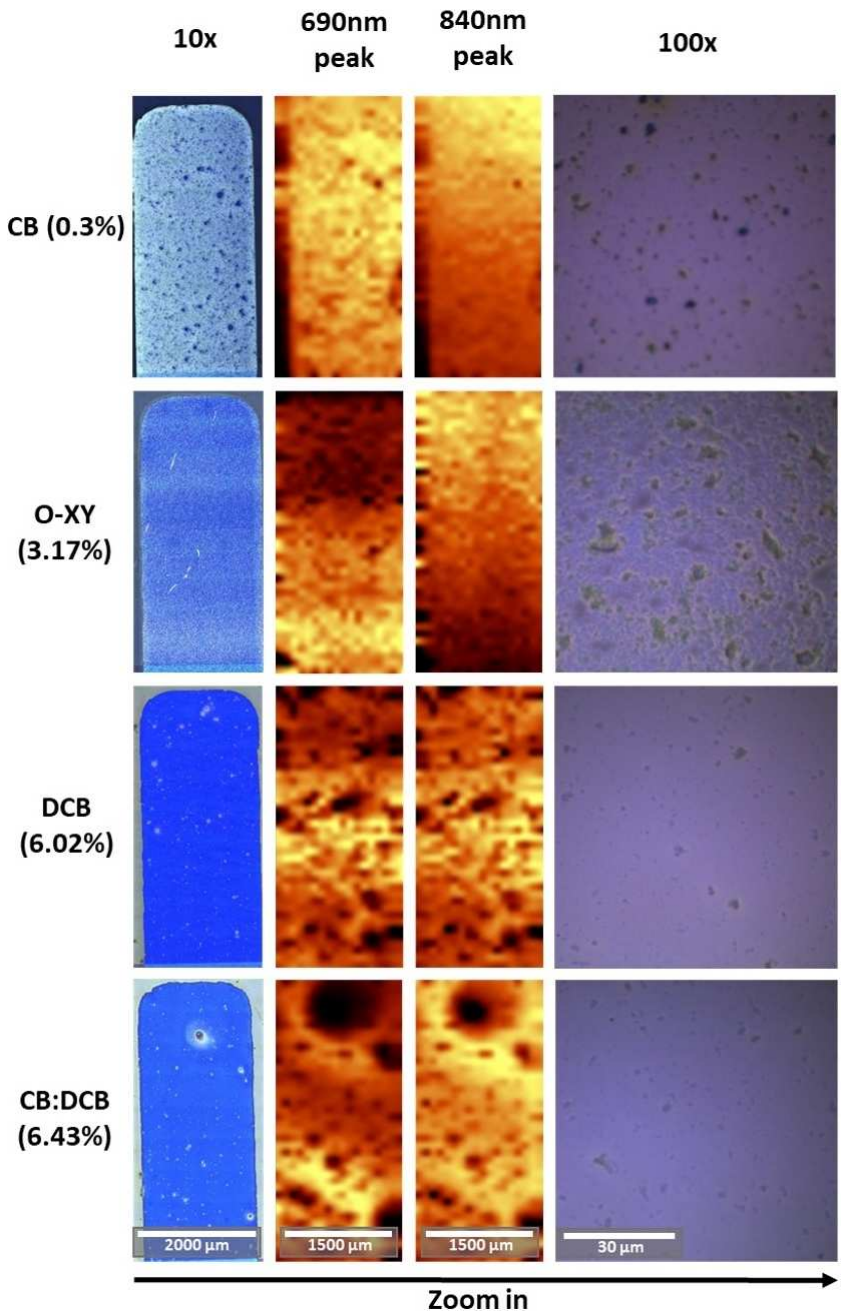


**Figure 5.** For the best device fabricated with each solvent (PCE in parentheses), from left to right: microscope image of device with 10× objective, integration of the 690 and 840 nm PL peaks, and microscope image with 100× objective, respectively. Note: PL measurements do *not* share the same intensity (color) scale.


© 2021 The Authors. ChemSusChem published by Wiley-VCH GmbH

centered at 690 nm and the other one at 840 nm, corresponding to PL from the donor and acceptor materials, respectively (see Figure S3).

Samples fabricated from CB are inhomogeneous at all length scales. The 100× optical microscopy images (Figure 5) show that large crystals have formed in all devices, but they reduce in size and number with increasing PCE, as well as the layer being more homogeneous (i.e., DCB and CB/DCB samples). Despite some larger defects and crystals appearing in the best-performing cells (10× images), the rest of the active layer is rather homogeneous, while in the less-efficient devices the crystals are more omnipresent throughout the device. The integrated PL over the whole pixel scales with the film thickness and overall composition, and it is shown in Figure S3. Comparing the PL magnitude, there are thickness or composition variations at the pixel level for all the substrates (note that the PL images do not share Y scale).

To gain further insights into the differences between solvents, and inspired by the fact that different solvents resulted in different "optimum" thickness, we looked at the thickness dependence of the morphology. Figures S4–S9 show a set of images for pixels with different active layer thickness as a function of deposition solvent. One general observation is that the number of micron-sized crystals strongly depend on thickness: thinner layers exhibit less crystallites. This could be due to the effect of geometrical confinement.[51] Alternatively, it may be a result of pre-aggregation: thicker films would naturally deposit a larger amount of solid content on the film, thus increasing the number of pre-aggregated crystallites. The low device PCE of some of the solvents might be explained through this excessive crystallization and phase separation. Moreover, this also explains why the optimum thickness for the worse solvents is thinner than for good solvents (Figure S2).

To understand the formation of these large aggregates, we performed high-resolution Raman spectroscopy imaging in the same samples. This helped us to confirm the composition of the crystallites and the blend around them. Upon subtraction of the background and cosmic rays, the Raman data was investigated by principal components analysis and compared to the Raman spectra of each material. This analysis allows to evaluate differences in the local composition of D/A. The results of this analysis are summarized in Figure 6.

At this length scale (25 μm×25 μm) several morphological issues could be detected. The Raman analysis shows that there are indeed variations in the local composition, specifically at defects and/or crystallites, that are in most cases, very rich in acceptor. This is consistent with the stronger tendency to crystallize for PF5-Y5 compared to the donor polymer, as reported in the literature by means of GIWAXS (Grazing-Incidence Wide-Angle X-ray Scattering).[16] If we take as proxy for the degree of phase separation the spectral difference between different regions, we can observe that the general trend is that films become more homogeneous when using solvents that lead to higher device efficiencies, probably due to unfavorable phase separation and/or crystallization of PF5-Y5. We note, however, that the spatial resolution of this experiment is still low compared to the exciton diffusion length. Interestingly, while some solvents resulting in moderate (O-XY) device efficiencies also exhibit variability in the blend composition at micron scale, as probed by Raman spectroscopy, the case of CB is different, as it looks particularly homogeneous in terms of composition judging by the similarity between spectra at different locations.

## Conclusions

We have demonstrated that one of the most important factors in the final power conversion efficiency (PCE) of all-polymer solar cells (all-PSCs) fabricated by blade coating is indeed solvent selection. We first found that there appears to be a minimum boiling point for the microstructure of the active layer obtained by blade coating to be acceptable. This is a necessary but not sufficient requirement as particular solubility values are also required. The importance of the solvent selection is exemplified with the appearance of large, micron-sized aggregates of the acceptor (PF5-Y5), which are either present in the solution or generated while depositing the layer and are detrimental to the performance of the device. The size and number of these crystallites depend on the thickness of the active layer and the solvent used, with more crystallites protruding in thicker layers. A consequence of this is that bad solvents only lead to functional devices for thin films, much thinner than the thickness the leads to the maximum interference of the electric field within the active layer. On the other hand, devices fabricated with better solvents can be fabricated thicker, yielding overall higher PCE.

The current study was done using our high-throughput method, which allowed us to complete the study with less than 24 mg of each material. This is only a small fraction of the material that would have been required for the same study and the same number of samples (648 devices) following conventional methodologies. The number of devices is enough to apply simple statistical analysis of the relevance of the different parameters, from which solvent solubility and boiling point are highlighted. We propose the visualization of the PCE in the Hansen space as a tool to guide the selection of solvents in all-PSC. Our methodology would allow to implement algorithms to find the most relevant processing parameter for optimal blend morphology in the complex structure–property relationships of all-PSC, instead of the daunting trial-and-error approach, and consequently optimize the performance of all-PSC.

## Experimental Section

### Materials

The glass substrates with patterned indium tin oxide (ITO; 100 nm thick) were purchased in Ossila. ZnO ink formulation was purchased from Avantama. PBDB-T (Poly[(2,6-(4,8-bis(5-(2-ethylhexyl)thiophen-2-yl)-benzo[1,2-b:4,5-b′]dithiophene))-alt-(5,5-(1′,3′-di-2-thienyl-5′,7′-bis(2-ethylhexyl)benzo[1′,2′-c:4′,5′-c′]dithiophene-4,8-dione)]) was purchased from Brilliant Matters. PF5-Y5 was synthesized as reported elsewhere.[16] The polymers were dissolved in a concen-


© 2021 The Authors. ChemSusChem published by Wiley-VCH GmbH

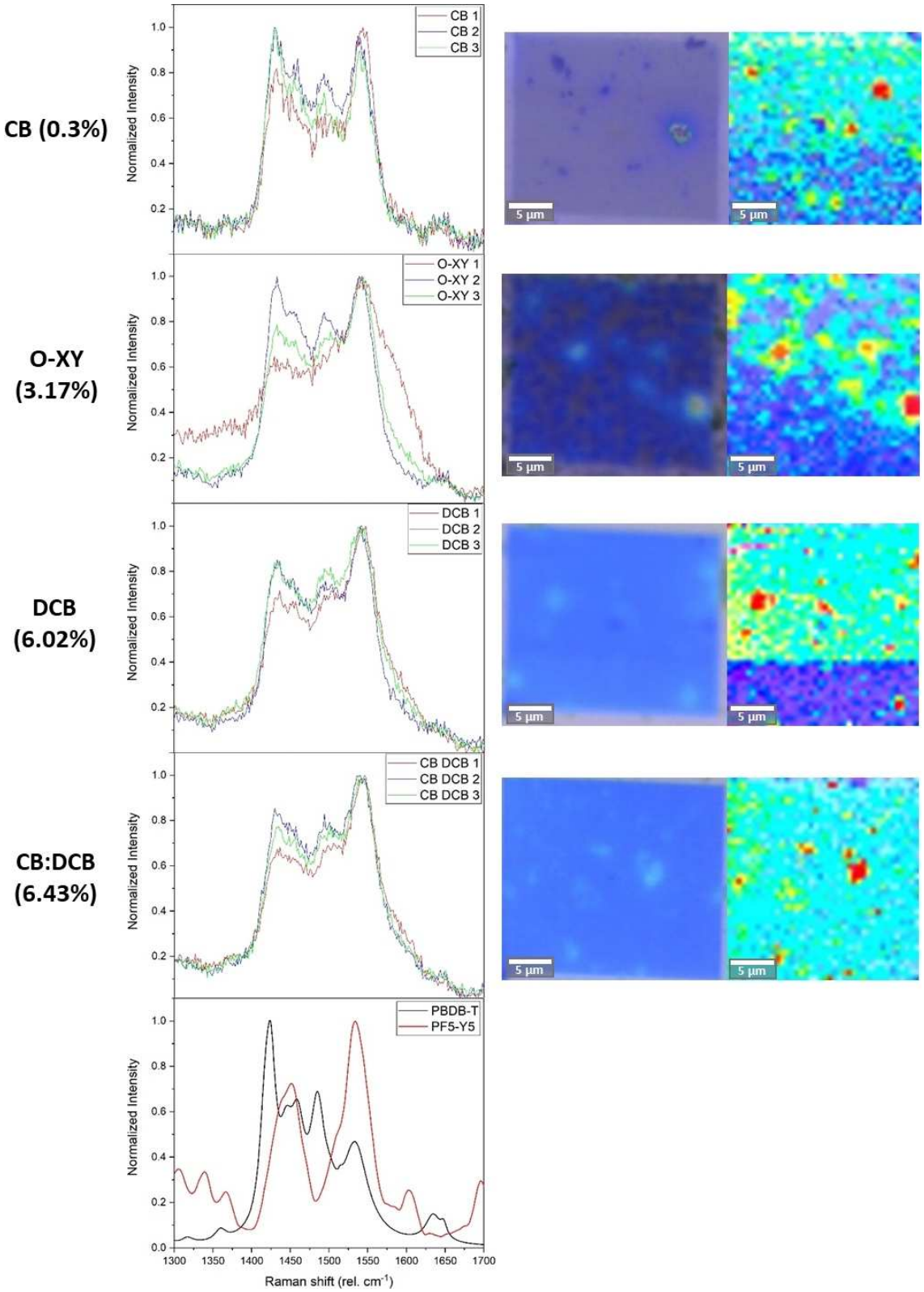


**Figure 6.** For the best device fabricated with each solvent (PCE in parentheses), left to right: comparison of the different spectra obtained in high-resolution Raman imaging; 100× microscopy image of the mapped zone; Raman mapping of the components, with acceptor-rich areas in red. Last plot is the reference Raman spectra of pure donor and pure acceptor. Note that, for clarity, the images do *not* share the same scale.


© 2021 The Authors. ChemSusChem published by Wiley-VCH GmbH

tration range of 15 mg mL$^{-1}$. Molybdenum oxide (MoOx) was acquired from Alfa Aesar.

### Sample preparation

The substrates were cleaned by consecutive sonication baths in acetone, Hellmanex 10 vol% solution in water, isopropanol (5 min each), and sodium hydroxide 10 vol% (10 min), rinsing with deionized (DI) water after each step. We fabricated the solar cells using an inverted structure. The bottom transport layer (ZnO), which acts as electron transport layer (ETL), was deposited using an automatic blade coater Zehntner ZAA 2300 with an aluminum applicator Zehntner ZUA 2000, in air conditions and at a constant speed of 5 mm s$^{-1}$, with a drop volume of 50 μL, and temperature set at 40 °C. All active layer materials were deposited using a second blade coater equipment (same brand and model) that included custom-made electronics to enable speed gradients, inside a nitrogen-filled and dry glovebox, with a blade gap of 200 μm, and temperature set at different temperatures depending on the solvent: CPME at 60 °C, CB and *o*-xylene at 80 °C, DCB at 105 °C. For mixtures we set the temperature to that corresponding to the solvent with highest boiling point. The drop volume used was 50 μL. For the processing of the thickness gradients the speed was configured as a linearly decelerating speed ramp, from 90 to 10 mm s$^{-1}$. The top transport layer, which acts as hole transport layer (HTL), and electrode (MoOx/Ag) were thermally evaporated at a rate of 0.1 Å s$^{-1}$ for the HTL and 1 Å s$^{-1}$ for the metal electrode, respectively.

### Solar cell characterization

*J–V* characteristics were automatically obtained by using a Keithley source meter and an Arduino based multiplexer/switcher, which allows measuring 24 devices in less than 6 min. As a lighting source, a SAN-EI Electric XES-100S1 AAA solar simulator was used to ensure a homogeneous illumination in a 10 cm × 10 cm area. The solar simulator was previously calibrated with a certified silicon solar cell (Oriel). EQE was measured with a homemade system that uses a supercontinuum light source (4 W, Fianium) coupled to a monochromator and normalized by the light power as measured by a silicon diode. We measured EQEs from 400 to 900 nm wavelength by focusing the laser on a spot of 50 mm in diameter.

### Thin film characterization

The film thickness was measured using a mechanical profilometer (Dektak 150, Bruker). The Raman scattering spectra and PL measurements performed in functional devices were acquired using a WITec alpha 300 RA+ confocal Raman setup, coupled to an Olympus objective with 10X magnification (NA 0.25). Two lasers centered at 488 and 633 nm were employed. The light was focused through the thick (1.1 mm), ITO-covered glass substrates and the laser power reduced accordingly to avoid photodegradation and bleaching of the active layer (3–5 mW at 488 nm excitation). All raw data were collected using WITec Project FIVE piece of software and fitted with a custom-made MATLAB software.[52] Absorption spectra measurements were obtained from bibliography.[16]

## Acknowledgements

*The authors acknowledge financial support from the Spanish Ministry of Science and Innovation through the Severo Ochoa" Program for Centers of Excellence in R&D (No. CEX2019-000917-S), and project PGC2018-095411-B–I00, as well as from the European Research Council (ERC) under Grant Agreement No. 648901.*

## Conflict of Interest

The authors declare no conflict of interest.

**Keywords:** energy conversion · Hansen solubility parameters · high-throughput screening · organic photovoltaics · solar cells

[1] Y. Cai, Y. Li, R. Wang, H. Wu, Z. Chen, J. Zhang, Z. Ma, X. Hao, Y. Zhao, C. Zhang, F. Huang, Y. Sun, *Adv. Mater.* **2021**, *36*, 2101733.
[2] M. Zhang, L. Zhu, G. Zhou, T. Hao, C. Qiu, Z. Zhao, Q. Hu, B. W. Larson, H. Zhu, Z. Ma, Z. Tang, W. Feng, Y. Zhang, T. P. Russell, F. Liu, *Nat. Commun.* **2021**, *12*, 309.
[3] B. Fan, W. Zhong, L. Ying, D. Zhang, M. Li, Y. Lin, R. Xia, F. Liu, H. L. Yip, N. Li, Y. Ma, C. J. Brabec, F. Huang, Y. Cao, *Nat. Commun.* **2019**, *10*, 4100.
[4] X. Liu, C. Zhang, S. Pang, N. Li, C. J. Brabec, C. Duan, F. Huang, Y. Cao, *Front. Chem.* **2020**, *8*, 302.
[5] T. Liu, T. Yang, R. Ma, L. Zhan, Z. Luo, G. Zhang, Y. Li, K. Gao, Y. Xiao, J. Yu, X. Zou, H. Sun, M. Zhang, T. A. Dela Peña, Z. Xing, H. Liu, X. Li, G. Li, J. Huang, C. Duan, K. S. Wong, X. Lu, X. Guo, F. Gao, H. Chen, F. Huang, Y. Li, Y. Li, Y. Cao, B. Tang, H. Yan, *Joule* **2021**, *5*, 914–930.
[6] G. Wang, F. S. Melkonyan, A. Facchetti, T. J. Marks, *Angew. Chem. Int. Ed.* **2019**, *58*, 4129–4142; *Angew. Chem.* **2019**, *131*, 4173–4186.
[7] C. Lee, S. Lee, G. U. Kim, W. Lee, B. J. Kim, *Chem. Rev.* **2019**, *119*, 8028–8086.
[8] H. Fu, Y. Li, J. Yu, Z. Wu, Q. Fan, F. Lin, H. Y. Woo, F. Gao, Z. Zhu, A. K. Y. Jen, *J. Am. Chem. Soc.* **2021**, *143*, 2665–2670.
[9] E. Pascual-San-José, X. Rodríguez-Martínez, R. Adel-Abdelaleim, M. Stella, E. Martínez-Ferrero, M. Campoy-Quiles, *J. Mater. Chem. A* **2019**, *7*, 20369–20382.
[10] Y. Yan, Y. Liu, Q. Zhang, Y. Han, *Front. Chem.* **2020**, *8*, 394.
[11] L. Gao, Z. G. Zhang, L. Xue, J. Min, J. Zhang, Z. Wei, Y. Li, *Adv. Mater.* **2016**, *28*, 1884–1890.
[12] S. Feng, C. Liu, X. Xu, X. Liu, L. Zhang, Y. Nian, Y. Cao, J. Chen, *ACS Macro Lett.* **2017**, *6*, 1310–1314.
[13] Y. Guo, Y. Li, O. Awartani, H. Han, J. Zhao, H. Ade, H. Yan, D. Zhao, *Adv. Mater.* **2017**, *29*, 1700309.
[14] H. Yao, F. Bai, H. Hu, L. Arunagiri, J. Zhang, Y. Chen, H. Yu, S. Chen, T. Liu, J. Y. L. Lai, Y. Zou, H. Ade, H. Yan, *ACS Energy Lett.* **2019**, *4*, 417–422.
[15] Z. G. Zhang, Y. Yang, J. Yao, L. Xue, S. Chen, X. Li, W. Morrison, C. Yang, Y. Li, *Angew. Chem. Int. Ed.* **2017**, *56*, 13503–13507; *Angew. Chem.* **2017**, *129*, 13688–13692.
[16] Q. Fan, Q. An, Y. Lin, Y. Xia, Q. Li, M. Zhang, W. Su, W. Peng, C. Zhang, F. Liu, L. Hou, W. Zhu, D. Yu, M. Xiao, E. Moons, F. Zhang, T. D. Anthopoulos, O. Inganäs, E. Wang, *Energy Environ. Sci.* **2020**, *13*, 5017–5027.
[17] W. Zhao, S. Li, H. Yao, S. Zhang, Y. Zhang, B. Yang, J. Hou, *J. Am. Chem. Soc.* **2017**, *139*, 7148–7151.
[18] G. Kumaraswamy, *Resonance* **2017**, *22*, 415–426.
[19] M. L. Huggins, *J. Chem. Phys.* **1941**, *9*, 440.
[20] M. Schubert, B. A. Collins, H. Mangold, I. A. Howard, W. Schindler, K. Vandewal, S. Roland, J. Behrends, F. Kraffert, R. Steyrleuthner, Z. Chen, K. Fostiropoulos, R. Bittl, A. Salleo, A. Facchetti, F. Laquai, H. W. Ade, D. Neher, *Adv. Funct. Mater.* **2014**, *24*, 4068–4081.
[21] L. Ye, X. Jiao, M. Zhou, S. Zhang, H. Yao, W. Zhao, A. Xia, H. Ade, J. Hou, *Adv. Mater.* **2015**, *27*, 6046–6054.
[22] W. Lee, C. Lee, H. Yu, D. J. Kim, C. Wang, H. Y. Woo, J. H. Oh, B. J. Kim, *Adv. Funct. Mater.* **2016**, *26*, 1543–1553.
[23] B. Fan, L. Ying, P. Zhu, F. Pan, F. Liu, J. Chen, F. Huang, Y. Cao, *Adv. Mater.* **2017**, *29*, 1703906.
[24] S. W. Kim, J. Choi, T. T. T. Bui, C. Lee, C. Cho, K. Na, J. Jung, C. E. Song, B. Ma, J. Y. Lee, W. S. Shin, B. J. Kim, *Adv. Funct. Mater.* **2017**, *27*, 2–9.
[25] Z. Li, W. Zhang, X. Xu, Z. Genene, D. Di Carlo Rasi, W. Mammo, A. Yartsev, M. R. Andersson, R. A. J. Janssen, E. Wang, *Adv. Energy Mater.* **2017**, *7*, 1602722.
[26] H. Kang, M. A. Uddin, C. Lee, K. H. Kim, T. L. Nguyen, W. Lee, Y. Li, C. Wang, H. Y. Woo, B. J. Kim, *J. Am. Chem. Soc.* **2015**, *137*, 2359–2365.


© 2021 The Authors. ChemSusChem published by Wiley-VCH GmbH

[27] C. Duan, Z. Li, S. Pang, Y. L. Zhu, B. Lin, F. J. M. Colberts, P. J. Leenaers, E. Wang, Z. Y. Sun, W. Ma, S. C. J. Meskers, R. A. J. Janssen, *Solar RRL* **2018**, *2*, 1800247.
[28] H. Hu, M. Ghasemi, Z. Peng, J. Zhang, J. J. Rech, W. You, H. Yan, H. Ade, *Adv. Mater.* **2020**, *32*, 2005348.
[29] J. Yuan, W. Ma, *J. Mater. Chem. A* **2015**, *3*, 7077–7085.
[30] J. Yuan, Y. Xu, G. Shi, X. Ling, L. Ying, F. Huang, T. H. Lee, H. Y. Woo, J. Y. Kim, Y. Cao, W. Ma, *J. Mater. Chem. A* **2018**, *6*, 10421–10432.
[31] T. Shan, Y. Hong, L. Zhu, X. Wang, Y. Zhang, K. Ding, F. Liu, C. C. Chen, H. Zhong, *ACS Appl. Mater. Interfaces* **2019**, *11*, 42438–42446.
[32] Y. J. Kim, C. E. Park, *Org. Electron.* **2018**, *52*, 301–308.
[33] Y. Xu, J. Yuan, S. Liang, J. De Chen, Y. Xia, B. W. Larson, Y. Wang, G. M. Su, Y. Zhang, C. Cui, M. Wang, H. Zhao, W. Ma, *ACS Energy Lett.* **2019**, *4*, 2277–2286.
[34] G. Wang, L. W. Feng, W. Huang, S. Mukherjee, Y. Chen, D. Shen, B. Wang, J. Strzalka, D. Zheng, F. S. Melkonyan, J. Yan, J. Fraser Stoddart, S. Fabiano, D. M. DeLongchamp, M. Zhu, A. Facchetti, T. J. Marks, *Proc. Natl. Acad. Sci. USA* **2020**, *117*, 17551–17557.
[35] Y. Xia, C. Musumeci, J. Bergqvist, W. Ma, F. Gao, Z. Tang, S. Bai, Y. Jin, C. Zhu, R. Kroon, C. Wang, M. R. Andersson, L. Hou, O. Inganäs, E. Wang, *J. Mater. Chem. A* **2016**, *4*, 3835–3843.
[36] T. Jia, J. Zhang, K. Zhang, H. Tang, S. Dong, C.-H. Tan, X. Wang, F. Huang, *J. Mater. Chem. A* **2021**, *9*, 8975–8983.
[37] A. Sánchez-Díaz, X. Rodríguez-Martínez, L. Córcoles-Guija, G. Mora-Martín, M. Campoy-Quiles, *Adv. Electron. Mater.* **2018**, *4*, 1700477.
[38] N. G. An, J. Y. Kim, D. Vak, *Energy Environ. Sci.* **2021**, *14*, 3438.
[39] G. E. B. Archer, A. Saltelli, I. M. Sobol, *J. Stat. Comput. Simul.* **1997**, *58*, 99–120.
[40] C. M. Stafford, K. E. Roskov, T. H. Epps, M. J. Fasolka, *Rev. Sci. Instrum.* **2006**, *77*, 023908.
[41] X. Rodríguez-Martínez, E. Pascual-San-José, Z. Fei, M. Heeney, R. Guimerà, M. Campoy-Quiles, *Energy Environ. Sci.* **2021**, *14*, 986.
[42] K. Watanabe, N. Yamagiwa, Y. Torisawa, *Org. Process Res. Dev.* **2007**, *11*, 251–258.
[43] Z. Li, L. Ying, P. Zhu, W. Zhong, N. Li, F. Liu, F. Huang, Y. Cao, *Energy Environ. Sci.* **2019**, *12*, 157–163.
[44] K. C. Choi, E. J. Lee, Y. K. Baek, M. J. Kim, Y. Do Kim, P. W. Shin, Y. K. Kim, *RSC Adv.* **2014**, *4*, 7160–7166.
[45] F. Deledalle, T. Kirchartz, M. S. Vezie, M. Campoy-Quiles, P. S. Tuladhar, J. Nelson, J. R. Durrant, *Phys. Rev. X* **2015**, *5*, 011032.
[46] L. Wengeler, M. Schmitt, K. Peters, P. Scharfer, W. Schabel, *Chem. Eng. Process. Process Intensif.* **2013**, *68*, 7.
[47] N. S. Güldal, M. Berlinghof, T. Kassar, X. Du, X. Jiao, M. Meyer, T. Ameri, A. Osvet, N. Li, G. L. Destri, R. H. Fink, H. Ade, T. Unruh, C. J. Brabec, *J. Mater. Chem. A* **2016**, *4*, 16136–16147.
[48] L. Zhang, Z. Ding, R. Zhao, F. Jirui, W. Ma, J. Liu, L. Wang, *J. Mater. Chem. C* **2020**, *8*, 5613–5619.
[49] C. Acton, R. Miller, J. Maltby, D. Fullerton, C. Acton, R. Miller, J. Maltby, D. Fullerton, *SPSS Soc. Sci.* **2009**, *6*, 183–198.
[50] E. Ostertagová, O. Ostertag, *Am. J. Mech. Eng.* **2013**, *1*, 256–261.
[51] C. Müller, L. M. Andersson, O. Peña-Rodríguez, M. Garriga, O. Inganäs, M. Campoy-Quiles, *Macromolecules* **2013**, *46*, 7325–7331.
[52] X. Rodríguez-Martínez, M. S. Vezie, X. Shi, I. McCulloch, J. Nelson, A. R. Goñi, M. Campoy-Quiles, *J. Mater. Chem. C* **2017**, *5*, 7270–7282.

Manuscript received: September 2, 2021
Revised manuscript received: December 17, 2021
Accepted manuscript online: December 20, 2021
Version of record online: [redacted], [redacted]


© 2021 The Authors. ChemSusChem published by Wiley-VCH GmbH

# FULL PAPERS

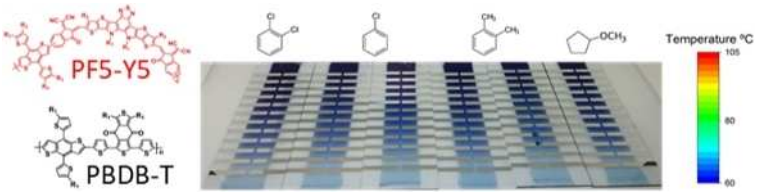


**High-throughput screening**: Less than 25 mg of the donor and acceptor materials are used to make over 648 devices in a combinatorial screening method that investigates processing parameters for blade-coated polymer: polymer photovoltaics. Representing power conversion efficiency in the Hansen solubility space may be the key for easily selecting solvent systems that optimize performance.

*A. Harillo-Baños, Dr. Q. Fan, Dr. S. Riera-Galindo, Prof. E. Wang, Prof. O. Inganäs*, Dr. M. Campoy-Quiles**

1 – 11

**High-Throughput Screening of Blade-Coated Polymer:Polymer Solar Cells: Solvent Determines Achievable Performance**

ChemSusChem

Supporting Information

# High-Throughput Screening of Blade-Coated Polymer: Polymer Solar Cells: Solvent Determines Achievable Performance

Albert Harillo-Baños, Qunping Fan, Sergi Riera-Galindo, Ergang Wang, Olle Inganäs,* and Mariano Campoy-Quiles*This publication is part of a collection of invited contributions focusing on “Advanced Organic Solar Cells”. Please visit  to view all contributions.© 2021 The Authors. ChemSusChem published by Wiley-VCH GmbH. This is an open access article under the terms of the Creative Commons Attribution License, which permits use, distribution and reproduction in any medium, provided the original work is properly cited.

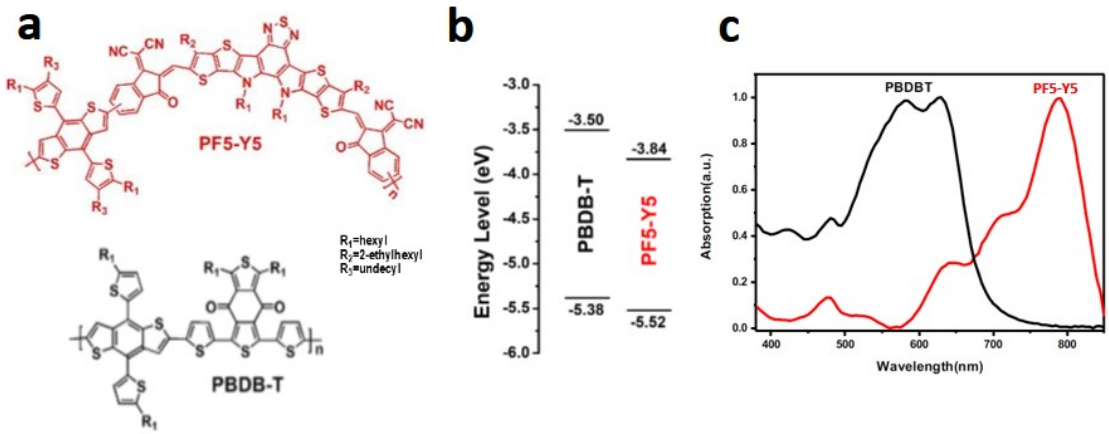


**Figure S1.** a) Chemical structures; b) Energy levels; and c) Normalized absorption of the two polymers [1]

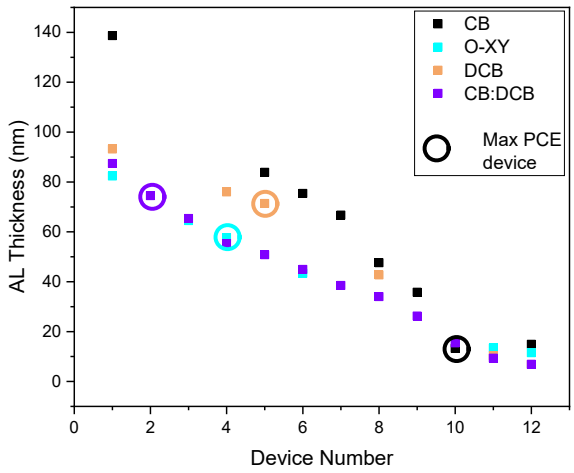


**Figure S2:** Thickness Gradient for each sample

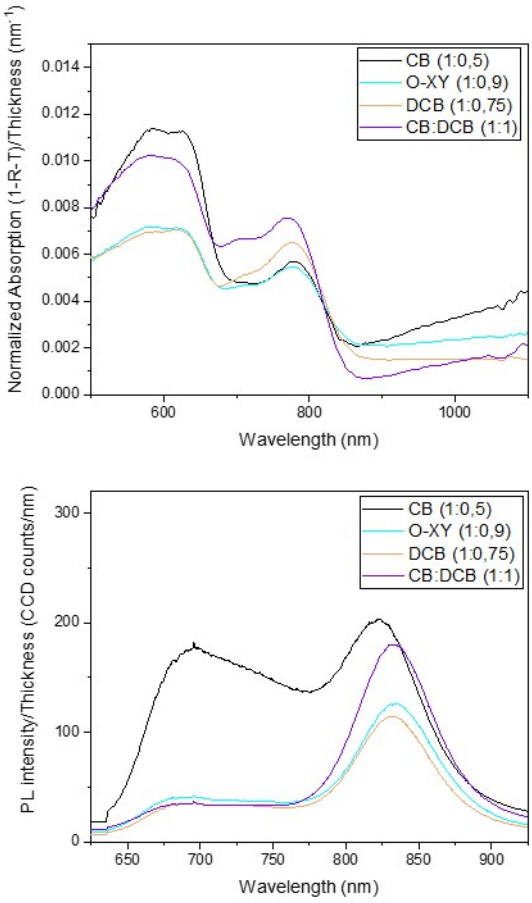


**Figure S3**: a) UV-Vis and b) PL measurements of the best device for each solvent. Between parenthesis is the D:A ratio of each device. In both cases, divided by the thickness of the Active Layer.

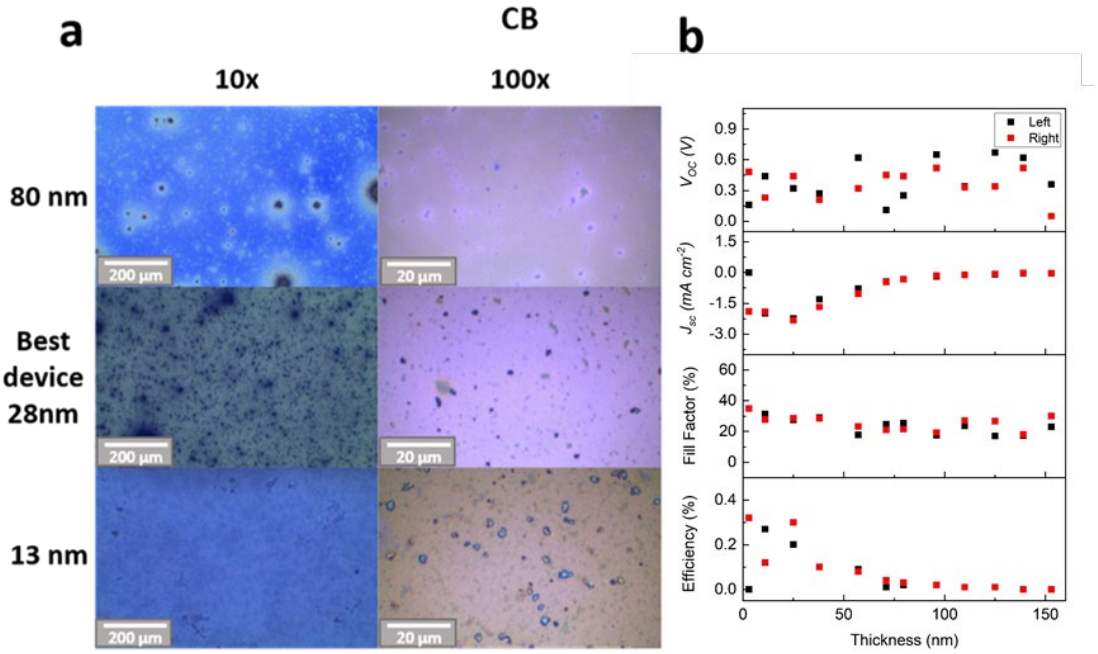


**Figure S4:** Optical microscopy images (10x and 100x) of the CB based sample

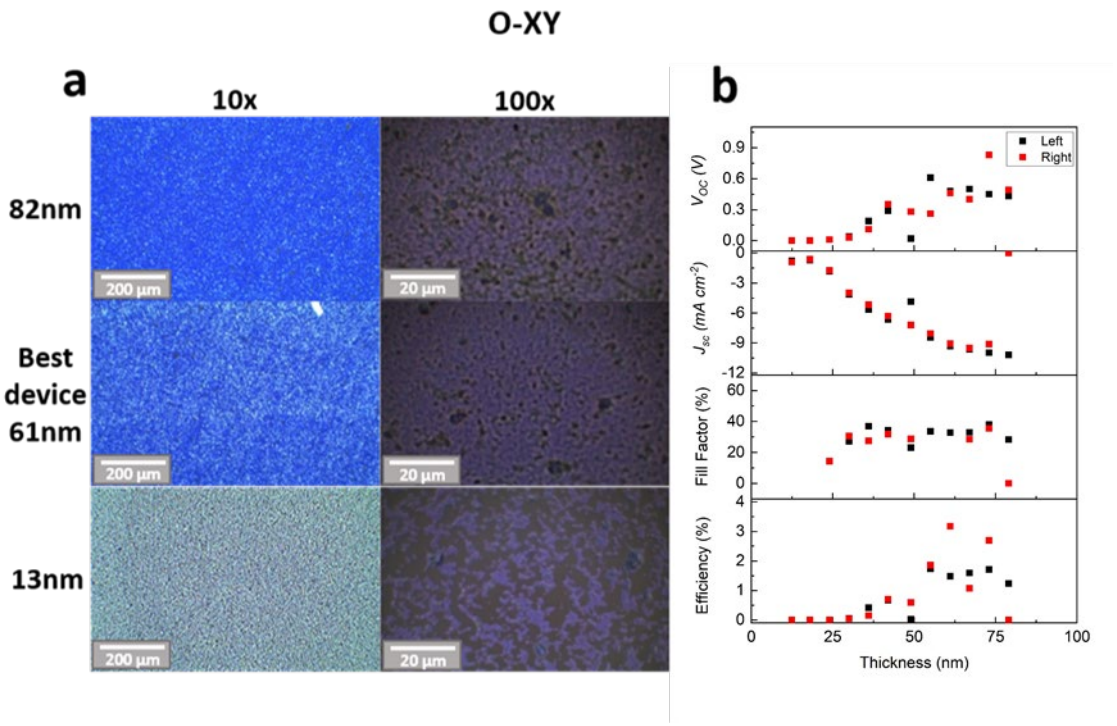


**Figure S5:** Optical microscopy images (10x and 100x) of the O-XY based sample

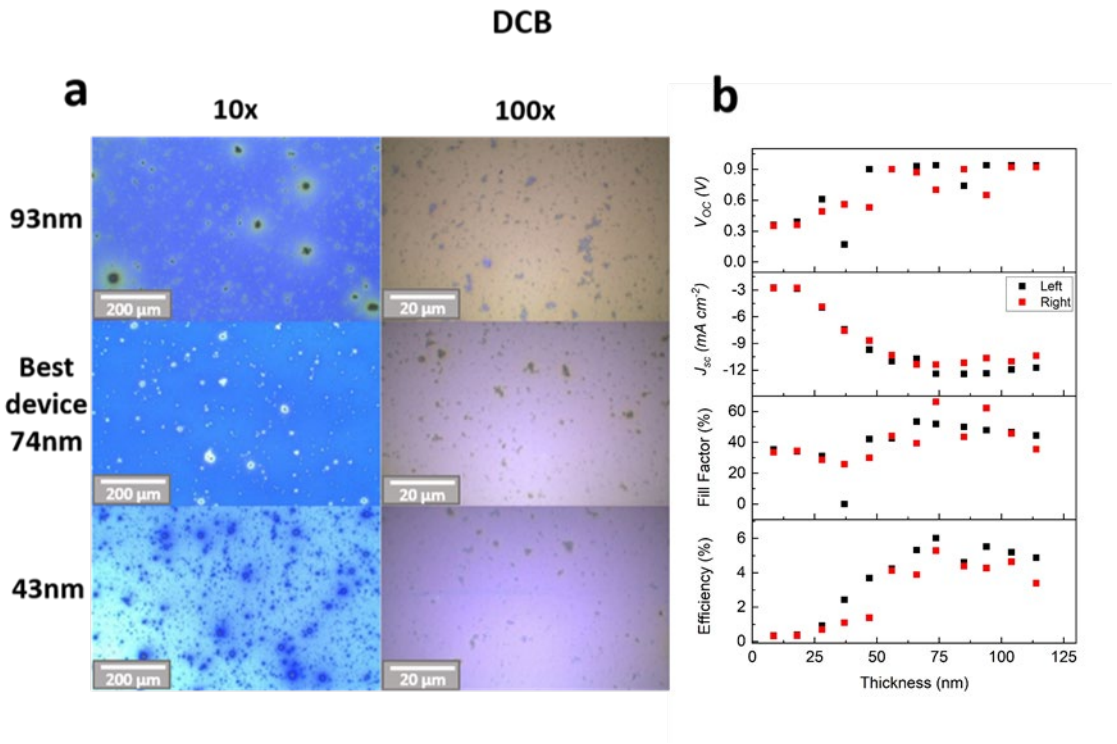


**Figure S6:** Optical microscopy images (10x and 100x) of the DCB based sample

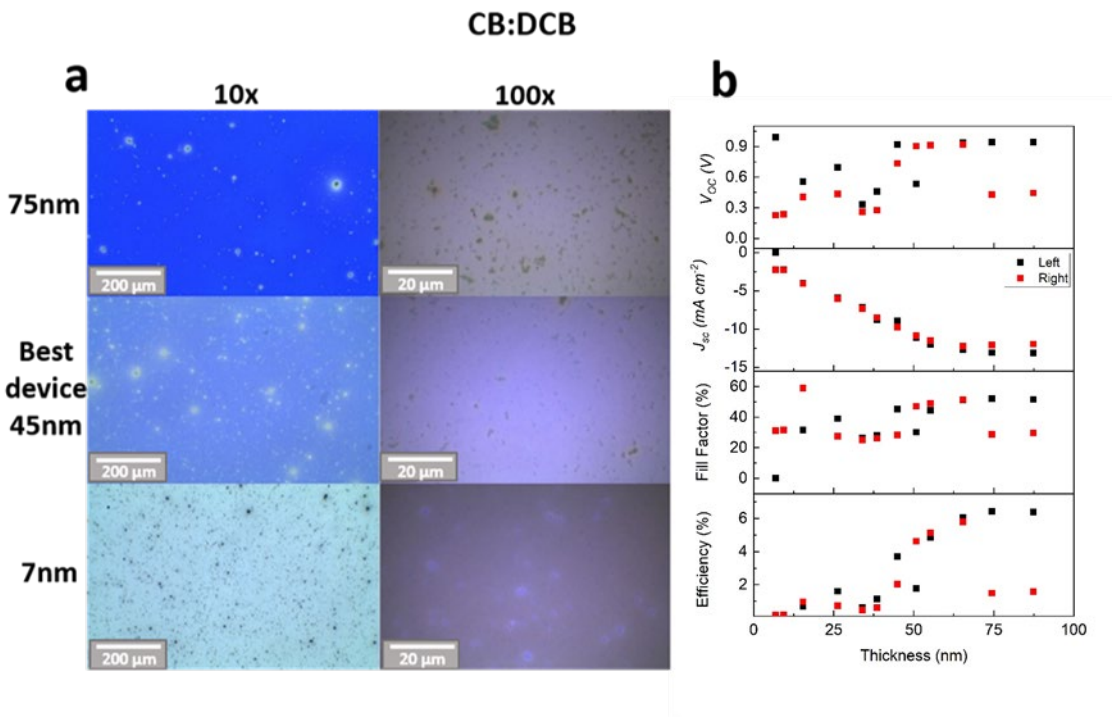


**Figure S7:** Optical microscopy images (10x and 100x) of the CB:DCB based sample

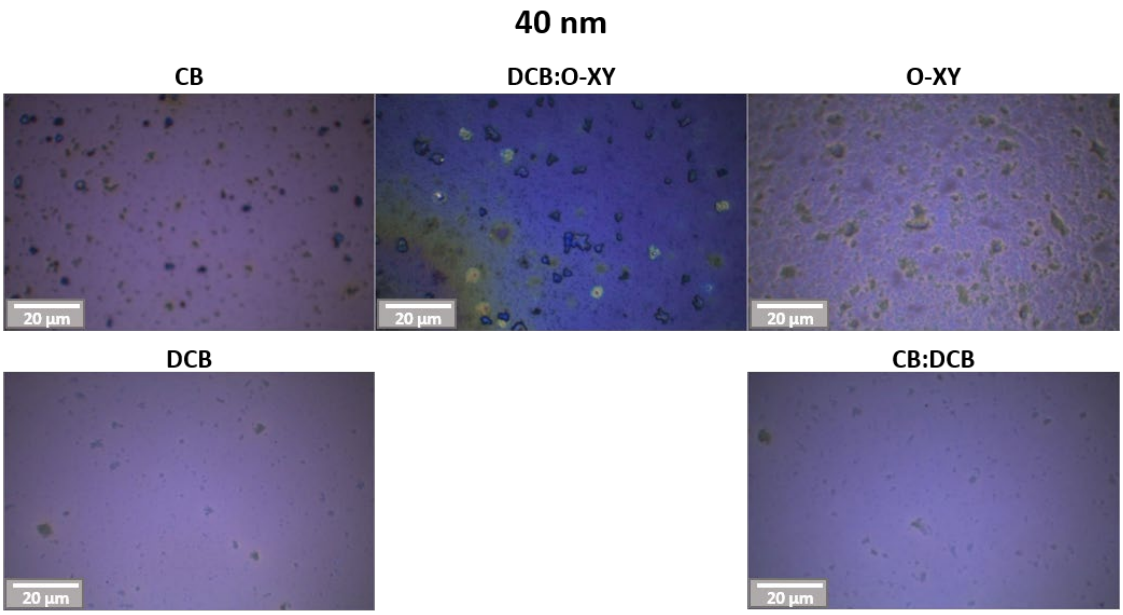


**Figure S8:** Optical microscopy images (100x) of different devices, with the same Active layer thickness (40nm).

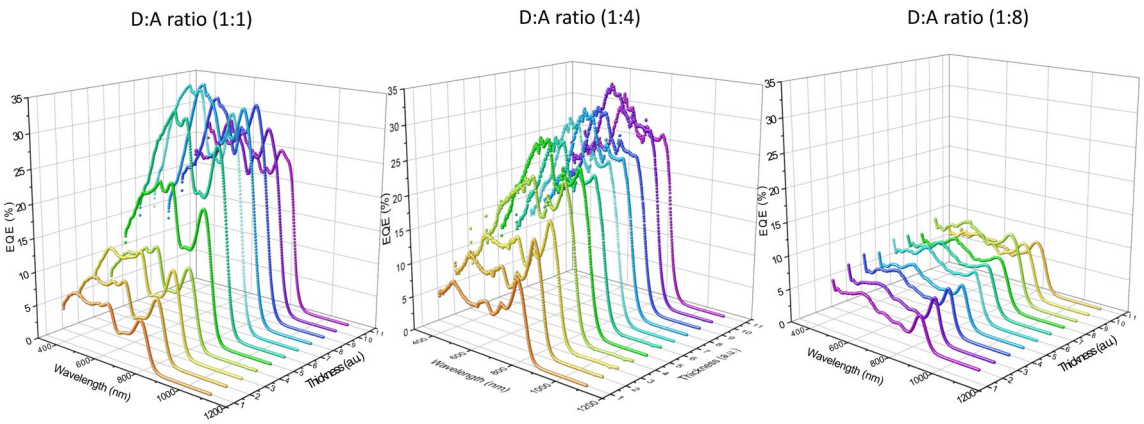


**Figure S9:** External Quantum Efficiency of PBDB-T:PF5-Y5 solar cells using DCB as a solvent at D:A ratio 1:1, 1:4 and 1:8 from left to right.

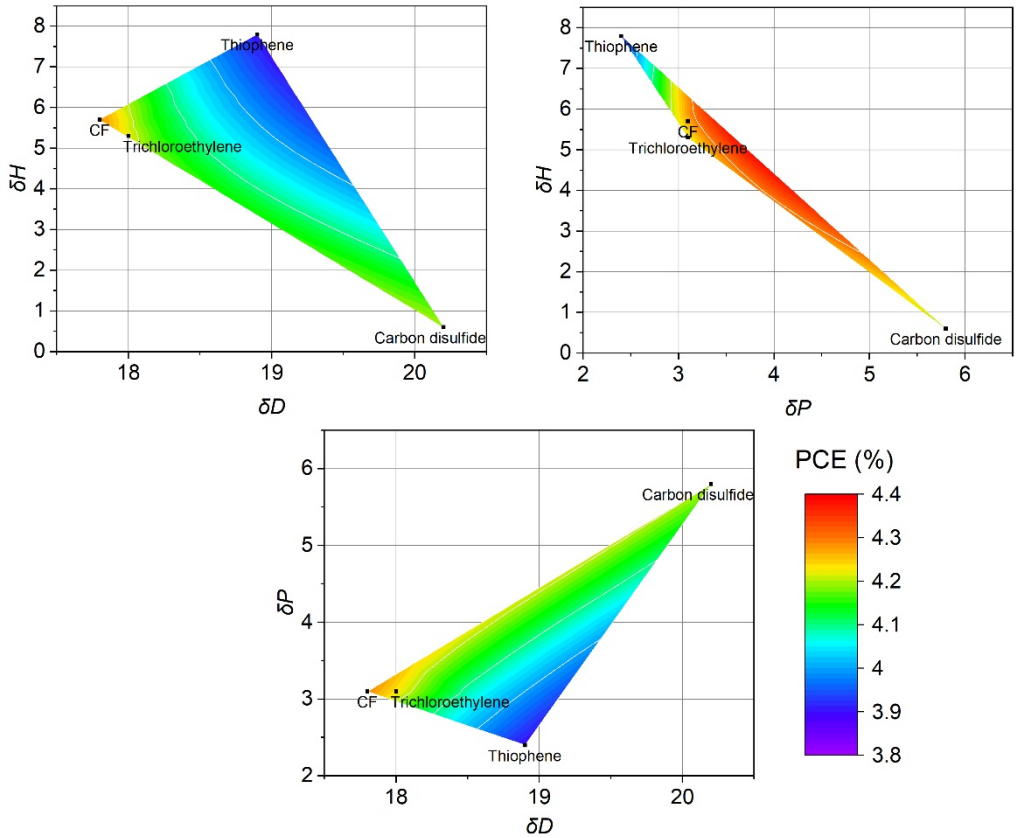


**Figure S10**. Performance landscape of DDP(TBFu)2:PC71BM solar cells represented on the Hansen solubility space, from bibliography [2]

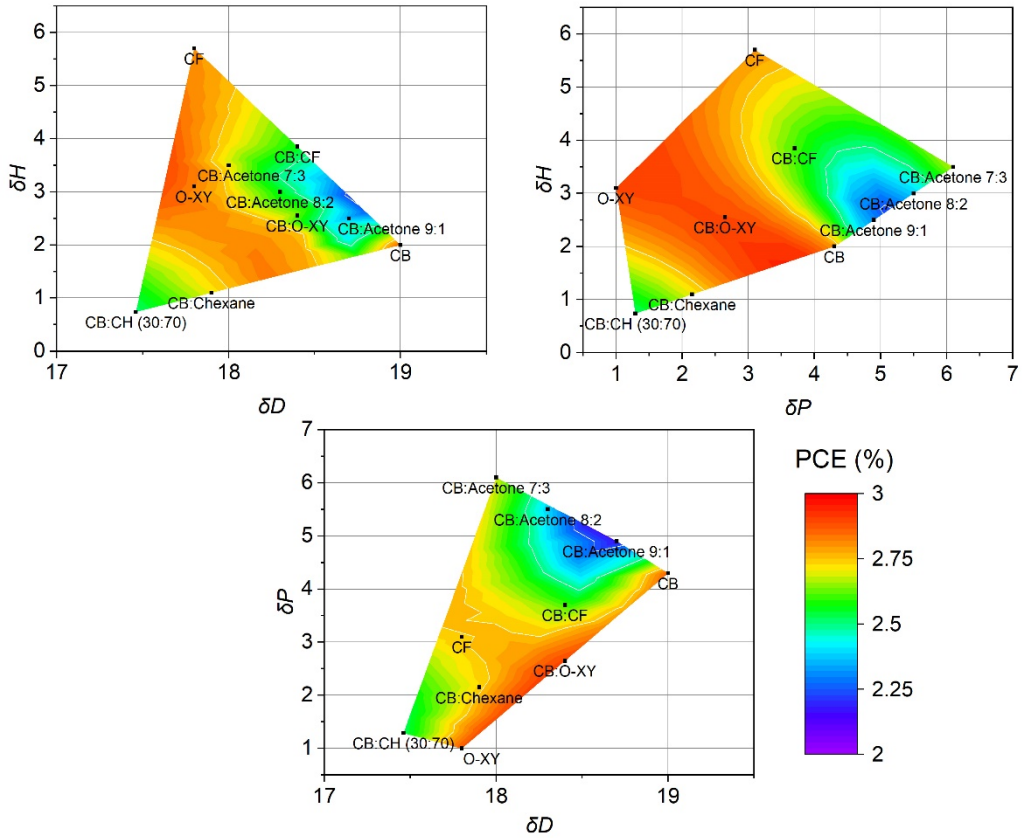


**Figure S11**. Performance landscape of P3HT:PC60BM solar cells represented on the Hansen solubility space, from bibliography [3]


[1] Q. Fan *et al.*, "Over 14% efficiency all-polymer solar cells enabled by a low bandgap polymer acceptor with low energy loss and efficient charge separation," *Energy Environ. Sci.*, vol. 13, no. 12, pp. 5017–5027, 2020.

[2] B. Walker *et al.*, "A systematic approach to solvent selection based on cohesive energy densities in a molecular bulk heterojunction system," *Adv. Energy Mater.*, vol. 1, no. 2, pp. 221–229, 2011.

[3] F. Machui, S. Abbott, D. Waller, M. Koppe, and C. J. Brabec, "Determination of solubility parameters for organic semiconductor formulations," *Macromol. Chem. Phys.*, vol. 212, no. 19, pp. 2159–2165, 2011.

# PAPER II

## Effective interplay of donor and acceptor groups for tuning optoelectronic properties in oligothiophene-naphthalimide assemblies.

Matías J. Alonso-Navarroa, Alexandra Harbuzaru, Paula de Echegaraya, Iratxe Arrechea-Marcos, Albert-Harillo-Baños, Alejandro de la Peña, M. Mar Ramos, J. Teodomiro López Navarrete, Mariano Campoy-Quiles, Rocío Ponce Ortiz, José L. Segura. Journal of Material Chemistry C 8, 15277–15289 (2020).

Journal of Materials Chemistry C

ROYAL SOCIETY OF CHEMISTRY

PAPER

View Article Online
View Journal | View Issue

Published on 06 August 2020. Downloaded by Instituto de Ciencia de Materiales de Barcelona (ICMAB) on 9/16/2023 2:19:05 PM.

Check for updates

Cite this: J. Mater. Chem. C, 2020, 8, 15277

# Effective interplay of donor and acceptor groups for tuning optoelectronic properties in oligothiophene–naphthalimide assemblies†

Matías J. Alonso-Navarro, ‡[ab] Alexandra Harbuzaru, ‡[c] Paula de Echegaray,§[ab] Iratxe Arrechea-Marcos,§[c] Albert Harillo-Baños,[d] Alejandro de la Peña,[ab] M. Mar Ramos,[b] J. Teodomiro López Navarrete,[c] Mariano Campoy-Quiles,[d] Rocío Ponce Ortiz *[c] and José L. Segura *[a]

Received 26th June 2020,
Accepted 6th August 2020

DOI: 10.1039/d0tc03026k

rsc.li/materials-c

In this work, a series of naphthalimide fused thienopyrazine derivatives was designed, and their synthesis and characterization are reported herein. The interaction of this building block with a donor terthiophene fragment laterally substituted by a series of donor and acceptor constituents was analyzed in depth. This strategy was proven to efficiently modulate both the energy and topology of the frontier molecular orbitals involved in the charge transport mechanism. The interplay between the donor and acceptor strengths of the different units composing the material structure is thus essential to efficiently modulate charge carriers and transport properties and to finely tune the optical and electronic structures of the presented organic semiconductors.

## 1. Introduction

Conjugated organic molecules are ideal semiconductors for the generation of low-cost electronics[1–4] due to the combination of their tunable optical and electronic properties and their excellent mechanical flexibility and processing. Thus, they provide a good platform for a wide variety of applications such as organic field effect transistors (OFETs),[5–7] organic thin-film transistors (OTFTs),[8] organic light emitting diodes (OLEDs)[9,10] and organic solar cells (OSCs).[11]

Concerning OFETs, charge carrier mobility is one of the most important device parameters for many of the targeted applications. In this respect, OFET mobilities exceeding 10 $cm^2 V^{-1} s^{-1}$ have already been reported for several organic semiconductors.[12–15] Nevertheless, these high mobility values have been mainly achieved by p-type organic semiconductors, in which holes are the charge carriers in the OFET channel. However, it is worth pointing out that n-channel OFETs, using n-type organic semiconductors that conduct electrons, are required for many electronic applications in order to make complementary metal oxide (CMOS)-like logic circuits in combination with the p-channel OFETs.[16,17] In order to obtain n-type organic semiconductors, it is necessary to synthesize π-conjugated electron deficient systems that allow electron hopping in films providing semiconducting properties to the material.[18] Among them, rylene imide derivatives have proven to be among the most efficient n-type organic semiconductors for application in OFETs due to their great optical and electrochemical properties, which can be tuned by chemical modifications.[19–27]

In this context, naphthalene-based imides have been extensively used within organic electronics due to their easy functionalization, tunable absorption spectrum, electron deficient core and low lying LUMO, stable radical anion and self-organization properties.[24,28–30] Especially noteworthy is that n-type mobilities above 8 $cm^2 V^{-1} s^{-1}$ have been reported for single-crystal field-effect transistors based on naphthalene diimide derivatives.[31]

In recent years, our groups have been developing a new series of oligothiophene–naphthalimide semiconductors that combine donor and acceptor units in order to create ambipolar or n-type materials by tuning efficiently their frontier orbital levels and modifying their optical, electrochemical and electronic properties (Fig. 1a).[32–36] Within the framework of this ongoing research, we report herein the synthesis of a family of terthiophene–naphthalimide assemblies (Fig. 1b) in which the electronic energy levels, emission and absorption spectra,

[a] Department of Organic Chemistry, Complutense University of Madrid, Faculty of Chemistry, Madrid 28040, Spain. E-mail: segura@ucm.es
[b] Chemical and Environmental Technology Department, Univ. Rey Juan Carlos, Móstoles, 28933, Spain
[c] Department of Physical Chemistry, University of Málaga, Málaga, 29071, Spain
[d] Institut de Ciencia de Materials de Barcelona (ICMAB-CSIC), 08193 Bellaterra, Spain

† Electronic supplementary information (ESI) available. See DOI: 10.1039/d0tc03026k

‡ These authors contributed equally to this work.

§ These authors contributed equally to this work.

Published on 06 August 2020. Downloaded by Instituto de Ciencia de Materiales de Barcelona (ICMAB) on 9/16/2023 2:19:05 PM.

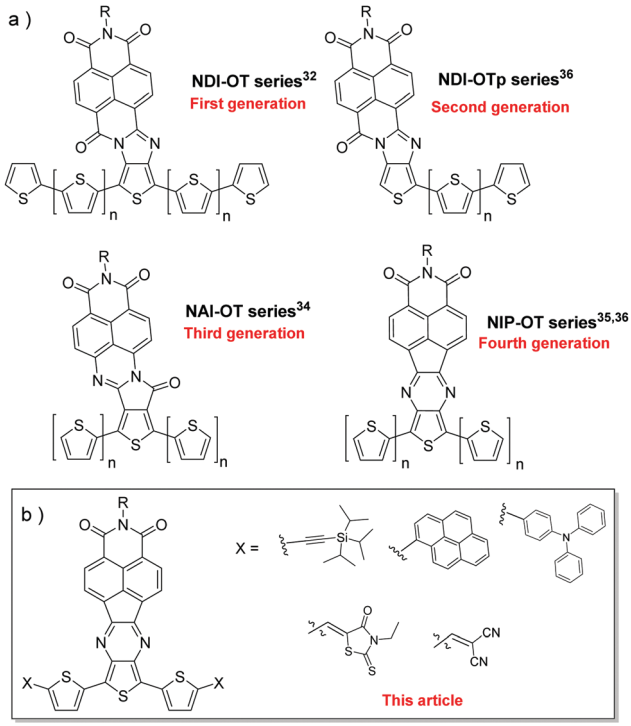


Fig. 1 (a) Molecular structure of oligothiophene–naphthalimide assemblies synthesized in our groups with good performances in OFETs and (b) new oligothiophene–naphthalimide assemblies investigated in this article.

and intermolecular stacking have been tuned effectively through chemical modification of the end groups located at terminal thiophene moieties in the oligothiophene–naphthalimide assemblies. The functionalities incorporated in the terthiophene–naphthalimide assemblies range from non-planar strong donor substituents, such as triphenylamine,[37–39] to planar π-conjugated donor substituents, such as pyrene moieties,[40–42] rigid linear and bulky substituents, such as triisopropylsilyl (TIPS) groups,[43–45] and strong electron accepting functions such as rhodanine[46–48] and dicyanovinylene[49–51] that promote planarity and extended conjugation. All these substituents have been selected because of their different electronic and structural characteristics and because they have been previously used successfully in the functionalization of π-conjugated molecular organic materials with good charge transport properties.

## 2. Results and discussion

The development of donor (D)–acceptor (A) assemblies based on oligothiophene derivatives has received a great deal of attention due to the tunability of their electrochemical and photophysical properties, which has allowed their incorporation in OFETs showing ambipolar field-charge transport.[52–58] Among them, oligothiophene–naphthalimide assemblies[59] are particularly appealing because of the significance of naphthalimide in supramolecular chemistry and as an air-stable n-type semiconductor.[29,54,60] Thus, we have synthesized different series of oligothiophene–naphthalimide assemblies (Fig. 1a) with good performances in OFETs in which both the acceptor and donor moieties are directly conjugated through rigid heterocyclic linkers.[33–36,61] It has been observed that the use of planar pyrazine moieties as heterocyclic conjugated linkers in oligothiophene–naphthalimide assemblies avoids skeletal distortions thus allowing extended intramolecular π-conjugation and permitting close intermolecular π–π stacking, which promote good film crystallinity.

In this article, we have carried out the chemical modification of the base skeleton of these oligothiophene–naphthalimide assemblies connected by pyrazine linkers in order to further functionalize them with different moieties at terminal thiophene positions with the aim to tune the electronic energy levels, emission and absorption spectra, and the intermolecular stacking of the assemblies. The donor–acceptor systems can be classified into two well-defined groups. First, donor–acceptor–donor (D–A1–D) systems, in which there are electron donor systems on each side of the acceptor thienopyrazine moiety, and, on the other hand, A2–D–A1–D–A2 systems, where the terminal positions of oligothiophene have been functionalized with strong electron acceptors. The synthetic route toward all the naphthalimide-fused thienopyrazine end-capped molecules reported in this work starts with 1,8-naphthalimide derivatives endowed with 1,2-diketone functionalities (**NIDa and NIDb**) previously described by our group.[35,36,62]

Suitably functionalized terthiophene–naphthalimide assemblies connected through pyrazine linkers have been obtained by condensing **NIDa** and/or **NIDb** with the corresponding diamines **1** or **5** (Schemes 1 and 2). Thus, the reaction between **NIDa** and 5″-dibromo-[2,2′:5′,2″-terthiophene]-3′,4′-diamine (**1**) allows obtaining an oligothiophene–naphthalimide assembly (**NIPa3T-Br**) functionalized with bromine groups at the terminal thiophene moieties in a good yield (Scheme 1). The synthesis of this derivative paves the way for the further functionalization of this D–A assembly through different C–C coupling reactions including Stille or Sonogashira reactions. Thus, Stille cross-coupling reaction between **NIPa3T-Br** and trimethyl[2-[tris(1-methylethyl)silyl]ethynyl]stannane (**2**) afforded an assembly functionalized with rigid and bulky triisopropylsilyl (TIPS) moieties (**NIPa3T-TIPS**) (Scheme 1). Alternatively, Suzuki cross-coupling reactions between **NIPa3T-Br** and boronic acid **3** or boronate ester **4** were used to functionalize the oligothiophene–naphthalimide assemblies, respectively, with non-planar strong donor triarylamine moieties (**NIPa3T-TA**) and electron-rich and planar pyrene units (**NIPa3T-Py**, Scheme 1).

In order to obtain the A2–D–A1–D–A2 systems, **NIPa3T** or **NIPb3T** moieties were formylated upon treatment with phosphorus oxychloride and *N*,*N*-dimethylformamide to afford **NIPa3T-CHO** and **NIPb3T-CHO**, respectively, with yields higher than 85% (Scheme 2). Knoevenagel-like reactions[63] involving the formylated derivatives were carried out in order to obtain the target molecules. Thus, reaction with 3-ethyl-2-thioxo-4-thiazolidinone (**6**) yielded oligothiophene–naphthalimide assemblies endowed with rhodanine moieties (**NIPa3T-Rd and NIPb3T-Rd**) while treatment with malononitrile (**7**) afforded parent systems **NIPa3T-DCV** and **NIPb3T-DCV** functionalized with dicyanovinylene groups (Scheme 2).

 This journal is © The Royal Society of Chemistry 2020

Published on 06 August 2020. Downloaded by Instituto de Ciencia de Materiales de Barcelona (ICMAB) on 9/16/2023 2:19:05 PM.

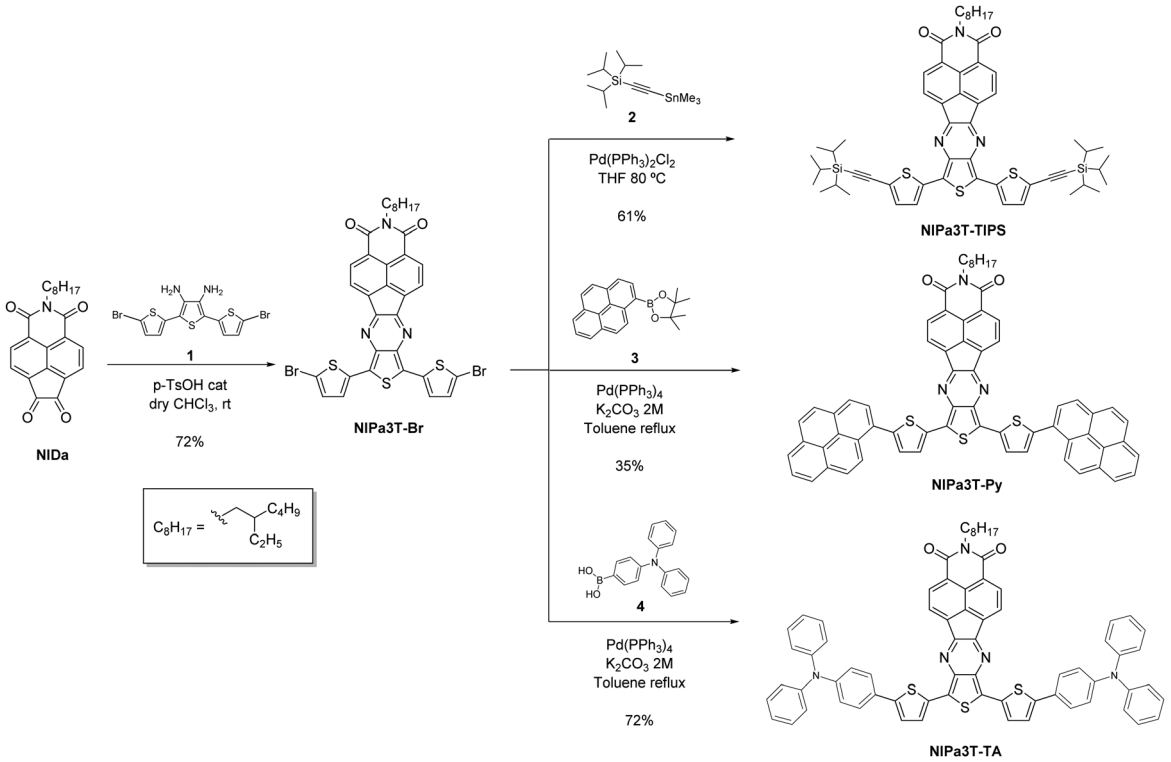


Scheme 1 Syntheses of the oligothiophene–naphthalimide assemblies functionalized with triisopropylsilyl (TIPS) moieties (**NIPa3T-TIPS**) and electron donor pyrene (**NIPa3T-Py**) and triphenylamine (**NIPa3T-TA**) groups.

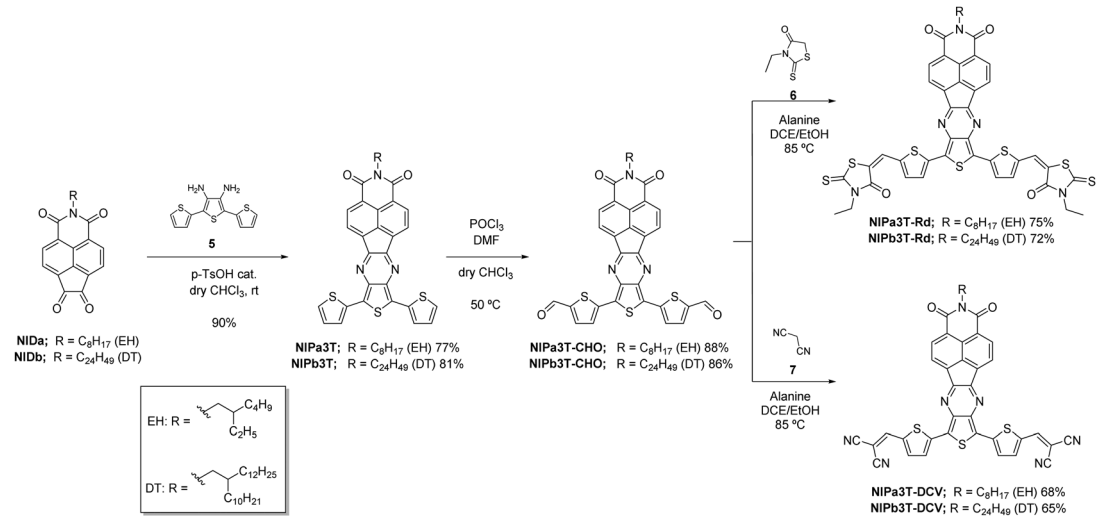


Scheme 2 Syntheses of the oligothiophene–naphthalimide assemblies functionalized with the electron acceptors rhodanine (**NIPa3T-Rd and NIPb3T-Rd**) and dicyanovinylene (**NIPa3T-DCV and NIPb3T-DCV**).

The presence of solubilizing alkyl chains at the imide nitrogen of the naphthalimide system allowed not only solid-state characterization methods but also $^{1}$H-NMR characterization in solution due to the acceptable solubility of all the intermediates and target compounds in deuterated solvents. In addition, $^{13}$C-NMR characterization of all the intermediates and most of the target compounds could be carried out except for those functionalized with dicyanovinylene or pyrene moieties, which could not be clearly resolved due to their extended planar systems with limited solubility because of their tendency towards aggregation.

The analysis of the $^{1}$H-RMN spectra (Fig. S1–S4, ESI†) revealed well-resolved patterns for all the novel assemblies. In comparison with the dibrominated assembly (**NIPa3T-Br**, Scheme 1), the D–A1–D systems (**NIPa3T-TIPS**, **NIPa3T-Py**, and **NIPa3T-TA**) do not show significant differences in the signals

Published on 06 August 2020. Downloaded by Instituto de Ciencia de Materiales de Barcelona (ICMAB) on 9/16/2023 2:19:05 PM.

corresponding to the naphthalimide moieties in the region between 8.60 and 7.50 ppm while those corresponding to the oligothiophene systems (7.80–6.50 ppm) are only slightly shifted after substitution. Thus, for **NIPa3T-TA**, the signals corresponding to the oligothiophene moiety are shielded in comparison to that of **NIPa3T-Br** due to the strong electron donor behavior of triarylamine. In the cases of **NIPa3T-TIPS** and **NIPa3T-Py**, the oligothiophene protons are quite deshielded compared with the starting material due to the extended conjugation provided by the TIPS or pyrene units.

In the case of the A2–D–A1–D–A2 systems, well-resolved patterns for all the novel assemblies (Fig. S5–S12, ESI†) were also observed. The characteristic signal of the hydrogen from the vinylene group appears at around 7.20 ppm for the rhodanine derivative and at around 7.05 ppm for the dicyanovinylene-substituted analogue as a singlet between the characteristic signals of the 1,8-naphthalimide (8.20–7.30 ppm) and thiophene protons (7.00–6.50 ppm). For these systems, there is a shielding effect in the signals corresponding to both 1,8-naphthalimide and oligothiophene. For the derivatives endowed with shorter 2-ethylhexyl chains at the imide nitrogens, the target molecules had to be characterized in deuterated tetrachloroethane or dimethyl sulfoxide, due to their lower solubility in deuterated chloroform. As depicted in the ESI† (Fig. S13 and S14), the temperature dependent NMR experiments performed for **NIPa3T-Rd** and **NIPa3T-DCV** show significant aggregation-induced shifts in the $^{1}$H-NMR signals.

The $^{13}$C-NMR spectra for the D–A1–D systems are quite similar for all of them; the signals in the down-field zone up to 160 ppm correspond to the imide carbons while those between 155 and 120 ppm are all sp$^2$ carbon signals, including those corresponding to the triarylamine substituents. On the other hand, the signals in the high-field zone correspond to the alkyl chains and the ethynyltriisopropyl carbons. In addition, for the assembly endowed with rhodanine moieties, the characteristic signal of the C═S group can be identified at 190 ppm.

In the IR spectra of all the novel assemblies, the diagnostic stretching bands corresponding to the imide group centered around 1700 cm$^{-1}$ and the characteristic ring stretch of the pyrazine moiety centered around 1600 cm$^{-1}$ can be observed. A clear band at 2220 cm$^{-1}$ corresponding to the characteristic C≡N tension is observed for the dicyanomethylene derivatives, while for the rhodanine moieties, a C═S tension around 1250 cm$^{-1}$ can be clearly identified. Finally, further evidence concerning the structure proposed for the novel assemblies was obtained by the analysis of the exact mass obtained *via* mass spectrometry, which provided mass values in accordance with the expected ones (Fig. S36–S47, ESI†).

### Molecular structures and packing

The optimization of the lowest energy molecular structures of the studied semiconductors shows, as indicated in Fig. 2 and Fig. S48 (ESI†), a completely planar skeleton for **NIP3T**. This unit and the complete conjugated skeleton remain planar upon the introduction of the non-bulky electron withdrawing substituents, both rhodanine and dicyanovinylene groups. In contrast, when bulkier pyrene and triphenylamine groups are used

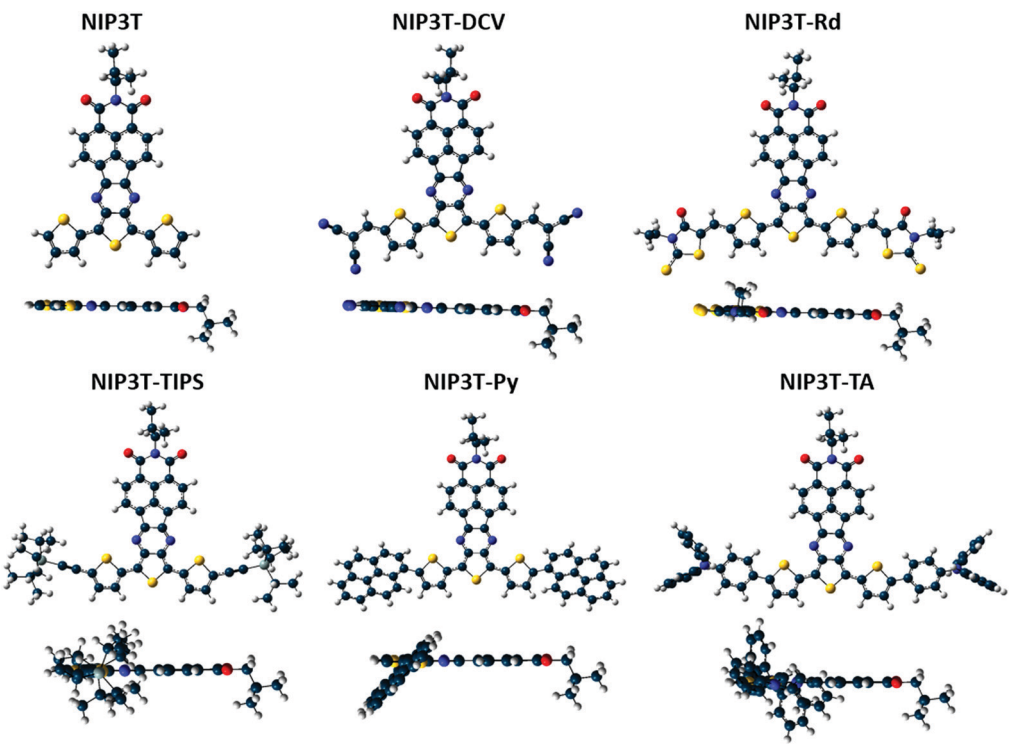


Fig. 2 DFT/B3LYP/6-31G** optimized molecular structures for the semiconductors under study.

 This journal is © The Royal Society of Chemistry 2020

Published on 06 August 2020. Downloaded by Instituto de Ciencia de Materiales de Barcelona (ICMAB) on 9/16/2023 2:19:05 PM.

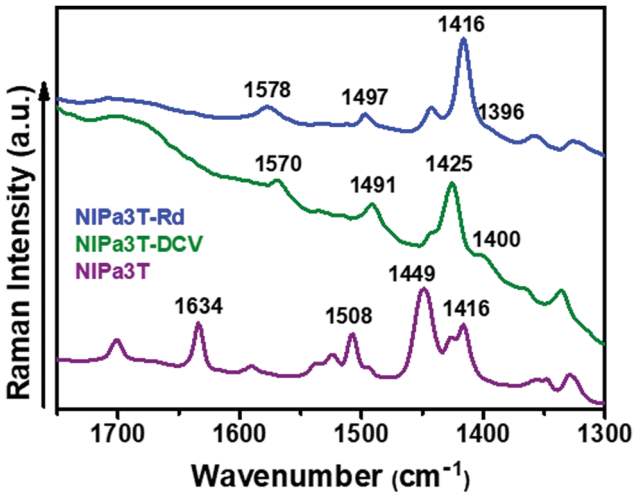


Fig. 3 FT-Raman spectra ($\lambda$ = 1064 nm) of **NIPa3T**, **NIPa3T-Rd** and **NIPa3T-DCV** derivatives as bulk materials.

as substituents in the **NIP3T** core, these units adopt a configuration that is not coplanar with the naphthalimide central unit.

FT-Raman spectra were thus recorded to analyze the effect of the lateral substituents on π-conjugation and molecular properties, and the data are shown in Fig. 3 and Fig. S57 (ESI†). To this end, we make use of ECC theory,[64,65] which has been widely probed to efficiently account for the degree of conjugation of molecular materials in a qualitative way,[66] and has been previously applied to naphthalene-modified oligothiophenes.[67]

Considering the Raman spectra shown in Fig. 3 and the selected eigenvectors shown in Fig. S58 (ESI†), the most intense Raman vibrations of **NIPa3T**, **NIPa3T-DCV** and **NIPa3T-Rd** are ascribed to the collective totally-symmetric $\nu$(C=C) vibration mode of the oligothiophene fragment, whose position can account for the molecular π-conjugation extent. This Raman vibration appears at 1449 $cm^{-1}$ in **NIPa3T** and greatly downshifts upon inclusion of electron withdrawing groups, being recorded at 1425 $cm^{-1}$ in **NIPa3T-DCV** and 1416 $cm^{-1}$ in **NIPa3T-Rd**. This remarkable downshift, up to 33 $cm^{-1}$ in **NIPa3T-Rd**, indicates an effective conjugation extension by the insertion of electron-withdrawing groups.

In contrast, the position of the terthiophene $\nu$(C=C) symmetric vibration undergoes less pronounced changes, up to 10 $cm^{-1}$ shifts, in **NIPa3T-TIPS**, **NIPa3T-Py** and **NIPa3T-TA** (Fig. S57, ESI†). This is probably due to the loss of planarity of the conjugated skeleton upon introduction of the lateral electron-donating groups, which interferes with the π-conjugation extension.

In addition, these different molecular geometries and combinations of donor and acceptor groups induce different molecular dipole moments and geometrical restrictions that also influence solid state packing.[32,34,61] Regarding the calculated molecular dipole moments, as shown in Table 1, they gradually decrease as the electron-rich character of the lateral substituents is enhanced. Thus, in **NIPa3T-DCV** and **NIPa3T-Rd**, the calculated dipole moments are 3.65 and 1.09 Debye, respectively, substantially lower than those of the rest of the studied compounds, which are around 4.5–4.7 Debye (Table 1).

Thus, we theoretically predicted, at the DFT/wB97XD/6-31G* level, the formation of dimeric structures for the different semiconducting systems (Fig. S55, ESI†). The wB97XD functional was used in this case instead of the B3LYP level, because it has an empirical dispersion correction term, proposed by Grimme, that can accurately predict π–π stacking interactions.[68] As shown in Table 1, while for **NIPa3T**, both the antiparallel and parallel configurations are quasi isoenergetic, the parallel configuration is predicted to be the most stable one for the laterally substituted derivatives.

In the case of **NIPa3T-DCV** and **NIPa3T-Rd**, the most stable parallel configuration with respect to **NIPa3T** (antiparallel, Fig. S55, ESI†) can be understood in terms of molecular dipole moments. The interplay between the electron withdrawing strengths of the electron-rich lateral groups and the NIP unit induces molecules with low dipole moments. In contrast, the parallel configuration of **NIPa3T-Py**, with a molecular dipole moment comparable to that of **NIPa3T**, is promoted by the formation of cooperative and close π–π interactions between the pyrene groups (Table 1).

### Optical and electrochemical properties

Fig. 4 and Fig. S59–S68 (ESI†) show the absorption spectra of the studied molecules and Table 2 and Table S1 (ESI†) summarize the experimental and theoretical TD-DFT predicted results, respectively.

**NIP3T** is considered in this study as the main building block, common to all the studied systems, and it presents a simple absorption spectral profile with two main bands, the lowest being the energy absorption band theoretically ascribed to the HOMO–LUMO transition. Thus, as indicated by the frontier molecular orbital topologies shown in Fig. 5, this electronic transition entails a clear intramolecular charge transfer character, from the more electron-rich part of the semiconductor, the terthiophene counterpart, to the more electron deficient unit, the naphthalimide group.

A similar scenario is found for the compounds **NIPa3T-TA**, **NIPa3T-TIPS** and **NIPa3T-Py**, where the lateral substitution of the terthiophene fragment with electron-rich groups redshifts and accentuates the charge transfer character of the lowest energy absorption. As can be seen experimentally with $\lambda_{abs}^{ons}$ and theoretically with $E_{H-L}$ shown in Table 2 and Table S1 (ESI†), respectively, the HOMO–LUMO energy gap gradually decreases as the electron-rich character of the lateral substituents is enhanced. Thus, the energy gap increases in the following direction: **NIPa3T-TA** (1.49 eV) < **NIPa3T-Py** (1.63 eV) < **NIPa3T** (1.77 eV) ≈ **NIPa3T-TIPS** (1.79 eV). This decrease in the HOMO–LUMO gap was also predicted theoretically, as shown in Fig. S50 (ESI†). Note that in these systems, the gap reduction is basically due to a destabilization of the HOMO orbital, without a noticeable variation in the LUMO energy level. This is due to the spatially separated frontier molecular orbitals (Fig. 5 and Fig. S49, ESI†), which permits selective fine tuning of either the HOMO or the LUMO energy levels.

In contrast, the absorption spectral profile of the semiconductors laterally substituted with electron deficient groups,

Published on 06 August 2020. Downloaded by Instituto de Ciencia de Materiales de Barcelona (ICMAB) on 9/16/2023 2:19:05 PM.

Table 1 DFT/wB97XD/6-31G* relative energy between parallel and antiparallel models of dimeric structures of the studied semiconductors. The less energetic configuration for each molecule is taken as a reference, and thus it has been assigned a zero value. Inset: DFT/wB97XD/6-31G* optimized geometry for the **NIPa3T-Py** dimeric model. The π–π interactions are shown in the table

| Molecules | Relative energy (kcal mol$^{-1}$) Parallel | Antiparallel | Conformers | Lower π–π distance (Å) | μ (Debye) |
|---|---|---|---|---|---|
| **NIPa3T** | 2, 3 | 0 | Antiparallel | 3.39 | 4.43 |
| **NIPa3T-Py** | 0 | 19, 67 | Parallel | 3.31 | 4.66 |
| **NIPa3T-DCV** | 0 | 7, 29 | Parallel | 3.36 | 3.65 |
| **NIPa3T-Rd** | 0 | 15, 45 | Parallel | 3.31 | 1.09 |

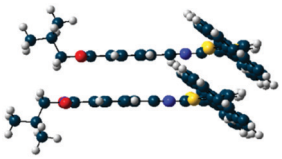

namely rhodanine and dicyanovinylene groups, is more complicated, with the presence of a vast number of electronic transitions (Fig. 4 and Fig. S65–S68, ESI†). The introduction of electron deficient groups at the terminal position of the thiophenes allows the formation of fully conjugated materials with absorption in the whole visible spectrum. In general, the lengthening of the branched alkyl chains has a small impact on the absorption spectra. However, although the two dicyanovinylene derivatives exhibit very similar UV-vis absorption profiles, the less soluble **NIPa3T-DCV** derivative shows an additional band at around 760 nm. This new band can be rationalized in terms of the formation of supramolecular aggregates. This particular behavior of the dicyanovinylene derivatives in the concentration range explored may be due to their lower solubility in comparison with the other **NIP-3T** derivatives. A dilution experiment has been carried out (Fig. S15, ESI†) in order to confirm this aggregation behavior of **NIPa3T-DCV**. Thus, this new band assigned to supramolecular aggregates disappears when the solution is diluted enough. TD-DFT calculations (Table S1, ESI†) predict the most intense electronic transition to be one electron excitation from the HOMO to the LUMO; however, in this case, the appearance of the vibronic structure indicates the absence of intramolecular charge transfer in this electronic transition (see calculated transition dipole moments in Fig. S56, ESI†). This is corroborated by the molecular orbital topologies, which indicate that both HOMOs and LUMOs are delocalized over the laterally substituted terthiophene unit (Fig. 5). The energy gaps, in this case, are calculated from the absorption onset as 1.60 and 1.38 eV for **NIP3T-Rd** and **NIP3T-DCV**, respectively. The decrease with respect to the parent compound **NIP3T** is related to a stabilization of both HOMO and LUMO energy levels, as shown in Fig. S51 (ESI†).

Cyclic voltammetry was carried out in an inert atmosphere using an electrochemical workstation at a scan rate of 200 mV s$^{-1}$ at 20 °C using tetrabutylammonium hexafluorophosphate (TBAHFP, 0.1 mol L$^{-1}$) as a supporting electrolyte in dichloromethane, and the data are compiled in Table 3.

Both reversible oxidation and reduction processes were recorded for all the semiconductors (Fig. S69–S77, ESI†). Due to the strong electron withdrawing effect of the dicyanovinylene groups, only one oxidation process is observed for both assemblies, **NIPa3T-DCV** and **NIPb3T-DCV**, and this process takes place very close to the solvent/electrolyte window (Fig. S76 and S77, ESI†). In contrast, **NIPa3T-Rd** is able to undergo multiple reversible oxidation and reduction processes, due to the largely extended conjugation as indicated *via* Raman spectroscopy (*vide supra*).

### Charged species study involving spectroelectrochemistry

In this section, we aim to analyze the structure and stability of the charge carriers present during the electron transport process. Considering the different LUMO topologies induced by the lateral substitution of the terthiophene fragment (Fig. 5), a different delocalization of the injected electrons over the π-conjugated structure must be expected during the charge transport process for the different analyzed molecules.

Fig. 6 and Fig. S78–S81 (ESI†) show the evolution of the UV/Vis/NIR spectra of the studied semiconductors obtained by progressive spectroelectrochemical reduction of low concentration solutions in the presence of a large excess of supporting electrolyte. Two different behaviors are found depending on the nature of the lateral substituents. Thus, when the oligothiophene fragment is either unsubstituted or connected to electron-rich units, a similar spectral profile evolution is recorded, the same applying when it is substituted with electron-deficient units.

Therefore, for **NIPa3T** and **NIPa3T-Py,** the UV-Vis absorption spectra of the neutral species (black curve) progressively evolve to a series of absorption bands recorded at 365, 517 and 600 nm (blue curve) in the case of **NIPa3T**, which are ascribed to the formation of radical anion species (see comparison with the theoretical results in Fig. S78, ESI†). Further electrochemical reduction provokes the vanishing of this spectral profile and the appearance of two new absorption peaks, one centered at *ca.* 372 and a redshifted band at 936 nm. A similar scenario has been previously observed upon the chemical reduction of naphthalenediimide derivatives,[69] therefore indicating that in **NIPa3T** and **NIPa3T-Py,** the injected negative charge is mainly stabilized over the naphthaleneimide fragment, as expected considering the LUMO topologies shown in Fig. 5. DFT calculations of **NIPa3T-Py** charged species indicate the stabilization of basically the totality of the injected charge on the naphthaleneimide subunit in the radical anion, while around 65% of the injected charge is stabilized by the NIP unit in the dianion species. Note that the pyrene lateral substituents, albeit considered an electron-rich group, help in the stabilization of the injected negative charge for the dianion, hosting around 30% of the charge (Fig. S52 and S53, ESI†).

 This journal is © The Royal Society of Chemistry 2020

Published on 06 August 2020. Downloaded by Instituto de Ciencia de Materiales de Barcelona (ICMAB) on 9/16/2023 2:19:05 PM.

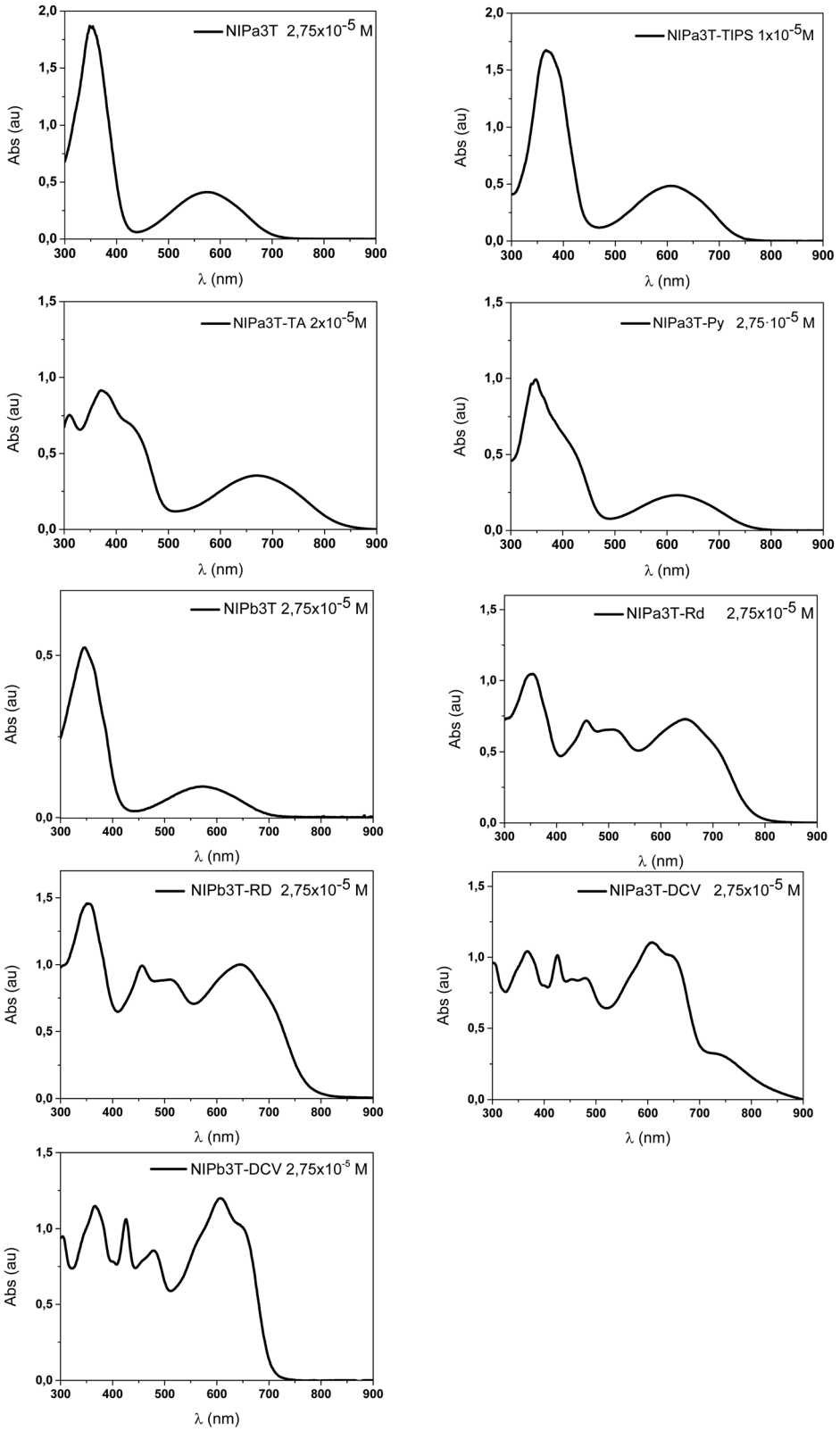


Fig. 4 UV-Vis absorption spectra of the **NIP3T** derivatives recorded in chloroform.

In marked contrast, **NIPa3T-DCV** and **NIPa3T-Rd**, where the terthiophene subunit is laterally substituted with electron-deficient groups, show an evolution of their UV/Vis/NIR spectra upon electron injection that resembles those of electron-deficient oligothiophene materials.[70] As an example, in the case of **NIPa3T-Rd**, two bands appear at 761 and 884 nm upon

Published on 06 August 2020. Downloaded by Instituto de Ciencia de Materiales de Barcelona (ICMAB) on 9/16/2023 2:19:05 PM.

Table 2 UV-vis absorption data

| | [C] (μM) | UV-vis[a] $\lambda_{max}$[b] (nm) | $\varepsilon_{\lambda_{max}}$[d] ($M^{-1}$ $cm^{-1}$) | $\lambda_{\varepsilon}$[c] (nm) | $\varepsilon_{\lambda\varepsilon}$[d] ($M^{-1}$ $cm^{-1}$) | $\lambda_{onset}$ (nm) | $E_g^{opt}$[e] (eV) |
|---|---|---|---|---|---|---|---|
| **NIPa3T-TIPS** | 0.100 | 349 | 167 000 | 576 | 48 000 | 689 | 1.79 |
| **NIPa3T-Py** | 0.275 | 348 | 36 000 | 620 | 8360 | 760 | 1.63 |
| **NIPa3T-TA** | 0.200 | 370 | 45 500 | 671 | 17 500 | 831 | 1.49 |
| **NIPa3T** | 0.275 | 348 | 68 000 | 574 | 14 910 | 698 | 1.77 |
| **NIPa3T-Rd** | 0.275 | 353 | 38 180 | 712 | 17 820 | 774 | 1.60 |
| **NIPa3T-DCV** | 0.275 | 609 | 40 360 | 735 | 11 640 | 899 | 1.38 |
| **NIPb3T** | 0.275 | 346 | 18 910 | 572 | 3636 | 694 | 1.79 |
| **NIPb3T-Rd** | 0.275 | 354 | 53 450 | 703 | 26 910 | 768 | 1.61 |
| **NIPb3T-DCV** | 0.275 | 607 | 43 270 | 650 | 36 730 | 704 | 1.76 |

[a] Absorption measurement in $CHCl_3$ solution. [b] Absorption maxima in solution. [c] Absorption band for the onset wavelength. [d] Molar absorption coefficient to the referred wavelength. [e] Energy band gap derived from the low-energy absorption edge using the equation $E_g^{opt} = 1240/\lambda_{onset}$.

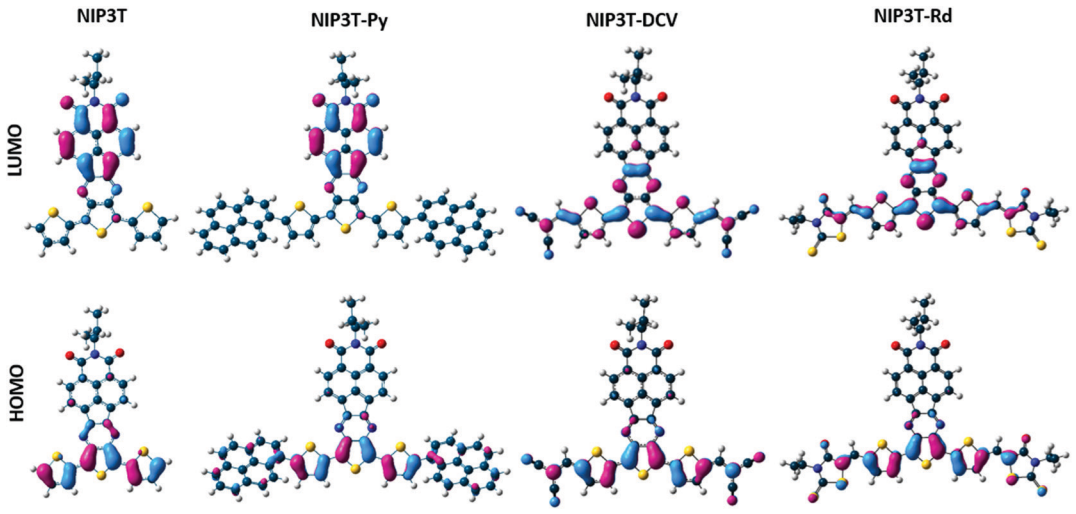


Fig. 5 DFT/B3LYP/6-31G** molecular orbital topologies of **NIP3T**, **NIP3T-Py**, **NIP3T-DCV** and **NIP3T-Rd**.

one electron reduction. A further increase of the applied potential is translated in a decrease of these bands with a new absorption increasing in intensity at higher energies that can be ascribed to the dianion species. In this case, the lateral electron-withdrawing groups are the ones bearing the majority of the injected charge (around 70%, Fig. S52 and S53, ESI†), which is stabilized through the terthiophene skeleton as indicated in the LUMO orbital topology.

### Electrical characterization

In order to evaluate the charge-transport characteristics of the studied semiconductors, field effect transistors in a

Table 3 Cyclic voltammetry data

| | Cyclic voltammetry[a] $E_{oxI}$ (V) | $E_{oxII}^{1/2}$ (V) | $E_{redI}^{1/2}$ (V) | $E_{redII}^{1/2}$ (V) | $E_{redIII}^{1/2}$ (V) | $E_{HOMO}$[c] (eV) | $E_{LUMO}$[b] (eV) | $E_{gap}^{elec}$ (eV) |
|---|---|---|---|---|---|---|---|---|
| **NIPa3T-TIPS** | 0.66[d] | — | −1.34 | −1.69 | — | −5.76 | −3.76 | 2.00 |
| **NIPa3T-Py** | 0.42[e] | — | −1.34 | −1.68 | — | −5.52 | −3.76 | 1.76 |
| **NIPa3T-TA** | 0.29[d] | 0.51 | −1.16 | −1.47 | — | −5.39 | −3.94 | 1.45 |
| **NIPa3T** | 0.50[e] | — | −1.30 | −1.81 | — | −5.60 | −3.80 | 1.80 |
| **NIPa3T-Rd** | 0.57[e] | 0.95 | −1.22 | −1.37 | −1.70 | −5.67 | −3.88 | 1.79 |
| **NIPa3T-DCV** | 0.93[d] | — | −1.03 | −1.31 | −1.72 | −6.03 | −4.07 | 1.96 |
| **NIPb3T** | 0.48[e] | — | −1.34 | −1.74 | — | −5.61 | −3.71 | 1.90 |
| **NIPb3T-Rd** | 0.60[e] | — | −1.24 | −1.36 | −1.70 | −5.76 | −3.86 | 1.90 |
| **NIPb3T-DCV** | 0.89[d] | — | −1.07 | −1.39 | −1.77 | −5.99 | −4.01 | 1.98 |

[a] Cyclic voltammetry recorded in DCM/$TBAPF_6$ (0.1 M) at a scan rate of 0.2 V $s^{-1}$ using Pt as the working and the counter electrode, and Fc/Fc+ as the reference electrode. [b] Estimated from $E_{LUMO} = -5.1$ eV $- E_{redI}^{1/2}$. [c] Estimated from $E_{HOMO} = -5.1$ eV $- E_{oxI}^{1/2}$. [d] Half wave potential of the reversible wave. [e] Anodic peak potential of the irreversible wave.


This journal is © The Royal Society of Chemistry 2020

Published on 06 August 2020. Downloaded by Instituto de Ciencia de Materiales de Barcelona (ICMAB) on 9/16/2023 2:19:05 PM.

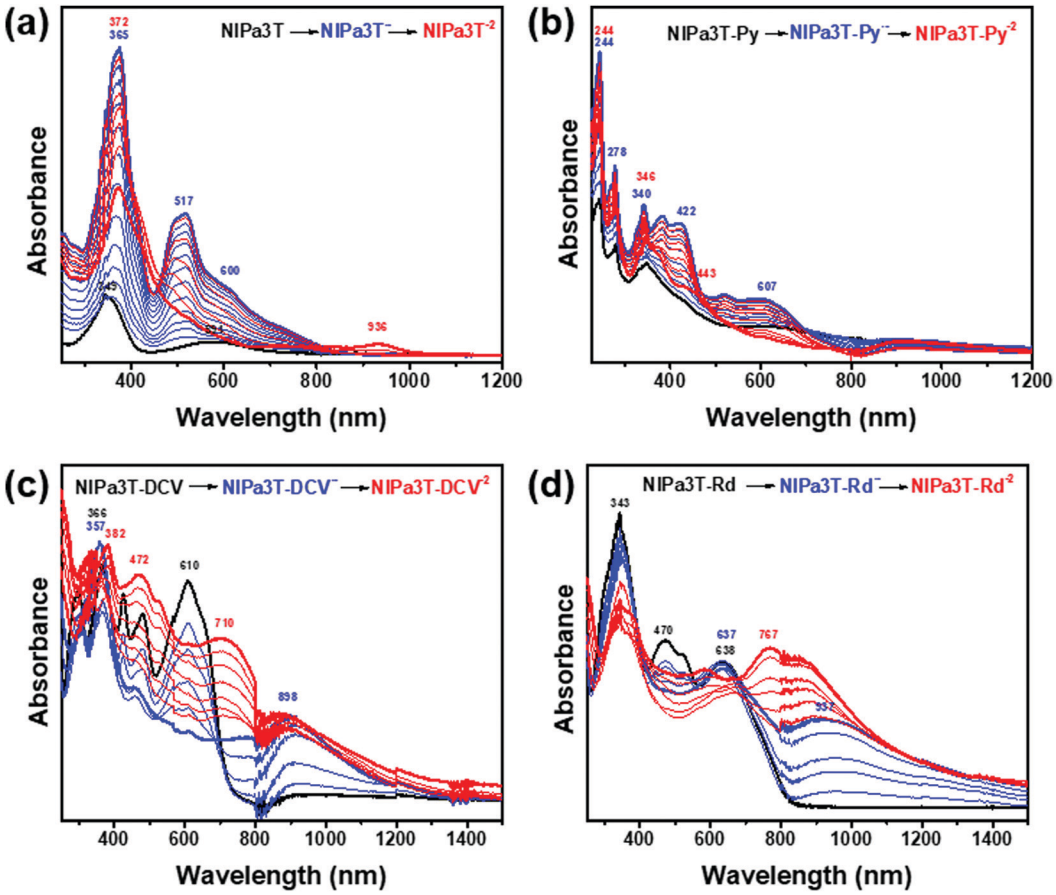


Fig. 6 UV-Vis-NIR absorption spectra recorded during the electrochemical reduction of (a) **NIPa3T**, (b) **NIPa3T-Py**, (c) **NIPa3T-DCV** and (d) **NIPa3T-Rd** in dichloromethane in the presence of $Bu_4NBF_4$ as a supporting electrolyte within an OTTLE cell.

top-contact/bottom-gate architecture were fabricated by the vapor deposition of the semiconductor thin films onto SAM-treated substrates (both octadecyltrichlorosilane and hexamethyldisilazane reactants were used for the superficial treatment of the $SiO_2$ dielectric layer). The deposited thin films were characterized using XRD (Fig. S82 and S83, ESI†) and AFM techniques (Fig. S84, ESI†). After the deposition of the semiconductors, gold electrodes were patterned by using shadow masks with various predefined channel lengths and widths. Performance parameters were extracted from the *I–V* response plots, recorded under vacuum conditions, in the saturation regime using the conventional transistor formalisms, and are summarized in Table 4.

The field effect mobilities of the studied semiconductors are all modest, with the maximum electron mobility of $10^{-2}$ cm$^2$ V$^{-1}$ s$^{-1}$ for **NIPa3T-Py** (see selected output and transfer plots in Fig. 7).

As previously demonstrated,[36] **NIPa3T** shows ambipolar transport, with balanced electron and hole mobilities of $4 \times 10^{-5}$ cm$^2$ V$^{-1}$ s$^{-1}$, quite high threshold voltages of ±47 V and low on/off ratios of $\sim 10^3$. The introduction of lateral electroactive groups in **NIPa3T**, however, modifies charge transport polarity. In fact, substitution with bulky TIPS groups in **NIPa3T-TIPS** results in a p-type semiconductor. In this case, the bulky substituents, which give poorly crystalline films, as shown in Fig. S83 and S84 (ESI†), may explain a non-optimal overlapping of LUMO–LUMO orbitals for electron transport.

Table 4 OFET electrical data for vapor deposited films of the indicated semiconductors measured in a vacuum. Average field-effect mobilities are shown

| Semiconductor | Deposition conditions | $\mu_e$ [cm$^2$ V$^{-1}$ s$^{-1}$] | $V_{TH}$ (V) | $I_{ON}/I_{OFF}$ | $\mu_h$ [cm$^2$ V$^{-1}$ s$^{-1}$] | $V_{TH}$ (V) | $I_{ON}/I_{OFF}$ |
|---|---|---|---|---|---|---|---|
| **NIPa3T**[36] | HMDS, 90 °C | $4 \times 10^{-5}$ | 47 | $7 \times 10^2$ | $4 \times 10^{-5}$ | −47 | $3 \times 10^3$ |
| **NIPa3T-DCV** | OTS, 90 °C | $2 \times 10^{-5}$ | 48 | $2 \times 10^4$ | | | |
| **NIPa3T-DCV** | HMDS, 90 °C | $2 \times 10^{-5}$ | 54 | $2 \times 10^6$ | | | |
| **NIPa3T-Rd** | OTS, 90 °C | $1 \times 10^{-4}$ | 47 | $3 \times 10^4$ | $1 \times 10^{-5}$ | −50 | $1 \times 10^2$ |
| **NIPa3T-Rd** | HMDS, 90 °C | $1 \times 10^{-4}$ | 46 | $5 \times 10^3$ | $5 \times 10^{-6}$ | −15 | $3 \times 10^1$ |
| **NIPa3T-Py** | HMDS, 90 °C | $4 \times 10^{-4}$ | 8 | $2 \times 10^2$ | | | |
| **NIPa3T-Py** | OTS, 90 °C | $1 \times 10^{-2}$ | 42 | $9 \times 10^2$ | | | |
| **NIPa3T-TIPS** | HMDS, 90 °C | | | | $4 \times 10^{-5}$ | −31 | $2 \times 10^1$ |

Published on 06 August 2020. Downloaded by Instituto de Ciencia de Materiales de Barcelona (ICMAB) on 9/16/2023 2:19:05 PM.

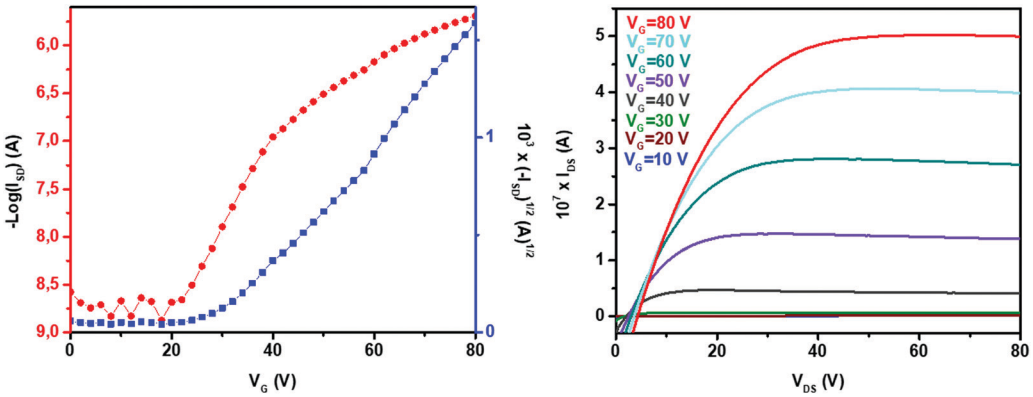


Fig. 7 OFET transfer and output characteristics of **NIPa3T-Py**.

In contrast, substitution with the rest of the electroactive groups reverses the charge polarity, resulting in n-type semiconductors, except when substituted with rhodanine groups, where ambipolarity is maintained. This can be related to its ability to stabilize multiple positive and negative charges, as seen in the electrochemical study. However, the transistor parameters are quite modest, which is probably due to the amorphous nature of the analyzed thin films. Note that no peaks were recorded by XRD measurements (Fig. S83, ESI†) while AFM images show a lack of crystalline grains. Nevertheless, an order of magnitude higher electron mobility is found for **NIPa3T-Rd** with respect to **NIPa3T-DCV**, due to the more extended π-conjugation, as shown *via* Raman spectroscopy (Fig. 3), as well as due to the stronger electron-withdrawing ability of the rhodanine groups in comparison with the dicyanovinylene groups. As depicted in Fig. S52 and S53 (ESI†), the rhodanine groups are able to stabilize a greater amount of negative charge upon electron injection. For both **NIPa3T-Rd** and **NIPa3T-DCV** semiconductors, threshold voltages are still high, but the on/off ratio is improved up to $2 \times 10^6$ when p-type transport is suppressed in **NIPa3T-DCV**.

Two orders magnitude higher field effect mobilities were recorded for **NIPa3T-Py**, with comparable threshold voltages but lower on/off ratio values compared to the compounds substituted with electron withdrawing groups, **NIPa3T-Rd** and **NIPa3T-DCV**. This suggests that in **NIPa3T-Py**, hole accumulation at zero or slightly negative $V_G$ voltages may not be completely suppressed, due to its low oxidation potential.

In addition, the higher electron mobility of **NIPa3T-Py** can be rationalized in terms of appropriate HOMO and LUMO levels and charge stabilization through the whole conjugated skeleton, since the pyrene units have been proved to also stabilize some of the injected charge (see Fig. S52 and S53, ESI†). Furthermore, close and cooperative π–π interactions, promoted by efficient interaction between the pyrene units, improve the supramolecular aggregation of this derivative, as suggested by the crystallinity enhancement shown in the XRD patterns and AFM images (Fig. S83 and S84, ESI†) on going from **NIPa3T** to **NIPa3T-Py**.

Table 5 **P3HT:NIPb3T-Rd** organic solar cell characterization

| D : A ratio | Open circuit voltage (V) | Short circuit current (mA cm$^{-2}$) | Fill factor (%) | Efficiency (%) |
|---|---|---|---|---|
| 0.7 : 0.3 | 0.42 | 1.5 | 40 | 0.25 |

### Organic photovoltaic proof of concept

We have additionally made a first evaluation of the potential of this type of molecules as non-fullerene acceptors in organic solar cells. For this, a series of bulk heterojunction devices was fabricated in inverted structures, using for the active layer a blend of **P3HT** as the donor and **NIPb3T-Rd** as the acceptor. We chose **NIPb3T-Rd** due to its low band gap, leading to complementary absorption with P3HT, a factor that could potentially help to absorb a large fraction of the sun spectrum.

After optimizing the system using a high-throughput method (Fig. S90 and S91, ESI†), the best performing sample contained 70% **P3HT** and 30% **NIPb3T-Rd** and yielded 0.25% efficiency (Table 5).

Fig. 8 shows that despite the low efficiency values, the solar cell functions correctly and can act as a working p–n junction. Performance, however, is very limited. We believe that the relatively low efficiency values are due to several reasons. On the one hand, the modest charge mobility, in comparison with other non-fullerene acceptors (Table 4), strongly affects the fill factor and possibly introduces large recombination rates (seen here as a low $V_{oc}$). On the other hand, the explored materials have broadband absorption, which is positive to harvest a large fraction of the solar spectrum. Unfortunately, the oscillator strength is very small, leading to extinction coefficients (see Fig. 8 and Table 1 for the dipole moment) around one order of magnitude lower than those of typical conjugated polymers and NFAs.[71,72] Effectively, this strongly affects the capability to absorb light in thin films based on this material, yielding small photocurrents. Moreover, the strong tendency observed for this molecule to phase separate from the polymer is believed to also reduce the charge generation capability of the system due to typically small exciton diffusion lengths observed in organic materials, further contributing to the limited measured photocurrent.

Although the device might have limited use as an organic solar cell, the broadband absorption of **NIPb3T-Rd** might be useful in the fabrication of photodetectors, where thicker films

 This journal is © The Royal Society of Chemistry 2020

Published on 06 August 2020. Downloaded by Instituto de Ciencia de Materiales de Barcelona (ICMAB) on 9/16/2023 2:19:05 PM.

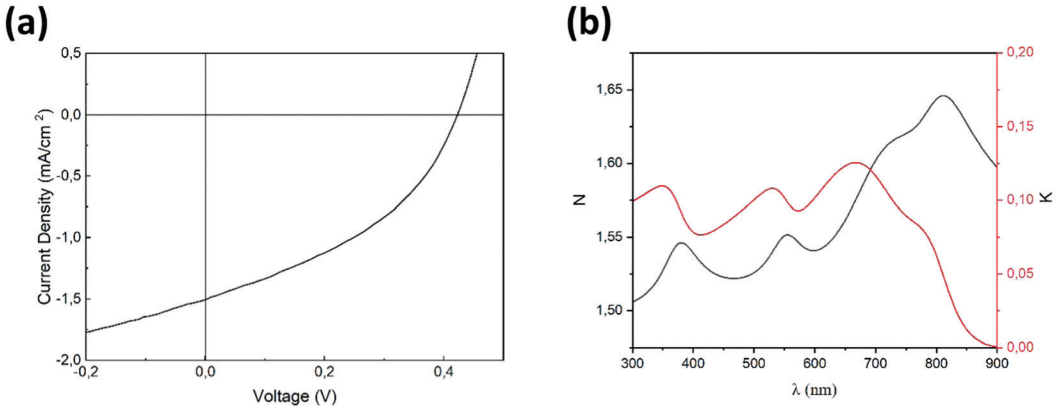


Fig. 8 (a) $J$–$V$ curve for the best performing **P3HT:NIPb3T-Rd** based solar cell. (b) Complex refractive index ($N$ and $K$) for the thin film **NIPb3T-Rd**.

would increase absorption, and the moderate mobilities would be compensated by the driving voltage. Further experiments are being carried out in this direction and will be the subject of a future publication.

## 3. Summary and conclusions

A series of naphthalimide fused thienopyrazine derivatives, laterally substituted by different donor and acceptor constituents, has been synthesized, aiming to design molecules in which the energy and topology of the frontier molecular orbitals involved in the charge transport mechanism could be modulated. This set of materials allows, using both a theoretical and experimental approach, analyzing the effects on charge stabilization and charge transport of oligothiophene–naphthalimide assemblies by introducing additional electron donor or electron acceptor substituents at the terminal positions of the oligothiophene moieties.

The molecular, optical and electronic properties have been thoroughly analyzed using DFT calculations, electrochemical measurements, optical and vibrational Raman spectroscopies and spectroelectrochemical studies.

The molecular dipole moments of the novel assemblies have been calculated given that dipole moments and geometrical restrictions are known to influence solid state packing. Interestingly, for the derivatives with strong electron acceptor lateral substituents, the interplay between the electron withdrawing strengths of the electron-rich lateral groups and the NIP unit yields molecules with small dipole moments and a more stable parallel configuration of stacking is predicted.

In addition, spectroelectrochemistry has been used to analyze the structure and stability of the charge carriers involved in the electron transport process. It is observed that in the assemblies with electron-donor lateral substituents, the injected negative charge is mostly delocalized over the naphthaleneimide fragment while in the assemblies with lateral electron-withdrawing groups, these groups are the ones bearing the majority of the injected charge.

The best mobility value has been obtained for the assembly with pyrene substituents. In this sense, the lateral pyrene units have proven to help both in charge stabilization and supramolecular aggregation, probably due to the appearance of close and cooperative π–π interactions between pyrene units of two stacked molecules. On the other hand, the derivative bearing a strong rhodanine moiety at terminal positions has an ambipolar behavior. This can be rationalized in terms of the strong electron-withdrawing ability of the rhodanine groups as well as because of the more effective conjugation extension shown in Raman spectroscopy by the insertion of these lateral substituents.

Finally, although the materials have broadband absorption, which is positive to harvest a large fraction of the solar spectrum, they have limited use as a non-fullerene acceptor in organic solar cells due to the low electronic transition oscillator strengths. However, some of these assemblies are potential candidates to be used as photodetectors, where the thicker films would increase overall light absorption, and the lower mobilities would be compensated by the driving voltage.

## Author contribution statement

Matías J. Alonso-Navarro: investigation, data curation, visualization, writing – original draft, writing – review & editing. Alexandra Harbuzaru: investigation, data curation, visualization, writing – original draft, writing – review & editing. Paula de Echegaray: investigation, data curation, visualization. Iratxe Arrechea-Marcos: investigation, data curation, visualization. Albert-Harillo-Baños: investigation, data curation, visualization. Alejandro de la Peña: investigation, data curation, visualization. M. Mar Ramos: visualization, writing – review & editing. J. Teodomiro López Navarrete: visualization, writing – review & editing. Mariano Campoy-Quiles: conceptualization, investigation, visualization, supervision, writing – review & editing. Rocío Ponce Ortiz: conceptualization, investigation, visualization, supervision, writing – review & editing, funding acquisition, project administration. José L. Segura: conceptualization, investigation, visualization, supervision, writing – review & editing, funding acquisition, project administration.

## Conflicts of interest

There are no conflicts to declare.

Published on 06 August 2020. Downloaded by Instituto de Ciencia de Materiales de Barcelona (ICMAB) on 9/16/2023 2:19:05 PM.

## Acknowledgements

This work was financially supported by MINECO (MAT2016-77608-C3-2-P), MICINN (PID2019-106268GB-C33) and the UCM (INV.GR.00.1819.10759). MJAN gratefully acknowledges Universidad Rey Juan Carlos for a predoctoral contract. The university of Málaga acknowledges support from Junta de Andalucia (UMA18-FEDERJA-080) and MICINN (PID2019-110305GB-I00). We also thank CIC NanoGune for technical support in OFET characterization measurements.

## References

1 M. Wang, P. Baek, A. Akbarinejad, D. Barker and J. Travas-Sejdic, *J. Mater. Chem. C*, 2019, **7**, 5534–5552.
2 B. Xie, Z. Chen, L. Ying, F. Huang and Y. Cao, *InfoMat*, 2019, **2**, 57–91.
3 E. K. Lee, M. Y. Lee, C. H. Park, H. R. Lee and J. H. Oh, *Adv. Mater.*, 2017, **29**, 1703638.
4 Y. Jiang, Y. Guo and Y. Liu, *Adv. Electron. Mater.*, 2017, **3**, 1700157.
5 D. Shi, Z. Liu, J. Ma, Z. Zhao, L. Tan, G. Lin, J. Tian, X. Zhang, G. Zhang and D. Zhang, *Adv. Funct. Mater.*, 2020, **30**, 1910235.
6 M. Al-Hashimi, Y. Han, J. Smith, H. S. Bazzi, S. Y. A. Alqaradawi, S. E. Watkins, T. D. Anthopoulos and M. Heeney, *Chem. Sci.*, 2016, **7**, 1093–1099.
7 J. Sun, Z. Liu, H. Luo, S. Yang, J. Yao, G. Zhang and D. Zhang, *J. Mater. Chem. C*, 2016, **4**, 9359–9365.
8 Y. Wang, H. Guo, A. Harbuzaru, M. A. Uddin, I. Arrechea-Marcos, S. Ling, J. Yu, Y. Tang, H. Sun, J. T. López Navarrete, R. P. Ortiz, H. Y. Woo and X. Guo, *J. Am. Chem. Soc.*, 2018, **140**, 6095–6108.
9 S. Izumi, H. F. Higginbotham, A. Nyga, P. Stachelek, N. Tohnai, P. d. Silva, P. Data, Y. Takeda and S. Minakata, *J. Am. Chem. Soc.*, 2020, **142**, 1482–1491.
10 C. Poriel and J. Rault-Berthelot, *J. Mater. Chem. C*, 2017, **5**, 3869–3897.
11 B. Kan, X. Chen, K. Gao, M. Zhang, F. Lin, X. Peng, F. Liu and A. K. Y. Jen, *Nano Energy*, 2020, **67**, 104209.
12 J. Li, Y. Zhao, H. S. Tan, Y. Guo, C.-A. Di, G. Yu, Y. Liu, M. Lin, S. H. Lim, Y. Zhou, H. Su and B. S. Ong, *Sci. Rep.*, 2012, **2**, 754.
13 I. Kang, H. J. Yun, D. S. Chung, S. K. Kwon and Y. H. Kim, *J. Am. Chem. Soc.*, 2013, **135**, 14896–14899.
14 G. Kim, S. J. Kang, G. K. Dutta, Y. K. Han, T. J. Shin, Y. Y. Noh and C. Yang, *J. Am. Chem. Soc.*, 2014, **136**, 9477–9483.
15 Y.-Q. Zheng, T. Lei, J.-H. Dou, X. Xia, J.-Y. Wang, C.-J. Liu and J. Pei, *Adv. Mater.*, 2016, **28**, 7213–7219.
16 J. Liu, J. Liu, J. Zhang, C. Li, Q. Cui, F. Teng, H. Li and L. Jiang, *J. Mater. Chem. C*, 2020, **8**, 4303–4308.
17 J. T. E. Quinn, J. Zhu, X. Li, J. Wang and Y. Li, *J. Mater. Chem. C*, 2017, **5**, 8654–8681.
18 H. Bronstein, C. B. Nielsen, B. C. Schroeder and I. McCulloch, *Nat. Rev. Chem.*, 2020, **4**, 66–77.
19 A. P. Dhondge, P. C. Tsai, C. Y. Nien, W. Y. Xu, P. M. Chen, Y. H. Hsu, K. W. Li, F. M. Yen, S. L. Tseng, Y. C. Chang, H. J. H. Chen and M. Y. Kuo, *Org. Lett.*, 2018, **20**, 2538–2542.
20 A.-J. Payne, N. A. Rice, S. M. McAfee, S. Li, P. Josse, C. Cabanetos, C. Risko, B. H. Lessard and G. C. Welch, *ACS Appl. Energy Mater.*, 2018, **1**, 4906–4916.
21 Y. Peng and Z. Li, *Mater. Chem. Phys.*, 2018, **214**, 260–264.
22 S. Vasimalla, N. V. V. Subbarao, M. Gedda, D. K. Goswami and P. K. Iyer, *ACS Omega*, 2017, **2**, 2552–2560.
23 Z. Zhao, S. Gao, X. Zheng, P. Zhang, W. Wu, R. T. K. Kwok, Y. Xiong, N. L. C. Leung, Y. Chen, X. Gao, J. W. Y. Lam and B. Z. Tang, *Adv. Funct. Mater.*, 2018, **28**, 1705609.
24 A. Nowak-Krol, K. Shoyama, M. Stolte and F. Wurthner, *Chem. Commun.*, 2018, **54**, 13763–13772.
25 S. Kumar, J. Shukla, Y. Kumar and P. Mukhopadhyay, *Org. Chem. Front.*, 2018, **5**, 2254–2276.
26 X. Zhan, A. Facchetti, S. Barlow, T. J. Marks, M. A. Ratner, M. R. Wasielewski and S. R. Marder, *Adv. Mater.*, 2011, **23**, 268–284.
27 P. Mayorga Burrezo, W. Zeng, M. Moos, M. Holzapfel, S. Canola, F. Negri, C. Rovira, J. Veciana, H. Phan, J. Wu, C. Lambert and J. Casado, *Angew. Chem., Int. Ed.*, 2019, **58**, 14467–14471.
28 J. Shukla and P. Mukhopadhyay, *Eur. J. Org. Chem.*, 2019, 7770–7786.
29 M. A. Kobaisi, S. V. Bhosale, K. Latham, A. M. Raynor and S. V. Bhosale, *Chem. Rev.*, 2016, **116**, 11685–11796.
30 M. J. Sung, A. Luzio, W.-T. Park, R. Kim, E. Gann, F. Maddalena, G. Pace, Y. Xu, D. Natali, C. de Falco, L. Dang, C. R. McNeill, M. Caironi, Y.-Y. Noh and Y.-H. Kim, *Adv. Funct. Mater.*, 2016, **26**, 4984–4997.
31 T. He, M. Stolte, C. Burschka, N. H. Hansen, T. Musiol, D. Kalblein, J. Pflaum, X. Tao, J. Brill and F. Wurthner, *Nat. Commun.*, 2015, **6**, 5954.
32 R. P. Ortiz, H. Herrera, R. Blanco, H. Huang, A. Facchetti, T. J. Marks, Y. Zheng and J. L. Segura, *J. Am. Chem. Soc.*, 2010, **132**, 8440–8452.
33 A. Riaño Carnerero, G. López Espejo, M. J. Mancheño Real, B. Eckstein, R. C. González-Cano, F. S. Melkonyan, A. Facchetti, T. J. Marks, J. Casado, J. T. López Navarrete, J. L. Segura and R. Ponce Ortiz, *J. Mater. Chem. C*, 2017, **5**, 9439–9450.
34 A. de la Pena, I. Arrechea-Marcos, M. J. Mancheno, M. C. Ruiz Delgado, J. T. Lopez Navarrete, J. L. Segura and R. Ponce Ortiz, *Chemistry*, 2016, **22**, 13643–13652.
35 I. Arrechea-Marcos, P. de Echegaray, M. J. Mancheno, M. C. Ruiz Delgado, M. M. Ramos, J. A. Quintana, J. M. Villalvilla, M. A. Diaz-Garcia, J. T. Lopez Navarrete, R. Ponce Ortiz and J. L. Segura, *Phys. Chem. Chem. Phys.*, 2017, **19**, 6206–6215.
36 R. Ponce Ortiz, H. Herrera, M. J. Mancheno, C. Seoane, J. L. Segura, P. Mayorga Burrezo, J. Casado, J. T. Lopez Navarrete, A. Facchetti and T. J. Marks, *Chemistry*, 2013, **19**, 12458–12467.
37 J. Wang, K. Liu, L. Ma and X. Zhan, *Chem. Rev.*, 2016, **116**, 14675–14725.
38 R. Dheepika, S. Sonalin, P. M. Imran and S. Nagarajan, *J. Mater. Chem. C*, 2018, **6**, 6916–6919.
39 S. Hüttner, M. Sommer, U. Steiner and M. Thelakkat, *Appl. Phys. Lett.*, 2010, **96**, 073503.

 This journal is © The Royal Society of Chemistry 2020

Published on 06 August 2020. Downloaded by Instituto de Ciencia de Materiales de Barcelona (ICMAB) on 9/16/2023 2:19:05 PM.

40 K. Oniwa, H. Kikuchi, H. Shimotani, S. Ikeda, N. Asao, Y. Yamamoto, K. Tanigaki and T. Jin, *Chem. Commun.*, 2016, **52**, 4800–4803.
41 X. Gong, C. Zheng, X. Feng, Y. Huan, J. Li, M. Yi, Z. Fu, W. Huang and D. Gao, *Chem. – Asian J.*, 2018, **13**, 3920–3927.
42 S. Y. Liu, W. Q. Liu, J. Q. Xu, C. C. Fan, W. F. Fu, J. Ling, J. Y. Wu, M. M. Shi, A. K. Jen and H. Z. Chen, *ACS Appl. Mater. Interfaces*, 2014, **6**, 6765–6775.
43 L. Wang, H. Liu, Z. Huai and S. Yang, *ACS Appl. Mater. Interfaces*, 2017, **9**, 28828–28837.
44 M. Chen, L. Yan, Y. Zhao, I. Murtaza, H. Meng and W. Huang, *J. Mater. Chem. C*, 2018, **6**, 7416–7444.
45 X. Yan, H. Fan, H. Gu, J. Zhang, X. Huang, R. Zhang and X. Zhan, *Dyes Pigm.*, 2015, **114**, 124–128.
46 M. Privado, V. Cuesta, P. de la Cruz, M. L. Keshtov, R. Singhal, G. D. Sharmad and F. Langa, *ACS Appl. Mater. Interfaces*, 2017, **9**, 11739–11748.
47 S. Badgujar, C. E. Song, S. Oh, W. S. Shin, S.-J. Moon, J.-C. Lee, I. H. Jung and S. K. Lee, *J. Mater. Chem. A*, 2016, **4**, 16335–16340.
48 Y. Kim, C. E. Song, S. J. Moon and E. Lim, *Chem. Commun.*, 2014, **50**, 8235–8238.
49 H. Z. C. Koerner, R. Fitzner, M. Riede, A. Mishra, P. Bäuerle and K. Leo, *Advances in Polymer Science*, Springer, Cham, 2017, vol. 272.
50 K. Wang, Y. Firdaus, M. Babics, F. Cruciani, Q. Saleem, A. El Labban, M. A. Alamoudi, T. Marszalek, W. Pisula, F. Laquai and P. M. Beaujuge, *Chem. Mater.*, 2016, **28**, 2200–2208.
51 J. Wu, Y. Ma, N. Wu, Y. Lin, J. Lin, L. Wang and C.-Q. Ma, *Org. Electron.*, 2015, **23**, 28–38.
52 M.-H. Yoon, S. A. DiBenedetto, A. Facchetti and T. J. Marks, *J. Am. Chem. Soc.*, 2005, **127**, 1348–1349.
53 J.-i. N. Shinji Ando, H. Tada, Y. Inoue, S. Tokito and Y. Yamashita, *J. Am. Chem. Soc.*, 2005, **127**, 5336–5337.
54 N. Sakai, J. Mareda, E. Vauthey and S. Matile, *Chem. Commun.*, 2010, **46**, 4225–4237.
55 N. Zheng, Z. Lin, Y. Zheng, D. Li, J. Yang, W. Zhang, L. Wang and G. Yu, *Org. Electron.*, 2020, **81**, 105684.
56 C. Xiao, C. Li, F. Liu, L. Zhang and W. Li, *J. Mater. Chem. C*, 2020, **8**, 5370–5374.
57 G. Liu, C. Xiao, F. Negri, Y. Li and Z. Wang, *Angew. Chem., Int. Ed.*, 2020, **59**, 2008–2012.
58 J. Lee, E.-S. Shin, Y.-J. Kim, Y.-Y. Noh and C. Yang, *J. Mater. Chem. C*, 2020, **8**, 296–302.
59 J. L. Segura, H. Herrera and P. Bäuerle, *J. Mater. Chem.*, 2012, **22**, 8717–8733.
60 S. L. Suraru and F. Wurthner, *Angew. Chem., Int. Ed.*, 2014, **53**, 7428–7448.
61 R. P. Ortiz, H. Herrera, C. Seoane, J. L. Segura, A. Facchetti and T. J. Marks, *Chemistry*, 2012, **18**, 532–543.
62 H. Herrera, P. de Echegaray, M. Urdanpilleta, M. J. Mancheno, E. Mena-Osteritz, P. Bauerle and J. L. Segura, *Chem. Commun.*, 2013, **49**, 713–715.
63 A. Riaño, P. Mayorga Burrezo, M. J. Mancheño, A. Timalsina, J. Smith, A. Facchetti, T. J. Marks, J. T. López Navarrete, J. L. Segura, J. Casado and R. Ponce Ortiz, *J. Mater. Chem. C*, 2014, **2**, 6376–6386.
64 C. Castiglioni, J. T. Lopez Navarrete, G. Zerbi and M. Gussoni, *Solid State Commun.*, 1988, **65**, 625–630.
65 G. Zerbi, M. Veronelli, S. Martina, A.-D. Schlüter and G. Wegner, *Adv. Mater.*, 1994, **6**, 385–388.
66 J. Albero, P. Atienzar, A. Corma and H. Garcia, *Chem. Rec.*, 2015, **15**, 803–828.
67 S. R. González, J. Casado, J. T. L. Navarrete, R. Blanco and J. L. Segura, *J. Phys. Chem. A*, 2008, **112**, 6732–6740.
68 S. Grimme, *J. Comput. Chem.*, 2004, **25**, 1463–1473.
69 S. Guha, F. S. Goodson, L. J. Corson and S. Saha, *J. Am. Chem. Soc.*, 2012, **134**, 13679–13691.
70 D. Branowska, E. Olender, W. Wysocki, Z. Karczmarzyk, I. Bancerz, P. Ledwon, M. Lapkowski, B. Mirosław, Z. Urbańczyk-Lipkowska and P. Kalicki, *Electrochim. Acta*, 2016, **214**, 19–30.
71 A. Harillo-Baños, X. Rodríguez-Martínez and M. Campoy-Quiles, *Adv. Energy Mater.*, 2020, **10**, 1902417.
72 M. S. Vezie, S. Few, I. Meager, G. Pieridou, B. Dörling, R. S. Ashraf, A. R. Goñi, H. Bronstein, I. McCulloch, S. C. Hayes, M. Campoy-Quiles and J. Nelson, *Nat. Mater.*, 2016, **15**, 746–753.

Electronic Supplementary Material (ESI) for Journal of Materials Chemistry C.
This journal is © The Royal Society of Chemistry 2020

# Supplementary information

## Effective interplay of donor and acceptor groups for optoelectronic properties tuning in Oligothiophene-Naphthalimide Assemblies

Matías J. Alonso-Navarro[a,c†], Alexandra Harbuzaru[b†], Paula de Echegaray[a,c‡], Iratxe Arrechea-Marcos[b‡], Albert-Harillo-Baños[d], Alejandro de la Peña [a,c] M. Mar Ramos,[c] J. Teodomiro López Navarrete[b], Mariano Campoy-Quiles[d], Rocío Ponce Ortiz[b]*, José L. Segura [a]*

[a]*Department of Organic Chemistry, Complutense University of Madrid, Faculty of Chemistry, Madrid 28040, Spain.*

[b]*Department of Physical Chemistry, University of Málaga, Málaga, 29071, Spain.*

[c]*Chemical and Environmental Technology Department. Univ. Rey Juan Carlos, Móstoles, 28933, Spain.*

[d]*Institut de Ciencia de Materials de Barcelona (ICMAB-CSIC), 08193 Bellaterra, Spain*

† These authors contributed equally to this work
‡ These authors contributed equally to this work

**Contents**

1. General information

2. Synthesis of compounds and characterization

3. DFT and TD-DFT calculations

4. FT-Raman

5. UV-Vis and Electrochemical data

6. Spectroelectrochemical measurements

7. DRX

8. AFM

9. Organic field effect transistors

10. Organic photovoltaics

11. References

## 1. General Information

All the chemicals were purchased from commercial suppliers and used without further purification. **NID**, **$NID_b$**, **1**, **2**, **3**, **5** and **6** were obtained as previously described.[1-8] Compounds **4** and **7** are commercially available. $^1$H-NMR and $^{13}$C-NMR spectra were recorded on a Bruker Advance 300 MHz and AMX 500 spectrometer. Chemical shifts are reported in ppm and referenced to the residual non-deuterated solvent frequencies ($CDCl_3$: δ 7.26 ppm for $^1$H, δ 77.0 ppm for $^{13}$C, $C_2D_2Cl_4$: δ 5.91 ppm for $^1$H, δ 77.8 ppm for $^{13}$C, DMSO-$d_6$: δ 2.50 ppm for $^1$H, δ 39.5 ppm for $^{13}$C). UV–vis absorption spectra of the compounds in HPLC chloroform solutions at 20 ºC were recorded on a Varian Cary 50 UV–vis spectrophotometer. Mass spectra were recorded on a Bruker Reflex 2 (MALDI-TOF). FTIR spectra were carried out in a Shimadzu FTIR 8300 spectrophotometer. Cyclic voltammograms were recorded in an inert atmosphere in electrochemical workstation at a scan rate of 200 mV·s-1 at 20 ºC using tetrabutylammonium hexafluorophosphate (TBAHFP, 0.1 mol $L^{-1}$) as supporting electrolyte in dichloromethane. Polymer-precoated platinum electrode, platinum–wire electrode, and $Ag/Ag^+$ electrode were used as working electrode, an auxiliary electrode, and reference electrode, respectively. Potentials were recorded versus $Fc/Fc^+$.

## 2. Synthesis of compounds and characterization

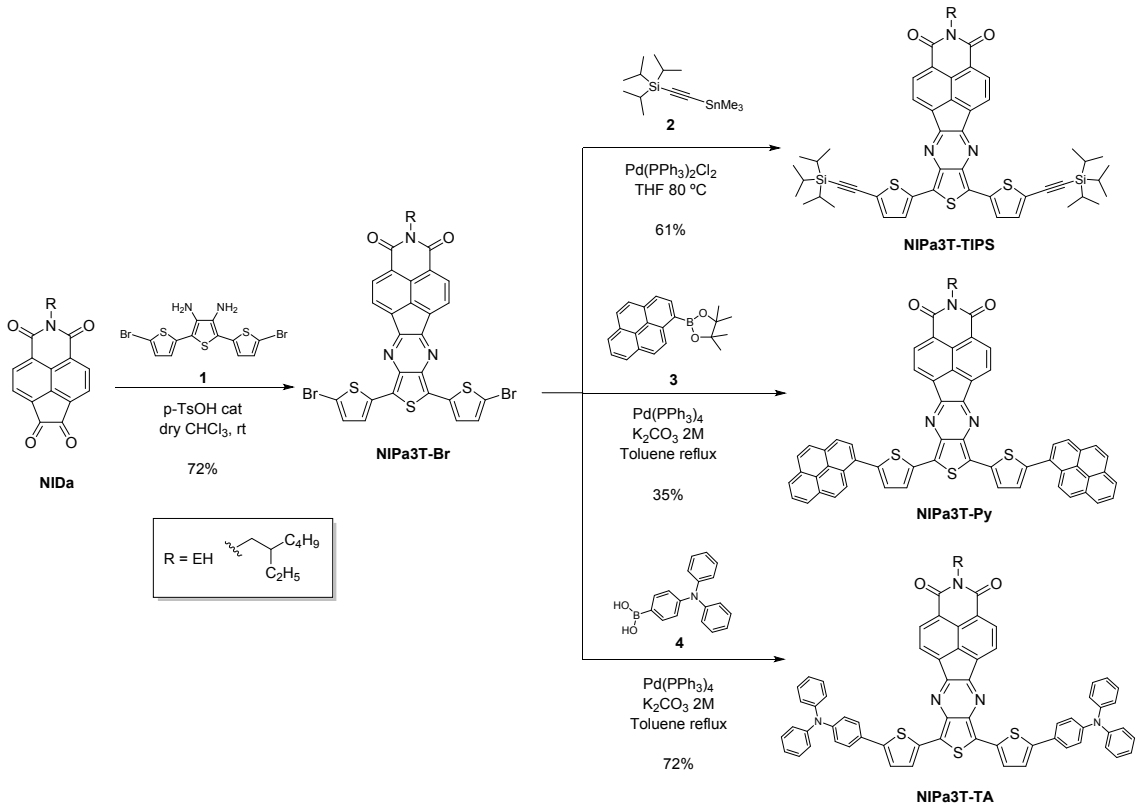


**Scheme S1** Synthetic route for the desired D-A1-D compounds.

**NIPa3T-Br**: To a 30 mL anhydrous chloroform solution of **NID** (271mg, 0.747mmol), a catalytic amount of p-TsOH (10%) was added and the mixture was stirred for 5 min. After that, an anhydrous chloroform solution of **1** (208mg, 0.747mmol) was added. The solution turns instantly to a dark blue color and it was stirred overnight at room temperature. The solvent was evaporated under reduce pressure and the crude was precipitated in MeOH. The solid was filtrated and washed with water, MeOH and hot MeOH to obtain 246mg (72%) of a dark blue solid.

$^1$H-NMR: 8.50 (d, J = 8.47 Hz, 2H), 8.10 (d, J = 8.08 Hz, 2H), 6.95 (d, J= 6.97 Hz, 2H), 6.85 (d, J= 6.86 Hz, 2H), 4.1 (m, 2H), 2 (s, 1H), 1.4 (m, 8H), 0.95 (m, 6H).

FTIR (ATR, $CHCl_3$): υ ($cm^{-1}$): 3754, 2953, 2923, 2852, 1699, 1664, 1635, 1591, 1450, 1422, 1324, 1232, 1168, 1060, 970, 813, 782, 748, 616.

MALDI-HRMS (m/z): calculated for $C_{34}H_{25}Br_2N_3O_2S_3$: 760.9476, found ($M^+$): 760.9501.

**NIPa3T-TIPS**: Under argon atmosphere, a mixture of **NIPa3T-Br** (118 mg, 0.1 mmol), **2** (122 mg, 0.35 mmol) and $Pd(PPh_3)Cl_2$ (11 mg, 0.035 mmol) in 12 mL of dry THF were heated at 80º C for 24h. The solvent was then removed under reduced pressure and the residue was dissolved in dichloromethane and washed with water (2 x 15 mL) and 15 mL of an ammonium chloride solution. The organic phase was dried over magnesium sulfate and the solvent was removed under reduced pressure. The solid was purified in flash column chromatography (dichloromethane/hexane 3:7) affording 59 mg (61%) of a deep blue solid.

$^1$H-NMR (300 MHz, $CDCl_3$) δ(ppm) = 8.55 (d, J= 8.54 Hz, 2H), 8.28 (d, J= 8.27 Hz, 2H), 7.44 (d, J= 7.43 Hz, 2H), 7.21 (d, J= 7.2 Hz, 2H), 4.13 (m, 2H), 1.95 (s, 1H), 1.3 (m, 8H), 1.1 (m, 42H), 0.85 (m, 6H).

$^{13}$C-NMR (75 MHz, $CDCl_3$): δ (ppm) = 163.47, 153.09, 137.43, 135.56, 134.62, 132.89, 132.11, 126.88, 125.50, 125.04, 123.77, 121.74, 99.47, 98.86, 38.24, 30.80, 28.75, 23.19, 18.80, 14.20, 11.44, 10.68.

FTIR (ATR, $CHCl_3$): υ ($cm^{-1}$) = 2927.08, 2860.73, 2139.37, 1706.81, 1672.80, 1640.45, 1461.26, 1376.08, 1329.54, 1234.55, 1168.35, 1045.50, 999.81, 883.18, 796.12, 755.35, 672.17.

MALDI-HRMS (m/z): calculated for $C_{56}H_{68}N_3O_2S_3Si_2$: 965.3934, found ($M^+$): 966.3991.

**NIPa3T-Py**: Under argon atmosphere, a mixture of **NIPa3T-Br** (70 mg, 0.092 mmol), **3** (67 mg, 0.21 mmol) and $Pd(PPh_4)$ (11 mg, 0.010 mmol) in 10 mL of dry toluene and 1 mL of $K_2CO_3$ 2M solution were refluxed overnight.. The solvent was then removed under reduced pressure and the residue was dissolved in chloroform and washed with water (2 x 15 mL) and 15 mL of an ammonium chloride solution. The organic phase was dried over magnesium sulfate and the solvent was removed under reduced pressure. The solid was purified in flash column chromatography (chloroform) affording 31 mg (35%) of a green solid.

$^1$H-NMR (300 MHz, $CDCl_3$)= 8.68 – 8.56 (m, 2H), 8.36 (d, *J* = 8.6 Hz, 2H), 8.28 – 7.98 (m, 18H), 7.88 (d, *J* = 8.5 Hz, 2H), 7.66 (d, *J* = 8.6 Hz, 2H), 4.13 (m, 2H), 1.94 (m, 1H), 1.37 (m, 8H), 0.91 (m, 6H).

FTIR (ATR, $CHCl_3$): υ ($cm^{-1}$) = 2957, 2925, 2855, 1736, 1702, 1666, 1455, 1371, 1233, 844, 757, 718.

MALDI-HRMS (m/z): calculated for $C_{66}H_{43}N_3O_2S_3$: 1005.2517, found ($M^+$): 1005.2524.

**NIPa3T-TA**: Under argon atmosphere, a mixture of **NIPa3T-Br** (82 mg, 0.11 mmol), **4** (68 mg, 0.24 mmol) and $Pd(PPh_4)$ (12 mg, 0.010 mmol) in 10 mL of dry toluene and 1 mL of $K_2CO_3$ 2M solution were refluxed overnight. The solvent was then removed under reduced pressure and the residue was dissolved in dichloromethane and washed with

water (2 x 15 mL) and 15 mL of an ammonium chloride solution. The organic phase was dried over magnesium sulfate and the solvent was removed under reduced pressure. The solid was purified in flash column chromatography (dichloromethane/hexane 7:3) affording 85 mg (72%) of a green solid.

$^{1}$H-NMR (300 MHz, $CDCl_3$): δ (ppm) = 8.02 (d, J= 7.2 Hz, 2H), 7.55 (d, J= 7.2 Hz, 2H), 7.30 (m, 8H), 7.16 (dd, J= 8.6, 1.2 Hz), 7.07 (t, J= 7.3 Hz, 4H), 6.96 (d, J= 8.6 Hz, 4H), 6.85 (d, J= 3.8 Hz, 2H), 6.64 (d, J= 3.8 Hz, 2H), 3.82 (m, 2H), 2.00 (m, 1H), 1.30 (m, 8H), 0.89 (m, 6H).

$^{13}$C-NMR (75 MHz, $CDCl_3$): δ (ppm) =163.2, 151.5, 147.3, 145.3, 136.2, 135.5, 132.0, 131.5, 129.3, 127.2, 126.2, 126.0, 124.9, 123.3, 122.8, 122.6, 31.9, 29.7, 26.6, 25.7, 23.1, 22.7, 14.2, 10.5.

FTIR (ATR, $CHCl_3$): υ ($cm^{-1}$) = 2924, 2854, 1700, 1665, 1590, 1490, 1456, 1374, 1324, 1261, 1086, 1019, 796, 753, 696, 614.

MALDI-HRMS (m/z): calculated for $C_{70}H_{53}N_5O_2S_3$: 1091.3361, found ($M^+$): 1091.3365.

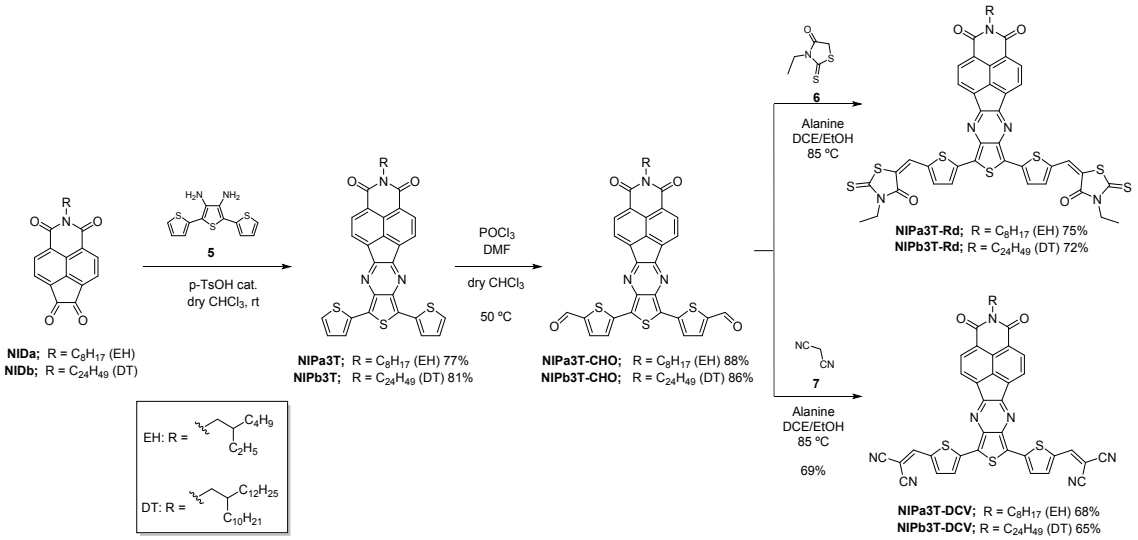


**Scheme S2** Synthetic route for the desired A1-D-A2-D-A1 compounds.

**General procedure for the synthesis of NIP3T derivatives**

To a 30 mL anhydrous chloroform solution of **NIDa** or **NIDb** (1 eq), a catalytic amount of p-TsOH (10%) was added and the mixture was stirred for 5 min. After that, an anhydrous chloroform solution of **5** (1 eq) was added. The solution turns instantly to a dark blue color and it was stirred overnight at room temperature. The solvent was evaporated under reduce pressure and the crude was precipitated in MeOH.

**NIPa3T**: The solid was filtrated and washed with water, MeOH and hot MeOH to obtain 246 mg (77%) of a dark purple solid.

$^{1}$H-NMR (300 MHz, $CDCl_3$) = 8.24 (d, *J* = 7.3 Hz, 2H), 7.83 (d, *J* = 7.3 Hz, 2H), 7.35 (d, *J* = 3.5 Hz, 2H), 7.30 (d, *J* = 4.9 Hz, 2H), 6.99 (dd, *J* = 4.9, 3.5 Hz, 2H), 4.14 – 4.05 (m, 2H), 1.98 – 1.90 (m, 1H), 1.46 – 1.33 (m, 8H), 1.04 – 0.86 (m, 6H).

$^{13}$C-NMR (75 MHz, $CDCl_3$) = 163.65, 152.57, 136.68, 136.16, 135.73, 133.81, 132.01, 27.48, 127.29, 127.01, 125.28, 124.97, 123.54, 121.21, 44.38, 38.38, 30.94, 28.89, 24.21, 23.32, 14.34, 10.81.

FTIR (ATR, $CHCl_3$) υ ($cm^{-1}$) = 3095, 2926, 2856, 2374, 1738, 1704, 1667, 1637, 1495, 1455, 1424, 1334, 1260, 1233, 1162, 1051, 851, 819, 753, 697, 651.

MALDI-HRMS (m/z): calculated for $C_{34}H_{27}N_3O_2S_3$: 605.1265, found ($M^+$): 605.1264.

**NIPb3T:** The precipitate was purified by chromatography column (silica gel flash, DCM/Hex 20:1) to obtain 240mg (81%) of a dark purple solid.

$^{1}$H-NMR (300 MHz, $CDCl_3$) = 8.37 (d, *J* = 7.3 Hz, 2H), 8.00 (d, *J* = 7.3 Hz, 2H), 7.49 (d, *J* = 3.6 Hz, 2H), 7.37 (d, *J* = 5.0 Hz, 2H), 7.07 (dd, *J* = 5.0, 3.7 Hz, 2H), 4.05 (d, *J* = 7.0 Hz, 2H), 2.02 – 1.91 (m, 1H), 1.24 (m, 40H), 0.86 (dt, *J* = 6.7 Hz, 6H).

$^{13}$C-NMR (75 MHz, $CDCl_3$) = 163.50, 152.22, 136.35, 135.87, 135.36, 133.70, 131.73, 127.33, 127.14, 126.74, 125.05, 123.35, 120.90, 44.69, 37.17, 32.10, 31.86, 30.36, 29.89, 29.55, 26.66, 22.86, 14.29. (some signals of the alkyl chain are overlapped)

FTIR (ATR, $CHCl_3$) υ ($cm^{-1}$) = 2922.76, 2852.78, 1703.10, 1667.72, 1635.38, 1454.90, 1326.10, 1231.32, 810.50, 751.23, 695.03

MALDI-HRMS (m/z): calculated for $C_{50}H_{59}N_3O_2S_3$: 829.3769, found ($M^+$): 829.3749.

General procedure for the synthesis of the dialdehyde derivatives:[9]

To a solution of the corresponding pyrazine derivative (**NIPa3T**, **NIPb3T**, 1eq) in 10 mL of chloroform, DMF was added (1 mL) and the solution was stirred for 5min. After that, $POCl_3$ (1 mL) was added carefully and the reaction was stirred at 50 ºC for 48h. 1M NaOH (20 mL) was added, the mixture was stirred vigorously, and the phases were separated. The aqueous phase was extracted with dichloromethane. The combined organic phases were washed with water and brine and dried over $MgSO_4$. The solvent was evaporated under reduced pressure and the crude was purified by chromatography column (silica gel flash, chloroform) to provide pure product.

**NIPa3T-CHO**: the product was obtained (66 mg, 88%) as a purple solid.

$^1$H-NMR (300 MHz, $CDCl_3$) = 9.65 (s, 2H), 8.09 (d, *J* = 7.1 Hz, 2H), 7.63 (d, *J* = 7.0 Hz, 2H), 7.31 (d, *J* = 3.6 Hz, 2H), 7.01 (d, *J* = 3.3 Hz, 2H), 3.97 (m, 2H), 1.89 – 1.76 (m, 1H), 1.42 – 1.30 (m, 8H), 1.02 – 0.81 (m, 6H).

$^{13}$C-NMR (75 MHz, $CDCl_3$) = 182.26, 162.94, 156.54, 153.07, 144.48, 141.22, 137.80, 135.55, 134.09, 131.91, 125.49, 124.55, 124.15, 122.06, 38.35, 30.84, 29.85, 28.80, 24.09, 23.30, 14.34, 10.69.

FTIR (ATR, $CHCl_3$) υ ($cm^{-1}$) = 3089, 3019, 2957, 2927, 2858, 1702, 1663, 1591, 1517, 1437, 1377, 1328, 1281, 1218, 1168, 1132, 1057, 863, 817, 794, 754, 664.

MALDI-HRMS (m/z): calculated for $C_{36}H_{27}N_3O_4S_3$: 661.1164, found ($M^+$): 661.1241.

**NIPb3T-CHO**: the product was obtained (132 mg, 86%) as a purple solid.

$^1$H-NMR (300 MHz, $CDCl_3$) = 9.79 (s, 2H), 8.29 (d, *J* = 7.3 Hz, 2H), 7.92 (d, *J* = 7.3 Hz, 2H), 7.49 (d, *J* = 4.0 Hz, 2H), 7.28 (d, *J* = 4.0 Hz, 2H), 4.02 (d, *J* = 6.4 Hz, 2H), 1.99 – 1.83 (m, 1H), 1.22 (m, 40H), 0.85 (t, *J* = 6.2 Hz, 6H).

$^{13}$C-NMR (75 MHz, $CDCl_3$) = 163.50, 152.22, 136.35, 135.87, 135.36, 133.70, 131.73, 127.33, 127.14, 126.74, 125.05, 123.35, 120.90, 44.69, 37.17, 32.10, 31.86, 30.36, 29.89, 29.55, 26.66, 22.86, 14.29 (some signals of the alkyl chain are overlapped).

FTIR (ATR, $CHCl_3$) υ ($cm^{-1}$) = 2921.00, 2851.56, 1740.19, 1703.55, 1659.05, 1456.17, 1437.92, 1259.49, 1221.02, 1058.41, 801.67.

MALDI-HRMS (m/z): calculated for $C_{52}H_{59}N_3O_4S_3$: 885.3668, found ($M^+$): 885.3710.

General procedure for the synthesis of the rhodanine end-capped derivatives:[10]

To a solution of the corresponding dialdehyde derivative (1eq) in 21 mL of a mixture of DCE/EtOH (5:2), **β-Alanine** (1.75eq) and **6** (3,25eq) was added and the mixture was stirred under reflux for 48h. The solvent was removed under reduced pressure and the residue was redisolved in DCM and precipitated in MeOH.

**NIPa3T-RD**: The solid was filtered and washed with water, MeOH and hot MeOH to obtain the product (46 mg, 75 %) as a black powder.

$^1$H-NMR (300 MHz, $C_2D_2Cl_4$, 343 K) = 8.14 (d, *J* = 7.2 Hz, 2H), 7.62 (d, *J* = 7.2 Hz, 2H), 7.37 (s, 2H), 7.04 (d, *J* = 3.7 Hz, 2H), 6.87 (d, *J* = 3.8 Hz, 2H), 4.19 – 4.05 (m, 4H), 4.02 – 3.87 (m, 2H), 1.91 – 1.79 (m, 1H), 1.39 – 1.18 (m, 14H), 1.01 – 0.80 (m, 6H).

$^{13}$C-NMR (175 MHz, $C_2D_2Cl_4$) = 190.33, 165.94, 162.05, 151.93, 139.31, 139.09, 136.91, 135.05, 133.42, 132.80, 131.22, 125.87, 125.48, 123.81, 123.26, 122.60, 121.14, 120.83, 119.77, 39.60, 37.54, 30.26, 29.41, 28.04, 23.54, 22.54, 13.63, 11.75, 10.04.

FTIR (ATR, $CHCl_3$) υ ($cm^{-1}$) = 3017, 2961, 2929, 2903, 1739, 1702, 1667, 1575, 1455, 1431, 1374, 1351, 1327, 1231, 1129, 1108, 1051, 1022, 877, 818, 759, 609, 565.

MALDI-HRMS (m/z): calculated for $C_{46}H_{37}N_5O_4S_7$: 947.0890, found ($M^+$): 947.0927.

**NIPb3T-RD**: the precipitate was purified in a chromatography column ($CHCl_3$/Hex 20:1), obtaining the pure product (46 mg, 72 %) as a black powder.

$^1$H-NMR (300 MHz, $CDCl_3$) = 7.97 (d, *J* = 7.0 Hz, 2H), 7.35 (d, *J* = 7.2 Hz, 2H), 7.14 (bs, 2H), 6.70 (bs, 2H), 6.64 (bs, 2H), 4.09 (bs, 4H), 3.85 (bs, 2H), 1.86 (m, 1H), 1.49-1.03 (m, 46H), 0.90 (t, *J* = 5.4 Hz, 6H).

$^{13}$C-NMR (75 MHz, $CDCl_3$) = 190.66, 166.45, 162.51, 152.29, 137.20, 135.49, 133.71, 133.31, 131.70, 124.29, 123.79, 121.75, 121.26, 49.40, 40.12, 31.97, 31.64, 30.33, 29.80, 29.46, 26.30, 22.75, 22.65, 14.19, 12.32. (some signals of the alkyl chain are overlapped)

FTIR (ATR, $CHCl_3$) υ ($cm^{-1}$) = 2923.01, 2852.90, 1704.82, 1667.20, 1567.26, 1455.38, 1323.47, 1238.10

MALDI-HRMS (m/z): calculated for $C_{62}H_{69}N_5O_4S_7$: 1171,3395, found ($M^+$): 1171.3437.

General procedure for the synthesis of the dicyanovinylene end-capped derivatives:[10]

To a solution of the corresponding dialdehyde derivative (1eq) in 21 mL of a mixture of DCE/EtOH (5:2), **β-Alanine** (1.75eq) and **7** (3,25eq) was added and the mixture was stirred under reflux for 48h. The solvent was removed under reduced pressure and the residue was dissolved in DCM and precipitated in MeOH. The solid was filtered and washed with water, MeOH and hot MeOH to obtain the product.

**NIPa3T-DCV**: the pure product was isolated (46 mg, 68 %) as a dark green powder.

$^1$H-NMR (700 MHz, DMSO-d6 333 K) = 8.01 (bs, 2H), 7.43 (bs, 2H), 7.06 (bs, 2H), 6.61 (bs, 2H), 6.56 (bs, 2H), 3.73 (m, 2H), 1.75 (m, 1H), 1.40 – 1.21 (m, 8H), 0.89 (m, 6H).

FTIR ($CHCl_3$) υ ($cm^{-1}$) = 2955, 2922, 2853, 2219, 1707, 1667, 1637, 1589, 1562, 1484, 1456, 1429, 1377, 1331, 1277, 1260, 1235, 1166, 1129, 1083, 1065, 1018, 868, 798, 752, 608.

MALDI-HRMS (m/z): calculated for $C_{42}H_{27}N_7O_2S_3$: 757.1388, found ($M^+$): 757.1389.

**NIPb3T-DCV**: the pure product was isolated (37 mg, 65 %) as a dark green powder.

$^1$H-NMR (300 MHz, $CDCl_3$) = 8.61 (d, $J$ = 7.3 Hz, 2H), 8.28 (d, $J$ = 7.3 Hz, 2H), 7.86 (s, 2H), 7.71 (d, $J$ = 4.2 Hz, 2H), 7.67 (d, $J$ = 4.1 Hz, 2H), 4.14 (d, $J$ = 7.0 Hz, 2H), 1.97 (m, 1H), 1.24 (m, 46H), 0.85 (t, $J$ = 6.7 Hz, 6H).

FTIR (ATR, $CHCl_3$) υ ($cm^{-1}$) = 2921.54, 2852.25, 2220.20, 1739.66, 1706.37, 1669.65, 1638.32, 1561.61, 1460.02, 1428.54, 1330.11, 1259.46, 1235.06, 1066.47, 1023.54, 842.89

MALDI-HRMS (m/z): calculated for $C_{58}H_{59}N_7O_2S_3$: 981.3892, found ($M^+$): 981.3940.

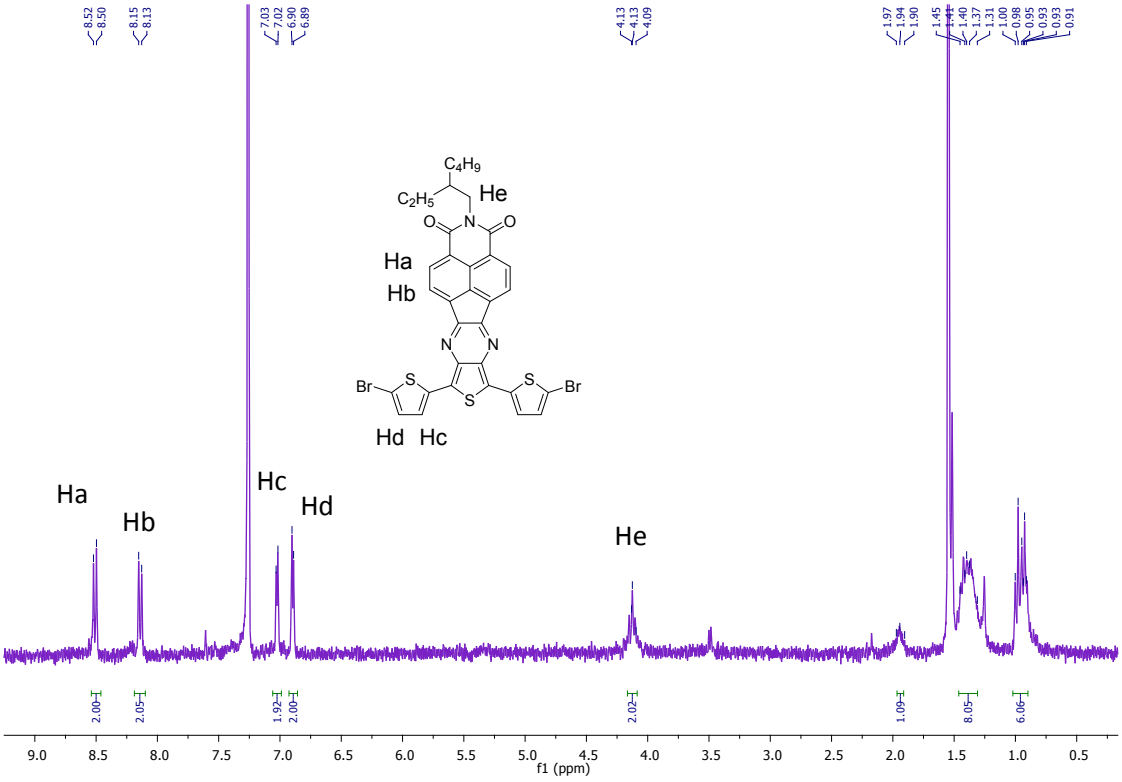


**Figure S1** $^{1}$H-NMR spectrum of **NIPa3T-Br** in $CDCl_3$.

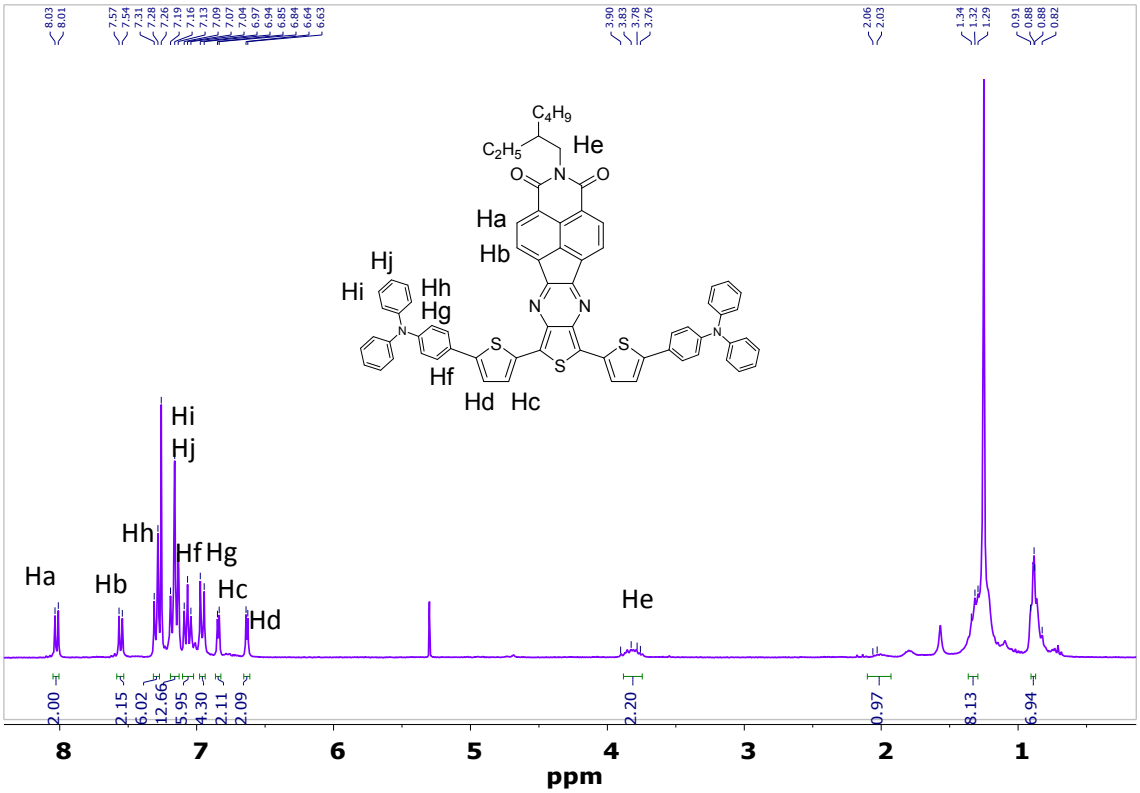


**Figure S2** $^{1}$H-NMR spectrum of **NIPa3T-TA** in $CDCl_3$.

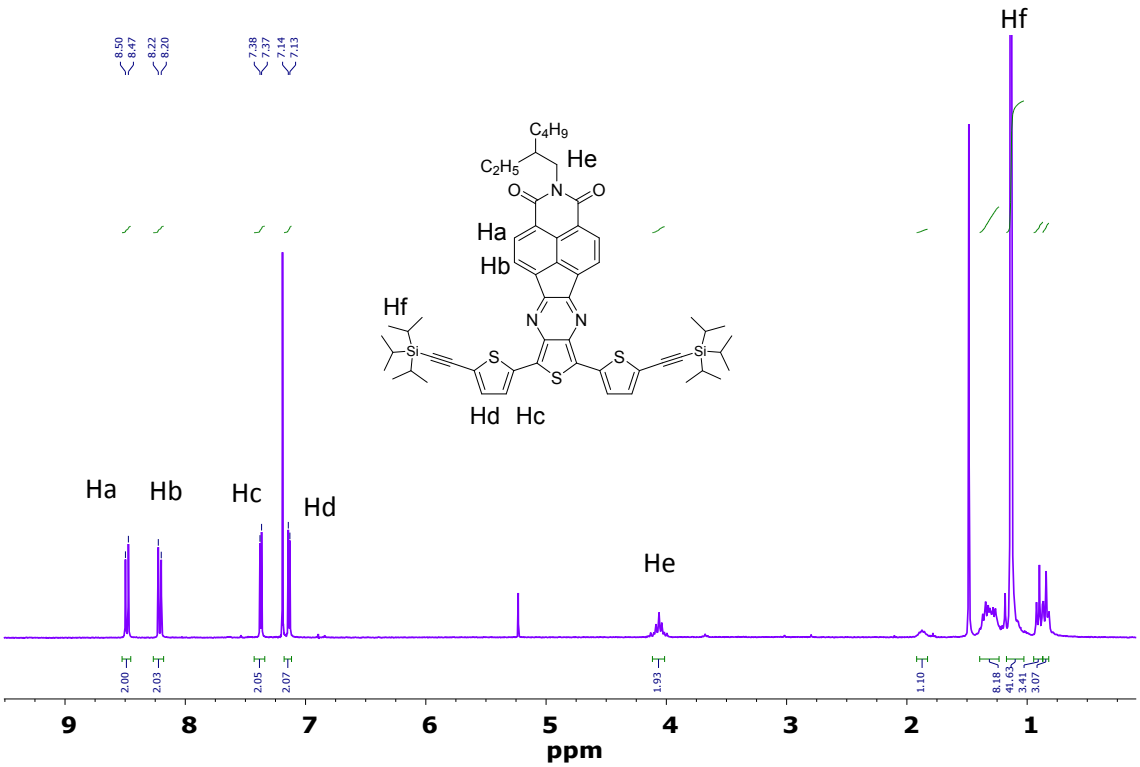


**Figure S3** $^1$H-NMR spectrum of **NIPa3T-TIPS** in $CDCl_3$.

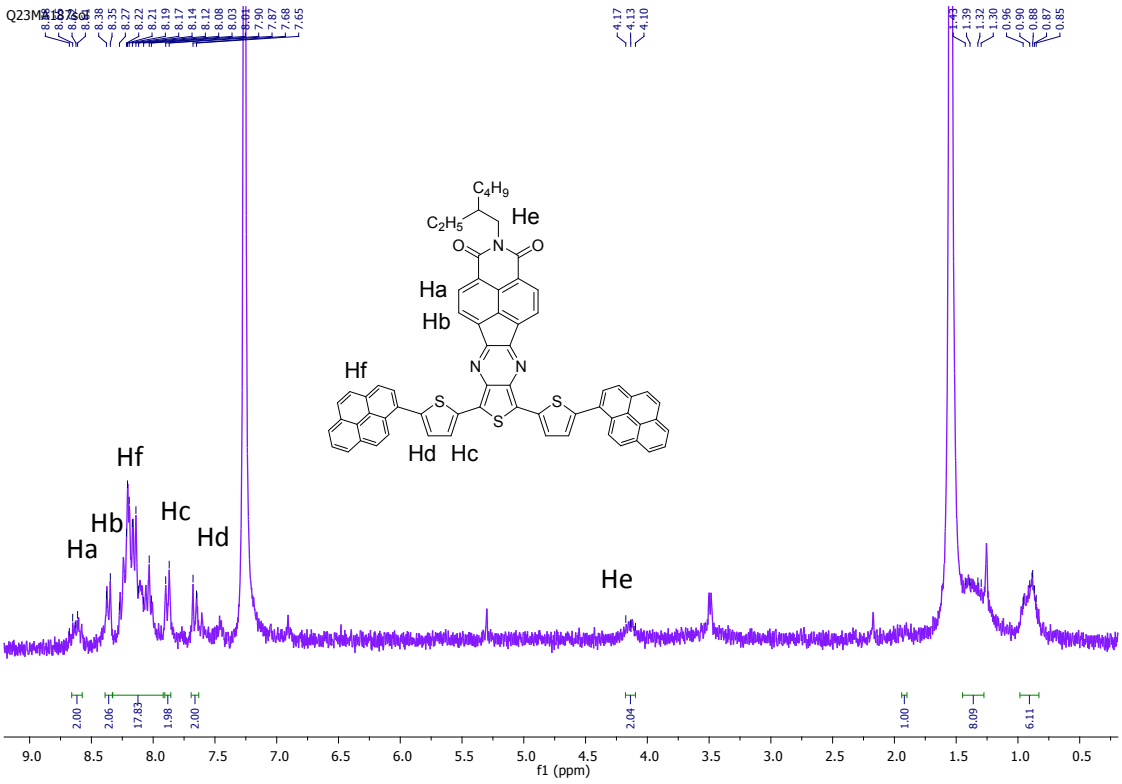


**Figure S4** $^1$H-NMR spectrum of **NIPa3T-Py** in $CDCl_3$.

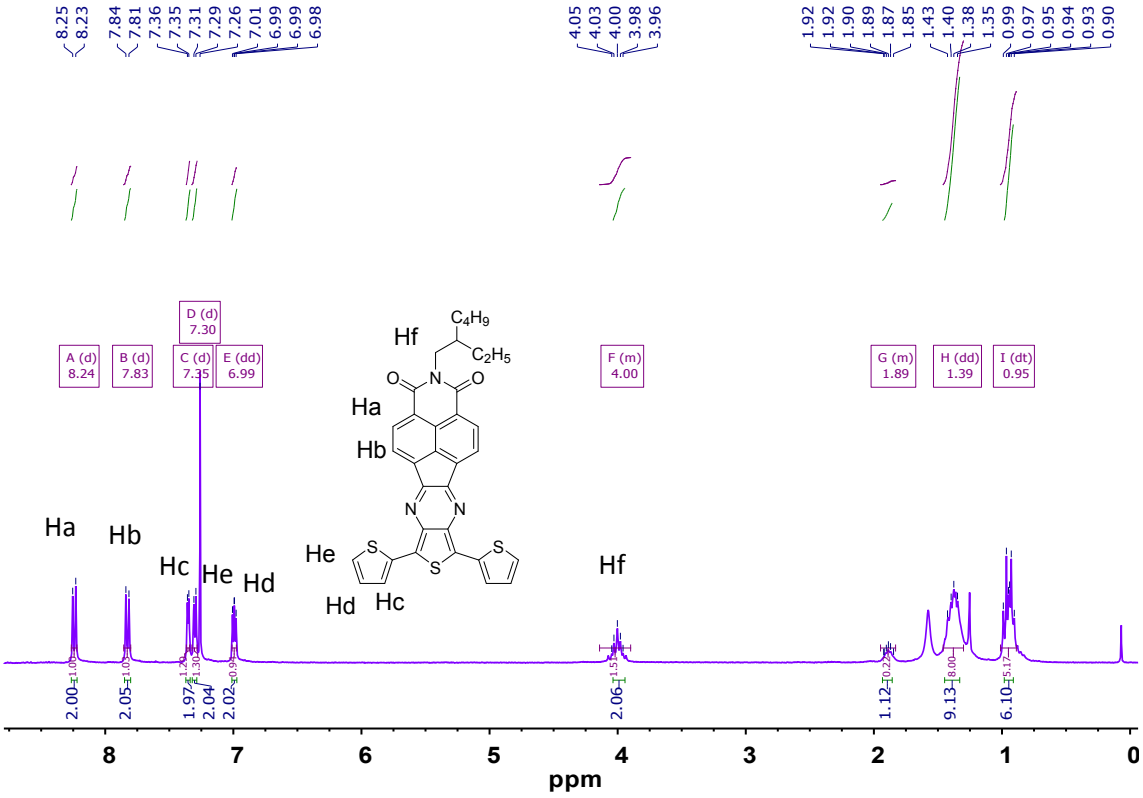


**Figure S5** $^{1}$H-NMR spectrum of **NIPa3T** in $CDCl_3$.

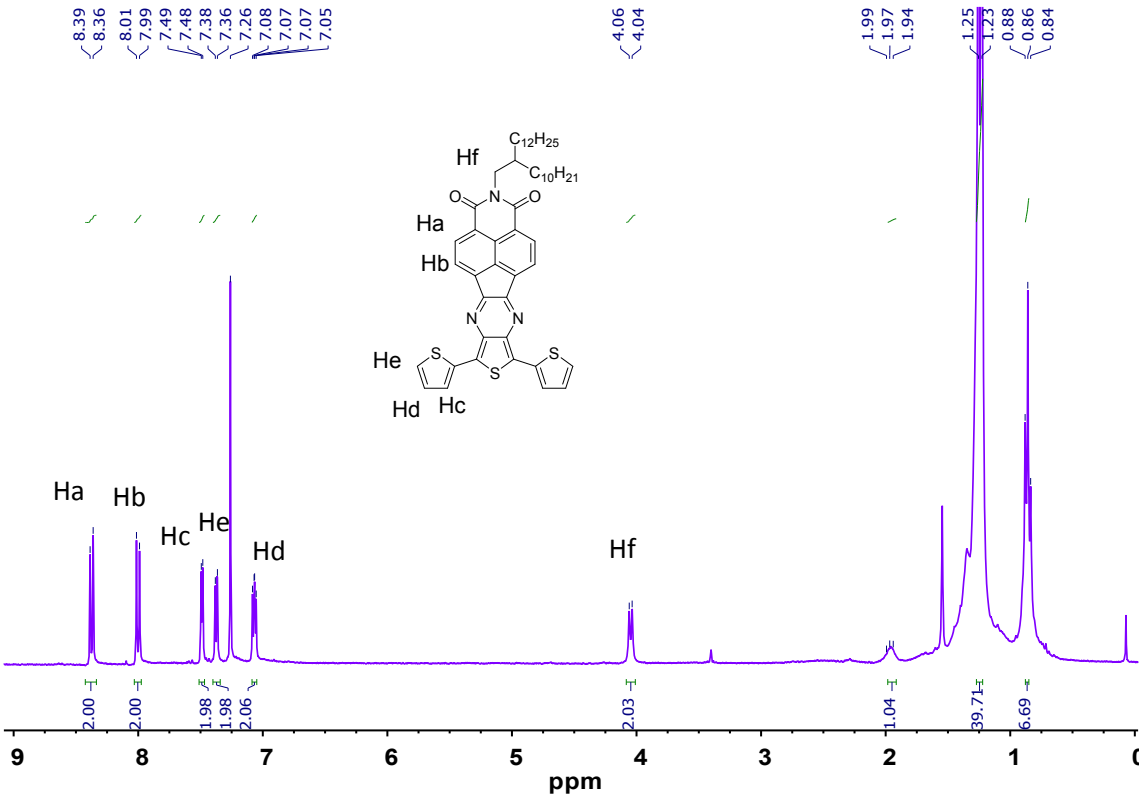


**Figure S6** $^{1}$H-NMR spectrum of **NIPb3T** in $CDCl_3$.

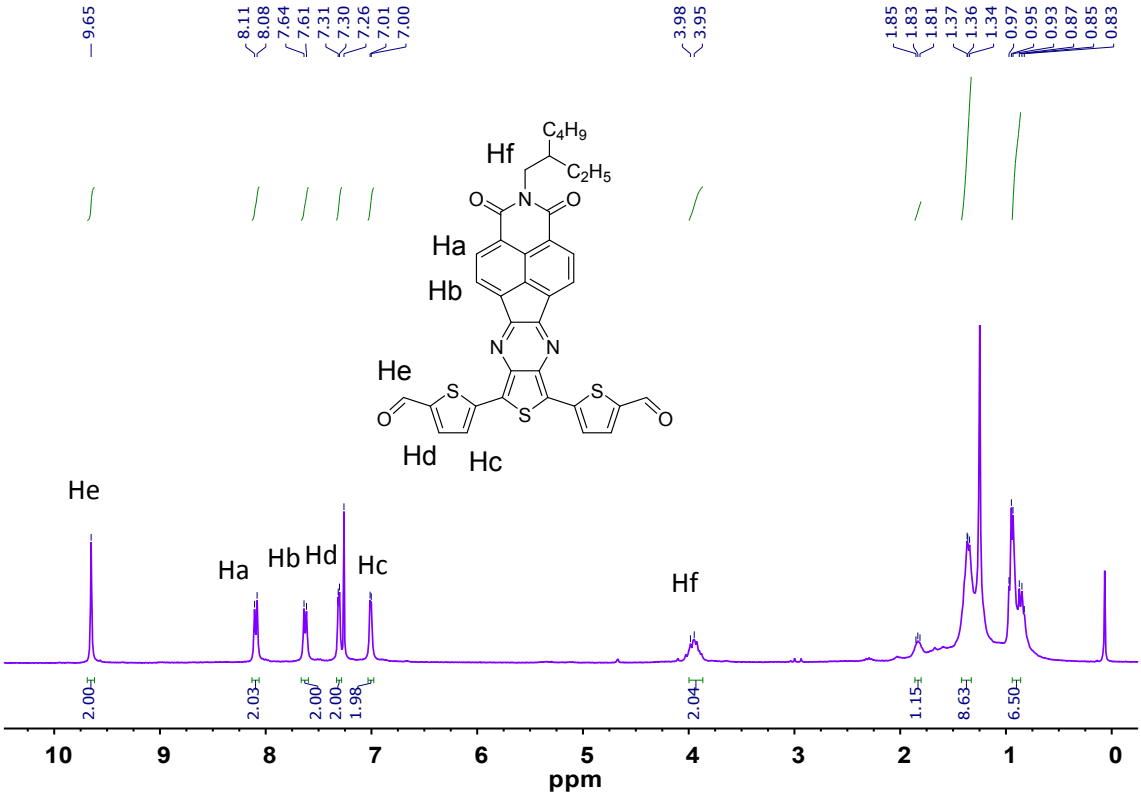


**Figure S7** $^{1}$H-NMR spectrum of **NIPa3T-CHO** in $CDCl_3$.

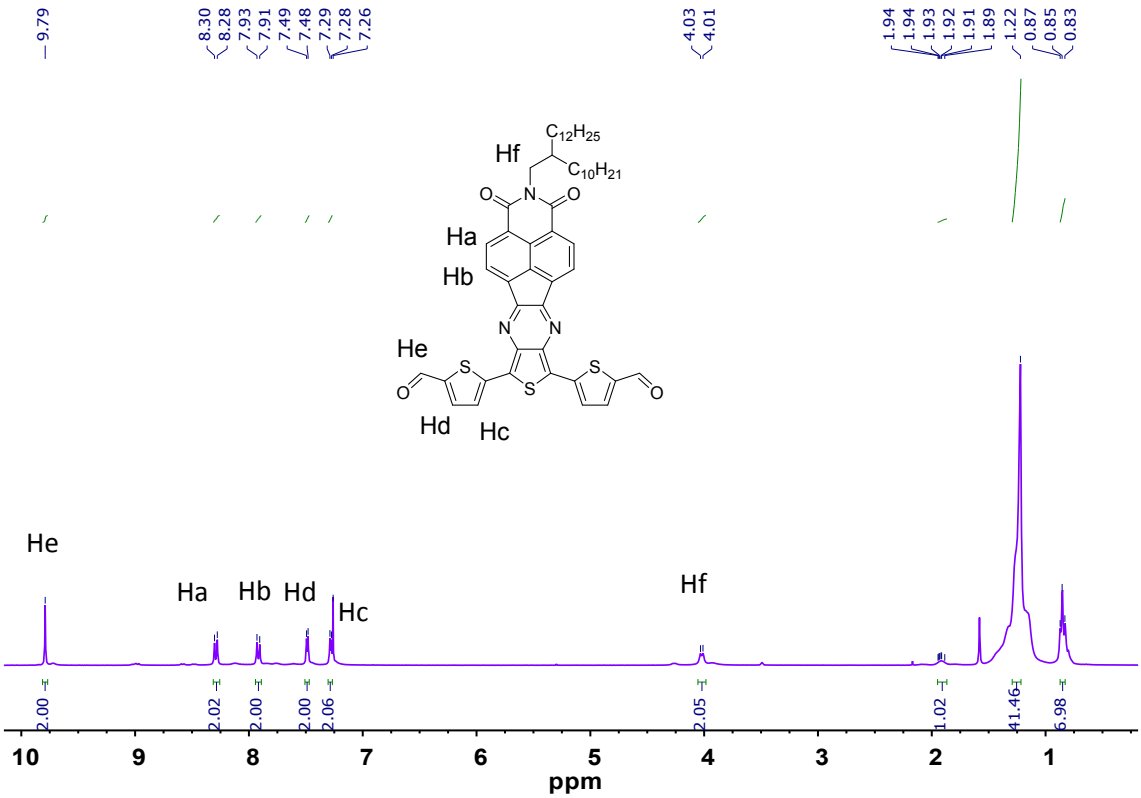


**Figure S8** $^{1}$H-NMR spectrum of **NIPb3T-CHO** in $CDCl_3$.

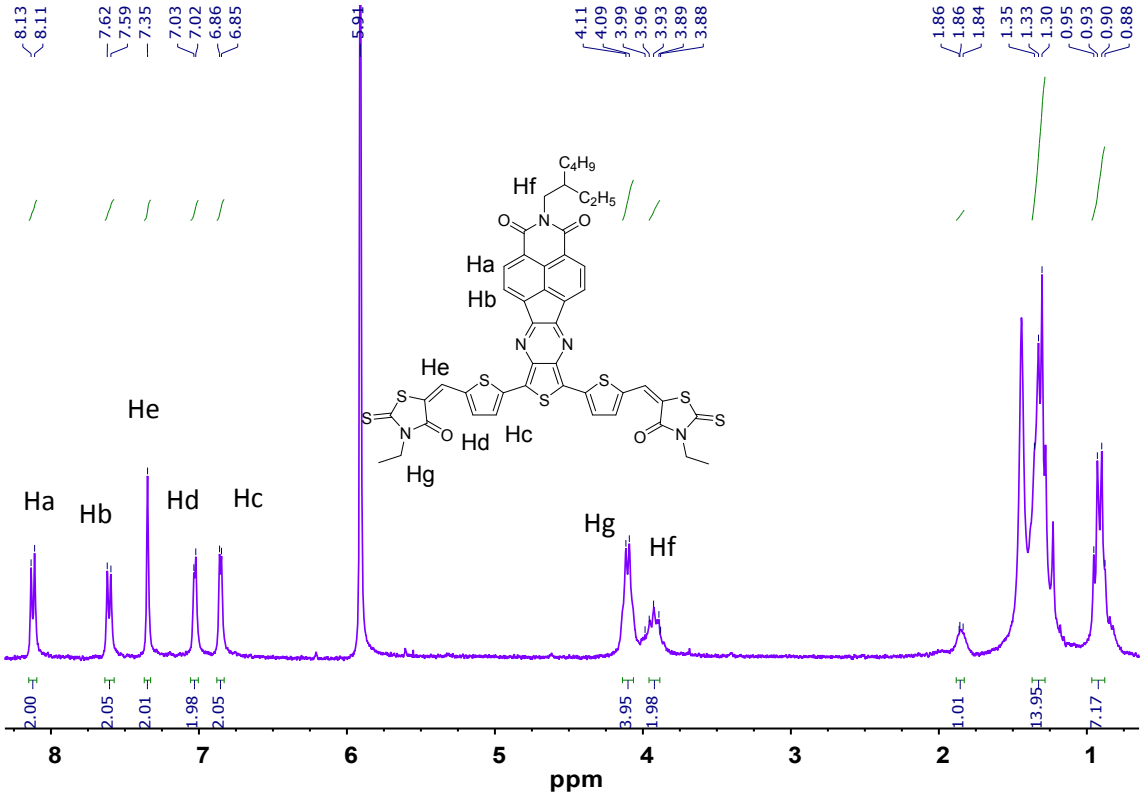


**Figure S9** $^1$H-NMR spectrum of **NIPa3T-Rd** in $C_2D_2Cl_4$ at 343 K.

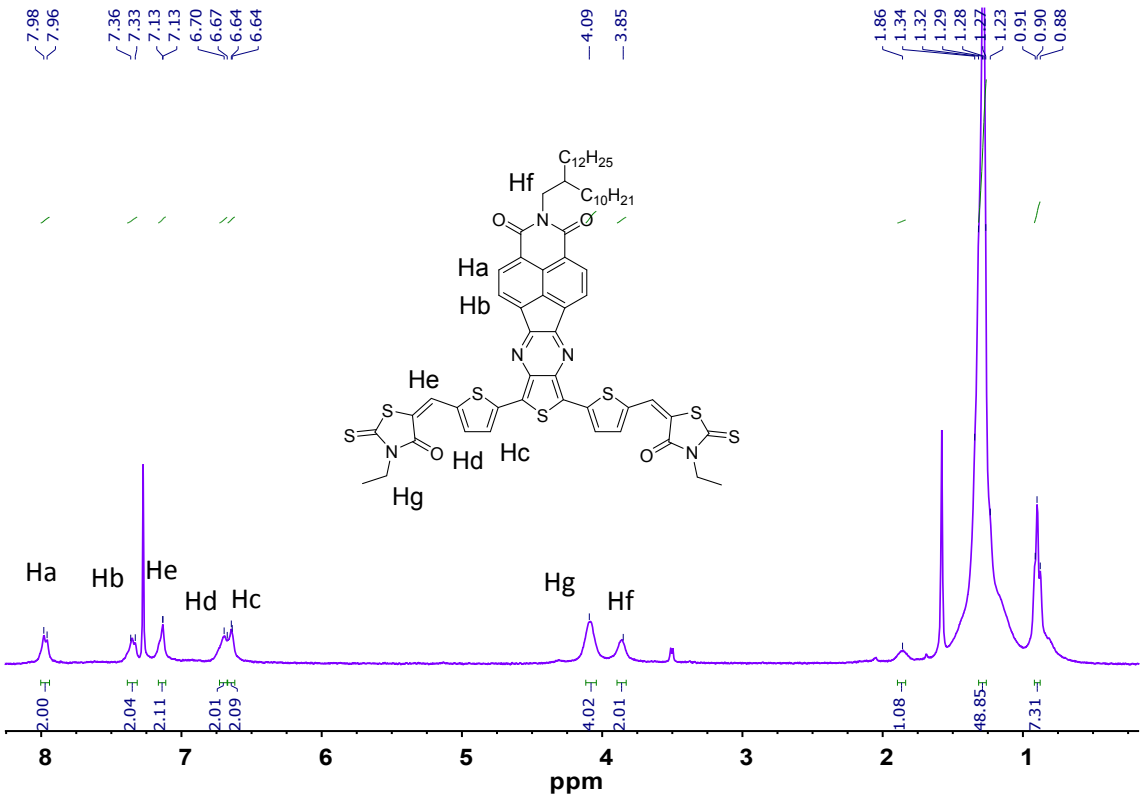


**Figure S10** $^1$H-NMR spectrum of **NIPb3T-Rd** in $CDCl_3$.

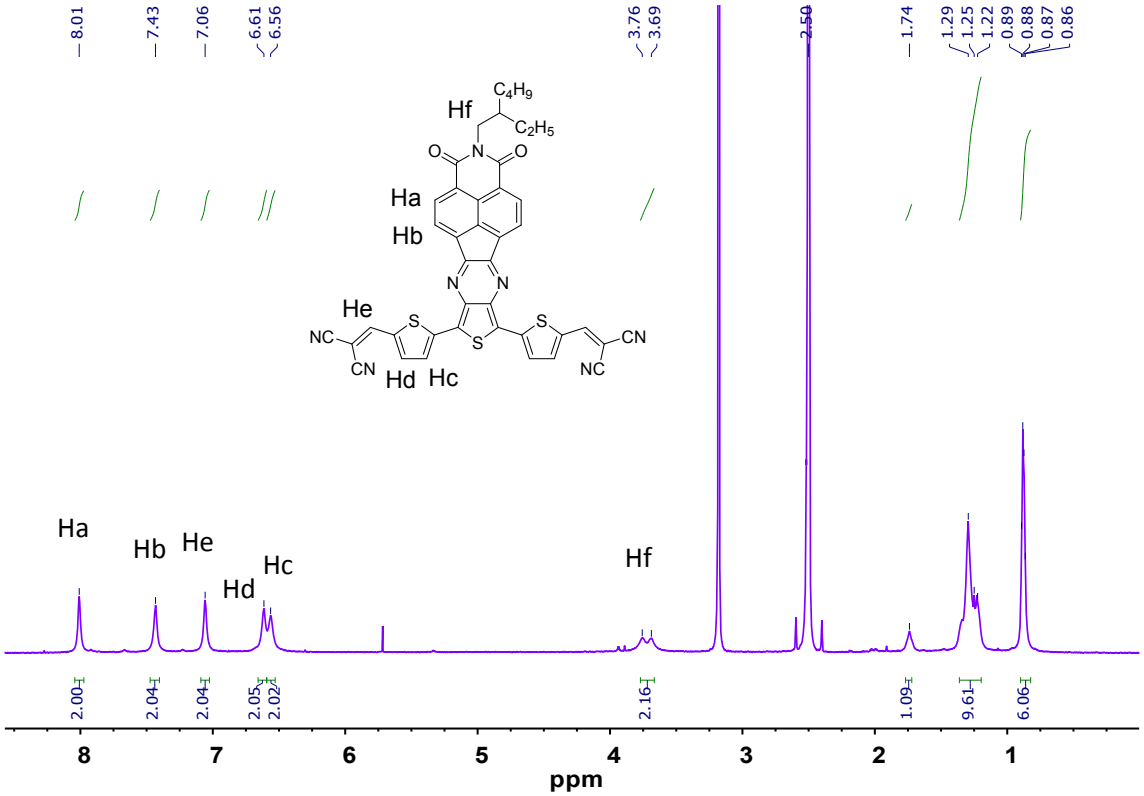


**Figure S11** $^{1}$H-NMR spectrum of **NIPa3T-DCV** in DMSO-$d_6$ at 343 K.

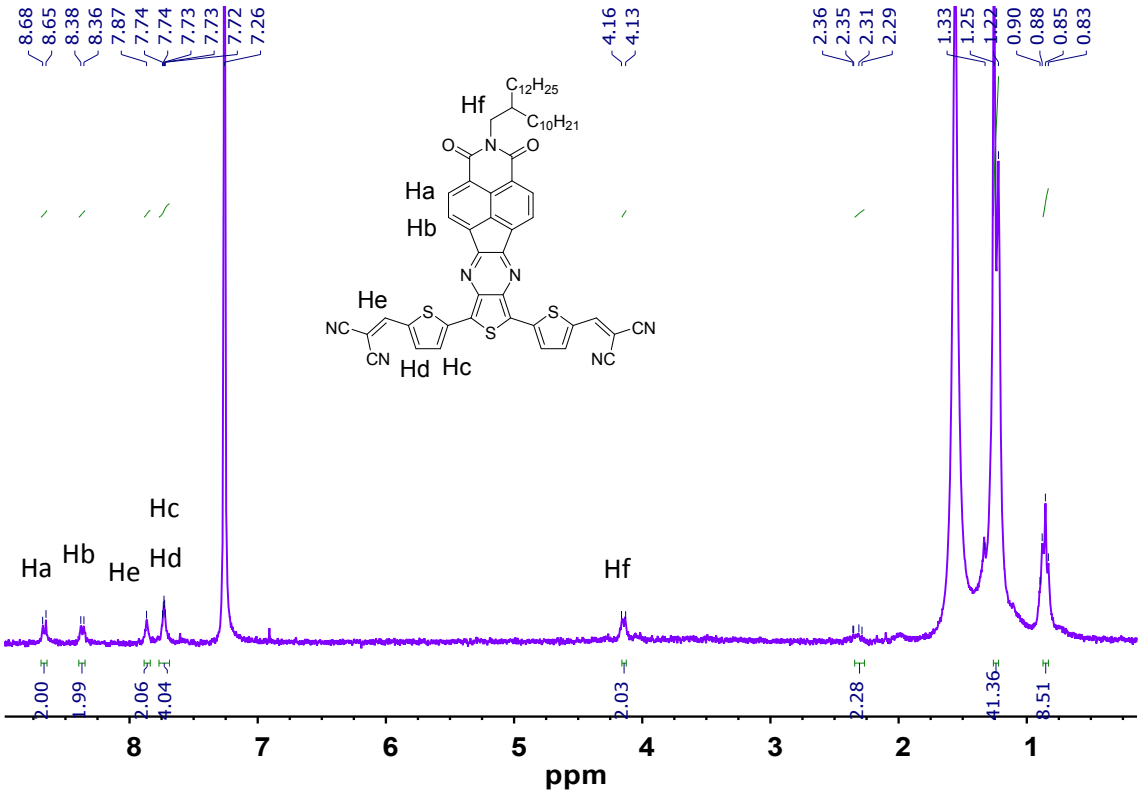


**Figure S12** $^{1}$H-NMR spectrum of **NIPb3T-DCV** in $CDCl_3$.

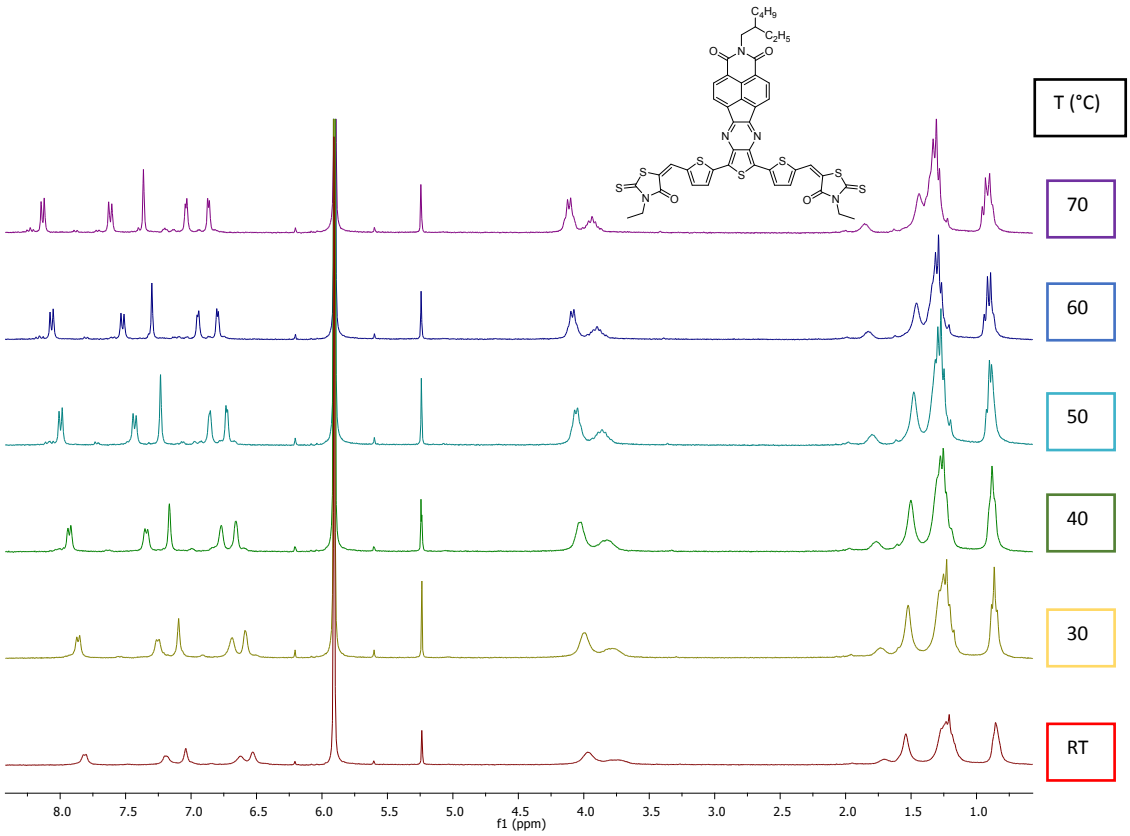


**Figure S13** $^{1}$H-NMR temperature dependent experiment spectrum of **NIPa3T-Rd** in $C_2D_2Cl_4$.

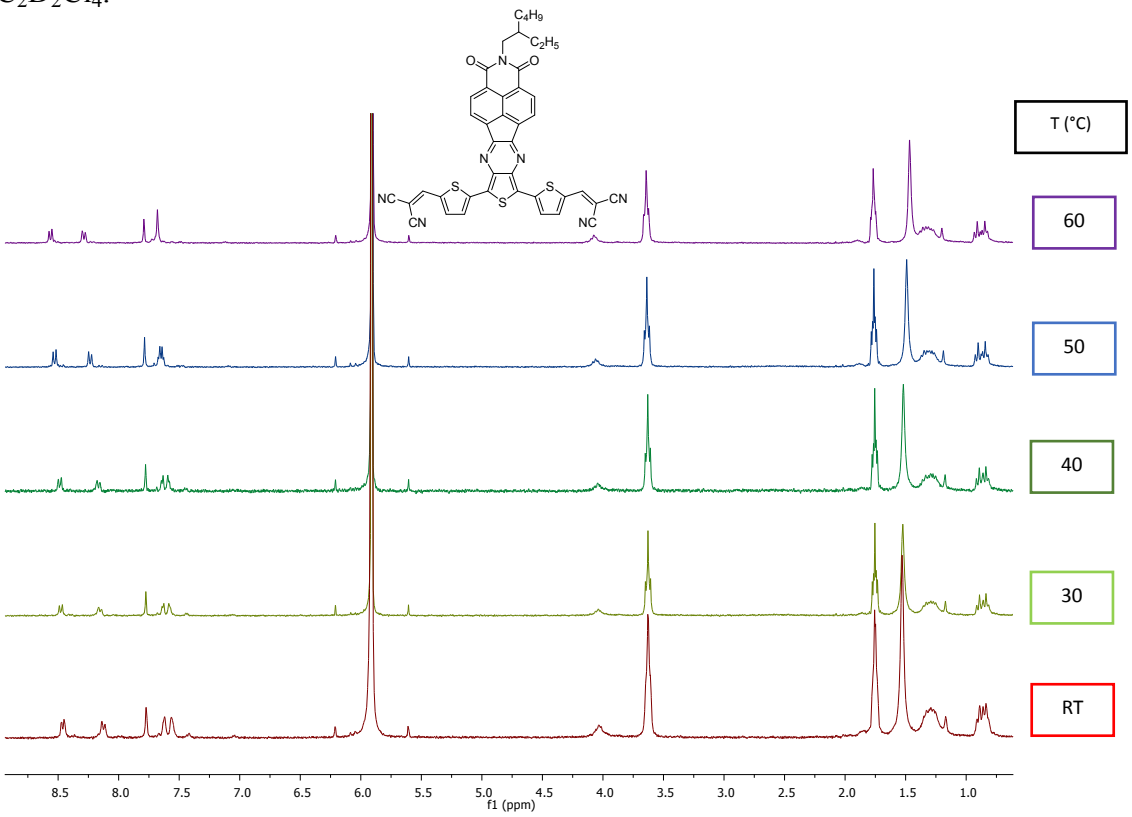


**Figure S14** $^{1}$H-NMR temperature dependent experiment spectrum of **NIPa3T-DCV** in $C_2D_2Cl_4$.

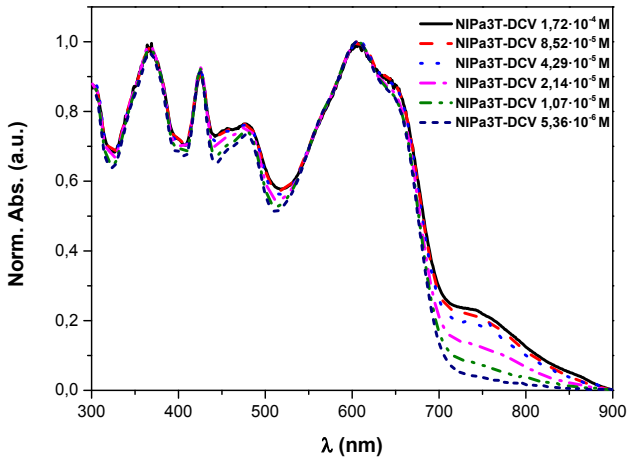


**Figure S15** UV-Vis concentration dependent experiment of **NIPa3T-DCV** in $CDCl_3$.

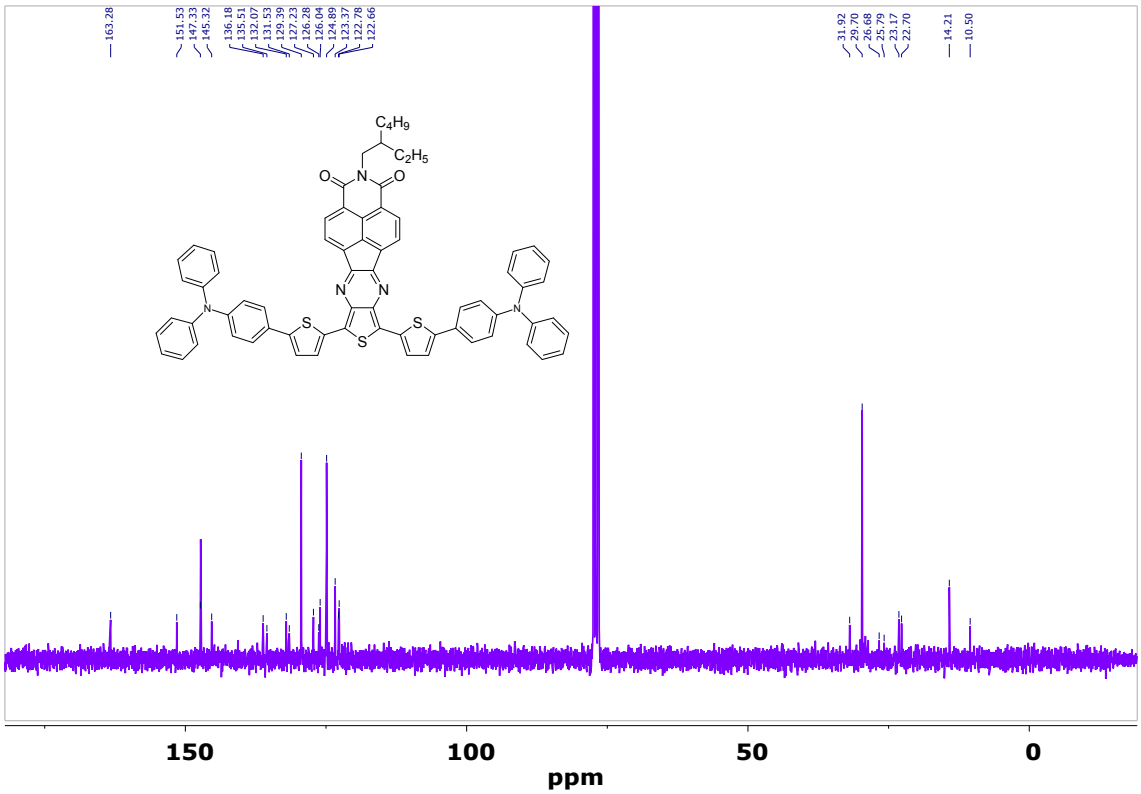


**Figure S16** $^{13}$C-NMR spectrum of **NIPa3T-TA** in $CDCl_3$.

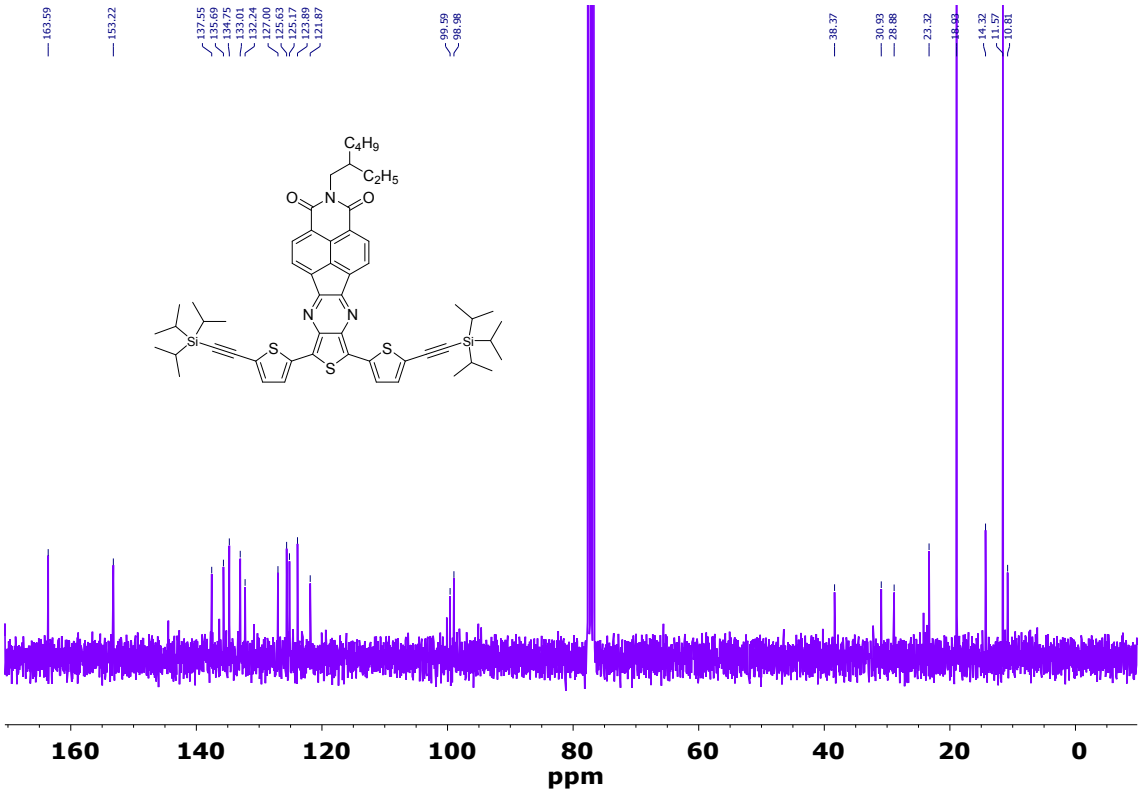


**Figure S17** $^{13}$C-NMR spectrum of **NIPa3T-TIPS** in $CDCl_3$.

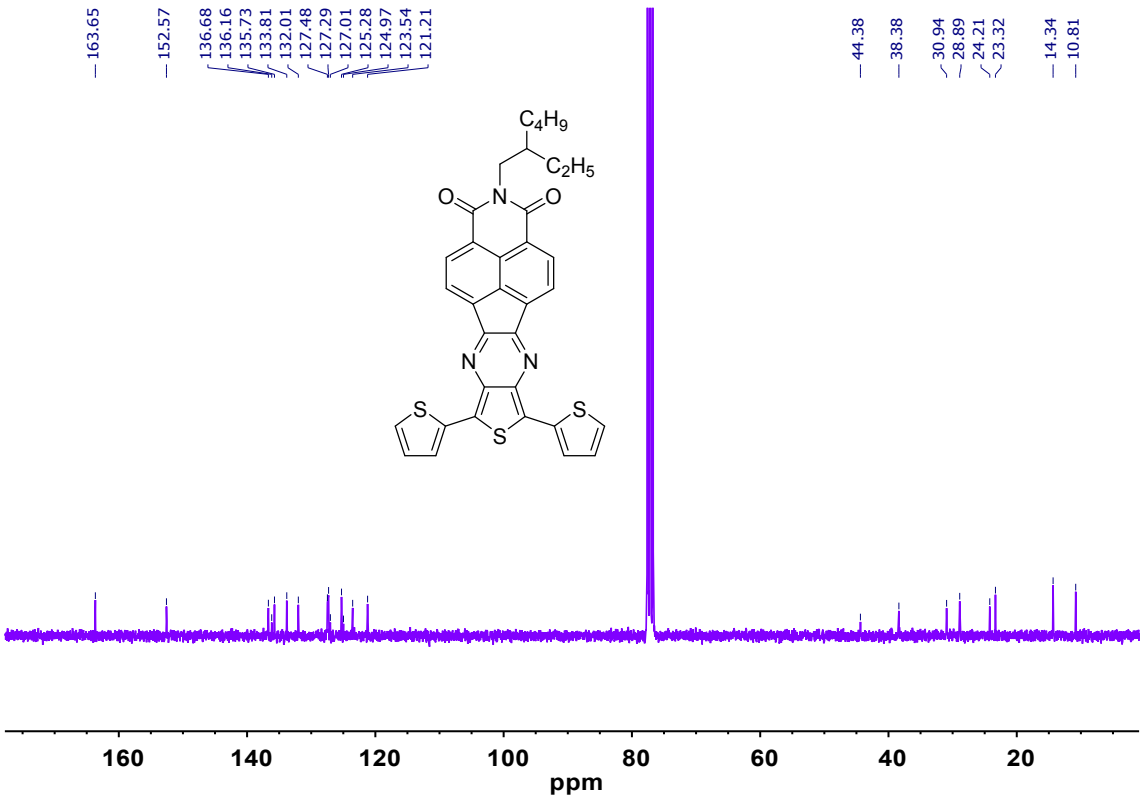


**Figure S18** $^{13}$C-NMR spectrum of **NIPa3T** in $CDCl_3$.

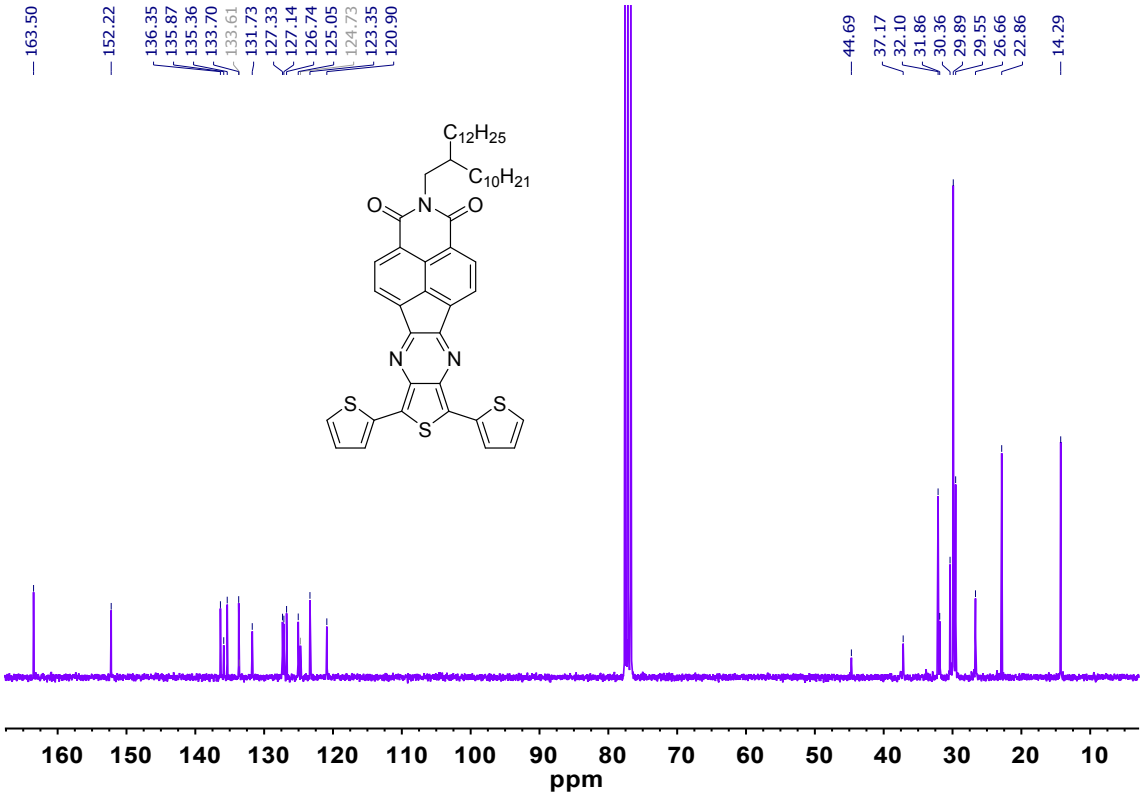


**Figure S19** $^{13}$C-NMR spectrum of **NIPb3T** in $CDCl_3$.

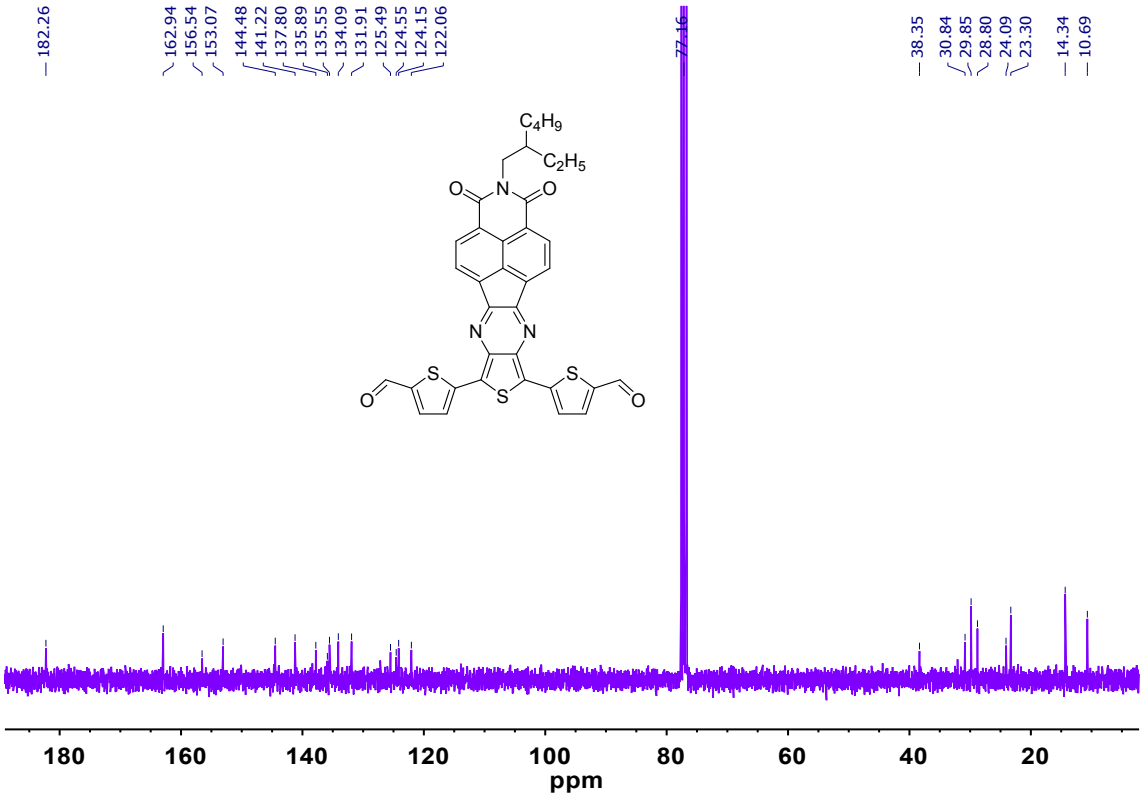


**Figure S20** $^{13}$C-NMR spectrum of **NIPa3T-CHO** in $CDCl_3$.

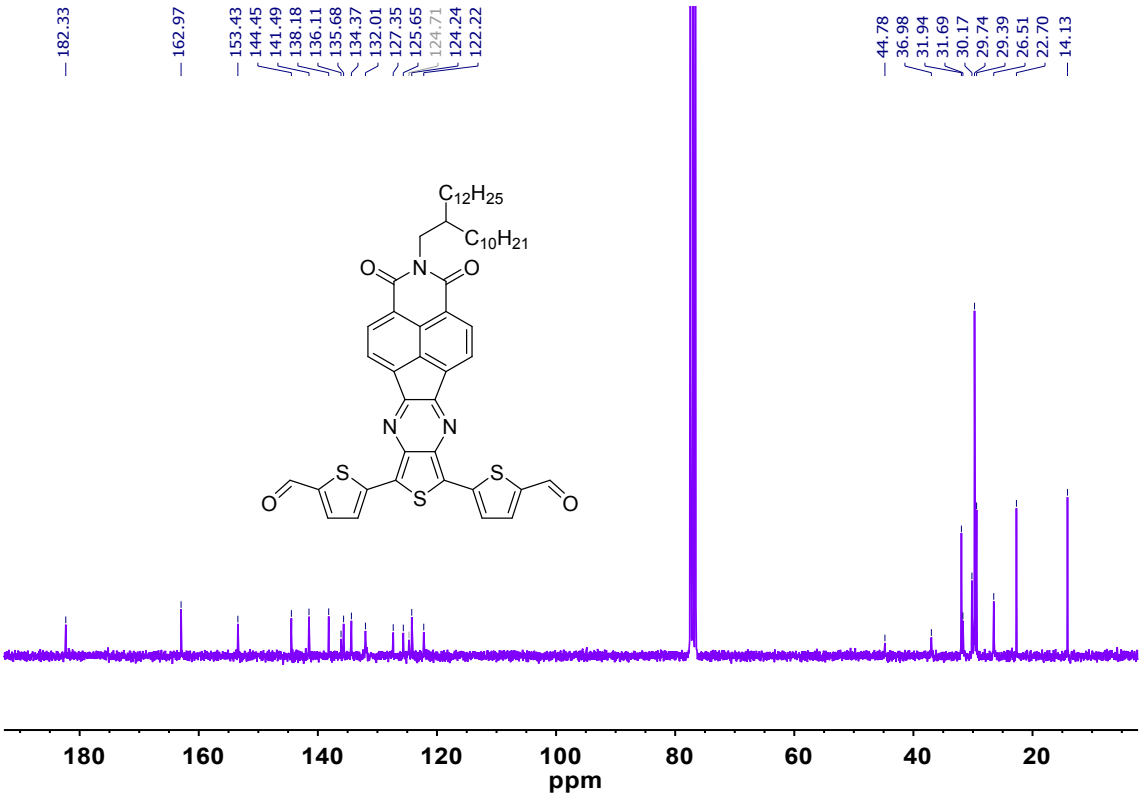


**Figure S21** $^{13}$C-NMR spectrum of **NIPb3T-CHO** in $CDCl_3$.

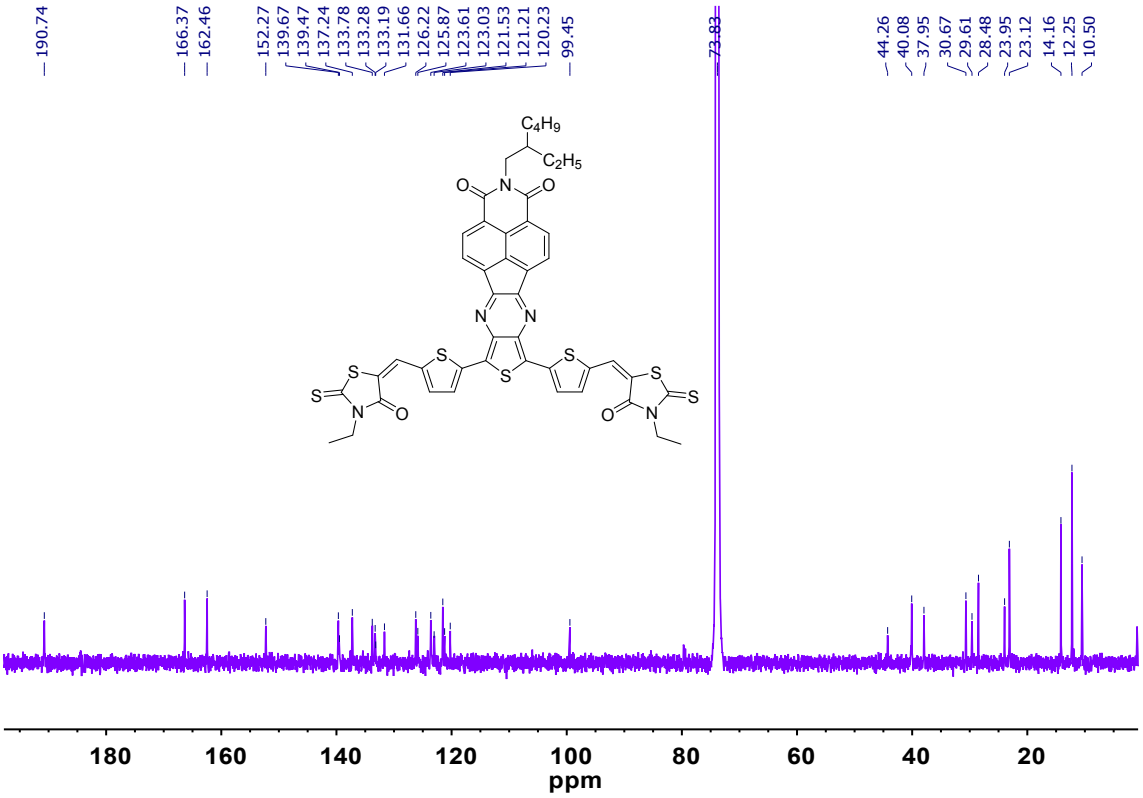


**Figure S22** $^{13}$C-NMR spectrum of **NIPa3T-Rd** in $C_2D_2Cl_4$.

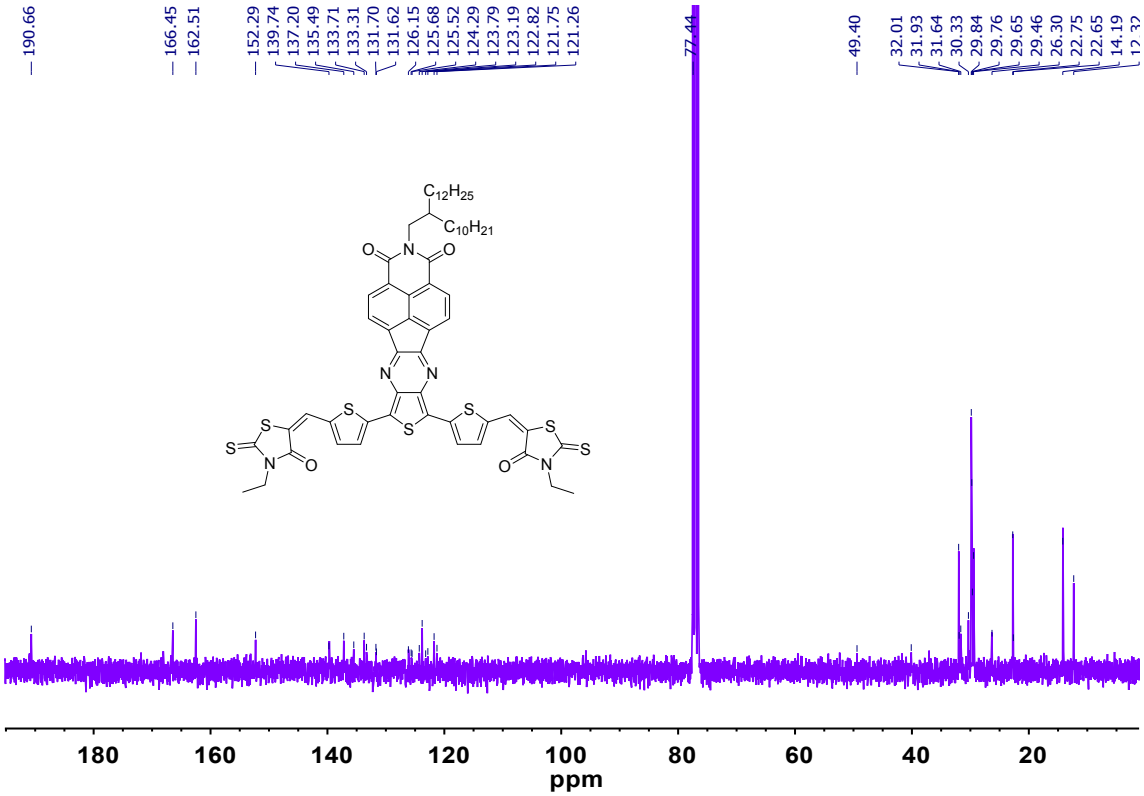


**Figure S23** $^{13}$C-NMR spectrum of **NIPb3T-Rd** in $CDCl_3$.

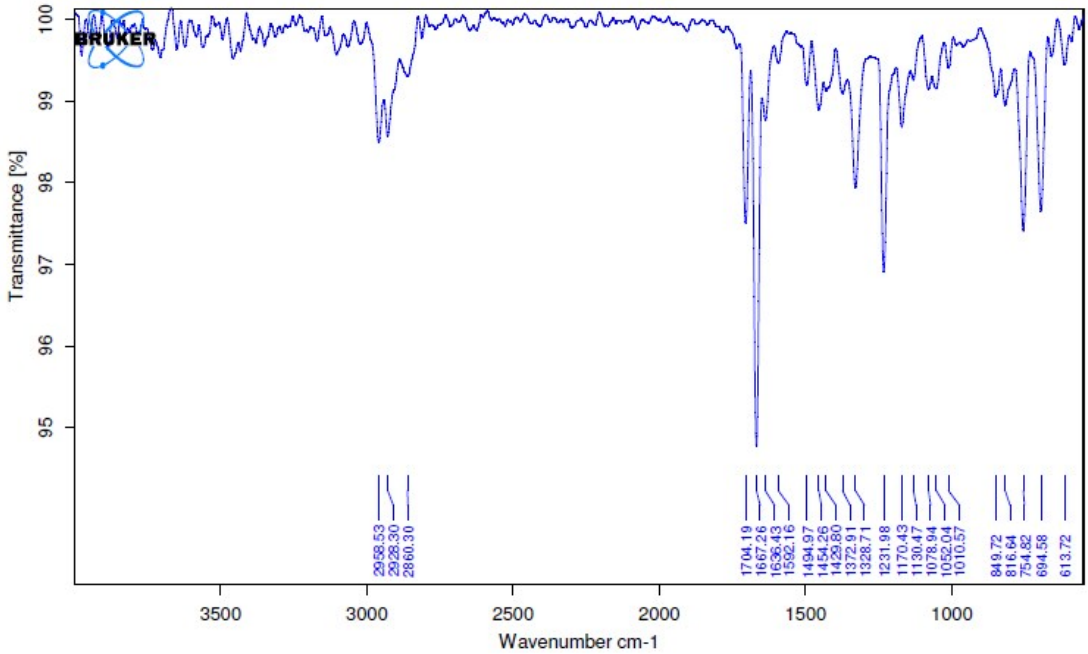


**Figure S24** IR spectrum of **NIPa3T-Br**.

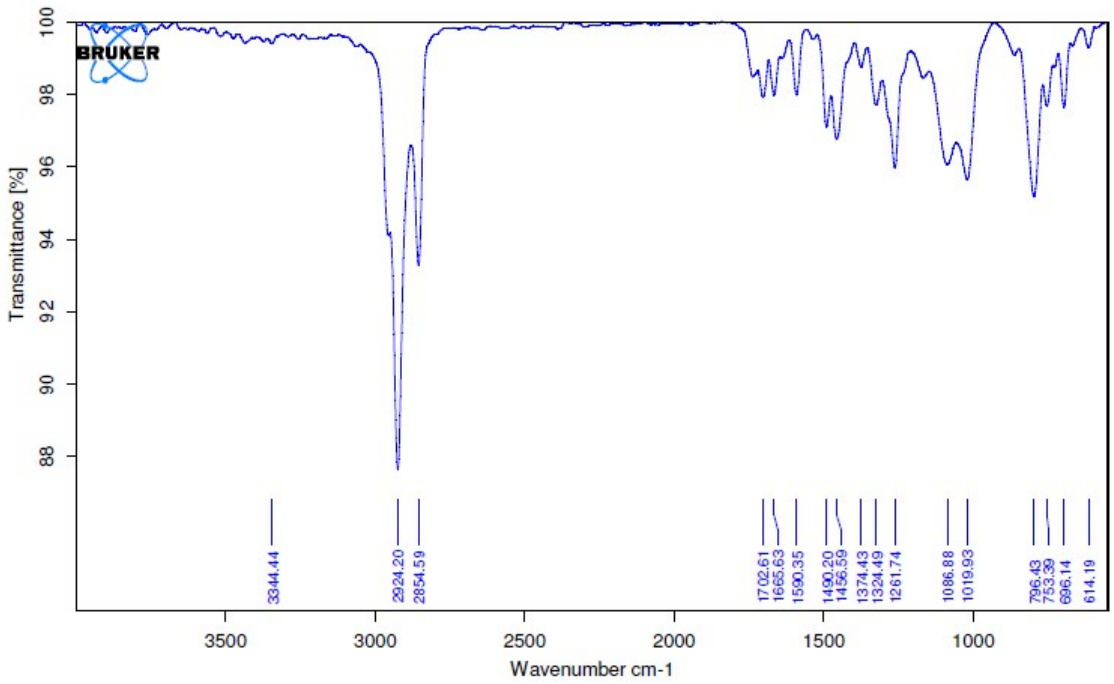


**Figure S25** IR spectrum of **NIPa3T-TA**.

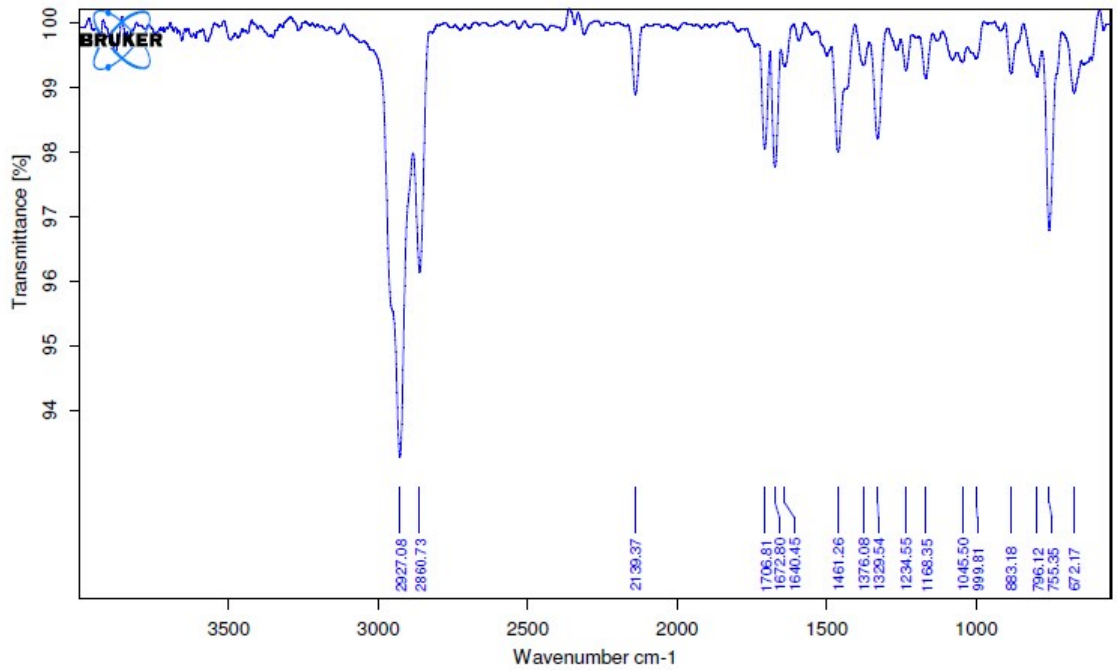


**Figure S26** IR spectrum of **NIPa3T-TIPS**.

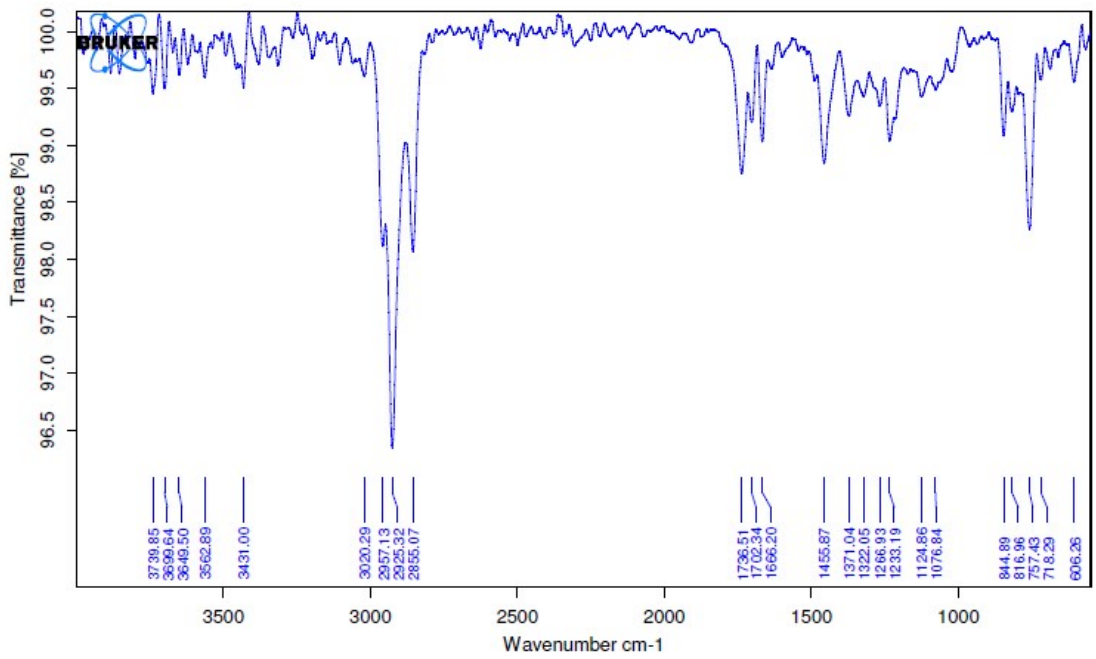


**Figure S27** IR spectrum of **NIPa3T-Py**.

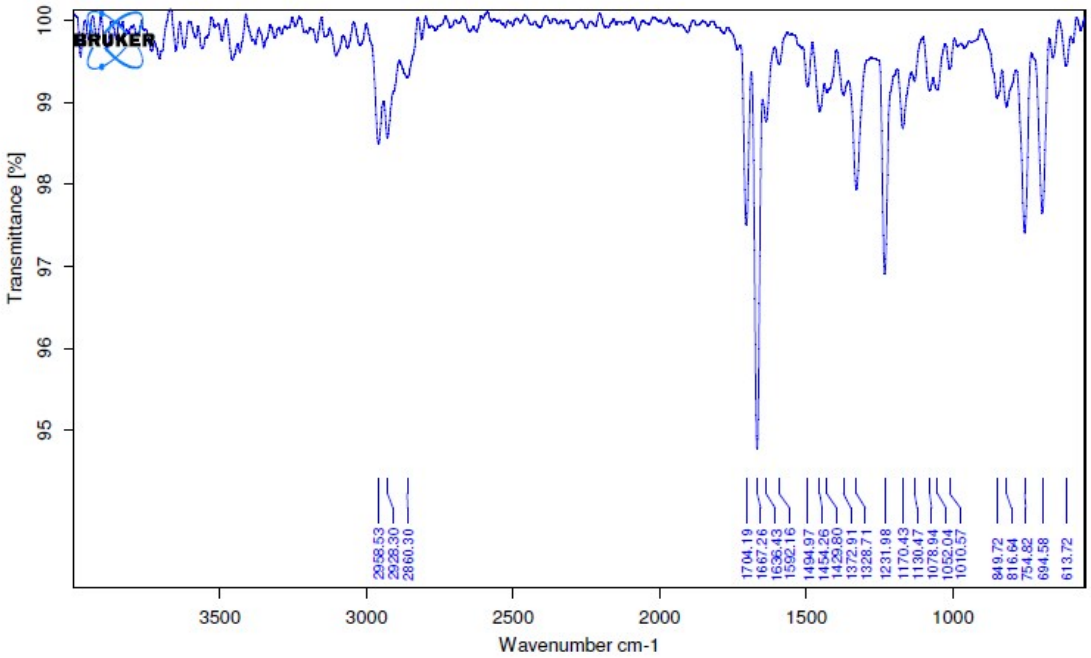


**Figure S28** IR spectrum of **NIPa3T**.

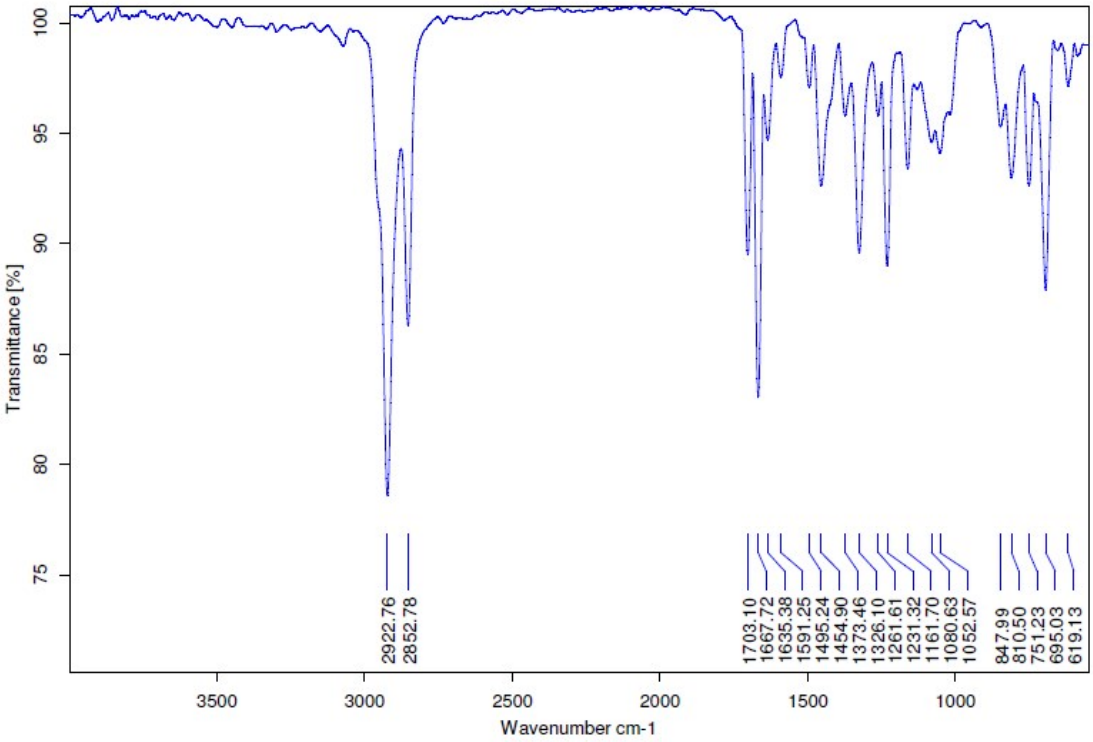


**Figure S29** IR spectrum of **NIPb3T**.

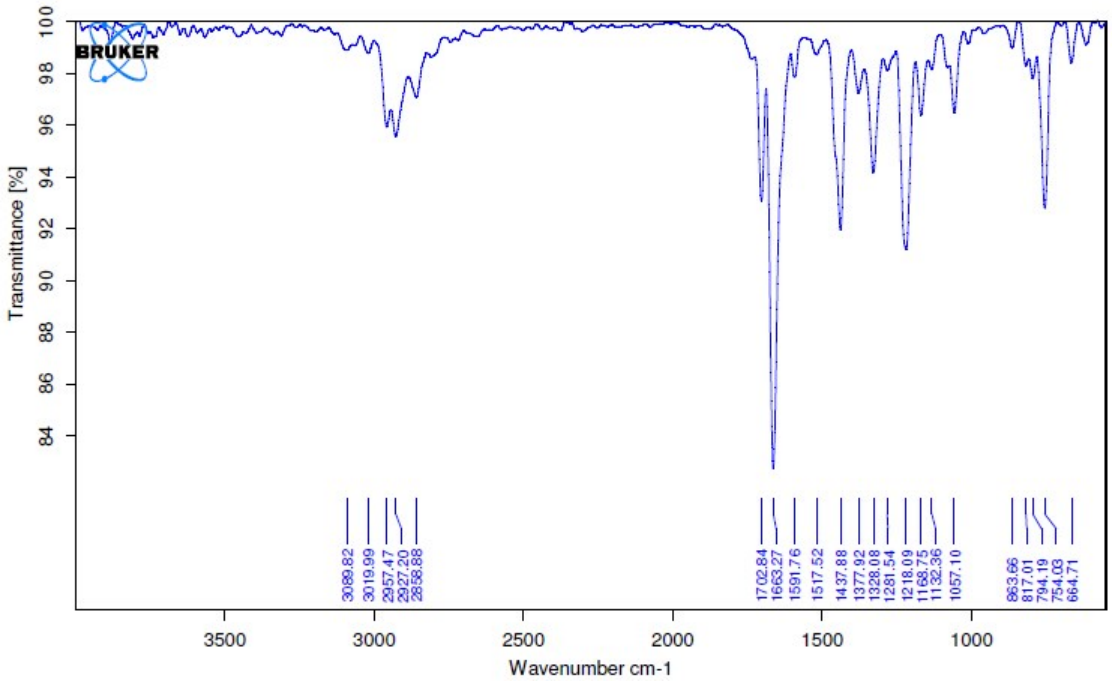


**Figure S30** IR spectrum of **NIPa3T-CHO**.

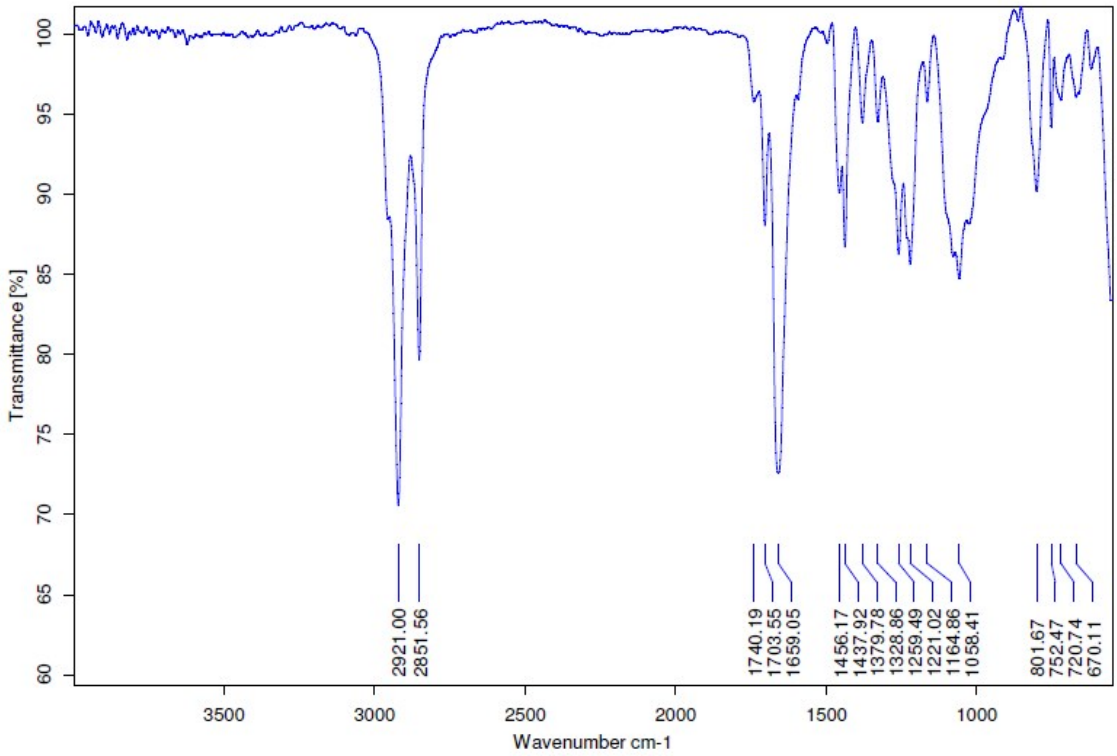


**Figure S31** IR spectrum of **NIPb3T-CHO**.

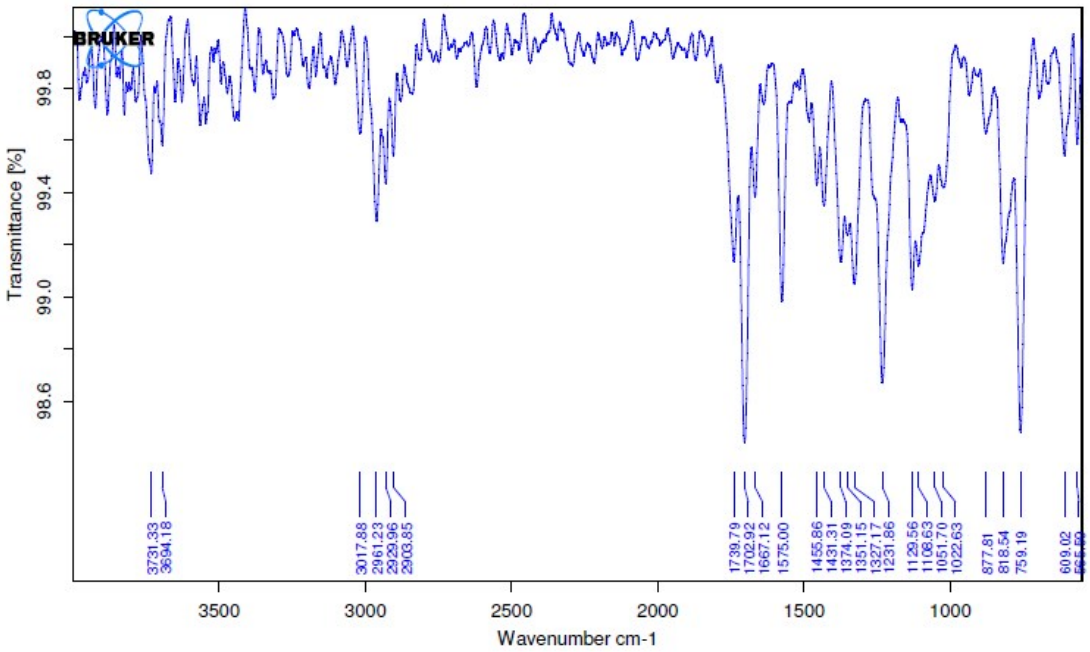


**Figure S32** IR spectrum of **NIPa3T-Rd**.

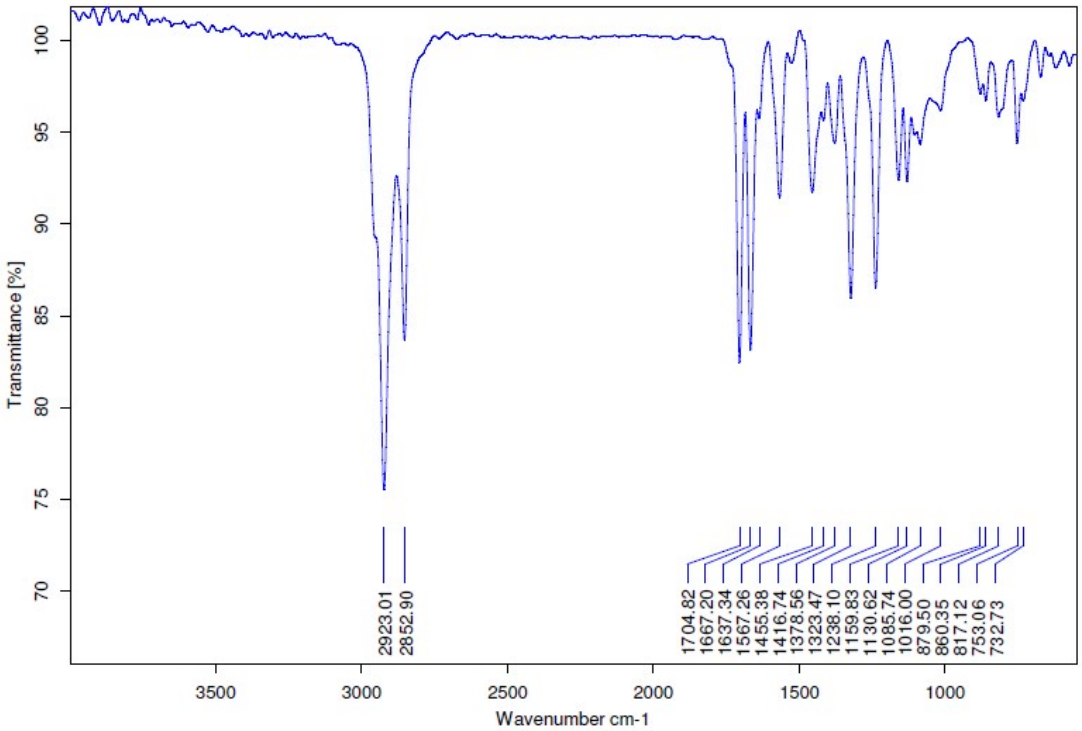


**Figure S33** IR spectrum of **NIPb3T-Rd**.

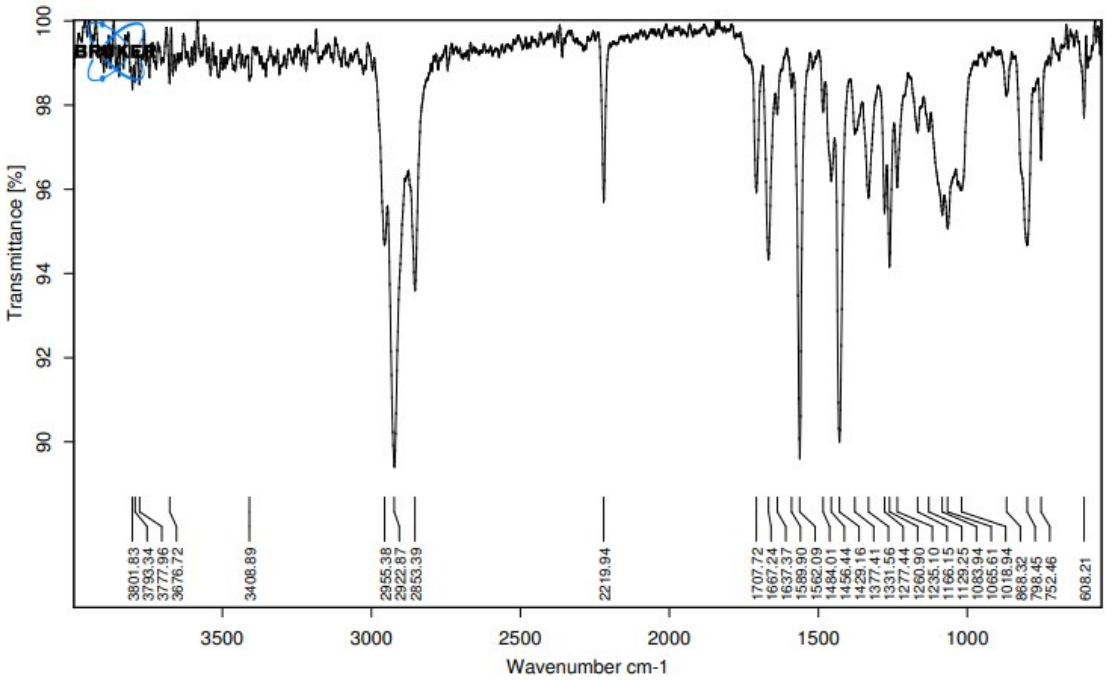


**Figure S34** IR spectrum of **NIPa3T-DCV**.

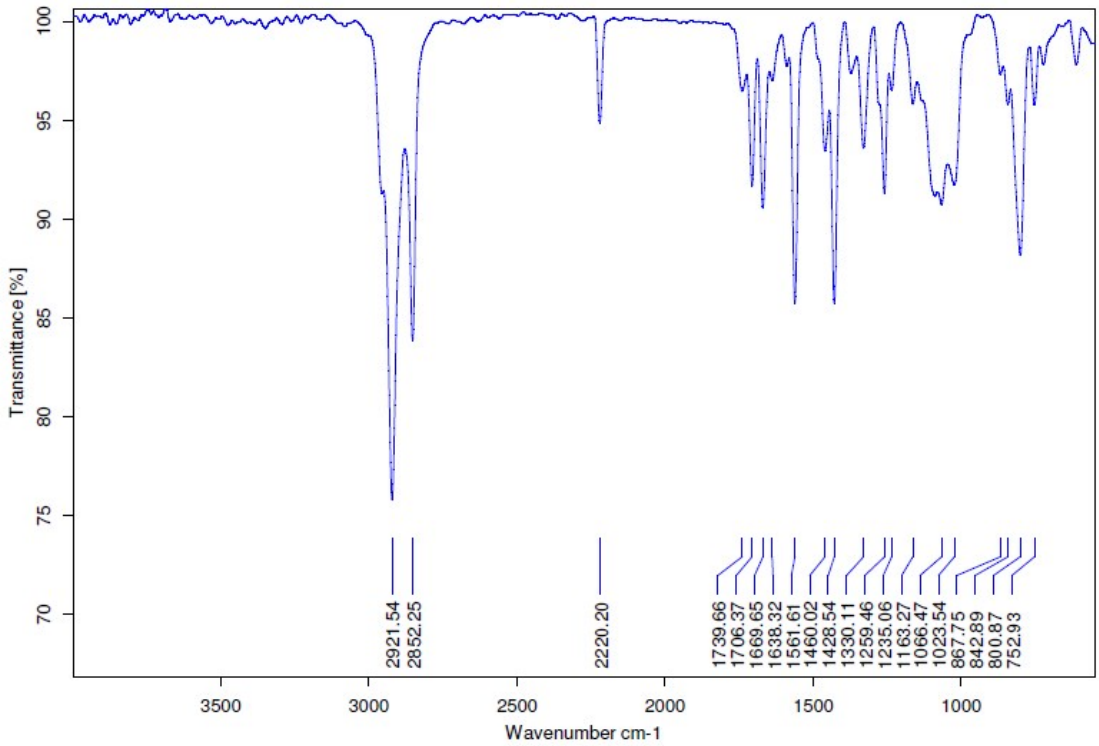


**Figure S35** IR spectrum of **NIPb3T-DCV**.

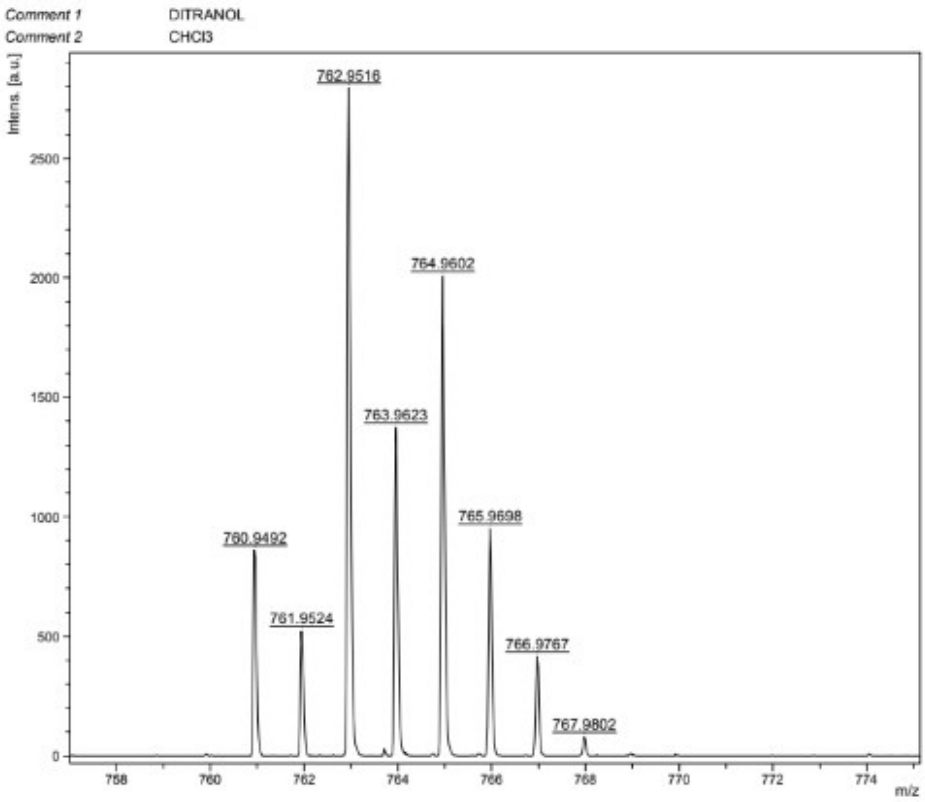


**Figure S36** MALDI-HRMS (m/z) spectrum of **NIPa3T-Br**.

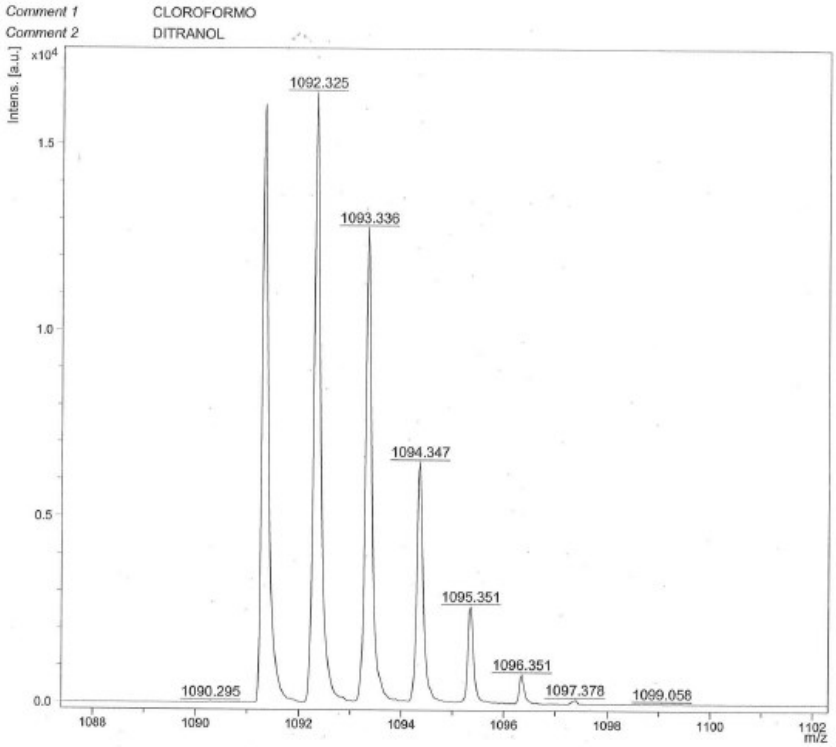


**Figure S37** MALDI-HRMS (m/z) spectrum of **NIPa3T-TA**.

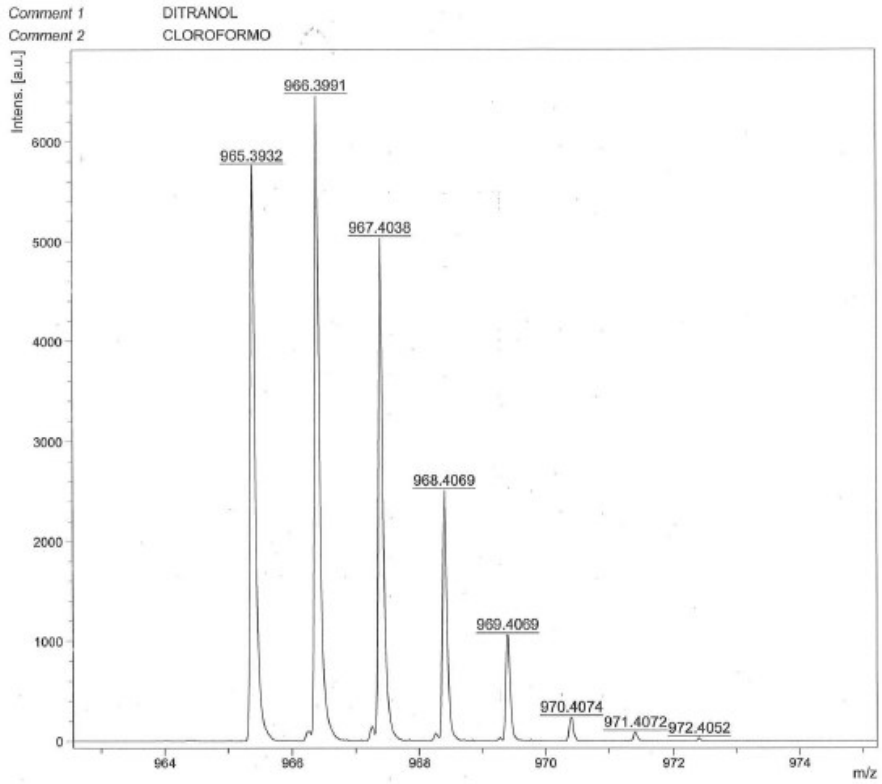


**Figure S38** MALDI-HRMS (m/z) spectrum of **NIPa3T-TIPS**.

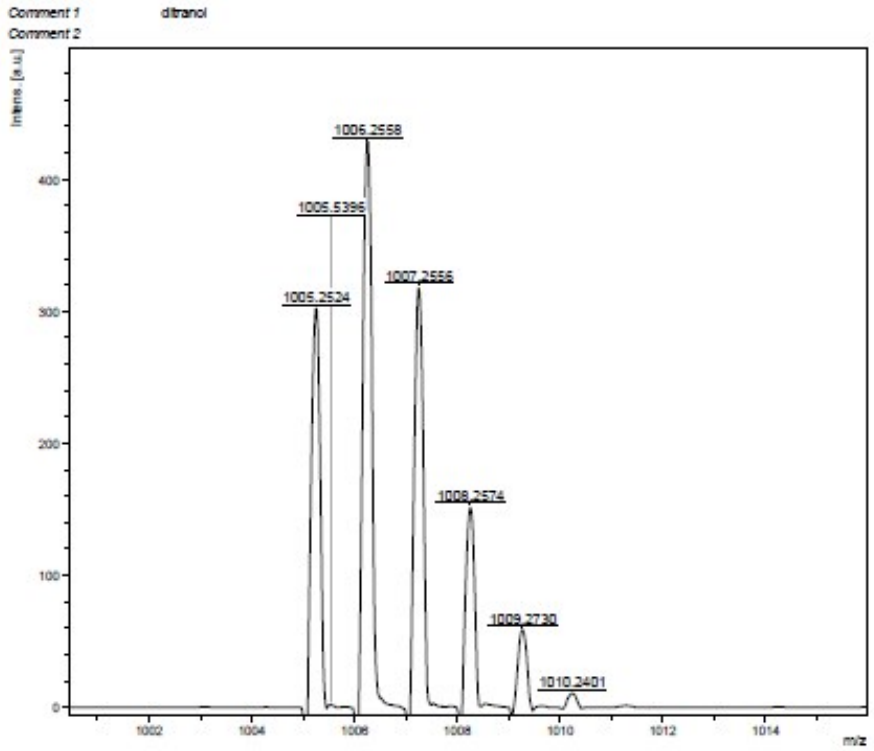


**Figure S39** MALDI-HRMS (m/z) spectrum of **NIPa3T-Py**.

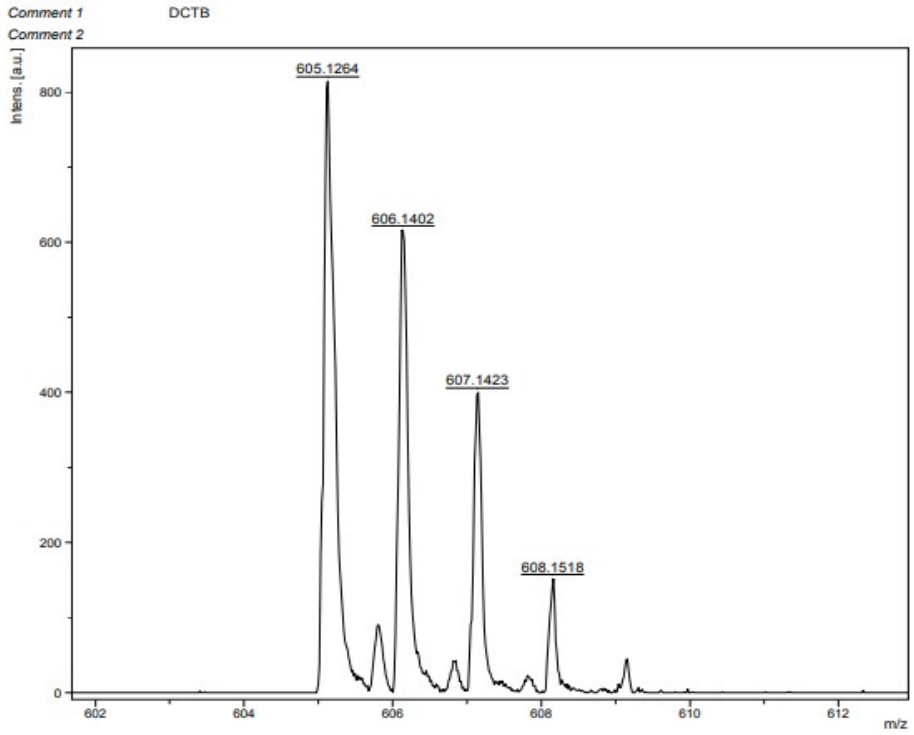


**Figure S40** MALDI-HRMS (m/z) spectrum of **NIPa3T**.

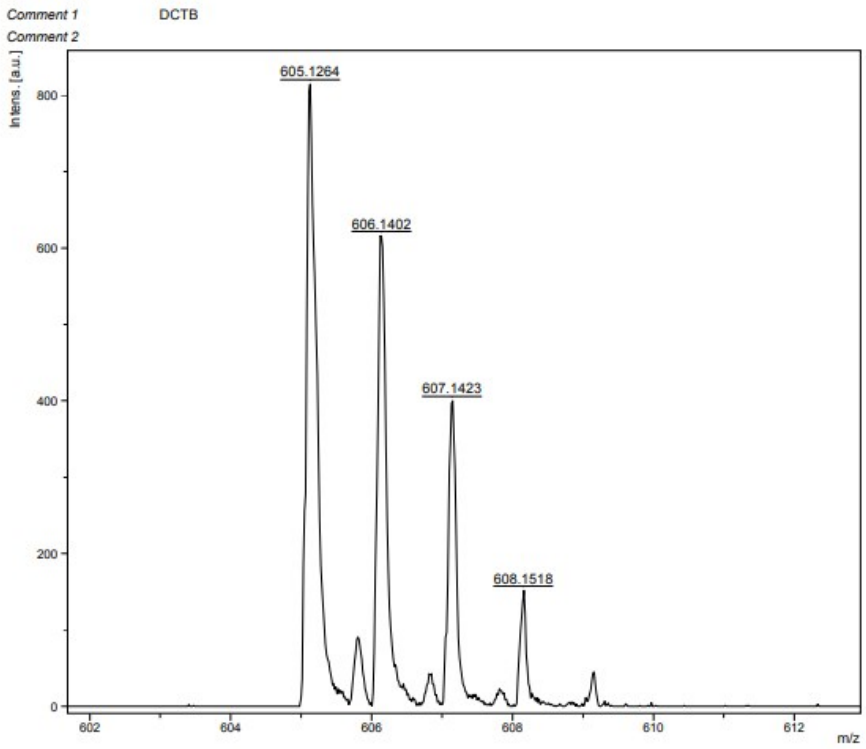


**Figure S41** MALDI-HRMS (m/z) spectrum of **NIPb3T**.

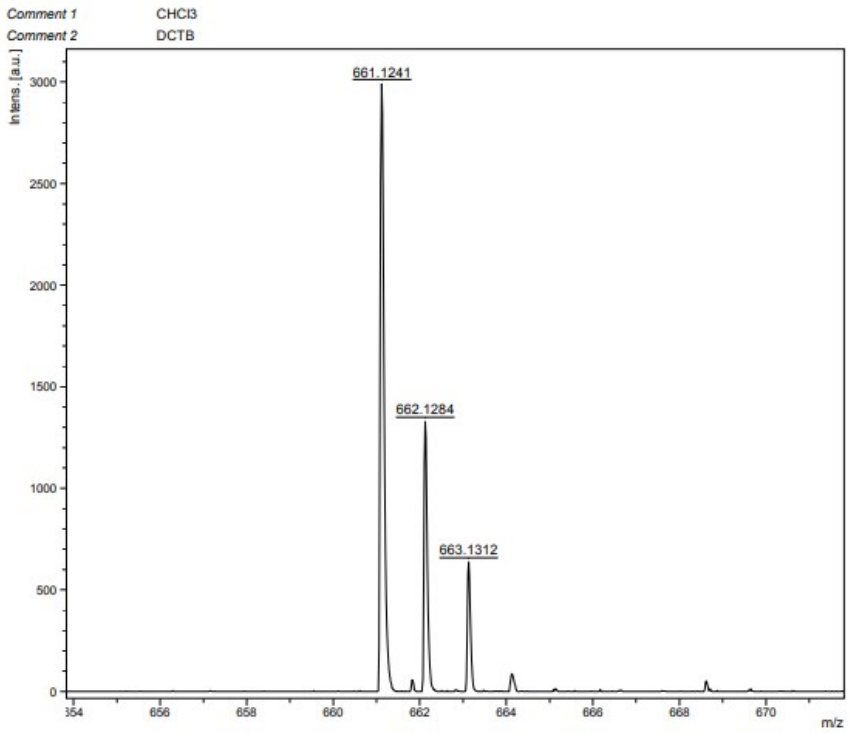


**Figure S42** MALDI-HRMS (m/z) spectrum of **NIPa3T-CHO**.

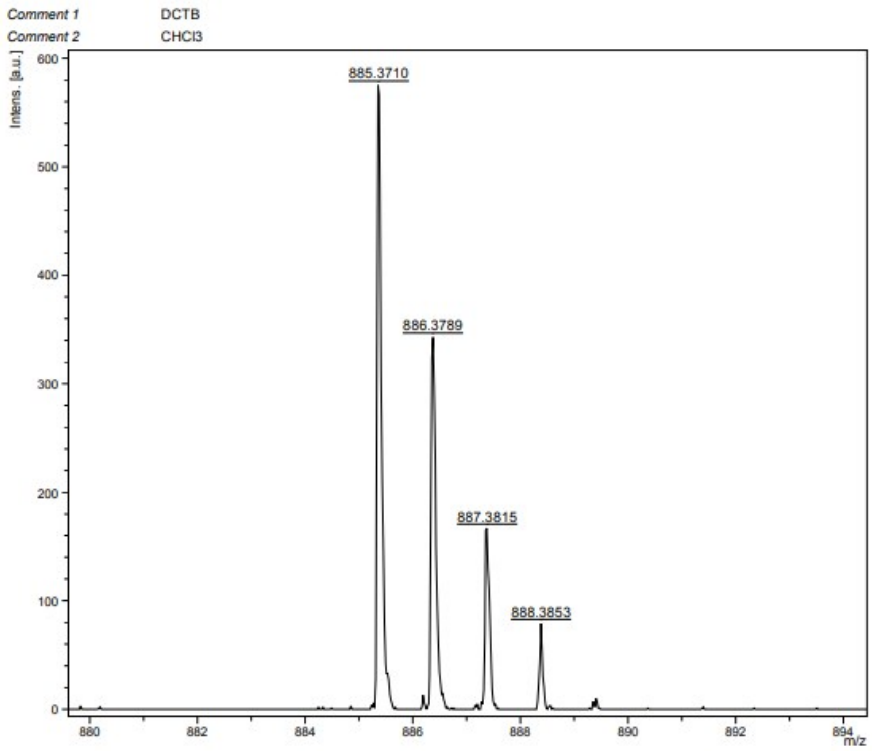


**Figure S43** MALDI-HRMS (m/z) spectrum of **NIPb3T-CHO**.

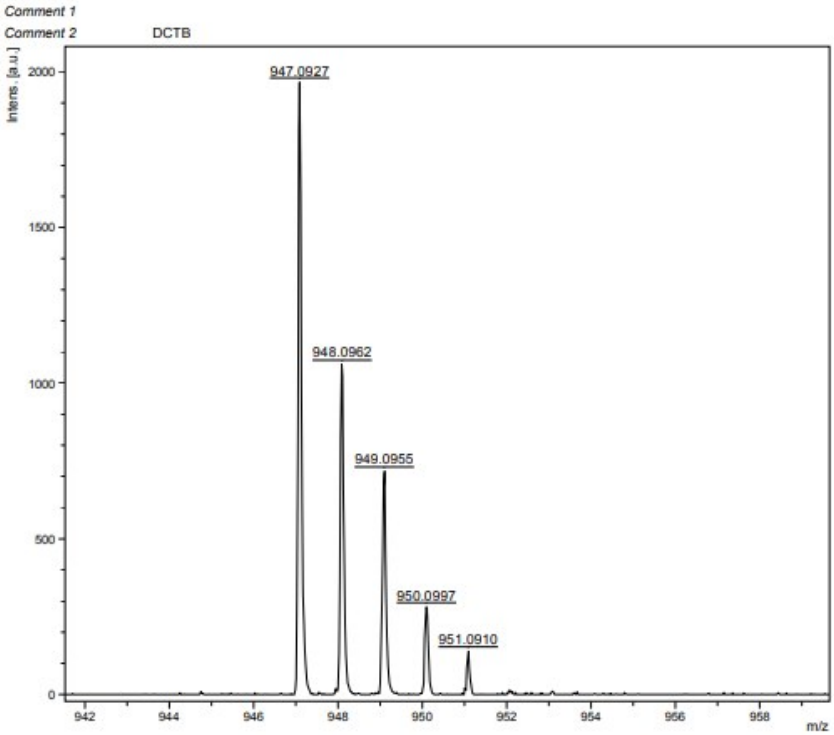


**Figure S44** MALDI-HRMS (m/z) spectrum of **NIPa3T-Rd.**

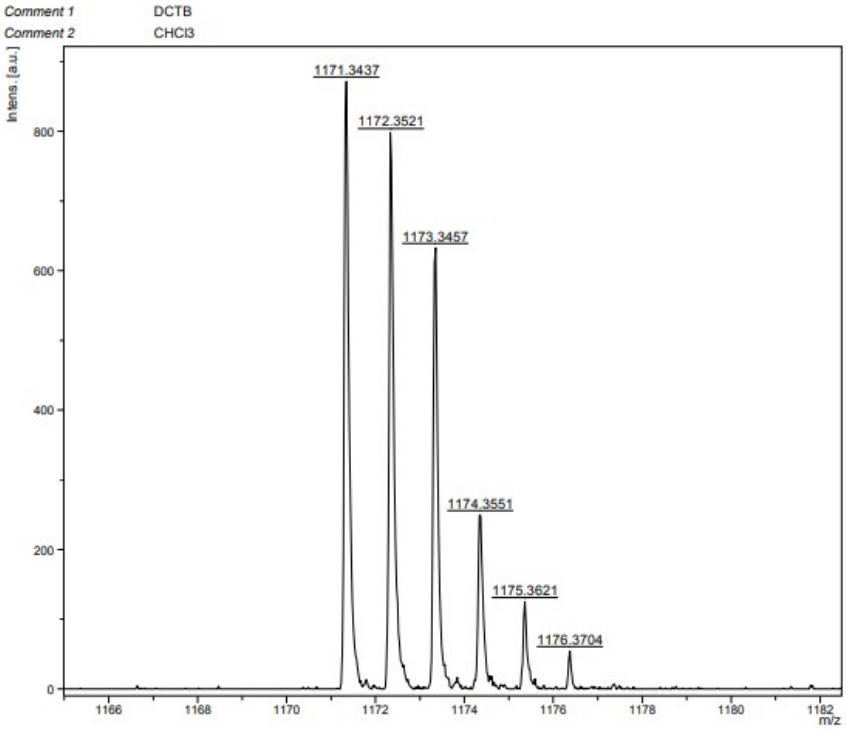


**Figure S45** MALDI-HRMS (m/z) spectrum of **NIPb3T-Rd.**

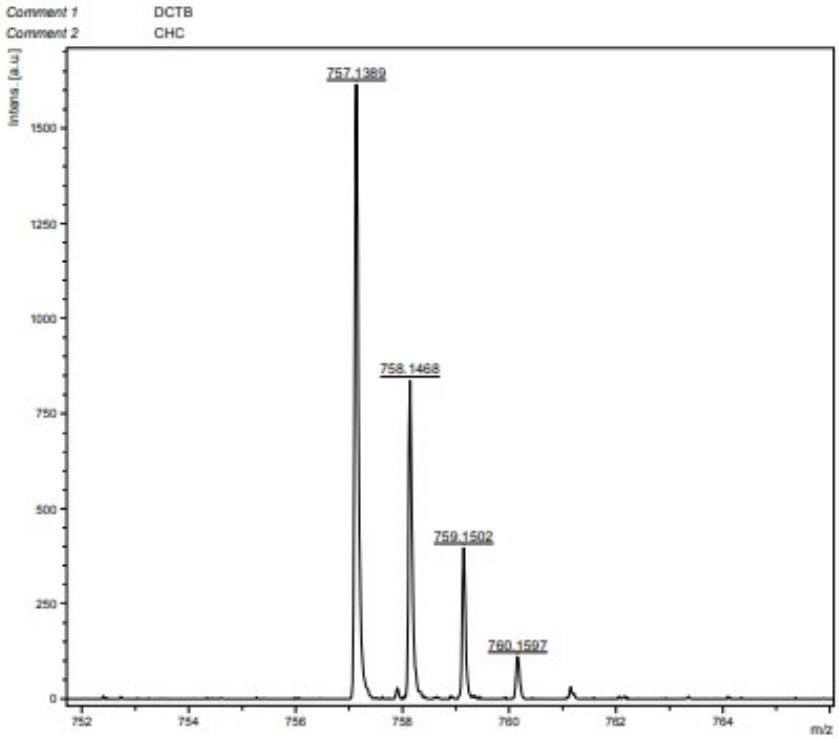


**Figure S46** MALDI-HRMS (m/z) spectrum of **NIPa3T-DCV**.

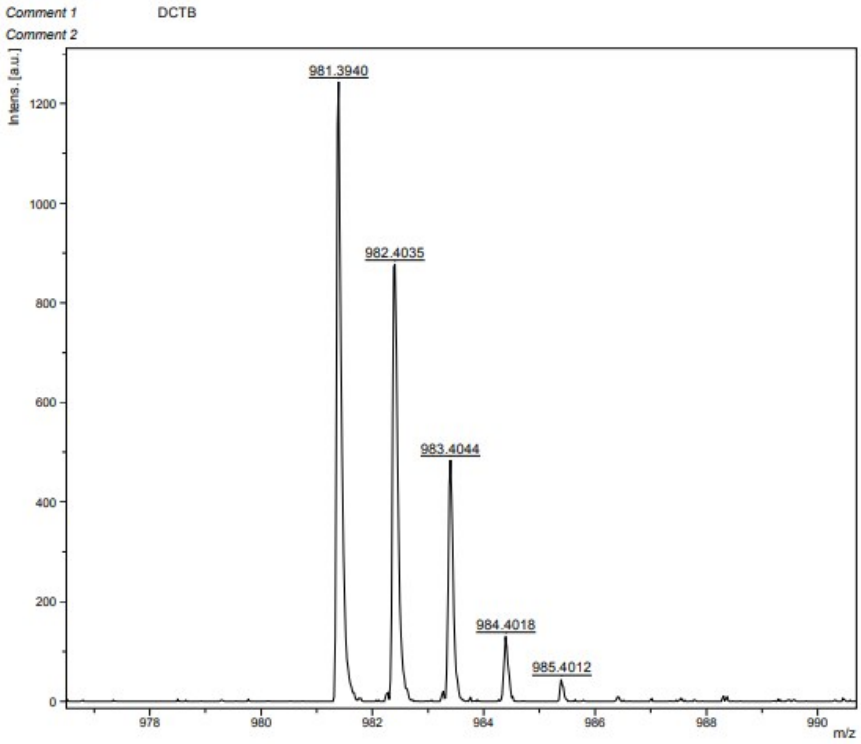


**Figure S47** MALDI-HRMS (m/z) spectrum of **NIPb3T-DCV**.

## 3. DFT calculations

Theoretical calculations for the NIPs monomers were carried out in the frame of density functional theory (DFT), using the B3LYP functional[11-13] and the 6-31G** basis set[14, 15] as implemented in the Gaussian 16 program.[16] 2-decyltetradecyl chains on the N-imide group of NIPs were replaced with isopropyl chains to simplify the calculations, for this reason NIP3T acronym is used to simplify the nomenclature. Geometry optimizations were performed without any symmetry constrains. On the basis of the resulting ground-state geometries, harmonic vibrational frequencies were calculated at the same theoretical level. The reorganization energies were calculated directly from the relevant points on the potential energy surfaces by using previously reported standard procedures. The formation of dimeric structures for the different semiconducting systems were theoretically predicted at the wB97XD[17, 18]/6-31G*[19] level, the formation of dimeric structures.

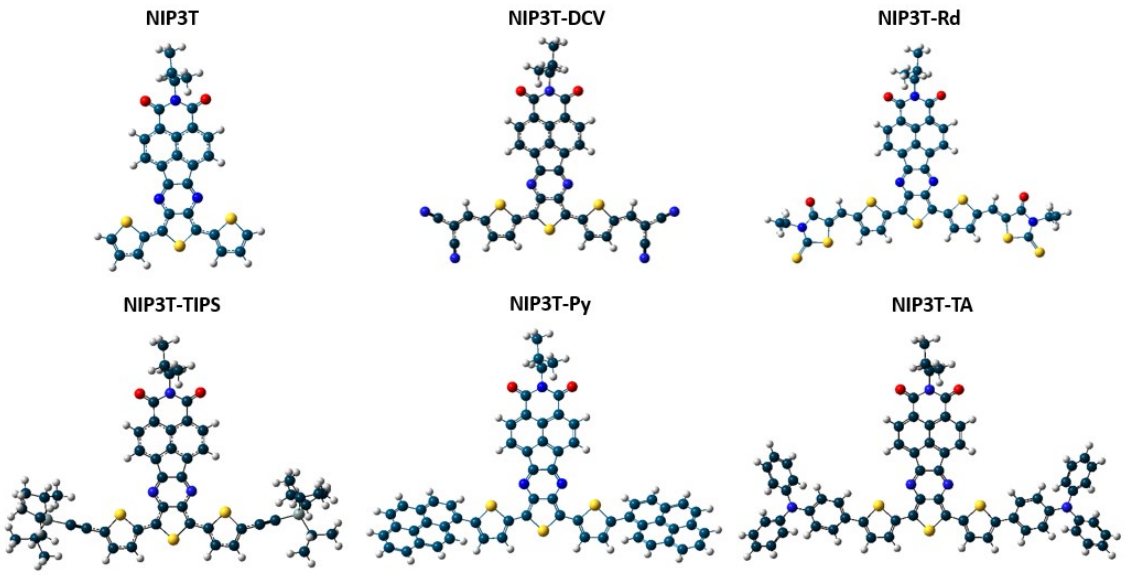


**Figure S48** B3LYP/6-31G** optimized geometries of NIPs.

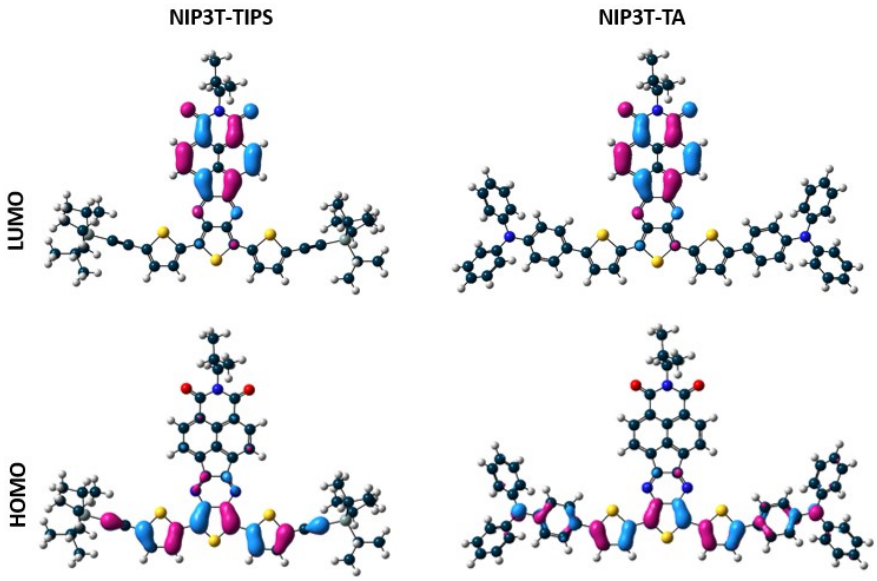


**Figure S49 5** B3LYP/6-31G** molecular orbital topologies of **NIP3T-TIPS** and **NIP3T-TA**.

**Table S1**. HOMO-LUMO gap energies and TDDFT-calculated vertical transition energies with the corresponding description at B3LYP/6-31G** level of theory. The oscillator strength values are given in brackets.

| | $E_{H-L}$ (eV) | λ (f) (nm) | Description |
|---|---|---|---|
| **NIP3T-TIPS** | 2.04 | 416 (1.18) | HOMO→L+2 (91%) |
| | | 695 (0.46) | HOMO→LUMO (99%) |
| **NIP3T-Py** | 1.91 | 465 (1.06) | HOMO→L+2 (96%) |
| | | 739 (0.61) | HOMO→L+1 (99%) |
| **NIP3T** | 1.73 | 327 (0.65) | H-5→L+1 (53%), H-3→L+1 (37%) |
| | | 357 (0.38) | H-3→LUMO (17%), H-1→LUMO (19%), HOMO→L+2 (48%) |
| | | 657 (0.23) | HOMO→LUMO (98%) |
| **NIP3T-TA** | 2.17 | 456 (1.38) | HOMO→L+2 (94%) |
| | | 797 (0.65) | HOMO→LUMO (99%) |
| **NIP3T-Rd** | 1.90 | 370 (0.28) | H-1→L+3 (59%), HOMO→L+4 (72%) |
| | | 508 (0.68) | HOMO→L+2 (89%) |
| | | 726 (1.04) | HOMO→LUMO (98%) |
| **NIP3T-DCV** | 2.00 | 416 (0.51) | H-1→LUMO (31%), HOMO→L+3 (51%) |
| | | 609 (0.20) | HOMO→L+1 (98%) |
| | | 665 (0.85) | HOMO→LUMO (98%) |

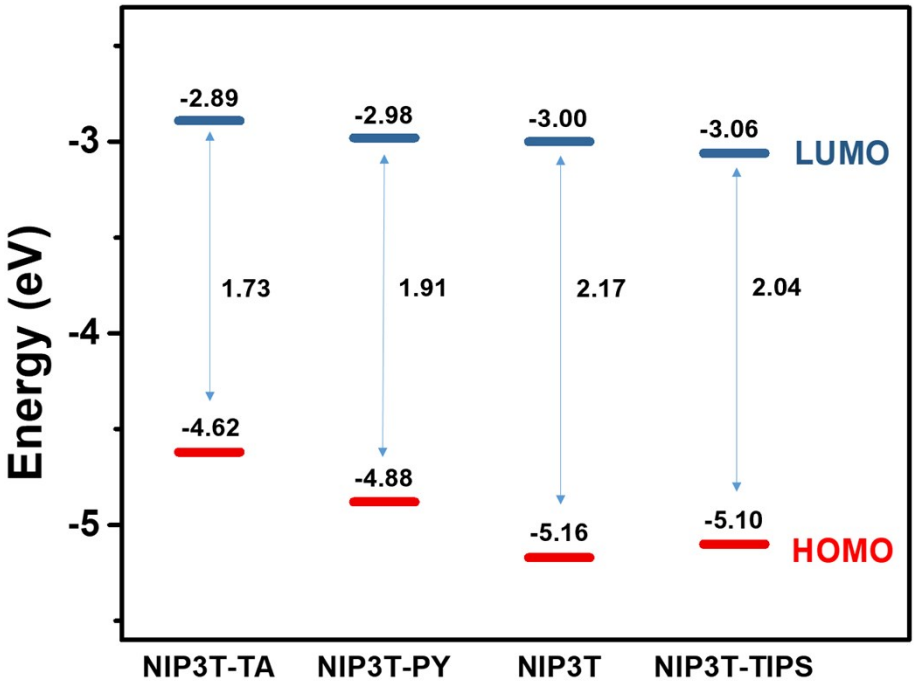


**Figure S50** B3LYP/6-31G** frontier molecular orbital topologies predicted for **NIP3T-TA**, **NIP3T-Py**, **NIP3T** and **NIP3T-TIPS** and the energy gap values.

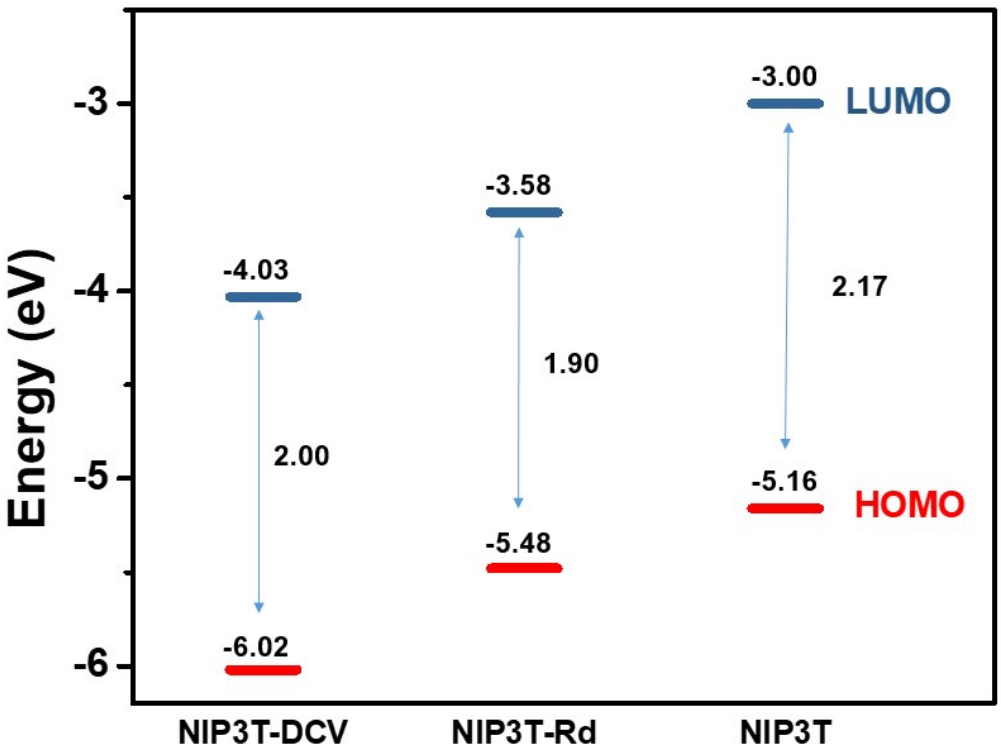


**Figure S51** B3LYP/6-31G** frontier molecular orbital topologies predicted for **NIP3T-DCV**, **NIP3T-Rd** and **NIP3T** and the energy gap values.

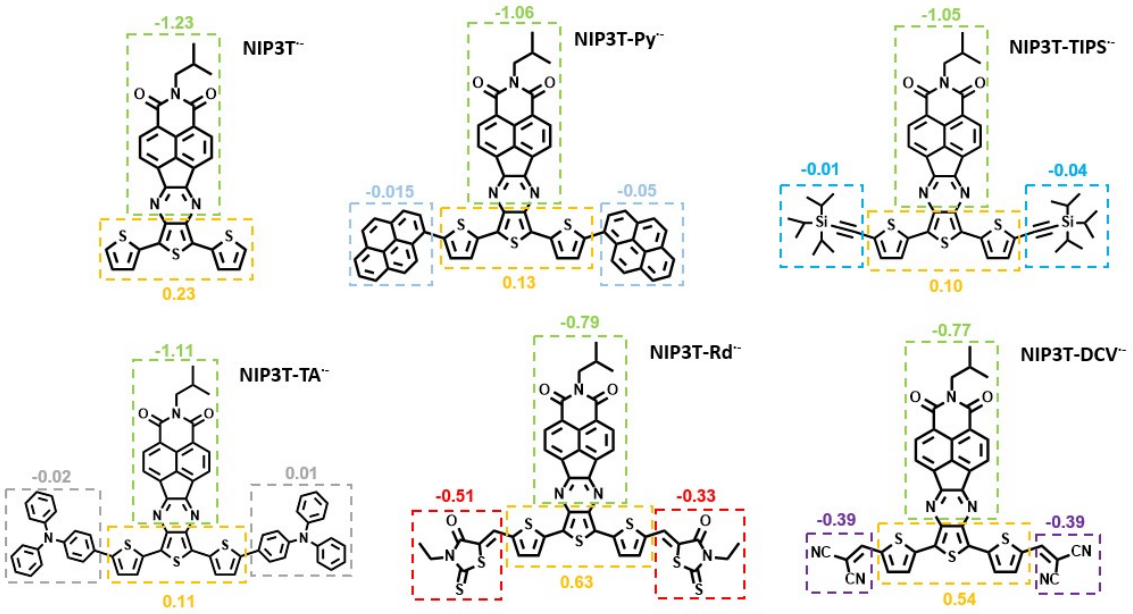


**Figure S52** B3LYP/6-31G**-charge distributions for a) **NIP3T**, b) **NIP3T-Py**, c) **NIP3T-TIPS**, d) **NIP3T-TA**, e) **NIP3T-Rd** and f) **NIP3T-DCV** as anion species.

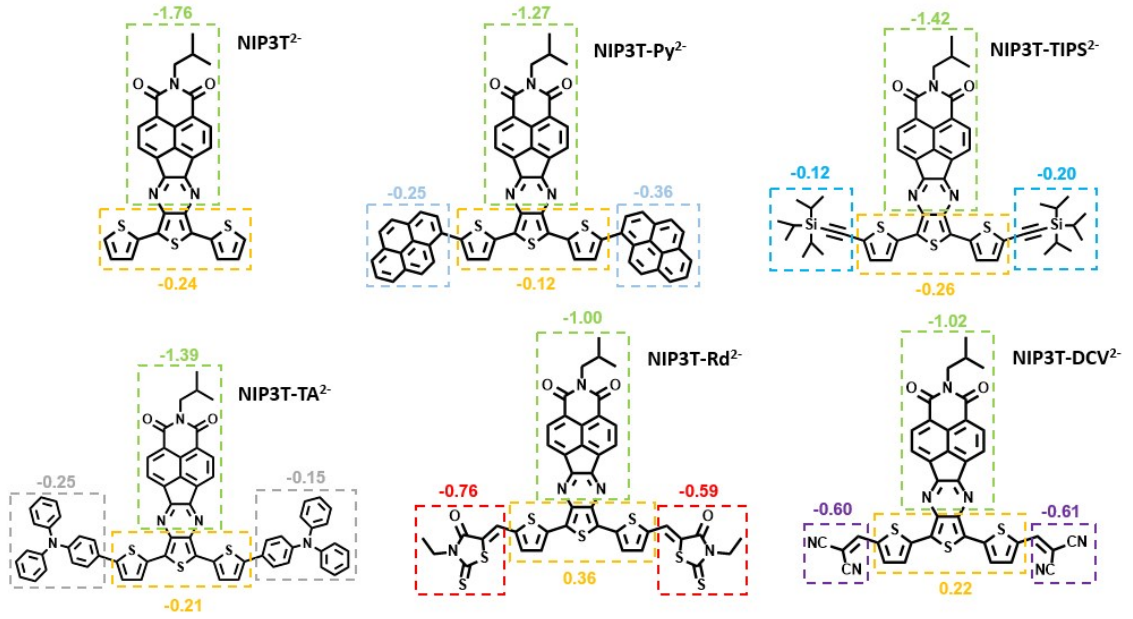


**Figure S53** B3LYP/6-31G**-charge distributions for a) **NIP3T**, b) **NIP3T-Py**, c) **NIP3T-TIPS**, d) **NIP3T-TA**, e) **NIP3T-Rd** and f) **NIP3T-DCV** as dianion species.

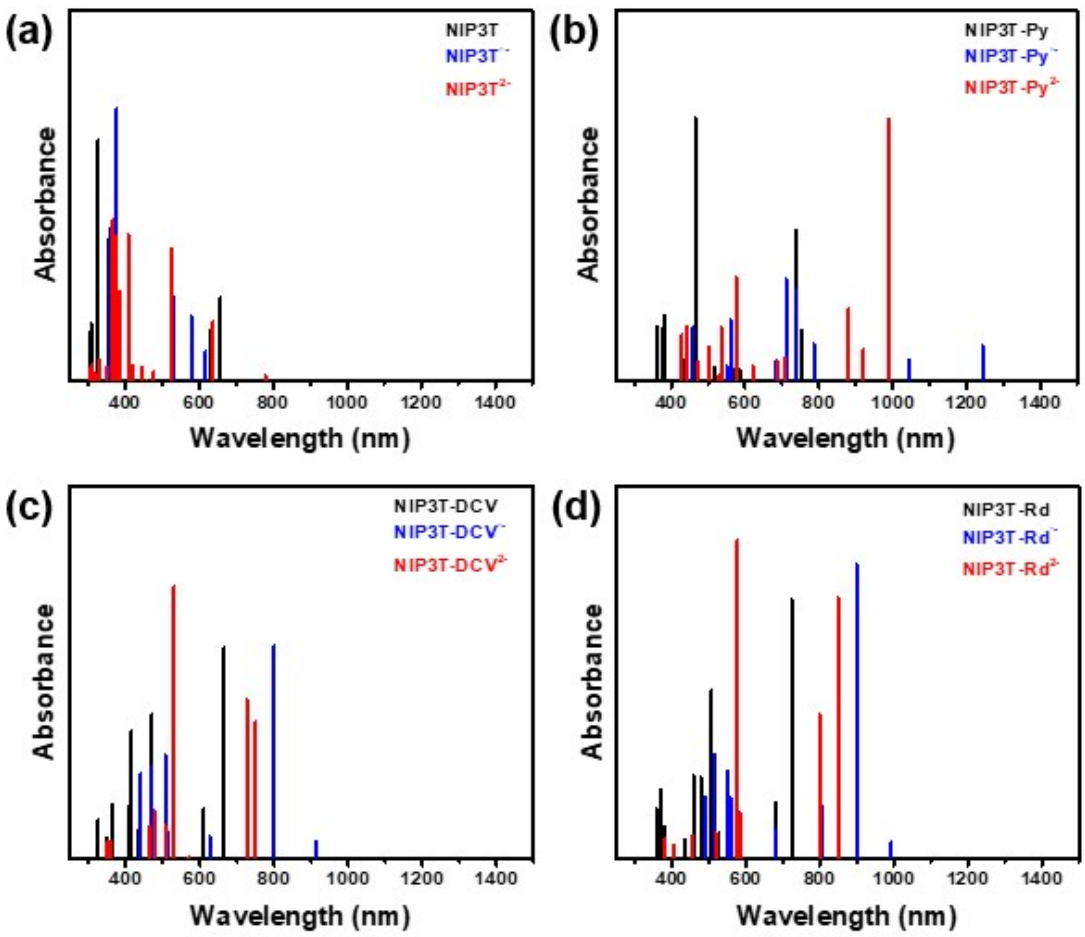


**Figure S54** TDDFT-B3LYP/6-31G**-calculated vertical transition energies for a) **NIP3T**, b) **NIP3T-Py**, c) **NIP3T-DCV** and d) **NIP3T-Rd** with the different reduced species. See the comparison with the experimental results in Figures S77-80.

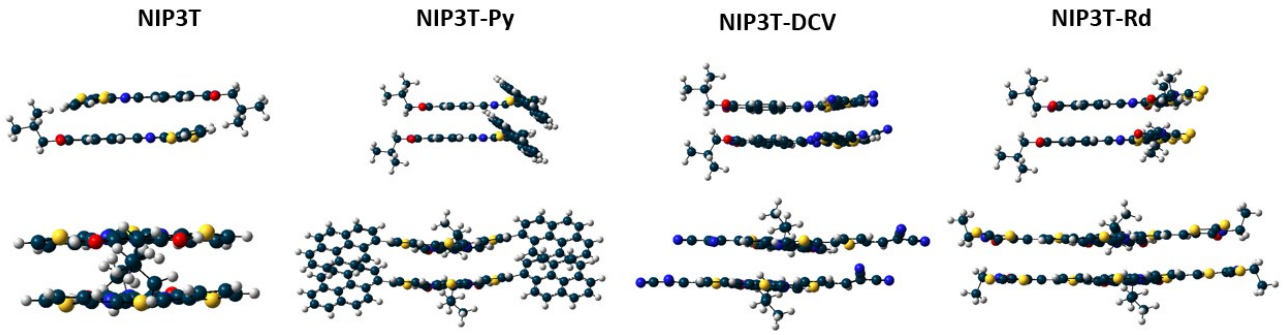


**Figure S55** wB97XD/6-31G* optimized geometries of NIPs dimers.

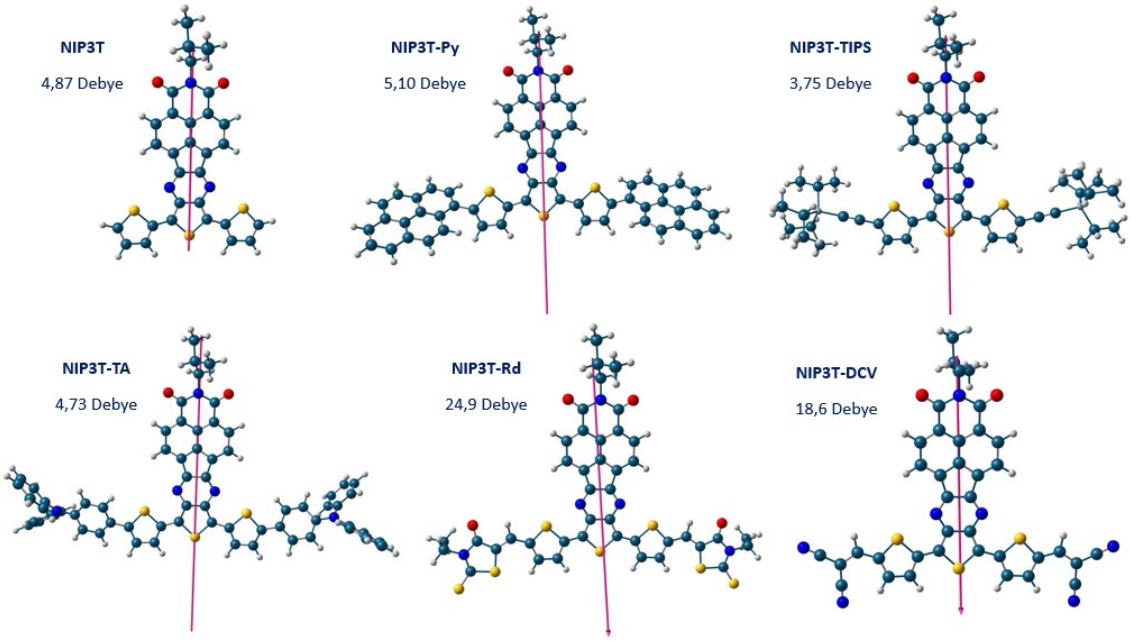


**Figure S56** Calculated transition dipole moments of NIP derivatives.

## 4. FT-Raman

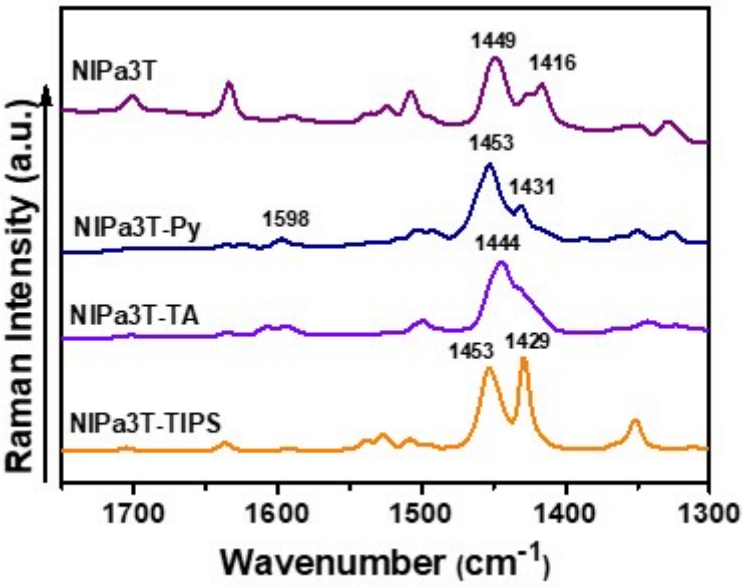


**Figure S57** Raman spectra (λ=1064 nm) of **NIPa3T**, **NIPa3T-Py**, **NIPa3T-TA** and **NIPa3T-TIPS** derivatives as bulk materials.

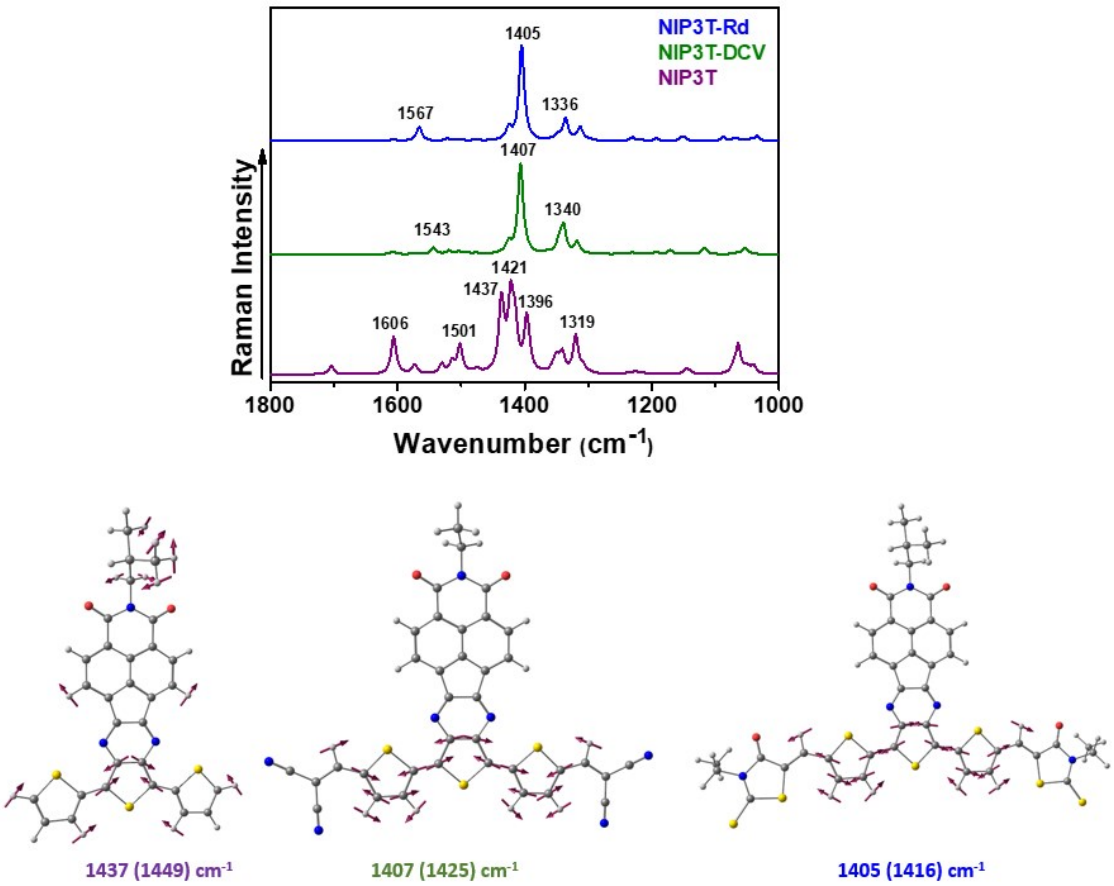


**Figure S58** B3LYP/6-31G** predicted Raman spectra for **NIP3T-Rd**, **NIP3T-DCV** and **NIP3T** and the corresponding eigenvectors.

## 5. UV-Vis and electrochemical data

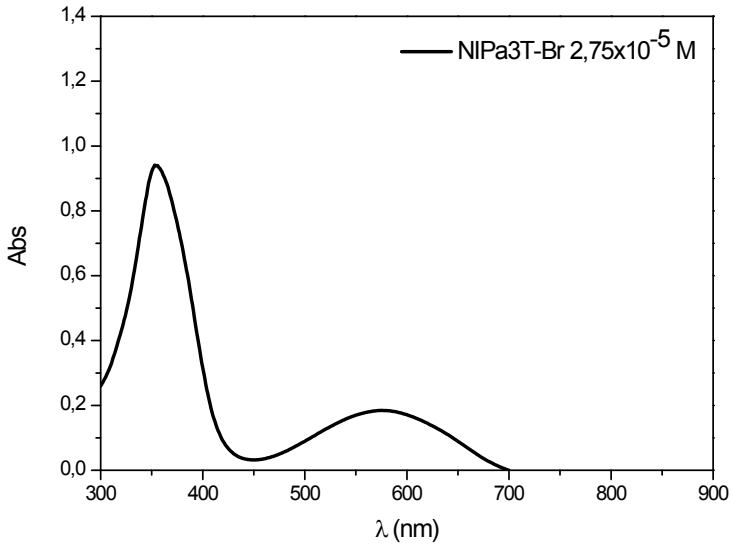


**Figure S59** UV-Vis spectra of **NIPa3T-Br** 2.75x10$^{-5}$ M in chloroform solution.

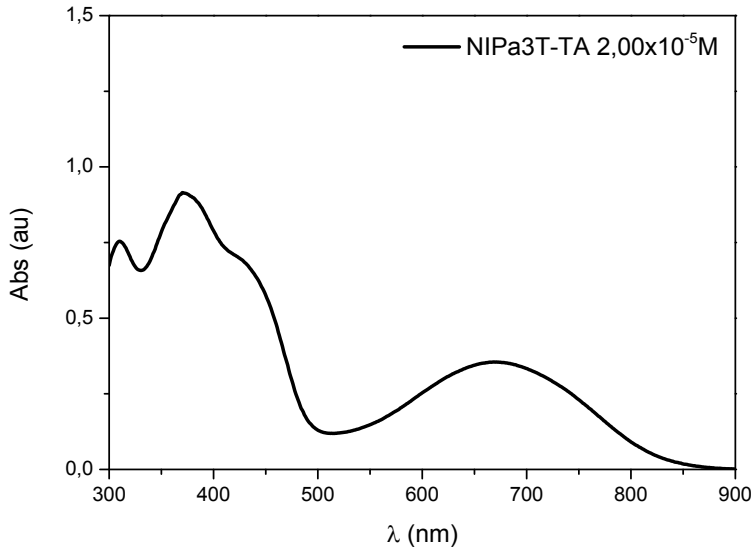


**Figure S60** UV-Vis spectra of **NIPa3T-TA** 2.00x10$^{-5}$ M in chloroform solution.

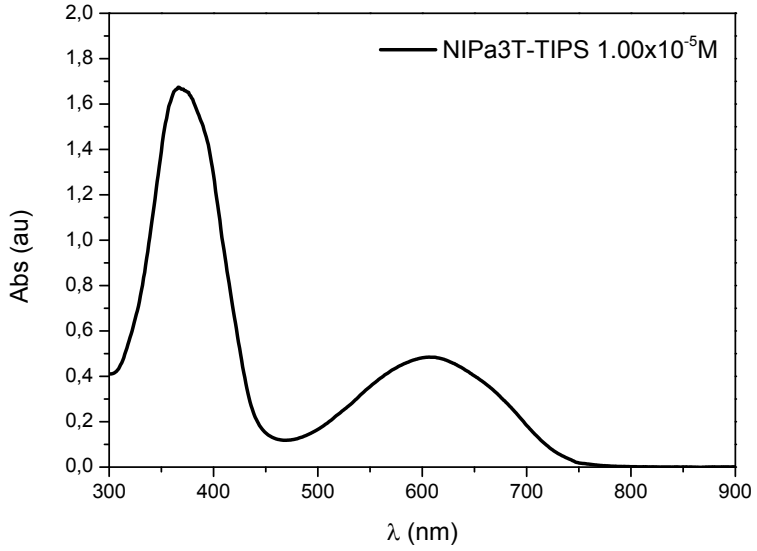


**Figure S61** UV-Vis spectra of **NIPa3T-TIPS** 1.00x10$^{-5}$ M in chloroform solution.

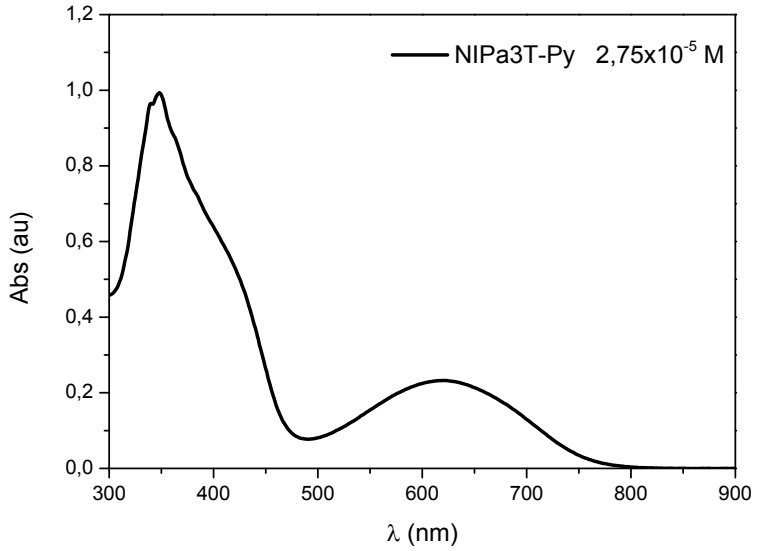


**Figure S62** UV-Vis spectra of **NIPa3T-Py** 2.75x10$^{-5}$ M in chloroform solution.

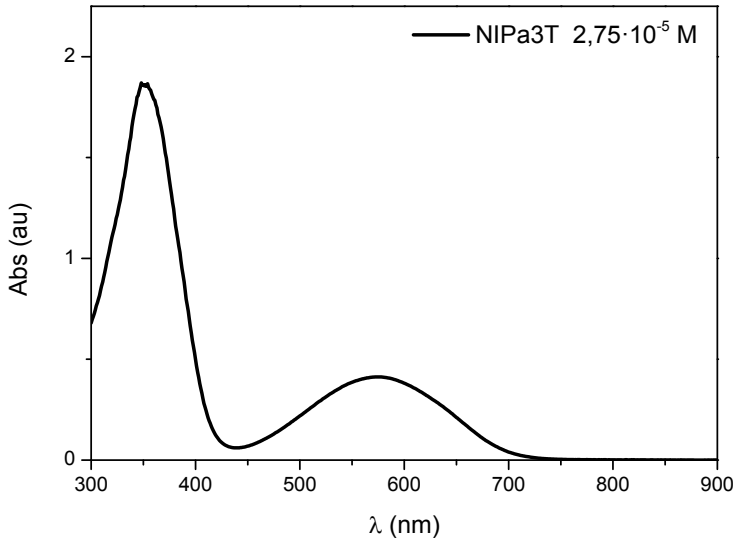


**Figure S63** UV-Vis spectra of **NIPa3T** 2.75x10$^{-5}$ M in chloroform solution.

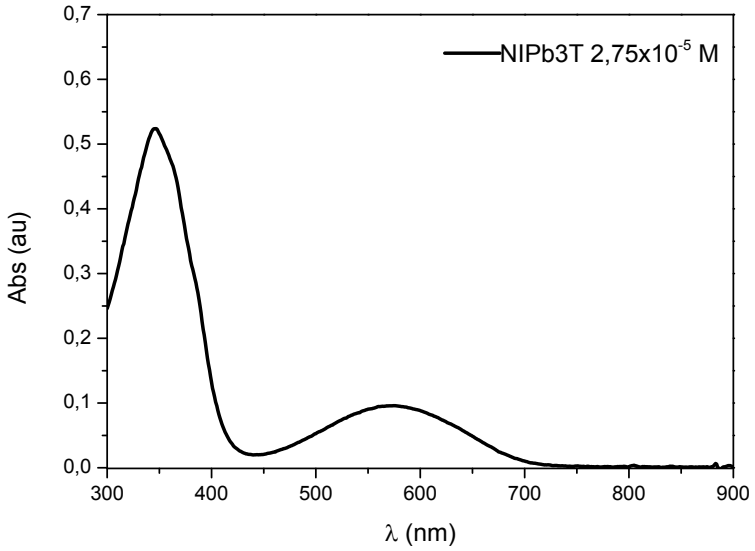


**Figure S64** UV-Vis spectra of **NIPb3T** 2.75x10$^{-5}$ M in chloroform solution.

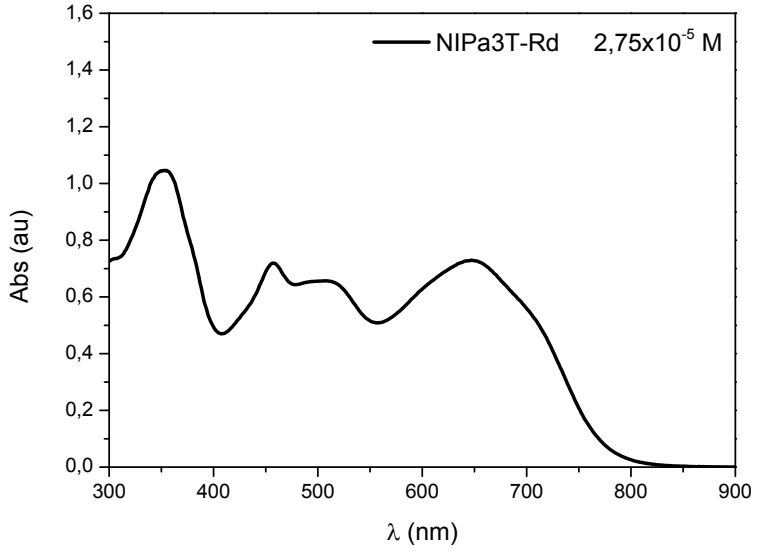


**Figure S65** UV-Vis spectra of **NIPa3T-Rd** 2.75x10$^{-5}$ M in chloroform solution.

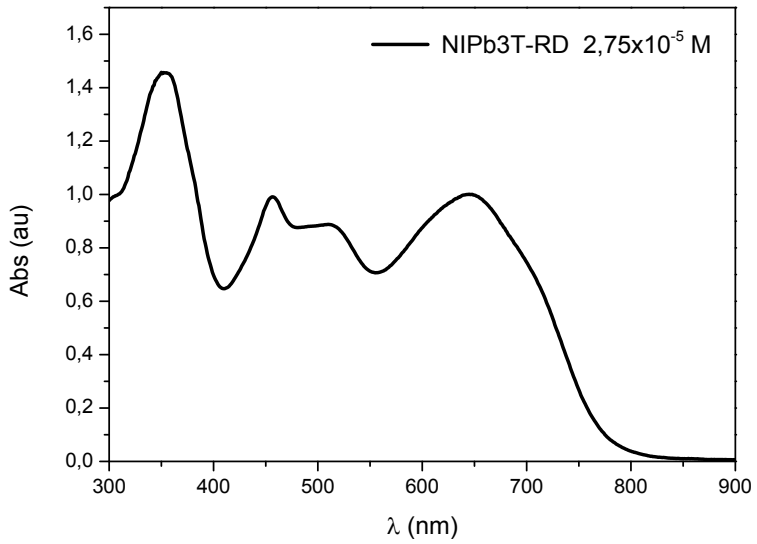


**Figure S66** UV-Vis spectra of **NIPb3T-Rd** 2.75x10$^{-5}$ M in chloroform solution.

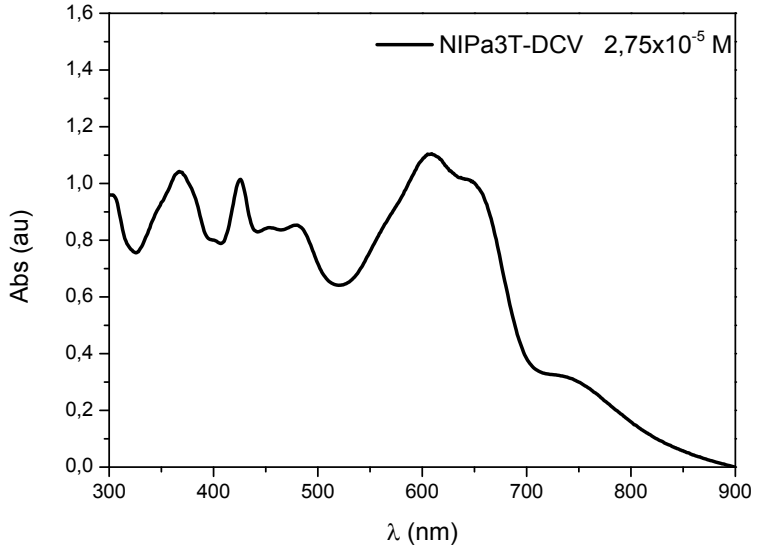


**Figure S67** UV-Vis spectra of **NIPa3T-DCV** 2.75x10$^{-5}$ M in chloroform solution.

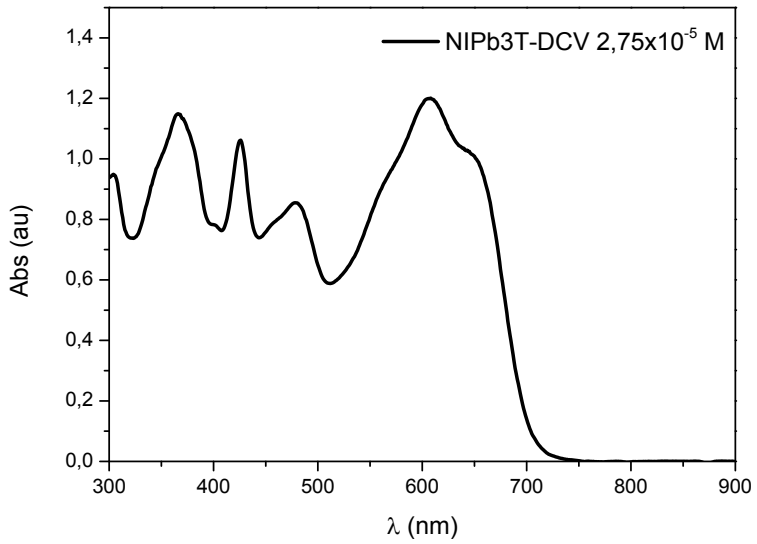


**Figure S68** UV-Vis spectra of **NIPb3T-DCV** 2.75x10$^{-5}$ M in chloroform solution.

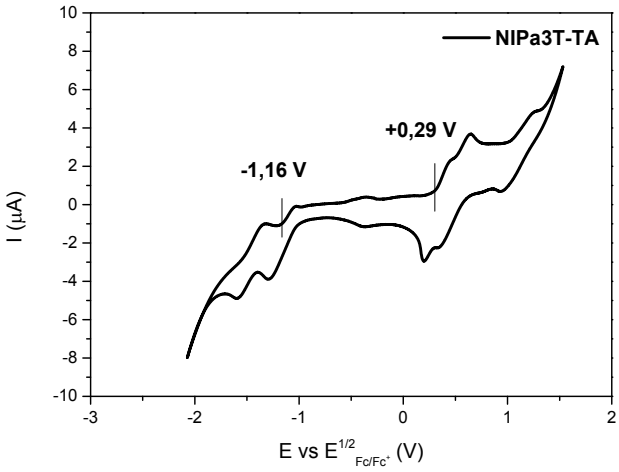


**Figure S69** Cyclic voltammetry of **NIPa3T-TA** and TBAHFP 0.1M in dichloromethane solution.

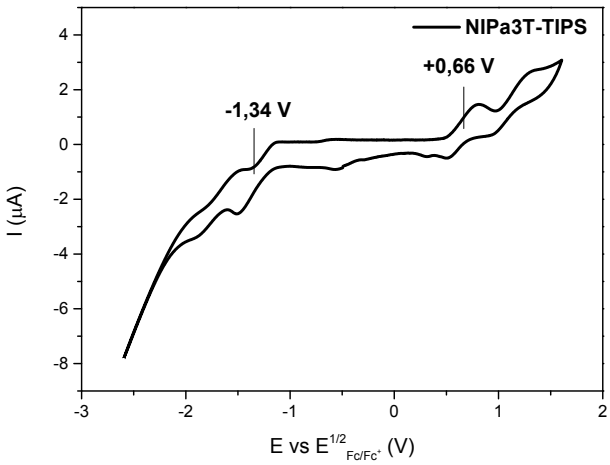


**Figure S70** Cyclic voltammetry of **NIPa3T-TIPS** and TBAHFP 0.1M in dichloromethane solution.

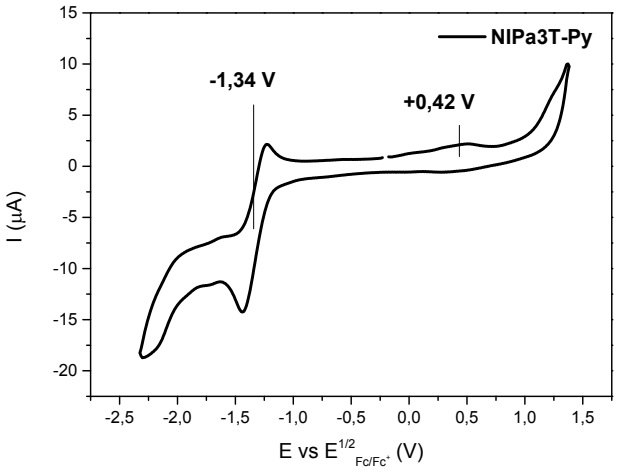


**Figure S71** Cyclic voltammetry of **NIPa3T-Py** and TBAHFP 0.1M in dichloromethane solution.

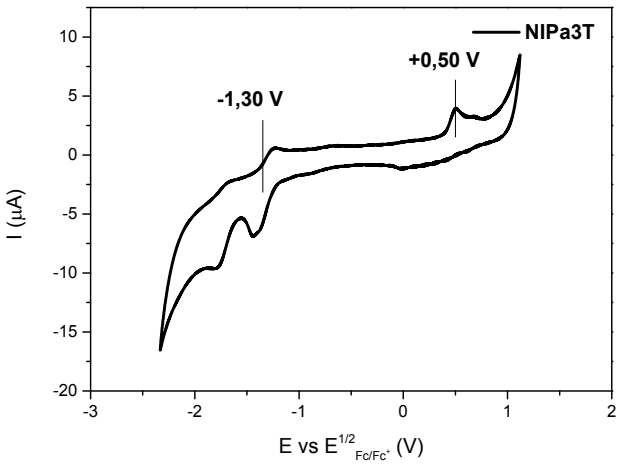


**Figure S72** Cyclic voltammetry of **NIPa3T** and TBAHFP 0.1M in dichloromethane solution.

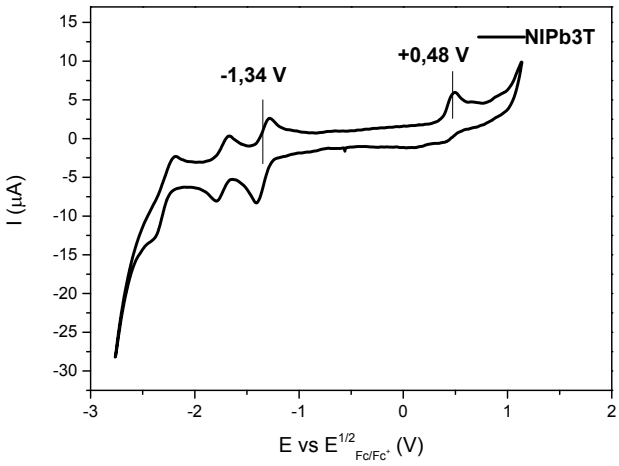


**Figure S73** Cyclic voltammetry of **NIPb3T** and TBAHFP 0.1M in dichloromethane solution.

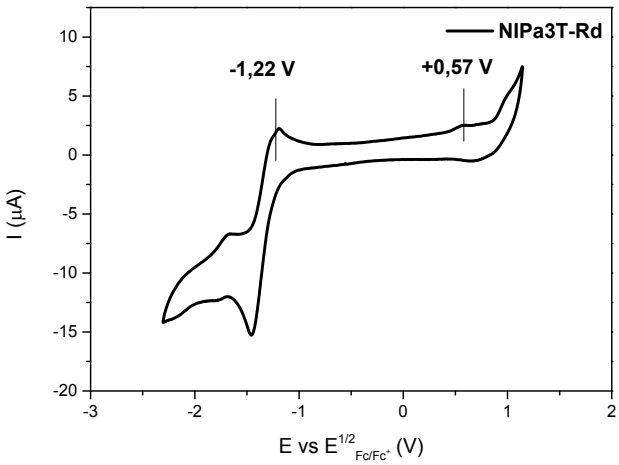


**Figure S74** Cyclic voltammetry of **NIPa3T-Rd** and TBAHFP 0.1M in dichloromethane solution.

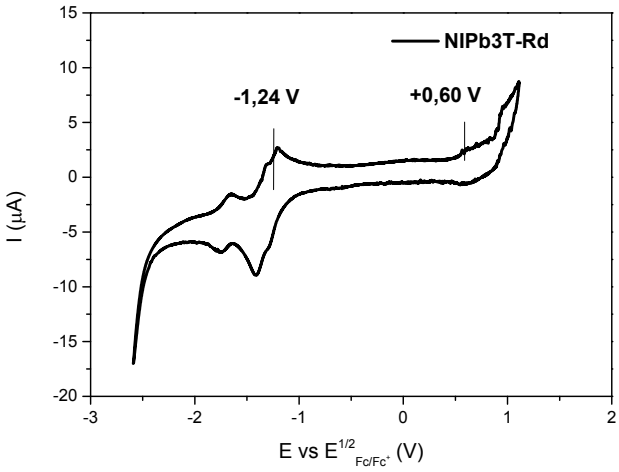


**Figure S75** Cyclic voltammetry of **NIPb3T-Rd** and TBAHFP 0.1M in dichloromethane solution.

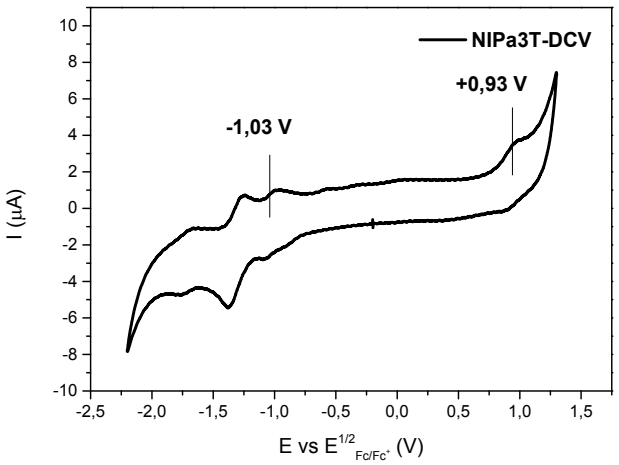


**Figure S76** Cyclic voltammetry of **NIPa3T-DCV** and TBAHFP 0.1M in dichloromethane solution.

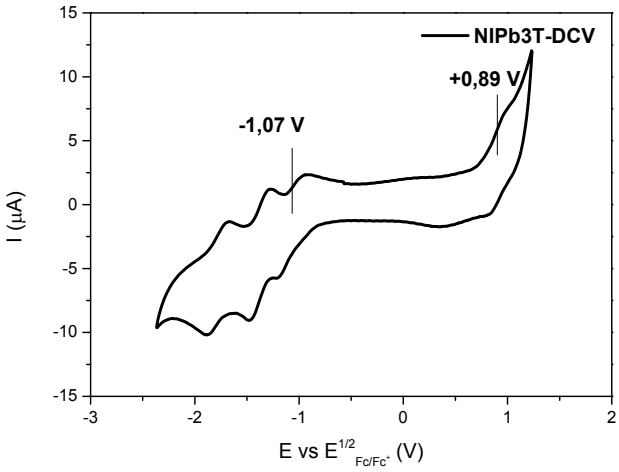


**Figure S77** Cyclic voltammetry of **NIPb3T-DCV** and TBAHFP 0.1M in dichloromethane solution.

## 6. Spectroelectrochemical measurements

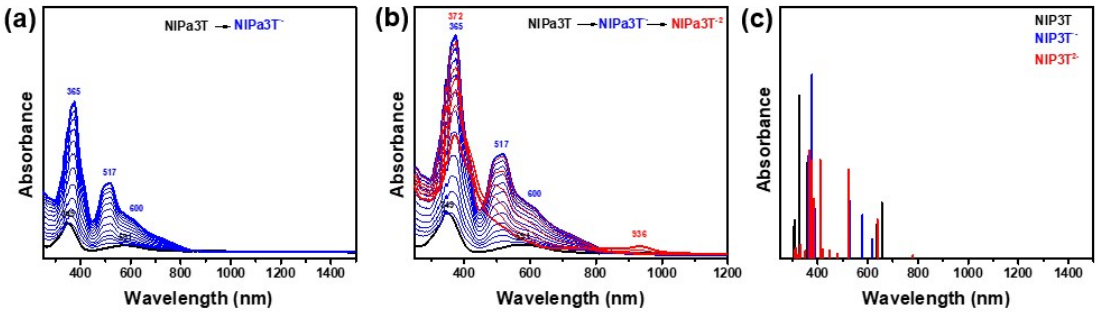


**Figure S78** (a),(b) UV-Vis-NIR absorption spectra of **NIP3T** electrochemically reduced by progressive increase of the reduction potential; (c) TDDFT-B3LYP/6-31G**-calculated vertical transition energies.

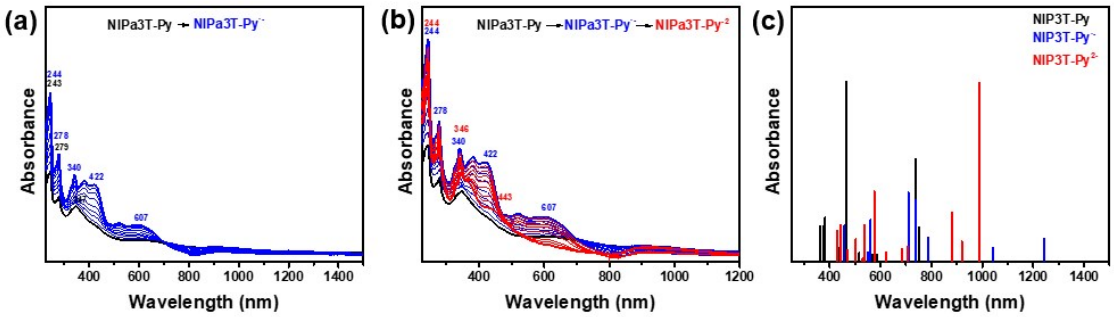


**Figure S79** (a),(b) UV-Vis-NIR absorption spectra of **NIP3T-Py** electrochemically reduced by progressive increase of the reduction potential; (c) TDDFT-B3LYP/6-31G**-calculated vertical transition energies.

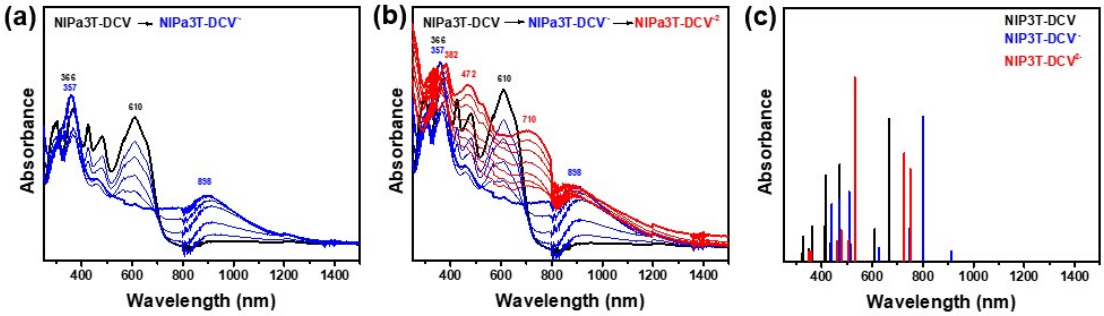


**Figure S80** (a),(b) UV-Vis-NIR absorption spectra of **NIPb3T-DCV** electrochemically reduced by progressive increase of the reduction potential; (c) TDDFT-B3LYP/6-31G**-calculated vertical transition energies.

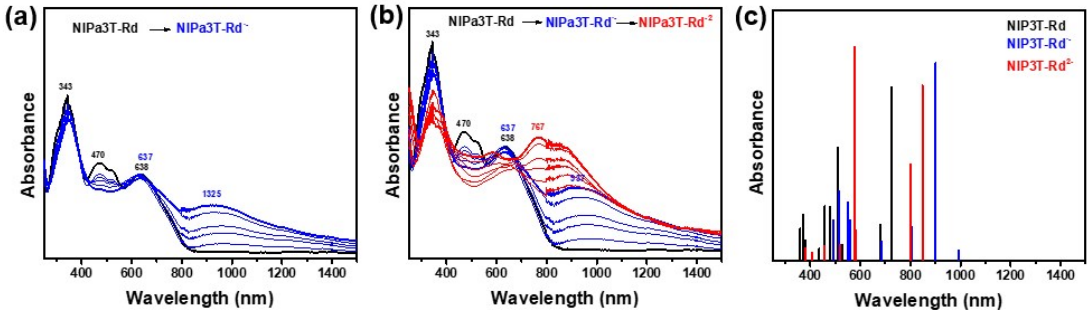


**Figure S81** (a),(b) UV-Vis-NIR absorption spectra of **NIPb3T-Rd** electrochemically reduced by progressive increase of the reduction potential ; (c) TDDFT-B3LYP/6-31G**-calculated vertical transition energies.

## 7. XRD

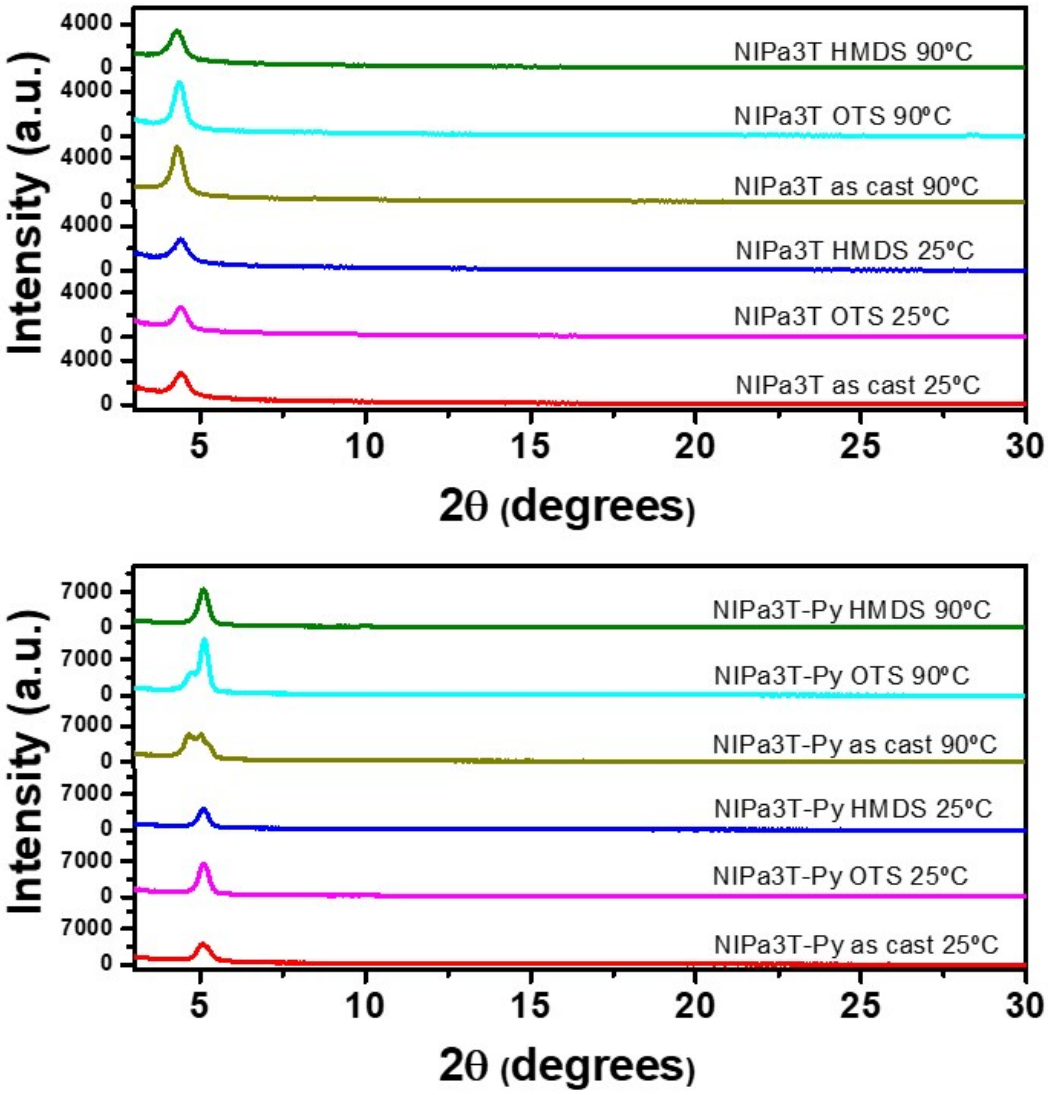


**Figure S82**. Θ-2Θ X-ray diffraction scans of vapor-deposited, **NIPa3T** and **NIPa3T-Py** thin films (Td = 25ºC and 90ºC) grown on as cast, OTS or HMDS-treated $Si/SiO_2$ substrates.

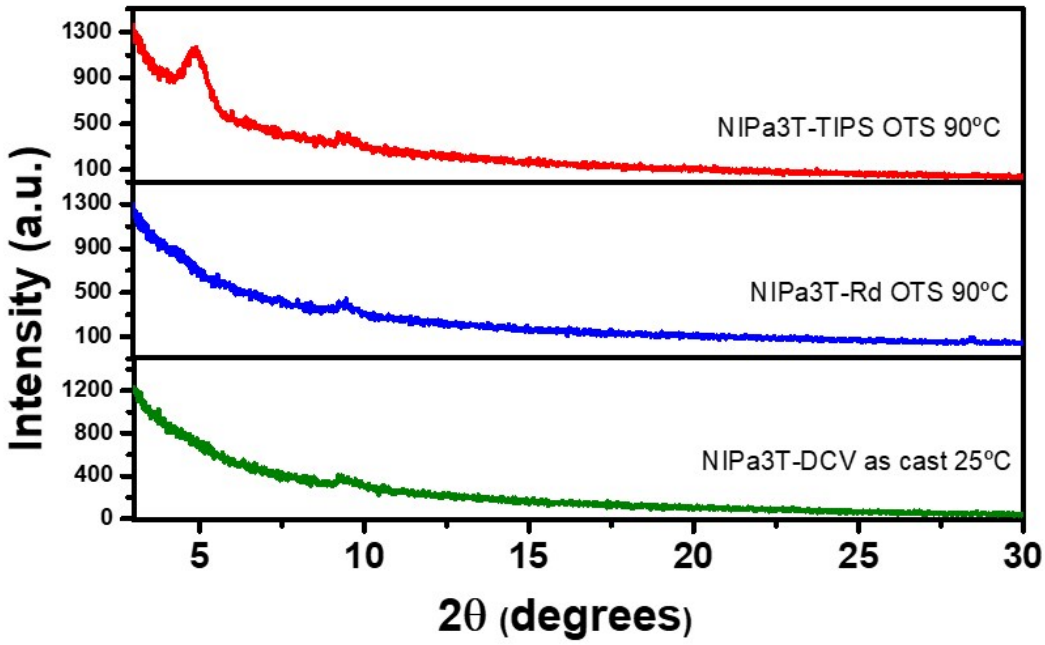


**Figure S83**. Θ-2Θ X-ray diffraction scans of vapor-deposited **NIPa3T-TIPS**, **NIPa3T-Rd** and **NIPa3T-DCV** thin films (Td = 90ºC) grown on OTS-treated $Si/SiO_2$ substrates.

## 8. AFM

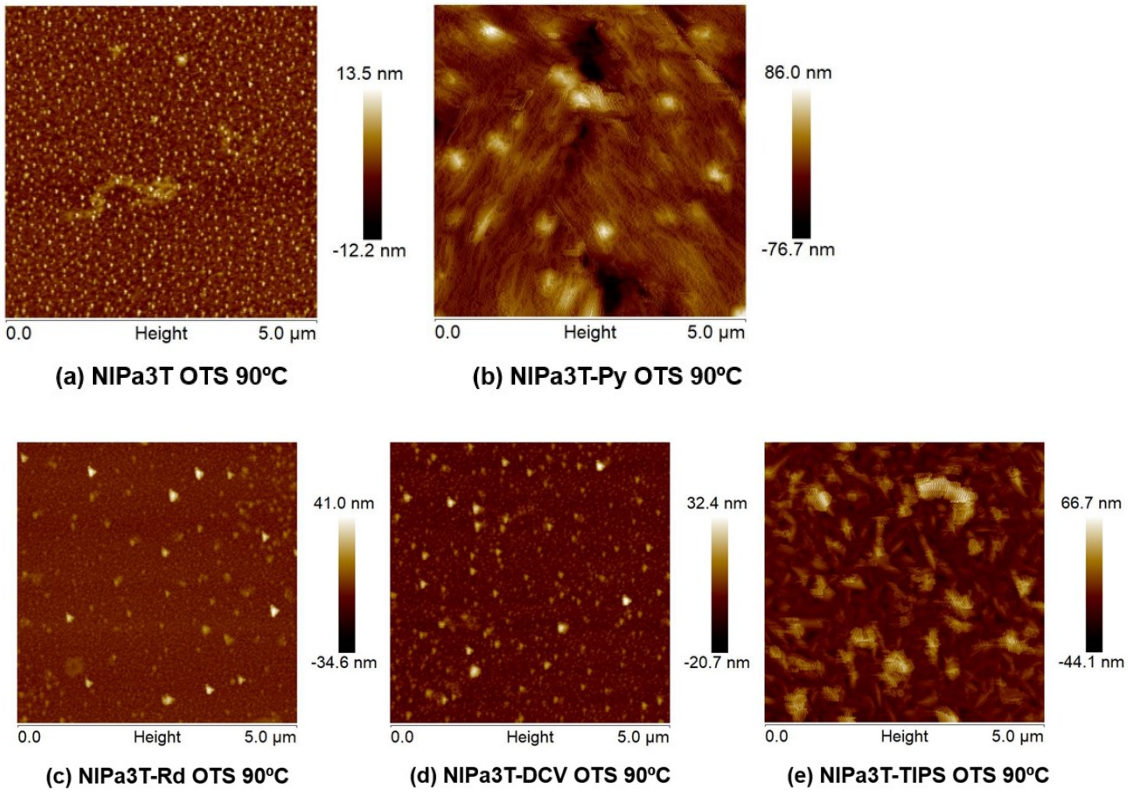


**Figure S84**. AFM images of the (a) NIPa3T, (b) NIPa3T-Py, (c) NIPa3T-Rd, (d) NIPa3T-DCV and (e) NIPa3T-TIPS vapor-deposited under conditions yielding optimum OFET performance. Image size: 5x5 mm.

## 9. Organic field effect transistor

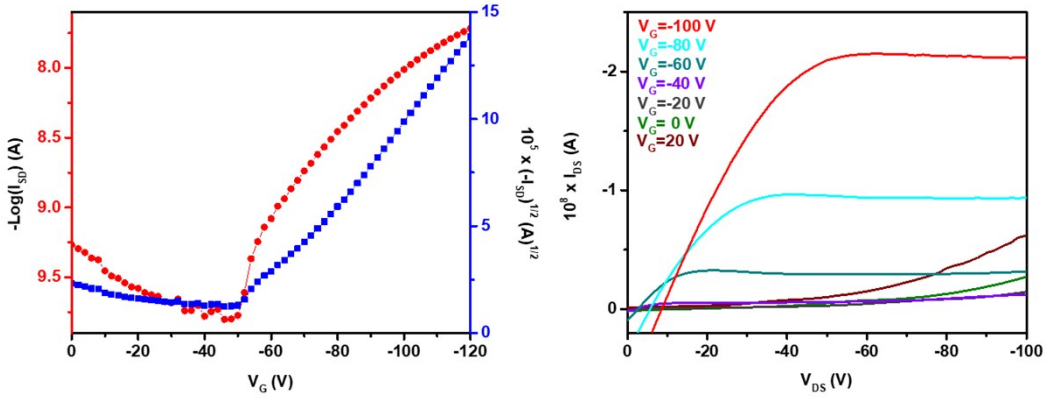


**Figure S85.** OFET transfer and output characteristics of **NIPa3T**.

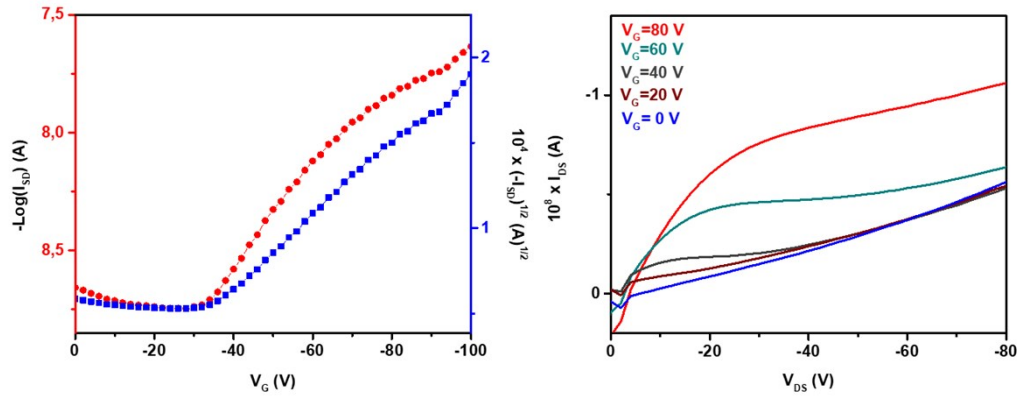


**Figure S86.** OFET transfer and output characteristics of **NIPa3T-TIPS**.

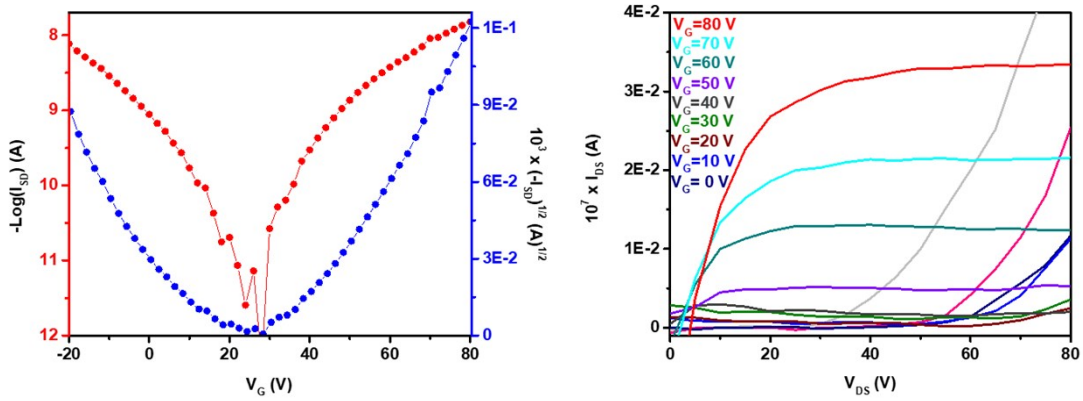


**Figure S87.** OFET transfer and output characteristics of **NIPa3T-Rd**.

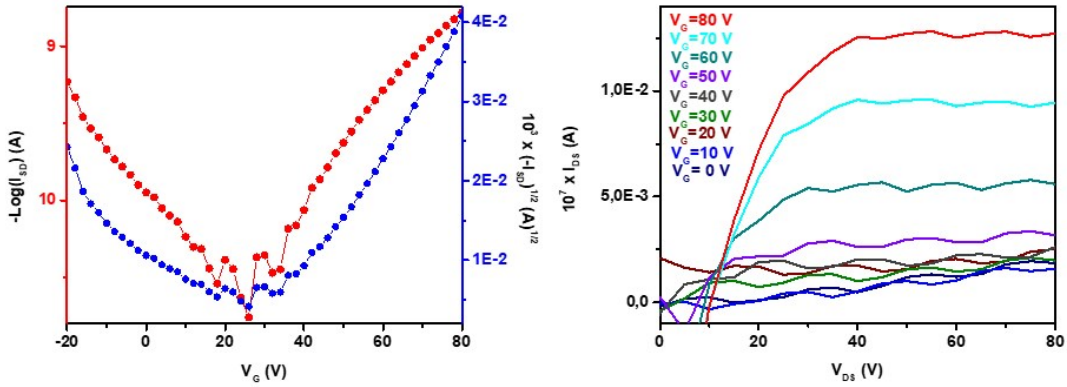


**Figure S88.** OFET transfer and output characteristics of **NIPa3T-DCV**.

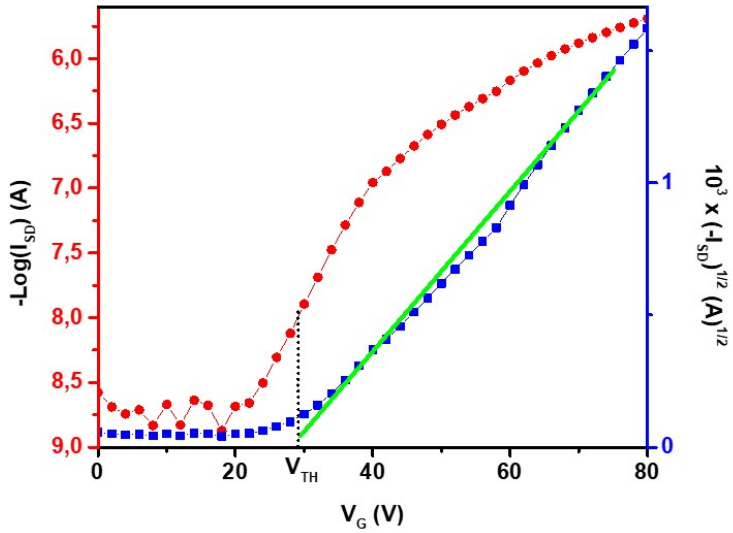


**Figure S89.** OFET transfer characteristics of **NIPa3T-Py** with the linear fitting used to calculate the electron mobility.

## 10. Organic solar cells (OSC)

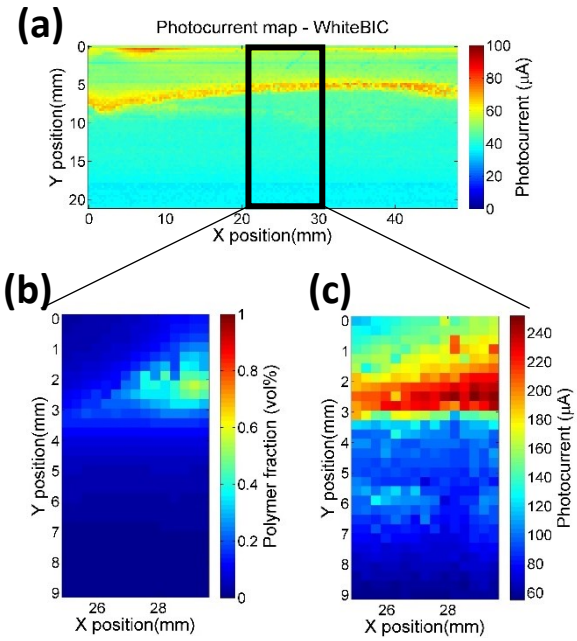


**Figure S90.** a) Local photocurrent under white light mapping of a **P3HT:NIPb3T-Rd** OSC with a composition gradient. b) P3HT fraction map, zoomed in. c) Local photocurrent under 488nm laser illumination, zoomed in.

One continuous organic solar cell (OSC) device was fabricated by blade coating, using a two-drop method to obtain a lateral composition gradient in order to efficiently explore all the possible compositions of donor:acceptor, following the method described in a previous work.[20]

The local photocurrent was extracted by illuminating the sample locally, and the local composition extracted by analyzing the Raman signal of the material.[21]

Raman cross-section for **NIPb3T-Rd** was calculated from the Raman signal of the pure material deposited as thin film with a thickness gradient on a glass slide, and the value obtained was $2.46*10^{-5}$. For this single sample, a first evaluation of the performance can be made. We deduced from here that the best efficiencies occurred for polymer rich compositions.

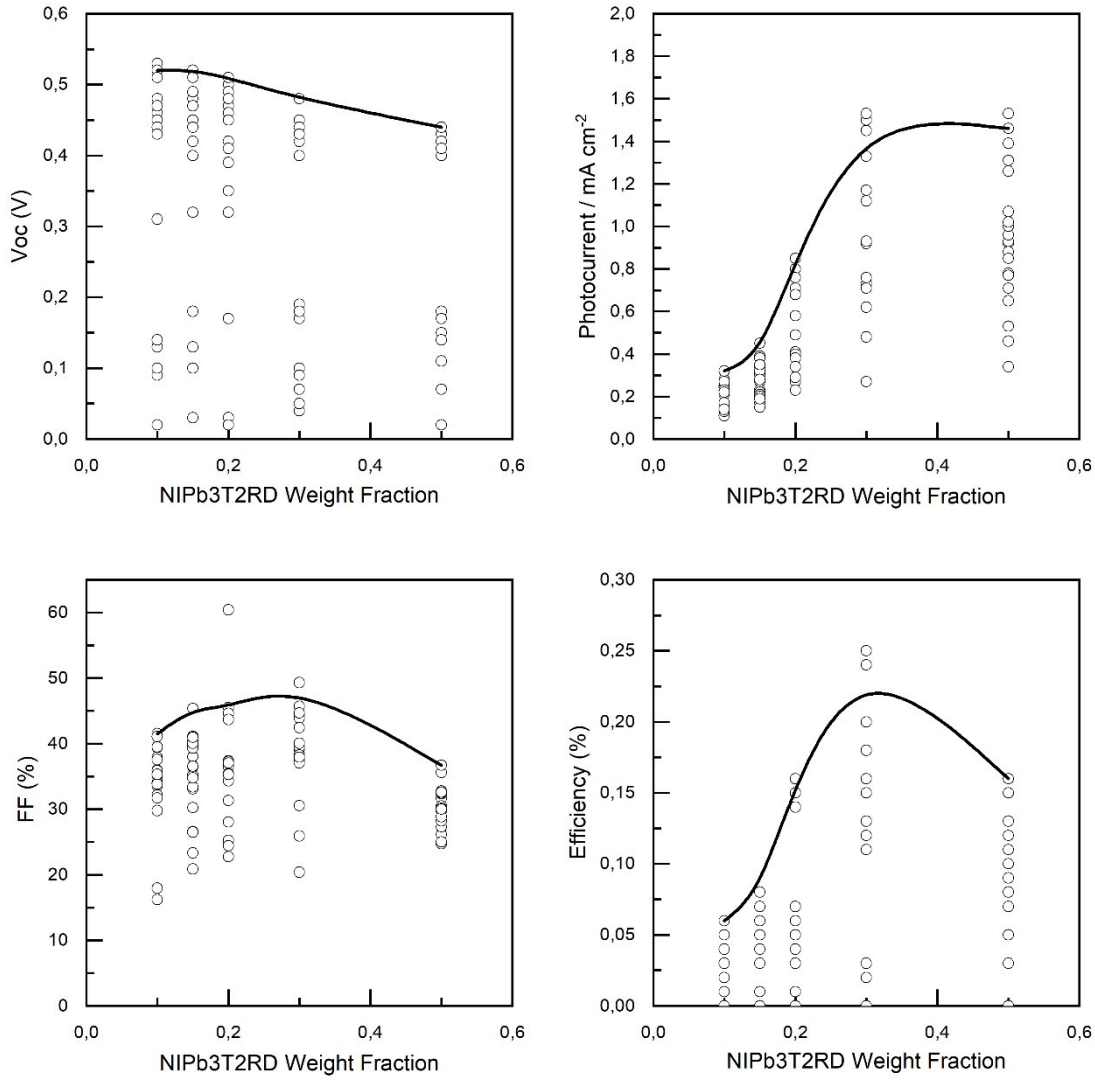


**Figure S91.** Electrical parameters of discrete OSC with a thickness gradient, for 5 different **P3HT:NIPb3T-Rd** composition ratios a) Open circuit voltage. b) Short circuit current c) Fill Factor d) Efficiency

In a second step, 5 discrete samples were fabricated in order to obtain all the electrical parameters for 5 different P3HT:NIPb3T-Rd composition ratios around the optimum found with the continuous sample above. Each sample contained 12 times 2 pixels. We fabricated the samples with a controlled thickness gradient, so each pixel had a slightly different local thickness, and thus the optimum thickness could be identified.

Both materials were premixed, dissolved in chlorobenzene, at 15mg/ml and stirred overnight at 80ºC, deposited in an inverted structure (Glass/ITO/ZnO/Active Layer/$MoO_3$/Ag) by blade coating at 80ºC, with a 200µm gap, applying a thickness gradient in each sample by varying linearly the deposition speed from 90 to 10 mm/s while depositing.[20]

## 11. References


1. P. de Echegaray, M. J. Mancheño, I. Arrechea-Marcos, R. Juárez, G. López-Espejo, J. T. López Navarrete, M. M. Ramos, C. Seoane, R. P. Ortiz and J. L. Segura, *J. Org. Chem.*, 2016, **81**, 11256-11267.
2. H. Li, F. S. Kim, G. Ren, E. C. Hollenbeck, S. Subramaniyan and S. A. Jenekhe, *Angew. Chem. Int. Ed.*, 2013, **52**, 5513-5517.
3. H. Herrera, P. de Echegaray, M. Urdanpilleta, M. J. Mancheño, E. Mena-Osteritz, P. Bäuerle and J. L. Segura, *Chem. Commun.*, 2013, **49**, 713-715.
4. R. C. DeCicco, A. Black, L. Li and N. S. Goroff, *Eur. J. Org. Chem.*, 2012, **2012**, 4699-4704.
5. W. Mammo, S. Admassie, A. Gadisa, F. Zhang, O. Inganäs and M. R. Andersson, *Sol. Energy Mater. Sol. Cells*, 2007, **91**, 1010-1018.
6. S. Ravi, K. K. Chiruvella, K. Rajesh, V. Prabhu and S. C. Raghavan, *Eur. J. Med. Chem.*, 2010, **45**, 2748-2752.
7. T. Wang, N. Zhang, K. Zhang, J. Dai, W. Bai and R. Bai, *Chem. Commun.*, 2016, **52**, 9679-9682.
8. W.-C. Yen, B. Pal, J.-S. Yang, Y.-C. Hung, S.-T. Lin, C.-Y. Chao and W.-F. Su, *J. POLYM. SCI. POL. CHEM.*, 2009, **47**, 5044-5056.
9. B. P. Karsten, R. K. M. Bouwer, J. C. Hummelen, R. M. Williams and R. A. J. Janssen, *J. Phys. Chem. B*, 2010, **114**, 14149-14156.
10. A. Riaño, P. Mayorga Burrezo, M. J. Mancheño, A. Timalsina, J. Smith, A. Facchetti, T. J. Marks, J. T. López Navarrete, J. L. Segura, J. Casado and R. Ponce Ortiz, *J. Mater. Chem. C*, 2014, **2**, 6376-6386.
11. C. Lee, W. Yang and R. G. Parr, *Phys. Rev. B Condens. Matter*, 1988, **37**, 785-789.
12. A. D. Becke, *J. Chem. Phys.*, 1993, **98**, 5648-5652.
13. A. D. Becke, *J. Chem. Phys.*, 1993, **98**, 1372-1377.
14. P. C. Hariharan and J. A. Pople, *Theoret. Chim. Acta*, 1973, **28**, 213-222.
15. W. J. Hehre and W. A. Lathan, *J. Chem. Phys.*, 1972, **56**, 5255-5257.
16. G. W. S. M. J. T. Frisch, H. B.; Scuseria, G. E.; Robb, M. A.; Cheeseman, J. R.; Scalmani, G.; Barone, V.; Petersson, G. A.; Nakatsuji, H.; Li, X.; Caricato, M.; Marenich, A. V.; Bloino, J.; Janesko, B. G.; Gomperts, R.; Mennucci, B.; Hratchian, H. P.; Ortiz, J. V.; Izmaylov, A. F.; Sonnenberg, J. L.; Williams-Young, D.; Ding, F.; Lipparini, F.; Egidi, F.; Goings, J.; Peng, B.; Petrone, A.; Henderson, T.; Ranasinghe, D.; Zakrzewski, V. G.; Gao, J.; Rega, N.; Zheng, G.; Liang, W.; Hada, M.; Ehara, M.; Toyota, K.; Fukuda, R.; Hasegawa, J.; Ishida, M.; Nakajima, T.; Honda, Y.; Kitao, O.; Nakai, H.; Vreven, T.; Throssell, K.; Montgomery, J. A., Jr.; Peralta, J. E.; Ogliaro, F.; Bearpark, M. J.; Heyd, J. J.; Brothers, E. N.; Kudin, K. N.; Staroverov, V. N.; Keith, T. A.; Kobayashi, R.; Normand, J.; Raghavachari, K.; Rendell, A. P.; Burant, J. C.; Iyengar, S. S.; Tomasi, J.; Cossi, M.; Millam, J. M.; Klene, M.; Adamo, C.; Cammi, R.; Ochterski, J. W.; Martin, R. L.; Morokuma, K.; Farkas, O.; Foresman, J. B.; Fox, D. J. Gaussian, Inc., Wallingford CT., 2016.
17. J. D. Chai and M. Head-Gordon, *J Chem Phys*, 2008, **128**, 084106.
18. L. M. d. Costa, *J. Comput.Chem.*, 2004, **25**, 1463.
19. R. Ditchfield, W. J. Hehre and J. A. Pople, *J. Chem. Phys.*, 1971, **54**, 724-728.
20. A. Sánchez-Díaz, X. Rodríguez-Martínez, L. Córcoles-Guija, G. Mora-Martín and M. Campoy-Quiles, *Adv. Electron. Mater.*, 2018, **4**, 1700477.

21. X. Rodríguez-Martínez, M. S. Vezie, X. Shi, I. McCulloch, J. Nelson, A. R. Goñi and M. Campoy-Quiles, *J. Mater. Chem. C*, 2017, **5**, 7270-7282.

# PAPER III

## Efficient Exploration of the Composition Space in Ternary Organic Solar Cells by Combining High-Throughput Material Libraries and Hyperspectral Imaging

Harillo-Baños, A., Rodríguez-Martínez, X. & Campoy-Quiles, M.
*Advanced Energy Materials*, 1902417, 1–12 (2019).

ADVANCED ENERGY MATERIALS
www.advenergymat.de

# Efficient Exploration of the Composition Space in Ternary Organic Solar Cells by Combining High-Throughput Material Libraries and Hyperspectral Imaging

*Albert Harillo-Baños, Xabier Rodríguez-Martínez, and Mariano Campoy-Quiles**

**Organic solar cells based on ternary active layers can lead to higher power conversion efficiencies than corresponding binaries, and improved stability. The parameter space for optimization of multicomponent systems is considerably more complex than that of binaries, due to both, a larger number of parameters (e.g., two relative compositions rather than one) and intricate morphology–property correlations. Most experimental reports to date reasonably limit themselves to a relatively narrow subset of compositions (e.g., the 1:1 donor/s:acceptor/s trajectory). This work advances a methodology that allows exploration of a large fraction of the ternary phase space employing only a few (<10) samples. Each sample is produced by a designed sequential deposition of the constituent inks, and results in compositions gradients with ≈5000 points/sample that cover about 15%–25% of the phase space. These effective ternary libraries are then colocally imaged by a combination of photovoltaic techniques (laser and white light photocurrent maps) and spectroscopic techniques (Raman, photoluminescence, absorption). The generality of the methodology is demonstrated by investigating three ternary systems, namely PBDB-T:ITIC:$PC_{70}BM$, PTB7-Th:ITIC:$PC_{70}BM$, and P3HT:O-IDFBR:O-IDTBR. Complex performance-structure landscapes through the ternary diagram as well as the emergence of several performance maxima are discovered.**

## 1. Introduction

Organic solar cells (OSCs) show increasing potential, recently achieving over 16% power conversion efficiencies (PCEs) for single-junction devices.[1] OSCs are a versatile technology due to their solution processability, compatibility with low cost roll-to-roll production, flexibility, lightweight, and aesthetically tunable properties,[2] which makes them appealing when compared to their inorganic counterparts.

Different strategies are being followed in order to improve the initially low PCE of OSCs, such as the synthesis of novel materials including low bandgap donor polymers and non-fullerene acceptors (NFAs); deeper understanding and control of the active layer morphology through side-chain engineering; improved hole- and electron-extracting interlayers;[3] multi-junction devices (tandem structures),[4] etc. Among them, the ternary bulk heterojunction (BHJ) has emerged as an efficient route to improve the photovoltaic performance of single-junction OSCs. In a ternary OSC, three materials are used in the active layer of the OSC instead of the original BHJ binary blend (donor:acceptor, D:A).[5,6] In most cases, the ternary consists of either one donor and two acceptors ($D:A_1:A_2$) or two donors and one acceptor ($D_1:D_2:A$). Ternary blends often result in improved performance of one or more of the photovoltaic parameters in the OSC compared to the corresponding binaries, thus increasing the final PCE.[7,8] While a full understanding of ternaries is yet to be developed, a number of mechanisms have been identified to contribute to this improvement. These include the increase in light harvesting by broadening of the absorption spectrum through the use of materials with complementary absorption spectra; a more efficient exciton dissociation and better charge carrier transport due to the formation of cascade energy levels; improved photocurrent due to tailored phase separation landscape and improved stability by lock-in microstructure; and enhanced open circuit voltage due to an effective alloying effect.[9–14]

Indeed, some ternary OSCs are among the best performing devices reported to date.[15] The performance of ternary OSCs depends greatly on several parameters that must be taken into account and optimized. The choice of donor and acceptor materials forming the active layer, its blending ratio and the final film thickness are just a few, and they require careful optimization to achieve the most favorable nanomorphology in the ternary BHJ layer.[12,16] The composition ratio affects the phase separation and crystallinity of the materials, ultimately modifying the electrical transport properties and the final PCE of the OSC.[17]

The most conventional optimization protocol in ternary OSCs relies on the fabrication of tens of samples, which is extremely tedious and resources-consuming. The composition

A. Harillo-Baños, X. Rodríguez-Martínez, Dr. M. Campoy-Quiles
Institut de Ciència de Materials de Barcelona (ICMAB-CSIC)
Carrer dels Til·lers s/n
Campus UAB, Bellaterra 08193, Spain
E-mail: mcampoy@icmab.es

The ORCID identification number(s) for the author(s) of this article can be found under https://doi.org/10.1002/aenm.201902417.

© 2019 The Authors. Published by WILEY-VCH Verlag GmbH & Co. KGaA, Weinheim. This is an open access article under the terms of the Creative Commons Attribution License, which permits use, distribution and reproduction in any medium, provided the original work is properly cited.

DOI: 10.1002/aenm.201902417

phase space is 2D, exponentially increasing the number of samples needed for a comprehensive study of the ternary system compared to binaries.[18] As a result, the vast majority of research done in ternary OSCs only partially explores the ternary composition phase space. Indeed, the most common strategy consists of keeping the total D:A ratio fixed (typically at 1:1), while varying the relative composition of the two materials that have the same electronic character, i.e., D:($A_{1,x}$, $A_{2,(1-x)}$) or ($D_{1,x}$, $D_{2,(1-x)}$)::A.[7,9,17] Nevertheless, there is no evidence, nor a fundamental principle, suggesting that the optimum blending ratio should be found along the 1:1 D:A composition trajectory.[12] In fact, many binary systems characterized by unbalanced transport or optical properties show optimum compositions far from the 1:1 ratio. Similar arguments could also be applicable to ternaries.[9,12,15] Moreover, since the optimization process typically performed is very limited, the absolute optimum performance might still remain unknown, which opens the possibility for an even greater improvement than what was initially thought and reported. There may even be more than one maximum in the composition phase space. The challenge, then, becomes finding a methodology that enables exploring the ternary phase space in an efficient fashion.

For the simpler case of BHJ binary blends, the optimum composition ratio lies along a 1D line, i.e., somewhere in between 1:0 and 0:1 D:A ratios. A discrete and limited exploration of the optimum blending ratio in a single binary blend requires the fabrication of several devices; the efficiency optimization requires simultaneously optimizing the active layer thickness for each composition, thus rapidly scaling up the number of samples required for evaluating a binary system. For this kind of complex multiparametric problems, we have recently proposed alternative approaches based on the high-throughput screening of BHJ binary systems and bilayered heterojunction devices.[19,20] The main concept of these methodologies is the fabrication of samples with gradients in the parameters of interest, and then imaging the performance over the gradient to locate the optimum conditions.

Inspired by the success of that work, here we present a novel methodology to perform high-throughput processing and evaluation of the performance in ternary BHJ OSCs. The methodology minimizes the use of samples and resources by fabricating large-area devices with lateral composition gradients which are equivalent to a large library of homogeneous samples. The fabrication of the samples is based on a layer-by-layer or sequential deposition of the active layer materials by means of blade coating.[21,22] All three materials are dissolved in individual solutions without the need for premixing them and deposited sequentially along different coating directions and with effective thickness gradients. The realization of orthogonal and lateral thickness gradients allows the creation of a broad library of blending ratios in a single sample, covering different regions of the ternary blend diagram. These samples are then hyperspectrally imaged by using 1) Raman imaging, which serves to quantify the local composition of the blend; 2) photoluminescence (PL) imaging, to assess the degree of mixing and infer potential $V_{oc}$ changes; 3) absorption spectra imaging, which can be connected to the local photocurrent; 4) light beam induced current (LBIC), using monochromatic laser beams to extract the local photocurrent and being able to address the different materials separately, at least in part, by changing the excitation wavelength when the materials exhibit non-overlapping absorption spectra; and 5) white light beam induced current (WhiteBIC) to correlate the local photocurrent with a more realistic performance in Sun operating conditions. The combination of these large datasets, which are acquired colocally using the same setup, reveals a complicated performance landscape including, in some cases, the emergence of more than one photocurrent maximum. We apply this machinery to three different D:$A_1$:$A_2$ ternary blends, namely, PBDB-T:ITIC:$PC_{70}BM$; PTB7-Th:ITIC:$PC_{70}BM$; and P3HT:O-IDFBR:O-IDTBR. Our results indicate that the usual strategies followed to optimize blending ratios in ternary blends, such as keeping fixed the total D:A ratio in the ternary blend, might lead to incomplete conclusions with underestimated performances. This finding is highly relevant for the ternary BHJ technology as it suggests that PCEs can be boosted even further by fully exploring the composition landscape.

## 2. Optical Characterization: Raman Imaging of Ternary BHJ Blends

### 2.1. General Considerations and Requirements

Currently, the realization of panchromatic active layers is feasible given the low bandgap nature of conjugated polymers (**Figure 1**c) and the bandgap tuning capability of conjugated small molecules (Figure 1d), specially the new generation of NFAs such as ITIC. Therefore, we have decided to investigate three different D:$A_1$:$A_2$ blends in the active layer: PTB7-Th:ITIC:$PC_{70}BM$; PBDB-T:ITIC:$PC_{70}BM$; and P3HT:O-IDFBR:O-IDTBR. The first two combinations are expected to maximize the absorption as they combine a low bandgap polymer (PTB7-Th or PBDB-T) with the low bandgap and highly absorbing ITIC, together with the UV-absorbing $PC_{70}BM$ which could help in harvesting shorter wavelength photons while improving the morphology of the film.[23,24] On the other hand, the ternary blend P3HT:O-IDFBR:O-IDTBR represents a paradigmatic example of complementary absorption that has recently been demonstrated to yield PCEs as high as 7.7%, which is a promising value given the low cost associated to the mass production of such active layer materials.[17]

The determination of the local composition of inhomogeneous blend films by means of Raman spectroscopy underpins our high-throughput methodology.[19,20,25] This technique enables the use of gradients produced from solution with moderate spatial control. It imposes certain restrictions, however, in the materials to be tested, which we need to pre-evaluate for the selected ternaries. First, all materials should be clearly distinguishable in terms of their vibrational fingerprint. In this sense, the heterogeneity of the conjugated backbones in organic semiconductors translates into peak-rich and characteristic vibrational spectra, mainly in the spectral window associated to C=C and C—C stretching modes (≈1200–1600 $cm^{-1}$).[25] Figure 1a depicts the vibrational Raman spectra of three different donor materials, namely PBDB-T (*aka* PCE12), PTB7-Th (*aka* PCE10), and the workhorse *p*-type polymer RR-P3HT. Figure 1b illustrates the Raman vibrational fingerprint of four different conjugated small molecules used as electron transporting materials: a fullerene acceptor, $PC_{70}BM$; and three


© 2019 The Authors. Published by WILEY-VCH Verlag GmbH & Co. KGaA, Weinheim

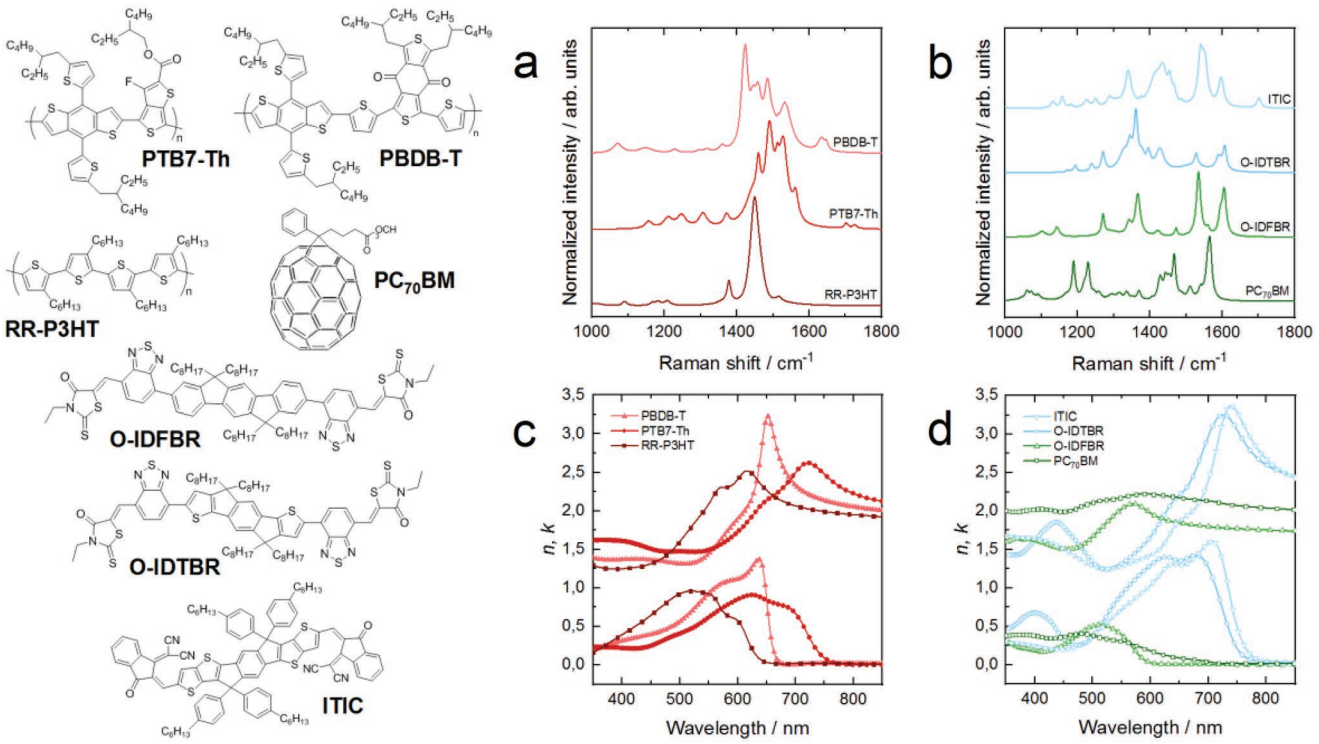


**Figure 1.** (Left) Chemical structures of the organic conjugated donor and acceptor materials used in this work. (Right) a) Normalized Raman spectra of donors and b) acceptors at 488 nm excitation. c) Refractive indices measured by means of variable-angle spectroscopic ellipsometry (VASE) of organic donors and d) organic acceptors.

NFAs, ITIC, O-IDTBR, and O-IDFBR. A thorough inspection of this vibrational library indicates that all possible ternary combinations should be, in principle, clearly identified. The Raman fingerprinting capability does not, hence, represent an important restriction in this sense (see also Ref. [25]).

Additionally, a successful analysis of ternary blend films requires the Raman cross-section of the materials to be similar enough to properly deconvolute the spectra and enable an accurate quantification of the composition of the film; otherwise, the large Raman intensity ratio between dissimilar materials might hinder or even impede a proper deconvolution.[20,25] **Table 1** summarizes our experimentally deduced Raman cross-section for the seven materials employed, a determination that requires previous knowledge of the complex refractive index of each material (see Figure 1) and the measurement of the thickness-dependent Raman signal using a sample with a thickness wedge.[25] Following our previous accuracy estimates, only those blends including RR-P3HT as donor and either ITIC or $PC_{70}BM$ as acceptor(s) would be problematic due to its cross-section ratio being larger than 30.[25] Note that the Raman cross-sections and refractive indices only need to be measured once per material, and can be also taken from literature.

**Table 1.** List of Raman cross-section ratios with respect to that of $PC_{70}BM$ at 488 nm excitation for the donor and acceptor materials used in this work. The Raman mode frequencies to which the Raman cross-sections are referred to and the reference spectra normalized by are also included.

| Material | Raman cross-section | Raman band [$cm^{-1}$] |
|---|---|---|
| RR-P3HT | 57 ± 11 | 1450 |
| PBDB-T | 5 ± 1 | 1424 |
| PTB7-Th | 2.4 ± 0.3 | 1490 |
| O-IDFBR | 9 ± 1 | 1535 |
| O-IDTBR | 4 ± 1 | 1361 |
| ITIC | 1.2 ± 0.3 | 1540 |
| $PC_{70}BM$ | 1 | 1557 |

### 2.2. Quantification of the Volumetric Composition in Ternary Blends

We have recently demonstrated that Raman spectroscopy constitutes a powerful tool for the mapping of film features such as thickness and composition by properly deconvoluting and quantifying the scattered Raman intensity.[19,20,25] The approach applies even to active layers in working devices as the thickness and complex refractive indices of the interlayers are considered in the transfer matrix modeling. So far, the methodology has been applied to binary BHJ blends as well as evaporated bilayer OSCs.[19,20] Nevertheless, the extension to BHJ ternary blends is straightforward as the third component is added as an extra term in the corresponding scattered field intensity calculations

$$I_{R,\text{blend}}(d,\nu_u,\omega) \propto \int_0^d |E_R(x,\nu_u)|^2 \mathrm{d}x \sum_{u=1}^{3} \nu_u \sigma_{R,u} I_{\text{ref},u}(\omega) \quad (1)$$


© 2019 The Authors. Published by WILEY-VCH Verlag GmbH & Co. KGaA, Weinheim

where $d$ stands for the thickness of the blend film; $v_u$ is the volumetric fraction of the $u$-th component; $\omega$ refers to the frequency or Raman shift; and $I_{\mathrm{ref},u}$ represents the reference Raman vibrational fingerprint of the $u$-th component normalized at the intensity of the mode associated with the cross-section $\sigma_{R,u}$ (see Table 1). The transfer matrix calculation computed to get the scattered intensity term, $|E_R(x,v_u)|^2$, depends on both the blend film thickness and its volumetric composition. The film thickness modulates the scattered intensity, while the volumetric blending ratio is assumed to weight the complex refractive index of the film as $\varepsilon_{\mathrm{blend}} = \sum_{u=1}^{3} v_u\, \varepsilon_u$.

In the case of ternary blends with complementary absorption profiles the Raman scattered intensity at 488 nm excitation sharply oscillates as a function of the active layer thickness, reaching the absolute maximum at ≈60–70 nm of film thickness; this is a consequence of the large oscillator strength exhibited throughout the visible regime in this sort of blends and also due to the interference enhancement of the metallic back electrode encountered in the functional device.[25] This fact constrains the accessible range and reliability of thickness values characterized by means of Raman spectroscopy to a window that is usually far from the optimum in OSCs (≈100–110 nm). Furthermore, the estimation of the complex refractive index in ternary blends as a weighted linear combination of the pristine indices might be too simplistic considering the morphological changes upon mixing.[26] This could be especially problematic when blending materials with large extinction coefficients in pristine films, such as PBDB-T, ITIC, or O-IDTBR (Figure 1), thus adding extra uncertainty to the transfer matrix calculations.

On the other hand, while the optical constants are highly dependent on the environment and surroundings of the embedded optical transition dipoles, we expect the Raman cross-sections, which respond to local vibrations of the conjugated backbone, to be much less affected upon blending. Based on these assumptions we simplified the Raman spectral modeling by substituting the transfer matrix integral by a free parameter, $\beta$, that weights the summation of the reference spectra, such that

$$I_{R,\mathrm{blend}}\left(\beta, v_u, \omega\right) \propto \beta \sum_{u=1}^{3} v_u\, \sigma_{R,u}\, I_{\mathrm{ref},u}\left(\omega\right) \tag{2}$$

Equation (2) enables the determination of local composition but not thickness. Note that in Equation (2), we have implicitly calculated and measured the Raman intensity versus film thickness dependence of the pristine materials to obtain their corresponding Raman cross-sections (see Ref. [25]), so the interference nature is taken into account in part. This determination was performed using their pristine optical constants as inputs in the transfer matrix calculation.

Interestingly, we have observed that in all types of D:$A_1$:$A_2$ blends explored in this work the corresponding vibrational fingerprints are somehow shifted with respect to our tabulated and reference Raman spectra obtained in pristine films (vide infra). The (blue) shift is especially pronounced in the case of donor polymers, a fact that is related with a decrease of $\pi$-electron delocalization due to shortened conjugation length and the increase of intermolecular interactions.[27] In blended films, the blue shifting is usually related to a larger miscibility of the materials involved and partial aggregation of the acceptor small molecules. Therefore, an extra degree of freedom is added to improve the goodness of fit, namely, a small rigid shift of the Raman peaks, $\delta_u$, finally yielding

$$I_{R,\mathrm{blend}}\left(\beta, v_u, \omega, \delta_u\right) \propto \beta \sum_{u=1}^{3} v_u\, \sigma_{R,u}\, I_{\mathrm{ref},u}\left(\omega + \delta_u\right) \tag{3}$$

Note that, experimentally, $\delta_u$ is < 0.5% the value of $\omega$. We have systematically observed that for the different samples and material combinations studied here, the model summarized in Equation (3) leads to significantly improved fits of the experimental data compared to the rigorous case in Equation (1). We show in Figure S1, Supporting Information, a comparison of these three methods in the fit of a ternary sample with gradients. Equation (3) model has the virtue of making fewer assumptions regarding the similarity of the structure in the pristine materials and their corresponding blends. Indeed, we will show below that imaging $\delta_u$ for the vibrations corresponding to each material provides useful insights into the degree of mixing and/or purity of the structural domains. An additional analysis of the sources of uncertainty in the determination of compositions can be found in the Supporting Information.

## 3. Generation of Ternary Blend Libraries

The high-throughput screening of ternary blends requires the generation of blend composition libraries covering the largest possible area in the ternary diagram. This should be realized using the minimum number of samples (i.e., time and resources) in combination with rapid characterization techniques to be truly effective and high-throughput experimentation. We have recently demonstrated that, for binary D:A blends, it is possible to cover the entire composition range (from 1:0 to 0:1) in a single large-area solar cell by blade coating two nearby drops of the pristine solutions.[19] The processing results in films showing lateral composition and thickness gradients when combined with accelerated blade coating. Their ulterior characterization by means of Raman spectroscopy mapping and LBIC yields, in a single run, the active layer parameters (thickness and composition) which maximize the photovoltaic performance. For the generation of ternary blend composition libraries, we first tried to adapt our previous experience on the generation of binary composition gradients.[19] We explored the coating of nearby drops atop a solid dried film, which resulted in limited and localized composition ratios in the ternary diagram. We therefore, explore a number of different deposition approaches which included multiple drops and sequential deposition. Among the variety of approaches we tested, we found that the sequential (or layer-by-layer) deposition of films yielded the more complete and reproducible ternary libraries. The details of this approach are described in the following paragraphs.

Ternary blend libraries are obtained by processing the active layer as a sequential deposition of each of the pristine solutions (D, $A_1$, and $A_2$), one on top of the other, while using the same solvent and processing parameters (stage temperature and blade speed). Interestingly, the sequential deposition using non-orthogonal solvents does not lead to the detachment of


© 2019 The Authors. Published by WILEY-VCH Verlag GmbH & Co. KGaA, Weinheim

the underneath layers but to a vertical intermixing and gradual vertical segregation in some cases. This approach is also known as layer-by-layer deposition and has recently been demonstrated to yield an optimized vertical phase segregation in some polymer:NFA binary OSCs when the devices are processed in accordance with their vertical architecture, i.e., with the donor (acceptor) layer facing the anode (cathode).[21,28]

Our exploration regarding $D:A_1:A_2$ blends indicates that the layer coating order matters to realize proper ternary active layer film libraries. The processing must start with the donor (polymer) first, followed by the acceptors (small molecules) in sequential layers. We hypothesize this requirement is related with the viscosity of the polymeric solution, which turns out to be critical when the donor is casted in second or third place. In such cases, we do not observe a significant exploration of the ternary composition diagram but the formation of either binary blends (when the polymer is deposited in second place) or even to the absence of blending (when the polymer is deposited in the last place), as evidenced from Raman scattering measurements.

The importance of viscosity is apparent for ternary combinations of the type $D_1:D_2:A$, containing two donor polymers and a small molecule acceptor. Figure S2, Supporting Information, shows the ternary phase diagram for one such sample, consisting of the P3HT:PCDTBT:$PC_{70}BM$ ternary. More than 80% of the composition space can be explored in a single sample by properly matching the ink viscosities and casting parameters.

Therefore, after first coating the donor polymer layer, we proceed with the sequential coating of the acceptor layers. These layers are processed by spreading the pristine solutions from collateral corners of the large aspect-ratio, 75 mm long by 25 mm wide, indium tin oxide (ITO) substrates we use as transparent conductive electrode (see **Figure 2**). By setting up the blade coating process to start at a sharp substrate corner we obtain a rather controllable thickness gradient driven by the variation of the wetting front width as the blade moves over the substrate. Experimentally this is an appealing approach to obtain gradients as it simply requires rotating the substrate by 45° with respect to the coating direction to get the steepest thickness gradient. Hence, by combining in a single sample the layer-by-layer deposition consisting of a homogeneous polymer film followed by two different small molecule acceptors blade coated from collateral corners, we explore a large area of the ternary composition diagram, as depicted in Figure 2a. The region explored can be tuned, at least in part (either I, II, or III in Figure 2a) depending on the thickness of the layers, which is mainly determined by the solution weight loading and the coating speed. In fact, we checked that by blade coating the first polymer layer in the form of a lateral thickness gradient (by accelerating the blade speed) we could purposely extent the range of donor loading explored in the ternary diagram (Figure 2b).

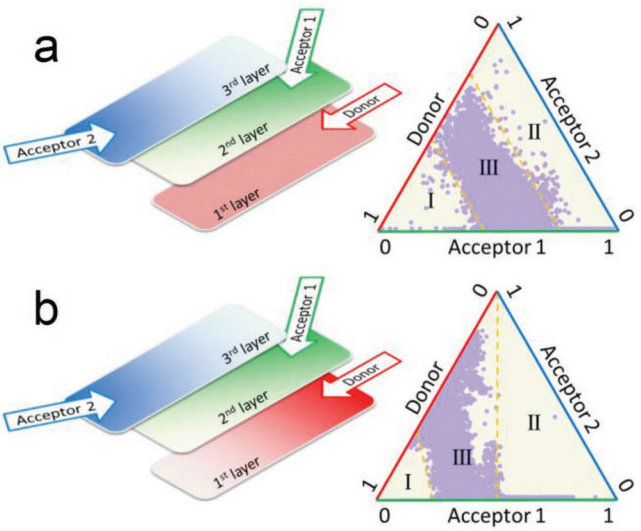


**Figure 2.** Sketches of the sequential blade coating deposition steps used to explore ternary blend composition diagrams for a) a homogeneous first donor layer and b) a thickness gradient as the first donor layer. The dots correspond to experimental data obtained for a RR-P3HT:O-IDFBR:O-IDTBR ternary.

## 4. Ultrafast Characterization of Ternary Libraries

**Figure 3** illustrates a set of the raw mapping data extracted from a single ternary sample of PTB7-Th:$PC_{70}BM$:ITIC processed according to the thickness gradient method depicted in Figure 2b. In this case, a PTB7-Th thickness gradient was deposited from left ([−20, $y$] coordinates in Figure 3a) to right ([25, $y$]); then a pristine solution of $PC_{70}BM$ was casted in diagonal from the top-left corner ([−20, 0]); and finally the ITIC layer was processed from the top-right corner of the sample ([25, 0]).

In order to minimize measuring time, we begin by performing a coarse (low-resolution, 45 × 25 positions) photocurrent map with white light illumination (Figure 3a) which takes less than 15 min to complete for a large area of 45 × 25 $mm^2$. This coarse photocurrent map is intended to quickly identify and locate the high performing areas of the device, thus the region of interest. This area is then zoomed in and imaged with higher resolution (Figure 3b) and several complementary techniques. During the acquisition of this high resolution photocurrent map, we simultaneously collect the reflectivity spectra of the full device stack ($R_s$) at each position. This reflection map, after normalization by the reflectivity of the back electrode (usually silver, $R_{Ag}$), yields the absorption ($A$) of the device as $A = 1 - R_s/R_{Ag}$ at each position. Absorption maps at selected wavelengths are shown in Figure 3f,g. We then proceed with the monochromatic characterization of the device by using a 633 nm laser to measure photocurrent (Figure 3d) and at the same time PL (Figure 3e) in a single run. While less precise than electroluminescence measurements, the energy of the PL maximum can be correlated in some cases with the charge transfer energy, and thus used as a proxy for effective *local* $V_{oc}$ (Figure S3, Supporting Information).[29] PL quenching could also be correlated with efficient charge transfer and thus, with the degree of mixing. Finally, we colocally measure the Raman scattered spectra (which integrated intensity is depicted in Figure 3h) and the photocurrent at 488 nm excitation (Figure 3c). The selection of 488 nm as excitation wavelength in Raman scattering is related to the cross-section compatibility between materials, the fulfillment of resonant conditions and the absence of disturbing PL


© 2019 The Authors. Published by WILEY-VCH Verlag GmbH & Co. KGaA, Weinheim

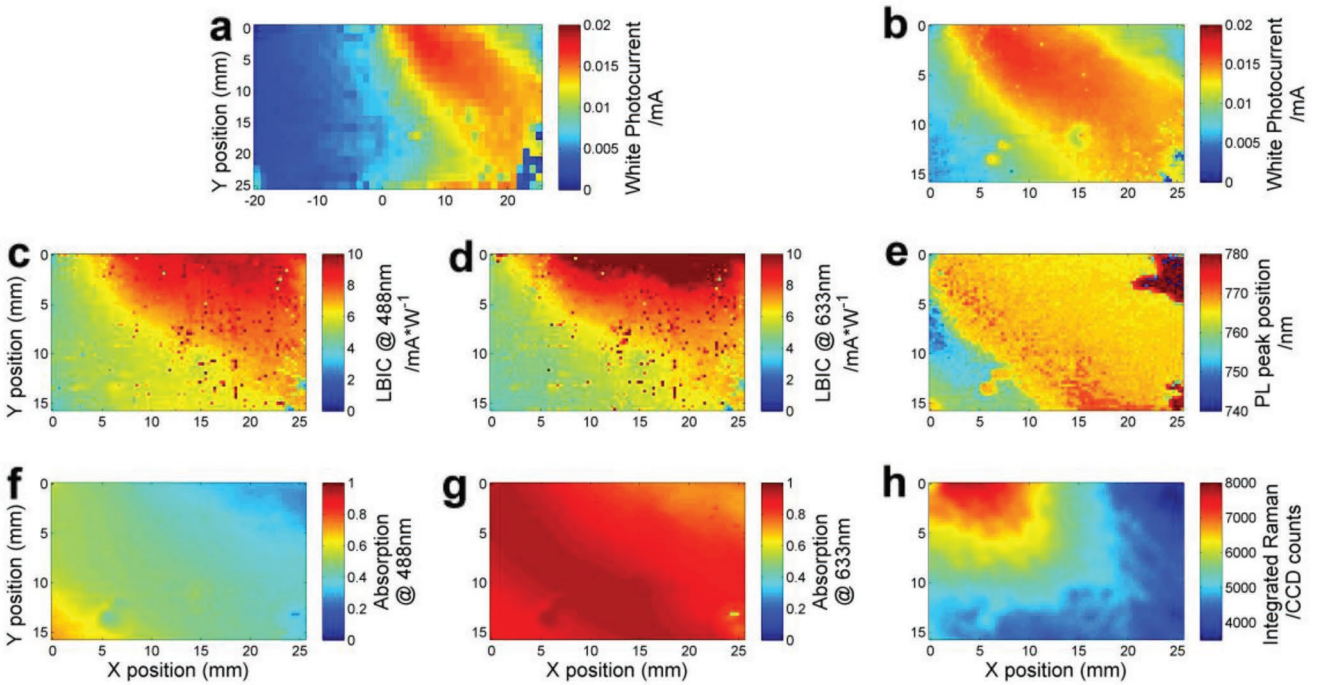


**Figure 3.** Full set of optical characterization maps performed in a sequentially deposited sample of PTB7-Th:$PC_{70}$BM:ITIC, with the donor layer processed as a thickness gradient. a) Coarse photocurrent map obtained with white light; b) higher resolution white light photocurrent map centered at the region of better performance; c) photocurrent map acquired at 488 nm excitation; d) photocurrent map acquired at 633 nm excitation; e) wavelength of the main PL peak measured at 633 nm excitation; f) absorption at 488 nm excitation wavelength; g) absorption at 633 nm excitation wavelength; h) integrated Raman scattered intensity from 1100 to 1600 $cm^{-1}$ at 488 nm excitation.

backgrounds which could potentially hinder the deconvolution of the spectra.[25] The complete set of optical characterization images includes two low resolution images, three 3D images (photocurrent with typically 86 × 50 spatial points each) and three 4D images (Raman, absorption, and PL spectra (86 × 50) points × 1024 spectral points), which add up to more than 13 million experimental data points. All these measurements are performed in a row and using a single (confocal Raman) setup in less than 3 h, thus representing a paradigmatic example of high-throughput evaluation of solar cells.

The white light photocurrent maps (Figure 3a,b) are acquired using the built-in lamp in our confocal Raman scattering setup, which due to technical limitations cannot be coupled to an external illumination source, such as an AM1.5 solar simulator. Even so, the emission spectrum of the lamp spans most of the visible/NIR range (Figure S4, Supporting Information), thus we expect the corresponding photocurrent maps being qualitatively similar to what we would obtain using a dedicated light source, albeit somehow UV and NIR poor, thus slightly underestimating the photocurrent of materials that absorb strongly on those regions. The importance of using broadband illumination instead of the more standard laser is apparent when comparing the WhiteBIC (Figure 3b) and LBIC at 488 nm (Figure 3c) and 633 nm (Figure 3d). The single-wavelength photocurrent maps clearly indicate that the maximum photocurrent is generated at a different location (i.e., a different active layer thickness and blend composition) with respect to what we observe with white light illumination. We could expect this type of behavior for systems with at least partially complementary absorptions in which all materials contribute to the photocurrent: monochromatic illumination may be indicating a region rich in a material with strong absorption at that specific wavelength, rather than the real optimum of the whole cell. This result indicates that white light should be employed in order to evaluate the performance of non-fullerene binaries and ternary devices in typical operating conditions. Furthermore, our experience suggests that the use of white light illumination focused as a large spot of ≈200 µm in diameter leads to qualitatively smoother photocurrent maps, i.e., less prone to suffering spatial photocurrent fluctuations associated to scattering by defects and dust. Despite using low magnification (10X) and low numerical aperture objectives (NA 0.25), the photocurrent maps measured using monochromatic sources of light (Figure 3c,d) generally show a larger density of photocurrent spikes. This is a result of the smaller spot size (typically 10 µm in diameter) and more pronounced focusing ability of monochromatic light, which is then more likely to scatter at the tiny defects (aggregates, scratches, dust) encountered throughout the layered device stack and the substrate. We would like to emphasize that the photocurrent images are not the result of a hidden thickness variation, as the thickness and photocurrent maps do not seem to be correlated (Figure S5b, Supporting Information).

The acquisition of monochromatic photocurrent maps is, however, useful to identify the relative contribution of the blended components to the generation of free charge carriers. For the ternary blend studied in Figure 3, we expect the absorption spectrum being largely panchromatic due to the complementary absorption of its components, PTB7-Th:$PC_{70}$BM:ITIC (Figure 1).


© 2019 The Authors. Published by WILEY-VCH Verlag GmbH & Co. KGaA, Weinheim

According to their complex refractive index, at 633 nm excitation PTB7-Th and ITIC domains should be selectively contributing to the photogeneration of excitons, while at 488 nm excitation all three materials are absorbing. Also, the overall extinction is likely to be higher at 633 nm (Figure 3g) than at 488 nm (Figure 3f) excitation due to the noticeable larger oscillator strength of PTB7-Th and ITIC at 633 nm than $PC_{70}BM$ at 488 nm excitation. Interestingly, the 633 nm LBIC follows quite closely the ITIC composition (Figure S5, Supporting Information), which is reasonable given the very high oscillator strength of this material at these photon energies (Figure 1d). The absorption map at 633 nm shown in Figure 3g correlates well with the total volumetric fraction of PTB7-Th and ITIC obtained from the quantitative analysis of the Raman scattered intensity (Figure S5d, Supporting Information). Conversely, the spatial variations observed in Figure 3f are closely matching the measured volumetric fraction map of $PC_{70}BM$ in the ternary blend (Figure S5e, Supporting information). Examples of the raw absorption, PL and Raman spectra at selected loci are given in Figure S6, Supporting Information. Interestingly, and despite the larger absorption at 633 nm, we observe that both monochromatic photocurrent maps are quantitatively similar (Figure 3c,d). The fact that the maximum white light photocurrent is displaced with respect to the monochromatic photocurrent maps and absorption maps suggests that the optimum composition results from the fine balance between optical properties and electronic transport (facilitated with increasing fullerene content). This is, for instance, reflected by the fact that the optimum composition for samples before and after annealing is different (Figure S7, Supporting Information, and discussion below).

Finally, the PL spectra (Figure S6a, Supporting Information) vary both in peak central position (Figure 3e) and in integrated intensity (Figure S5a, Supporting Information) throughout the sample. We generally observe that the PL intensity is larger in the ITIC-rich regions that are depleted of donor; in fact, the PL intensity map resembles an inverted PTB7-Th volumetric loading image. This finding confirms that PL quenching is a good proxy for efficient charge transfer. Regarding the position of the maximum in the PL spectra we notice that it slightly redshifts as the loading ratio of ITIC (PTB7-Th) is decreased (increased); conversely, the highly enriched PTB7-Th regions appear blueshifted possibly due to the fact that the PL of the polymer becomes dominant in the therein collected spectra. The redshifted PL on the highly mixed regions may be an indicative of the contribution of the charge transfer PL to the overall sample PL. If this interpretation is correct, the small PL shift (about 20 meV) in the region where photocurrent is high (Figure 3b) would suggest that the potential changes in $V_{oc}$ throughout the composition phase diagram are relatively small (<3%) compared to the large photocurrent changes. In other words, the PCE of the ternary will probably be dominated by photocurrent changes, and thus Figure 3b would represent well the cell efficiency.

## 5. Performance Phase Diagram in Ternary Systems

The colocal acquisition of the characterization maps illustrated in Figure 3 and Figure S5 (Supporting Information) enables the removal of their spatial dependence. Therefore, the relevant parameters can be plotted in ternary composition diagrams by matching them with the composition maps extracted by means of Raman imaging spectroscopy (Figure S5, Supporting Information). **Figure 4** depicts the corresponding diagrams for two different and thermally annealed PTB7-Th:ITIC:$PC_{70}BM$ devices. In the two samples, acceptor layers were processed in different order to cover complementary areas of the diagram. Note that in these plots only the regions of highest performance were zoomed in and analyzed with increased spatial resolution.

Figure 4a depicts the local photocurrent extracted under white light illumination over the phase diagram of the ternary. We identify up to three different photocurrent maxima on a relatively smooth landscape. The first and lower one is centered at a blending ratio of PTB7-Th:ITIC:$PC_{70}BM$ 0.35:0.60:0.05 (v:v:v), which matches the single maximum we observed in the same sample prior to the annealing process (Figure S7, Supporting Information). Upon thermal annealing, a second photocurrent maximum emerges at a ratio of 0.2:0.6:0.2 (v:v:v) which is indicative of an improved film morphology motivated by the annealing process (see below). The third and markedly higher photocurrent maximum corresponds to a ratio of 0.2:0.2:0.6 (v:v:v). The first two maxima may be absorption dominated cases (ITIC exhibits high oscillator strength, see Figure 1), while the third may correspond to a ternary composition characterized by good-extraction properties. A deep minimum in performance is found for a ratio of 0.5:0.3:0.2 (v:v:v) which is observed in both samples. Interestingly, such minimum lies on the usual blending ratio scheme followed in the literature, i.e., keeping the donor loading fixed at 50%, while varying the ratio of both acceptors. We observe that the high performing areas are located in regions of low polymer loading (15–30 vol%); then, the three maxima differ in the ratio of the acceptors, being the more favorable a larger $PC_{70}BM$ loading in the present case. The reason for this dissimilar optimization blending ratios is likely to be related to the aforementioned optical versus transport compromise, together with a variable degree of phase separation and type of nanomorphology attained for each composition.[16]

In order to doublecheck the existence of two photocurrent maxima scenario in PTB7-Th:ITIC:$PC_{70}BM$ ternary blends, we have fabricated samples with fixed stoichiometry. These samples were fabricated to exhibit a thickness gradient in order to fully explore the parametric landscape. In this set of samples the donor weight fraction was kept constant at 25 wt%, while the relative acceptor loadings were varied accordingly to follow the composition trajectory that included several maxima in the ternary library (Figure 4a). The results depicted in **Figure 5**c (including two binaries and four ternary combinations) indicate that when looking at the top performing shell of devices an acute photocurrent drop occurs close to 0.25:0.35:0.40 (w:w:w) ternary ratio, resulting in two photocurrent maxima. Upon extraction of the corresponding volumetric loading ratios through Raman spectroscopy (Figure 5b) we observe that the location of the minimum and both maxima matches the previously found ratios (Figure 4a). Note that due to the dissimilar typical densities of polymers (1.0–1.1 g $cm^{-3}$) and small molecules (1.3–1.7 g $cm^{-3}$), there is a large shift between volumetric and weight loading ratios that has to be considered when interconverting such


© 2019 The Authors. Published by WILEY-VCH Verlag GmbH & Co. KGaA, Weinheim

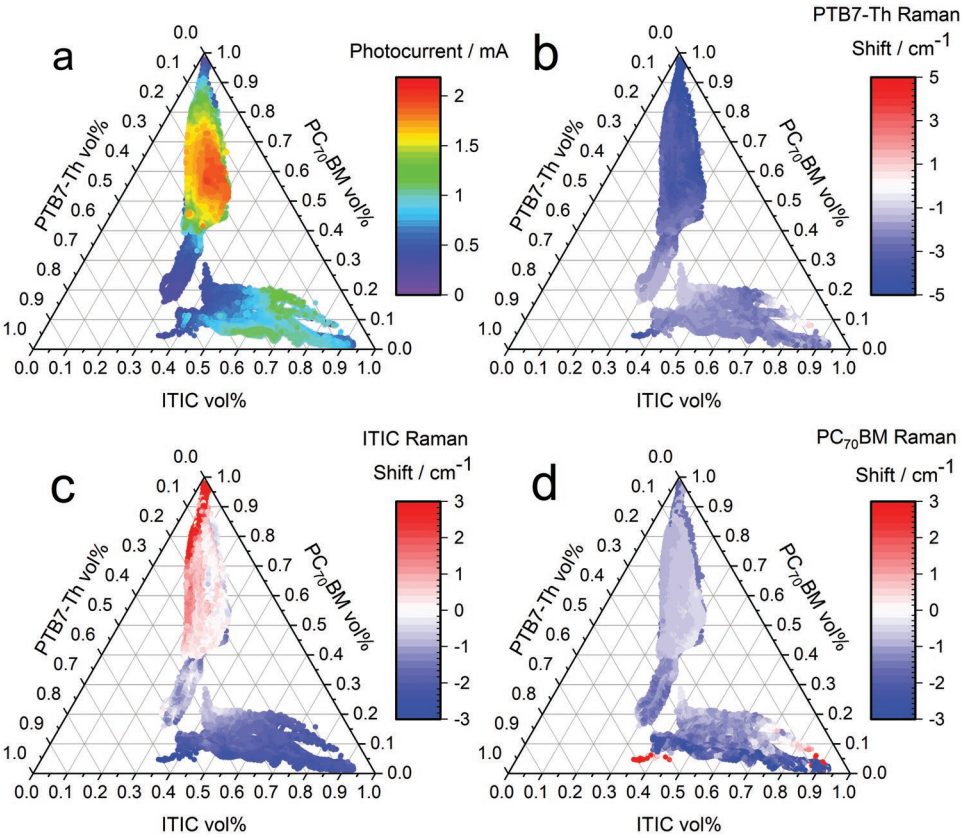


**Figure 4.** Ternary composition diagrams for two ANNEALED PTB7-Th:ITIC:$PC_{70}BM$ devices processed changing the coating order of the acceptor materials. The color scales refer to: a) photocurrent under white light illumination. b) Raman peak shift attributed to PTB7-Th, c) ITIC, and d) $PC_{70}BM$.

magnitudes. It is important to highlight that due to the dispersion in photocurrent induced by the active layer thickness variations ($y$-axis in Figure 5c) ternary libraries might lead to incomplete performance landscapes if such parameter is not fully explored. However, this limitation can be circumvented through the complementary use of active layer thickness gradients once the optimum performance ratio is identified.

This set of stoichiometrically controlled devices serves to validate the high-throughput generation of ternary libraries as in terms of photovoltaic performance it leads to the same conclusions obtained following the traditional sample-by-sample methodology, albeit with a noticeably increased statistical meaning and reduced use of resources and time. Furthermore, we have confirmed that: i) in ternary systems multiple

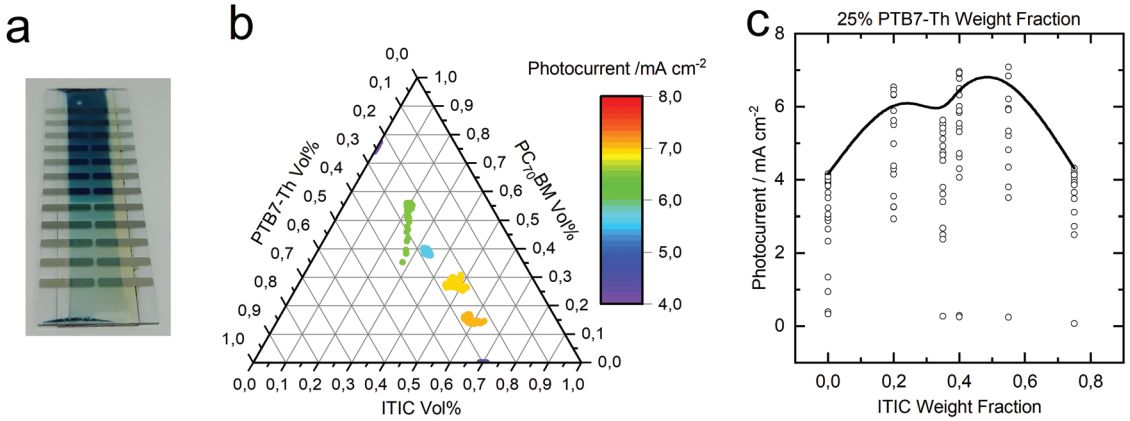


**Figure 5.** a) Optical image of a sample consisting of 24 different devices (12 per side) with the ternary PBT7-Th:ITIC:$PC_{70}BM$ blend as active layer. The active layer was blade-coated as a lateral thickness gradient. b) Representation of the ternary composition diagram of six different samples (24 devices each, of variable thickness and fixed stoichiometric ratios), with the highest photocurrent obtained in the sample as color scale. c) Photocurrent dispersion obtained for all wedge-like samples (keeping fixed PTB7-Th loading at 25 wt%) as a function of ITIC wt%. The black line is a guide to the eye.


© 2019 The Authors. Published by WILEY-VCH Verlag GmbH & Co. KGaA, Weinheim

photocurrent maxima are feasible; ii) the thickness exploration using gradients is sufficient to capture the essence of the problem; and iii) the error in the determination of the composition using Raman is typically of the order of 5%–10%, which is an estimation based on the dispersion observed in Figure 5b for stoichiometrically controlled devices. Further details regarding the accuracy and error estimations of the Raman methodology are provided in the Supporting Information.

To gain further insights about the extent in which the film morphology is critical for the device performance, we performed further analysis of the Raman spectra, focusing now on the shifts of the corresponding vibrational modes. Raman mode shifting in conjugated polymers constitutes a phenomenon typically observed upon blending with small molecules. Depending on their degree of miscibility, the small molecules are able to intercalate throughout the polymer domains disturbing their planarity and conjugation length while affecting the intermolecular interactions. For simplicity, we perform the Raman shift analysis by assuming that the vibrational fingerprint of each material is rigidly shifted according to a corresponding $\delta_u$ parameter (see Equation (3)). In the case of PTB7-Th (Figure 4b), we notice that its vibrational bands are blueshifted with respect to the reference spectra took in pristine polymer films. Still, the shift is not as large as that observed upon degradation for the related compound PTB7,[30] thus suggesting that the observed dispersion is likely due to changes in the morphology of the film. Interestingly, the high performing areas explored in Figure 4a correlate well with large blueshifts (≈3 $cm^{-1}$) in PTB7-Th, being more pronounced at high $PC_{70}BM$ loadings (≈5 $cm^{-1}$); conversely, in the low performing areas, the Raman shift of PTB7-Th vibrational bands is, in average, close to zero. These findings suggest, on the one hand, that PTB7-Th requires a thorough intermixing with the acceptors to yield an efficient splitting of the photogenerated excitons; and, on the other hand, that the miscibility of $PC_{70}BM$ with PTB7-Th is larger than that of ITIC. The corresponding ternary diagrams for the Raman shift of ITIC (Figure 4c) and $PC_{70}BM$ (Figure 4d) do not show a significant dispersion close to the highest photocurrent maximum, thus suggesting that purer ITIC and $PC_{70}BM$ domains coexist in this blending ratio regime. In the case of ITIC there is a moderate up shifting as its fraction in the film decreases. Consequently, the analysis of the Raman shifts in PTB7-Th:ITIC:$PC_{70}BM$ blends indicates that the optimum composition corresponds to a morphology consisting of well-mixed donor:acceptor domains with about 15%–30% polymer content (large mode shifts), together with relatively pure (small mode shifts) domains of the two acceptors.

It is insightful to look at the same sample before and after annealing (Figure 4 and Figure S7, Supporting Information). A second optimum composition emerges within the phase diagram. In this case, annealing places the second optimum at higher fullerene contents, which could be a result of its more favorable steric interdiffusion through the film and subsequent improvement in the extraction of charges. An optimum composition dependent on the thermal treatment has also been observed for binary systems.

To show the generality of the high-throughput methodology, in the next series of experiments we extended the ternary blend library generation and colocal acquisition of Raman/PL/Absorption and photocurrent maps to two additional ternary blend systems, namely, PBDB-T:ITIC:$PC_{70}BM$ and P3HT:O-IDFBR:O-IDTBR (see **Figure 6**). In both cases, the devices were fabricated following the procedures described above, and changing the ordering of the acceptor layers to broaden the area covered in the ternary diagrams (see the Experimental Section). The extended data for these systems can be found in Figures S8–S12, Supporting Information.

Figure 6a shows that for PBDB-T:ITIC:$PC_{70}BM$ blends the highest performance corresponds to blending ratios spanning between 10 and 30 vol% of $PC_{70}BM$ loading. More specifically, the photocurrent maximum locates at a blending ratio of 0.45:0.30:0.25 (v:v:v, PBDB-T:ITIC:$PC_{70}BM$). The here obtained optimum blending ratio is in very good agreement with what has been recently found in ternary spin coated devices, i.e., 0.5:0.4:0.1 (w:w:w, PBDB-T:ITIC:$PC_{70}BM$).[23] (Note that converting from volume to weight percentage can easily be done when the material densities are known) In this system, the polymer has an almost overlapping absorption with ITIC, which in turn shows in the fact that both LBIC and WhiteBIC

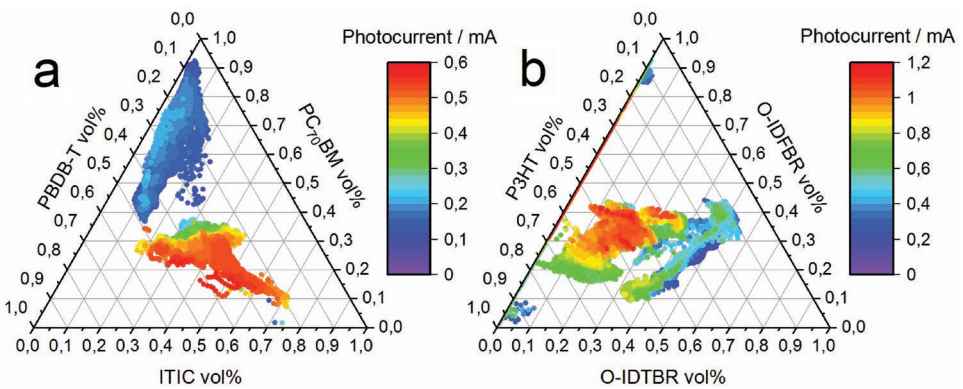


**Figure 6.** Ternary composition diagrams of the regions with the highest performance corresponding to a) two PBDB-T:ITIC:$PC_{70}BM$ devices processed changing the coating order of the acceptor materials; and b) two RR-P3HT:O-IDFBR:O-IDTBR devices processed changing the coating order of the acceptor layers and two extra devices processed following the two-drop processing method. The color scale corresponds to the photocurrent extracted under white light illumination.


© 2019 The Authors. Published by WILEY-VCH Verlag GmbH & Co. KGaA, Weinheim

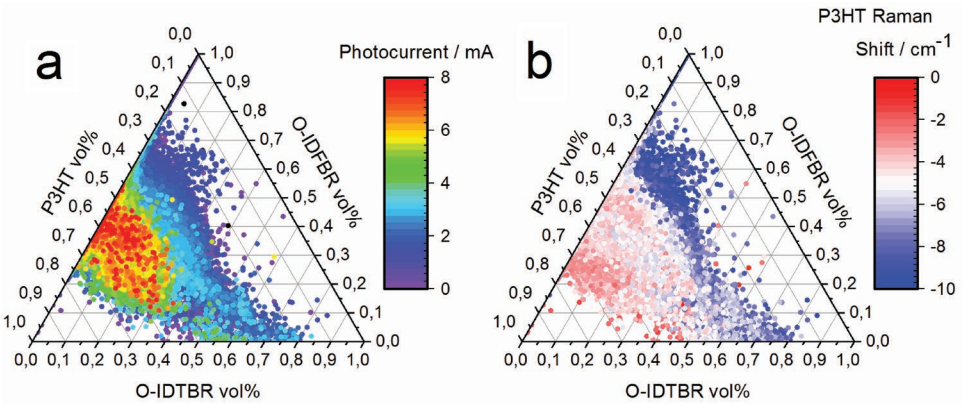


**Figure 7.** Ternary composition diagrams corresponding to seven different RR-P3HT:O-IDFBR:O-IDTBR devices (≈150 000 data points per plot). The color scale corresponds to a) photocurrent at 488 nm excitation; and b) Raman peak shift of RR-P3HT.

have a similar spatial distribution (Figures S8 and S9, Supporting Information). Moreover, the contribution to the total photocurrent of relatively long wavelengths (633 nm) is larger than that of higher energies (488 nm), as seen in the corresponding LBIC maps and as expected by the corresponding absorption profiles. A series of samples with fixed stoichiometry has also been fabricated and are shown in Figure S12 (Supporting Information).

Regarding RR-P3HT:O-IDFBR:O-IDTBR blends (Figure 6b), a single white light photocurrent maximum is obtained for a ratio of 0.5:0.4:0.1 (v:v:v). This value lies relatively far from what has been previously reported for spin-coated devices, i.e., 0.5:0.15:0.35 (w:w:w).[17] P3HT has a very large Raman cross-section that can yield higher uncertainties on the composition determination compared to the other systems. The deviation from published results is, however, larger than the expected uncertainty on our composition. Therefore, we believe that the discrepancy may be related to the known factors affecting the efficiency in this system, such as molecular weight of the polymer, different attained morphologies between spin and blade coating and/or actual differences in the optimum composition depending on the specific drying kinetics associated to each processing method. Similar to the case of PTB7-Th based ternaries, which show an annealing dependence optimum composition, we believe that morphology is the most likely cause of the observed shift. Evidence supporting a strong dependence of efficiency in morphology can be extracted from the almost three times larger PL shifts (Figures S10 and S11, Supporting Information) observed in this ternary compared to the other two.

In order to gain further insights into the observed discrepancy, an additional series of RR-P3HT:O-IDFBR:O-IDTBR samples were prepared. In this case, the samples were prepared in conventional geometry (ITO/poly(3,4-ethylenedioxythiophene):poly(styrenesulfonate) (PEDOT:PSS)/ternary/LiF/Al). For this ternary, the 488 nm LBIC maps are spatially well correlated with the WhiteBIC maps (Figure S10, Supporting Information), thus both techniques should lead to the same optimum compositions. For these experiments, we chose to measure the photocurrent at 488 nm excitation as it can be measured simultaneously with the Raman image from which composition is deduced, and so is the fastest exploration possible. **Figure 7** shows the results for a total of seven (non-annealed) RR-P3HT:O-IDFBR:O-IDTBR devices and ≈150 000 data points per plot. The large and statistically meaningful dataset included in Figure 7a yields an area of high performing blending ratios in agreement with the previous batch under white light illumination (Figure 6b). From this we conclude, first that the experiments are quite reproducible, and second, that our finding of a different maximum is not related to the sequential deposition producing large vertical phase segregation.

The Raman peak shift analysis of the RR-P3HT vibrational signature (Figure 7b) shows that the highest photocurrent occurs for moderate blueshifts (≈4–6 $cm^{-1}$ with respect to a pristine RR-P3HT film), while both large (≈10 $cm^{-1}$) and small (≈0–2 $cm^{-1}$) blueshifts are detrimental for the device performance. Since at 488 nm excitation both crystalline and amorphous RR-P3HT domains contribute to the Raman scattered intensity,[31,32] these results indicate that the film morphology in RR-P3HT:O-IDFBR:O-IDTBR ternary blends, and more specifically the degree of crystallinity attained at the polymer domains, is critical to achieve high performance devices. Neither largely amorphous (large blueshifts) nor strongly crystalline (small blueshifts) RR-P3HT domains are favorable for the photovoltaic device performance. Instead, a tradeoff between their purity (improved percolation) and the degree of intermixing with the acceptors (improved charge separation) is needed, as suggested by the moderate blueshifts observed in the high performing areas of the phase diagram. So, it is possible that for non-annealed blade-coated devices, the degree of crystallinity of the components is hindered at the O-IDTBR rich compositions. A systematic annealing study, which goes beyond the scope of the current manuscript, would possibly help to clarify further the apparent discrepancy between our data and published data for the P3HT based ternary.

One useful observation deduced when comparing the three material systems is the fact that the high efficiency region spans over a relatively large area of the ternary phase diagram. One way to quantify this is to determine how many crossing points between composition lines are included in the red area of each sample: between two and five. In fact, the whole ternary surfaces are relatively smooth. In other words, if one explores the ternary phase diagram with 10% steps in relative composition, there are good chances to find at least two


© 2019 The Authors. Published by WILEY-VCH Verlag GmbH & Co. KGaA, Weinheim

samples close to the absolute maximum. A rational, resource saving, approach for optimizing ternary blends would then commence by exploring the phase space in 20% steps, which would result in four samples of one binary, another four samples of the other binary, and six ternaries. The ternaries should, however, be equally spaced in the phase diagram rather than following the D:A 1:1 trajectory. This exploration would define the region of interest for a zoomed in second round with six extra devices. A total of 20 devices would then be sufficient for a first evaluation of the potential of a new ternary. While our approach, which would use around four samples to cover the whole phase space, is more accurate and statistically meaningful, the 20 devices approach has the advantage that can be implemented in most labs working on the field.

Finally, we would like to remark that, clearly, in this first manuscript we have not fully explored all the information hidden within the large amount of data points and colocal measurements. These large, self-consistent, varied and statistically meaningful datasets might be of use for data science studies, and therefore we have made it available at the CSIC repository for other researchers to use freely (http://hdl.handle.net/10261/194041).

## 6. Conclusion

We have introduced a solution-based methodology to produce large libraries of organic solar cells that effectively explore the ternary phase diagram. Each sample covers ≈15%–25% of the composition space with typically close to 5000 different composition/thickness values. Colocal hyperspectral images of such samples, which produced millions of data points, enables the correlation of performance with composition as well as local morphology. In particular, we show that Raman shifts are a useful tool to address the degree of mixing and purity of domains. Importantly, this broad exploration of the phase diagram enables the determination of the composition (and number) of performance maxima, which we find to sometimes lie outside the conventionally targeted D:A 1:1 trajectory. Our results were in relatively good agreement with a large series of devices fabricated with fixed composition. This type of high-throughput evaluation is, therefore, a very useful and timely contribution that will help to identify absolute performance maxima in promising multicomponent solar cells. Interestingly, the large body of data produced can open the possibility to use data science techniques in the development of solar cells through the availability of coherent and statistically meaningful data sets.

## 7. Experimental Section

*Materials*: Regioregular poly(3-hexylthiophene-2,5-diyl) (RR-P3HT) with average molecular weight of 20–45 kDa was purchased from Sigma-Aldrich, Lot# MKCD8731. Poly[(2,6-(4,8-bis(5-(2-ethylhexyl) thiophen-2-yl)-benzo[1,2-b:4,5-b′]dithiophene))-alt-(5,5-(1′,3′-di-2-thienyl-5′,7′-bis(2-ethylhexyl)benzo[1′,2′-c:4′,5′-c′]dithiophene-4,8-dione)] (PBDB-T), Lot# YY12062; (5Z,5′Z)-5,5′-(((4,4,9,9-tetraoctyl-4,9-dihydro-s-indaceno[1,2-b:5,6-b′]dithiophene-2,7-diyl)bis(benzo[c][1,2,5]thiadiazole-7,4-diyl))bis(methaneylylidene))bis(3-ethyl-2-thioxothiazolidin-4-one) (O-IDTBR), Lot# DW4035P; (5Z,5′Z)-5,5′-(((6,6,12,12-tetraoctyl-6,12-dihydroindeno[1,2-b]fluorene-2,8-diyl)bis(benzo[c][1,2,5]thiadiazole-7,4-diyl))bis(methaneylylidene))bis(3-ethyl-2-thioxothiazolidin-4-one) (O-IDFBR), Lot# YY12073; and 3,9-bis(2-methylene-(3-(1,1-dicyanomethylene)-indanone))-5,5,11,11-tetrakis(4-hexylphenyl)-dithieno[2,3-d:2′,3′-d′]-s-indaceno[1,2-b:5,6-b′]dithiophene (ITIC), Lot# YY12073, were obtained from 1-Material. Poly[4,8-bis(5-(2-ethylhexyl)thiophen-2-yl)benzo[1,2-b;4,5-b′]dithiophene-2,6-diyl-alt-(4-(2-ethylhexyl)-3-fluorothieno[3,4-b]thiophene-)-2-carboxylate-2-6-diyl)] (PTB7-Th), batch M261; [6,6]-Phenyl-C71-butyric acid methyl ester ($PC_{70}BM$); as well as the indium tin oxide (ITO) substrates were purchased from Ossila. PEDOT:PSS was purchased from Heraeus. The ZnO nanoparticles dispersion was obtained from Avantama.

*Sample Preparation*: All materials were dissolved in chlorobenzene (CB), in a concentration range of 10–15 mg $mL^{-1}$ for the acceptors, and 15–20 mg $mL^{-1}$ for the donor polymers. Two opposite corners of the ITO coated substrates were etched with diluted HCl and solid Zn, to electrically isolate them and obtain one top and one bottom electrode per side. Then the substrates and cut glasses for encapsulation were cleaned by consecutive sonication baths in acetone, soap, isopropanol (5 min each), and sodium hydroxide 10 vol% (10 min), rinsing with DI water after each step. The top transport layer, either PEDOT:PSS or ZnO depending on the device architecture, was deposited using an automatic blade coater Zehntner ZAA 2300 with an aluminum applicator Zehntner ZUA 2000, in air conditions and at a constant speed of 5 mm $s^{-1}$. The drop volume used was 100 µL for PEDOT:PSS and 50 µL for ZnO. The temperature was set to 60 and 40 °C for PEDOT:PSS and ZnO, respectively. All active layer materials were deposited using a second blade coater equipment (same brand and model) that included custom-made electronics to enable speed gradients, inside a nitrogen-filled and dry glove box, at 80 °C, while setting a blade gap of 200 µm. The drop volume used was 50 µL for the donor polymer in the first layer, and 40 µL for the acceptors. The speed was set to 30 mm $s^{-1}$ for constant speed film processing, while a linearly decelerating speed ramp was configured from 90 to 10 mm $s^{-1}$ for the processing of a thickness gradient in the first layer as well as in the standard composition fixed devices. The bottom transport layer and electrode, either LiF/Al or $MoO_3$/Ag, were thermally evaporated at a rate of 0.1 Å $s^{-1}$ for the transport layer and 1 Å $s^{-1}$ for the electrode. Samples were encapsulated using a cut glass slide and epoxy resin, then cured with an UV lamp for 5 min. The annealing process, when done, was performed in the nitrogen-filled and dry glove box by placing the samples in a hot plate at 120 °C for 10 min.

*Optical Measurements*: Variable-angle spectroscopic ellipsometry (VASE) data were acquired at a minimum of three angles of incidence using a Sopralab GES-5E rotating polarizer spectroscopic ellipsometer (SEMILAB) coupled to a charge-coupled device (CCD) detector. The ellipsometric data were modeled using WinElli piece of software and the standard critical point model.

All the optical characterization measurements performed in functional devices (Raman scattering, PL, reflection, LBIC, and WhiteBIC) were acquired using a WITec alpha 300 RA+ confocal Raman setup, coupled to an Olympus objective with 10X magnification (NA 0.25). The built-in lamp of the setup was used for the white light measurements. Two lasers centered at 488 and 633 nm were employed for the Raman, LBIC, and PL measurements. The light was focused through the thick (1.1 mm), ITO-covered glass substrates and the laser power reduced accordingly to avoid photodegradation and bleaching of the active layer (3-5 mW at 488 nm excitation). Samples were placed in a motorized stage and connected to a variable gain low noise current amplifier DLPCA-200 manufactured by FEMTO Messtechnik GmbH. All raw data were collected using WITec Project FIVE piece of software, while the Raman analysis was performed using a home-made MATLAB routine following the methodology described elsewhere.[25]

## Supporting Information

Supporting Information is available from the Wiley Online Library or from the author.


© 2019 The Authors. Published by WILEY-VCH Verlag GmbH & Co. KGaA, Weinheim

## Acknowledgements

A.H.B. and X.R.M. acknowledge the departments of Physics, Chemistry and Geology of the Autonomous University of Barcelona (UAB) as coordinators of the PhD programme in Materials Science. The authors would like to acknowledge financial support from the Spanish Ministry of Economy, Industry and Competitiveness through the "Severo Ochoa" Programme for Centers of Excellence in R&D (SEV-2015-0496) and project reference PGC2018-095411-B-I00 as well as the European Research Council (ERC) under Grant Agreement No. 648901 and Agència de Gestió d'Ajuts Universitaris i de Recerca (Grant Numbers 2017-SGR-00488). The authors also thank Dr. Bernhard Dörling (ICMAB) for the customization of the blade coating setup, and Enrique Pascual, Martí Gibert, and Dr. Miquel Garriga (ICMAB) for fruitful discussions.

## Conflict of Interest

The authors declare no conflict of interest.

## Keywords

high-throughput screening, layer-by-layer deposition, organic solar cells, Raman imaging, ternaries

Received: July 24, 2019
Revised: October 7, 2019
Published online:

[1] Y. Cui, H. Yao, J. Zhang, T. Zhang, Y. Wang, L. Hong, K. Xian, B. Xu, S. Zhang, J. Peng, Z. Wei, F. Gao, J. Hou, *Nat. Commun.* **2019**, *10*, 2515.
[2] E. Pascual-San José, A. Sánchez-Díaz, M. Stella, E. Martínez-Ferrero, M. I. Alonso, M. Campoy-Quiles, *Sci. Technol. Adv. Mater.* **2018**, *19*, 823.
[3] Z. Zheng, Q. Hu, S. Zhang, D. Zhang, J. Wang, S. Xie, R. Wang, Y. Qin, W. Li, L. Hong, N. Liang, F. Liu, Y. Zhang, Z. Wei, Z. Tang, T. P. Russell, J. Hou, H. Zhou, *Adv. Mater.* **2018**, *30*, 1801801.
[4] G. Li, W.-H. Chang, Y. Yang, *Nat. Rev. Mater.* **2017**, *2*, 17043.
[5] G. Yu, J. Gao, J. C. Hummelen, F. Wudl, A. J. Heeger, *Science* **1995**, *270*, 1789.
[6] J. J. M. Halls, C. A. Walsh, N. C. Greenham, E. A. Marseglia, R. H. Friend, S. C. Moratti, A. B. Holmes, *Nature* **1995**, *376*, 498.
[7] Y. Sun, G. Li, L. Wang, Z. Huai, R. Fan, S. Huang, G. Fu, S. Yang, *Sol. Energy Mater. Sol. Cells* **2018**, *182*, 45.
[8] Q. An, F. Zhang, L. Li, J. Wang, Q. Sun, J. Zhang, W. Tang, Z. Deng, *ACS Appl. Mater. Interfaces* **2015**, *7*, 3691.
[9] X. Sun, J. Ni, C. Li, L. Huang, R. Xu, Z. Li, H. Cai, J. Li, J. Zhang, *Org. Electron.* **2016**, *37*, 222.
[10] P. Cheng, J. Wang, Q. Zhang, W. Huang, J. Zhu, R. Wang, S.-Y. Chang, P. Sun, L. Meng, H. Zhao, H.-W. Cheng, T. Huang, Y. Liu, C. Wang, C. Zhu, W. You, X. Zhan, Y. Yang, *Adv. Mater.* **2018**, *30*, 1801501.
[11] M. Campoy-Quiles, Y. Kanai, A. El-Basaty, H. Sakai, H. Murata, *Org. Electron.* **2009**, *10*, 1120.
[12] A. D. de Zerio, C. Müller, *Adv. Energy Mater.* **2018**, *8*, 1702741.
[13] C.-H. Chen, C.-H. Hsieh, M. Dubosc, Y.-J. Cheng, C.-S. Hsu, *Macromolecules* **2010**, *43*, 697.
[14] Y. Chen, P. Ye, X. Jia, W. Gu, X. Xu, X. Wu, J. Wu, F. Liu, Z.-G. Zhu, H. Huang, *J. Mater. Chem. A* **2017**, *5*, 19697.
[15] Z. Xiao, X. Jia, L. Ding, *Sci. Bull.* **2017**, *62*, 1562.
[16] N. Gasparini, A. Salleo, I. McCulloch, D. Baran, *Nat. Rev. Mater.* **2019**, *4*, 229.
[17] D. Baran, R. S. Ashraf, D. A. Hanifi, M. Abdelsamie, N. Gasparini, J. A. Röhr, S. Holliday, A. Wadsworth, S. Lockett, M. Neophytou, C. J. M. Emmott, J. Nelson, C. J. Brabec, A. Amassian, A. Salleo, T. Kirchartz, J. R. Durrant, I. McCulloch, *Nat. Mater.* **2017**, *16*, 363.
[18] D. Angmo, M. Bjerring, N. C. Nielsen, B. C. Thompson, F. C. Krebs, *J. Mater. Chem. C* **2015**, *3*, 5541.
[19] A. Sánchez-Díaz, X. Rodríguez-Martínez, L. Córcoles-Guija, G. Mora-Martín, M. Campoy-Quiles, *Adv. Electron. Mater.* **2018**, *4*, 1700477.
[20] X. Rodríguez-Martínez, A. Sánchez-Díaz, G. Liu, M. A. Niño, J. Cabanillas-Gonzalez, M. Campoy-Quiles, *Org. Electron.* **2018**, *59*, 288.
[21] R. Sun, J. Guo, C. Sun, T. Wang, Z. Luo, Z. Zhang, X. Jiao, W. Tang, C. Yang, Y. Li, J. Min, *Energy Environ. Sci.* **2019**, *12*, 384.
[22] Y. Cho, T. L. Nguyen, H. Oh, K. Y. Ryu, H. Y. Woo, K. Kim, *ACS Appl. Mater. Interfaces* **2018**, *10*, 27757.
[23] B. Wang, Y. Fu, C. Yan, R. Zhang, Q. Yang, Y. Han, Z. Xie, *Front. Chem.* **2018**, *6*, 1.
[24] S. Zhang, H. Shen, X. Zhang, P. Fan, B. Zhou, J. Yu, J. Huang, *IEEE J. Photovoltaics* **2018**, *8*, 171.
[25] X. Rodríguez-Martínez, M. S. Vezie, X. Shi, I. McCulloch, J. Nelson, A. R. Goñi, M. Campoy-Quiles, *J. Mater. Chem. C* **2017**, *5*, 7270.
[26] M. Campoy-Quiles, C. Müller, M. Garriga, E. Wang, O. Inganäs, M. I. Alonso, *Thin Solid Films* **2014**, *571*, 371.
[27] A. Milani, L. Brambilla, M. Del Zoppo, G. Zerbi, *J. Phys. Chem. B* **2007**, *111*, 1271.
[28] M. Granström, K. Petritsch, A. C. Arias, A. Lux, M. R. Andersson, R. H. Friend, *Nature* **1998**, *395*, 257.
[29] K. Tvingstedt, K. Vandewal, A. Gadisa, F. Zhang, J. Manca, O. Inganäs, *J. Am. Chem. Soc.* **2009**, *131*, 11819.
[30] J. Razzell-Hollis, J. Wade, W. C. Tsoi, Y. Soon, J. Durrant, J.-S. Kim, *J. Mater. Chem. A* **2014**, *2*, 20189.
[31] W. C. Tsoi, D. T. James, J.-S. J. S. Kim, P. G. Nicholson, C. E. Murphy, D. D. C. Bradley, J. Nelson, J.-S. J. S. Kim, *J. Am. Chem. Soc.* **2011**, *133*, 9834.
[32] J. Gao, A. K. Thomas, R. Johnson, H. Guo, J. K. Grey, *Chem. Mater.* **2014**, *26*, 4395.


© 2019 The Authors. Published by WILEY-VCH Verlag GmbH & Co. KGaA, Weinheim

Copyright WILEY-VCH Verlag GmbH & Co. KGaA, 69469 Weinheim, Germany, 2019.

ADVANCED ENERGY MATERIALS

# Supporting Information

for *Adv. Energy Mater.*, DOI: 10.1002/aenm.201902417

# Efficient Exploration of the Composition Space in Ternary Organic Solar Cells by Combining High-Throughput Material Libraries and Hyperspectral Imaging

*Albert Harillo-Baños, Xabier Rodríguez-Martínez, and Mariano Campoy-Quiles**

Copyright WILEY-VCH Verlag GmbH & Co. KGaA, 69469 Weinheim, Germany, 2019.

# Supporting Information

## Efficient exploration of the composition space in ternary organic solar cells by combining high-throughput material libraries and hyperspectral imaging

*Albert Harillo-Baños, Xabier Rodríguez-Martínez and Mariano Campoy-Quiles**

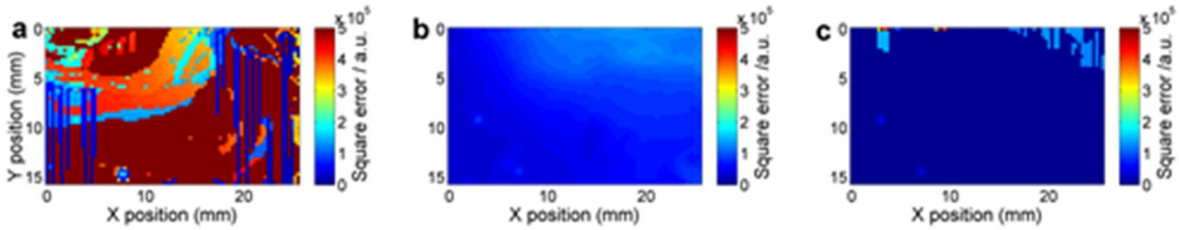


**Figure S1.** Squared norm of the residual for the Raman spectral modelling performed according to a) Equation 1 b) Equation 2 and c) Equation 3 as labeled in the main text. The dead regions observed in Figure S1a and S1c are ascribed to errors in the Raman model fitting, i.e. particular locations in which the algorithm is unable to find a univocal solution. This usually happens in zones where there is only one material (due to an acute loss of sensitivity) or where an imperfection of the sample causes the algorithm to drag the same result for several pixels before being able to correct. In all cases, these spikes and higher error pixels are omitted in a later step prior to plotting the ternary composition diagram.

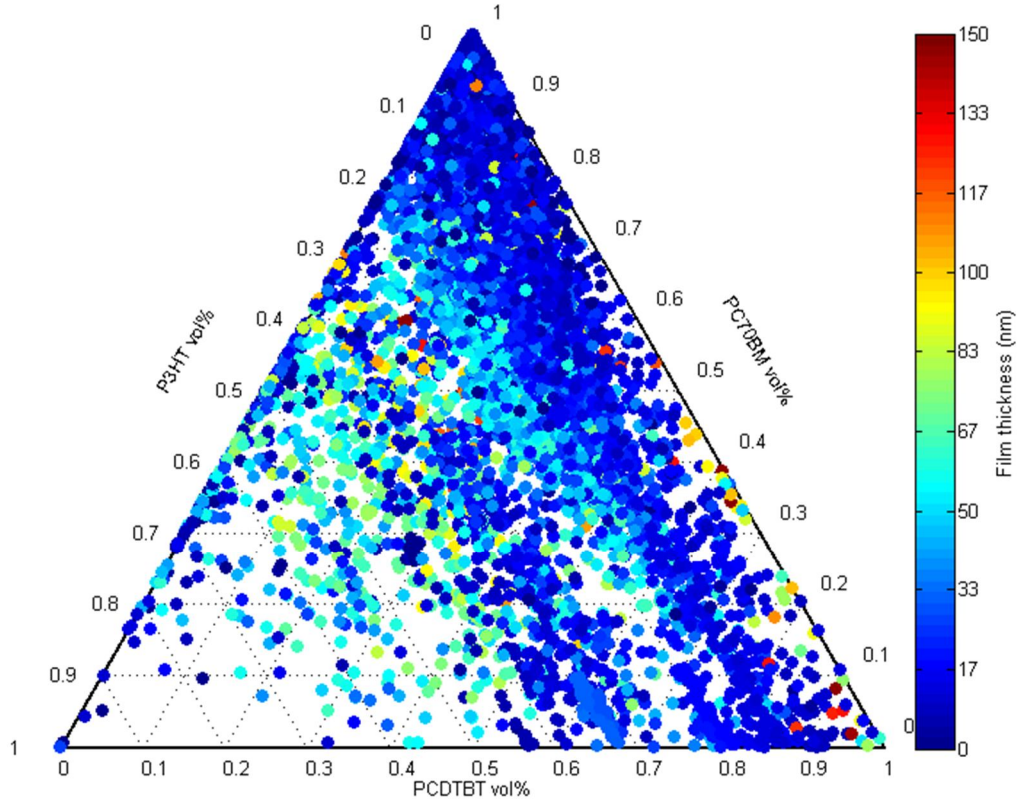


**Figure S2.** Ternary composition diagram for a single $D_1$:$D_2$:A blend film consisting of RR-P3HT:PCDTBT:$PC_{70}BM$.

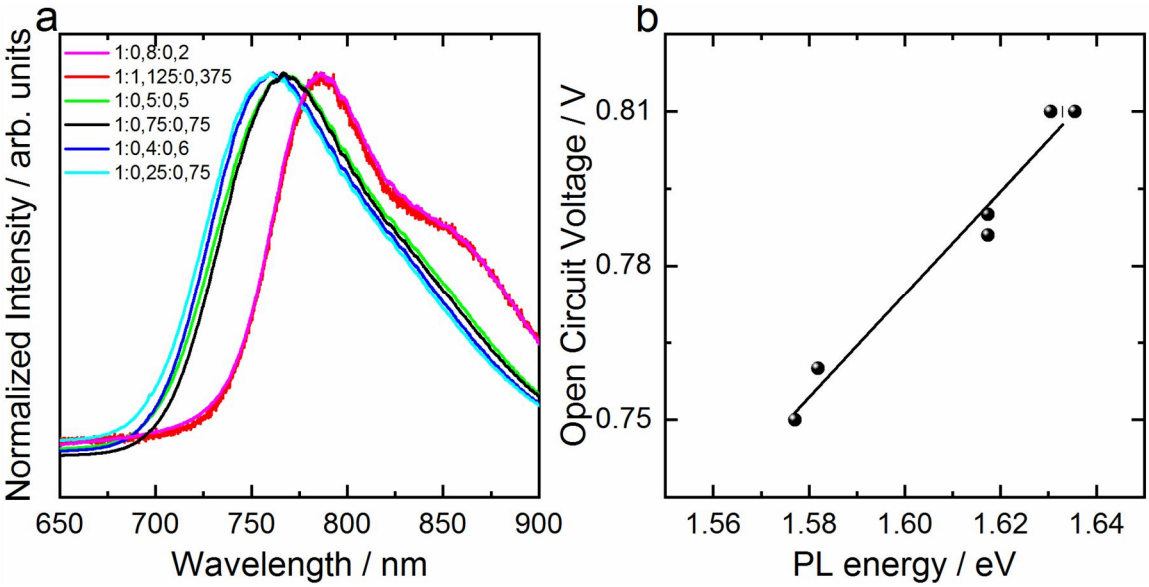


**Figure S3.** a) Normalized photoluminescence (PL) spectra for a series of P3HT:O-IDFBR:O-IDTBR homogeneous devices with different compositions; b) correlation between the energy

of the PL maximum ($E_{PL}$) for each sample and the corresponding experimental $V_{oc}$. The linear trend obtained can be written as

$$V_{oc}[V] = 1.003E_{PL}[eV] - 0.830 \quad \text{(S1)}$$

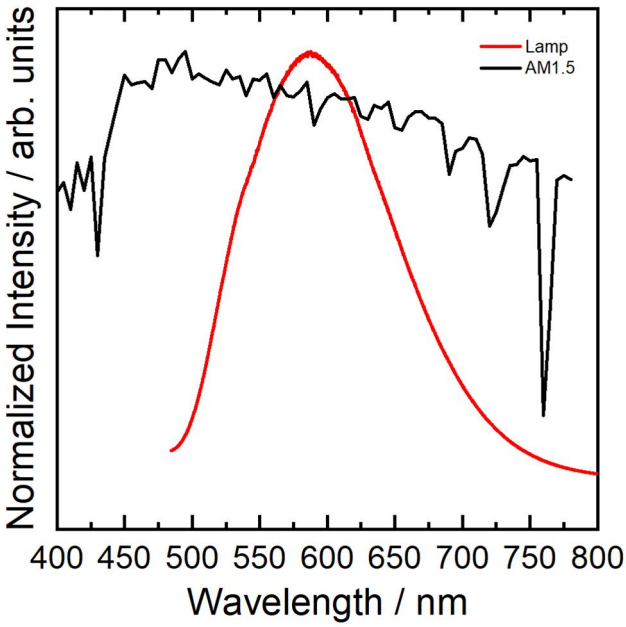


**Figure S4.** (Solid red line) Normalized emission spectrum of the built-in lamp in the WITec alpha 300 RA+ setup measured upon reflection on a silver mirror; (solid black line) reference AM1.5 irradiance spectrum.

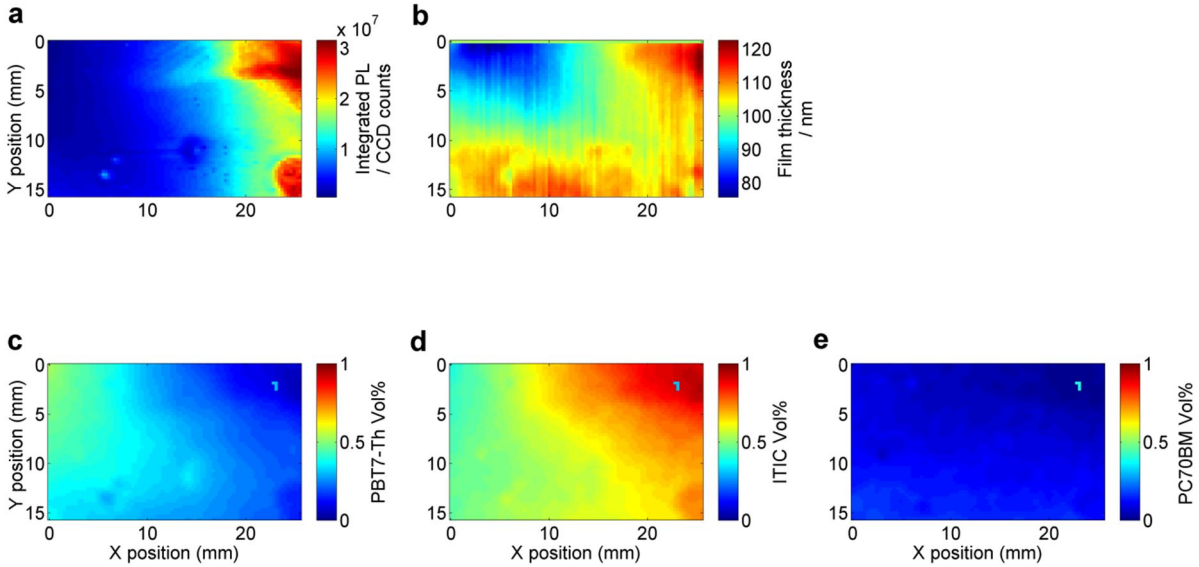


**Figure S5.** Additional optical characterization datasets for a PTB7-Th:$PC_{70}$BM:ITIC device showing maps of a) integrated photoluminescence spectra; b) film thickness; and volumetric

compositions of c) PTB7-Th, d) ITIC and e) $PC_{70}BM$ obtained from modelling the Raman scattered intensities and spectra.

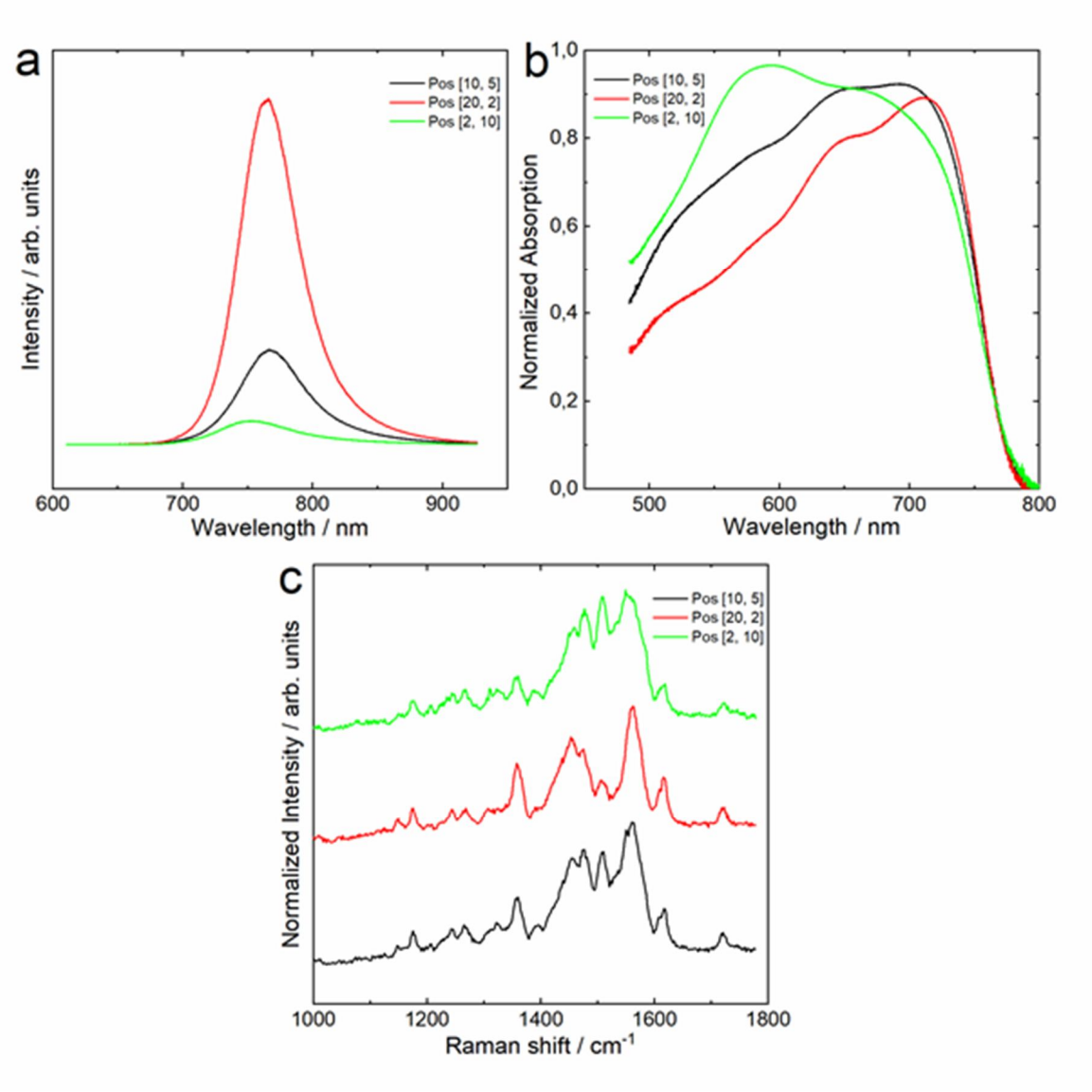


**Figure S6**. Representative a) photoluminescence, b) absorption and c) Raman spectra at three different XY locations of the PTB7-Th:$PC_{70}BM$:ITIC sample depicted in Figure S5 and Figure 3 in the main manuscript.

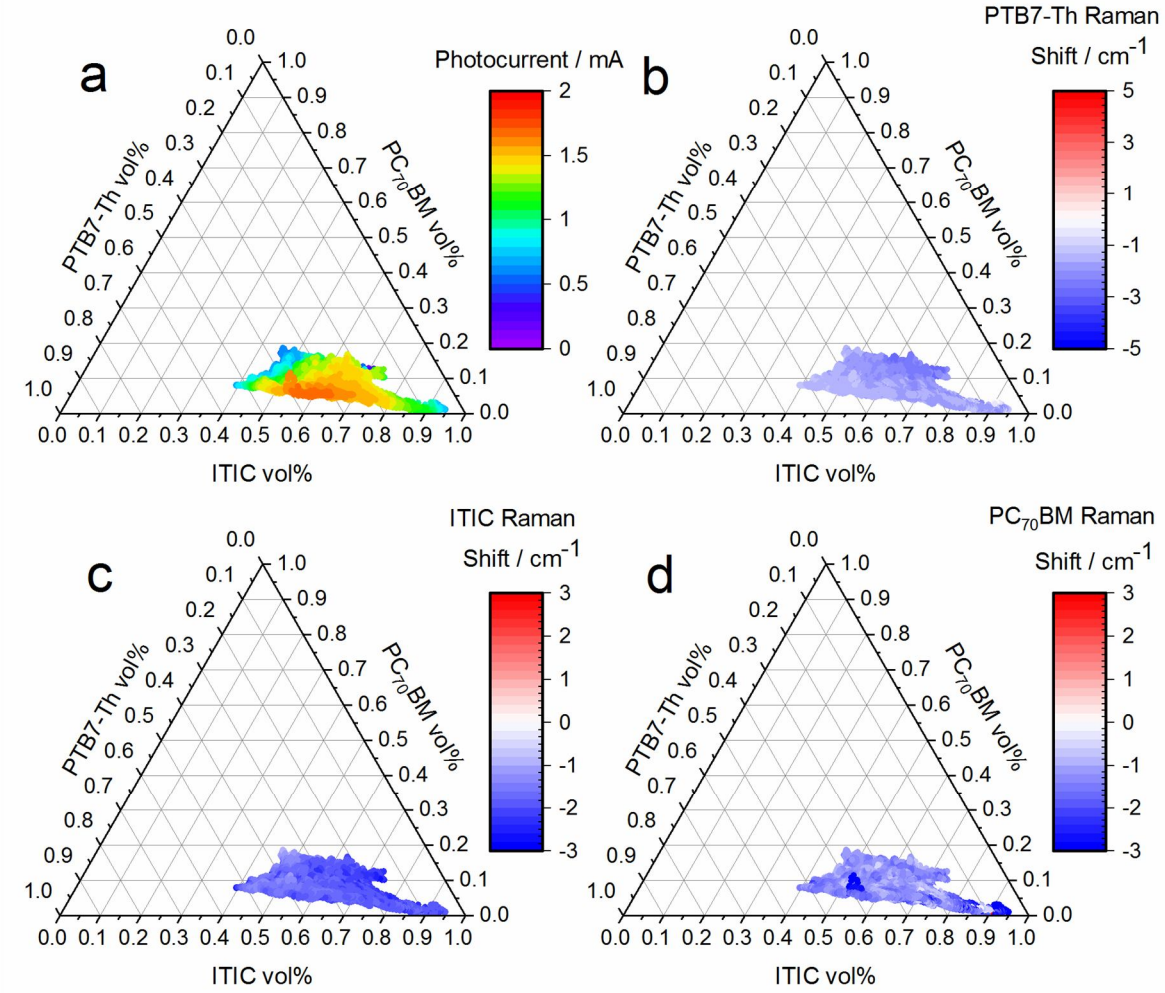


**Figure S7**. Ternary composition diagrams of a non-annealed PTB7-Th:ITIC:$PC_{70}BM$ sample. The colour scales refer to: a) photocurrent under white light illumination; b) Raman peak shift of PTB7-Th, c) ITIC and d) $PC_{70}BM$.

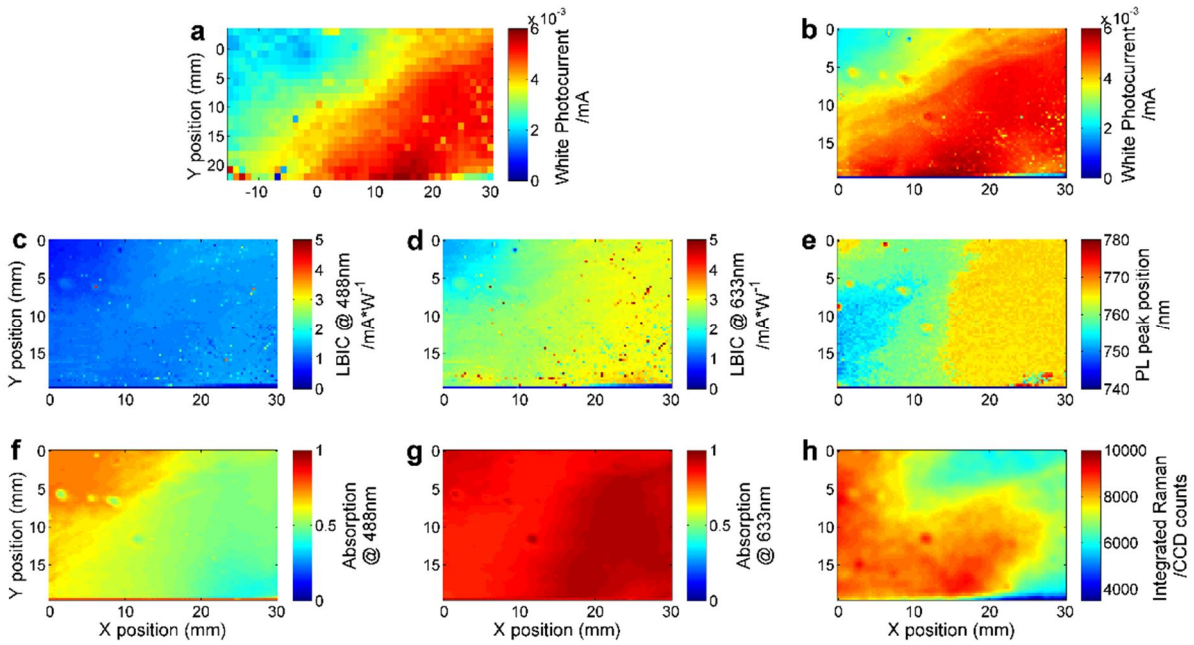


**Figure S8.** Full set of optical characterization maps performed in a sequentially deposited sample of PBDB-T:ITIC:$PC_{70}BM$, with the donor layer processed as a thickness gradient. a) Coarse photocurrent map obtained with white light; b) higher resolution white light photocurrent map centred at the region of better performance; c) photocurrent map acquired at 488 nm excitation; d) photocurrent map acquired at 633 nm excitation; e) wavelength of the main photoluminescence peak measured at 633 nm excitation; f) absorption at 488 nm excitation wavelength; g) absorption at 633 nm excitation wavelength; h) integrated Raman scattered intensity at 488 nm excitation.

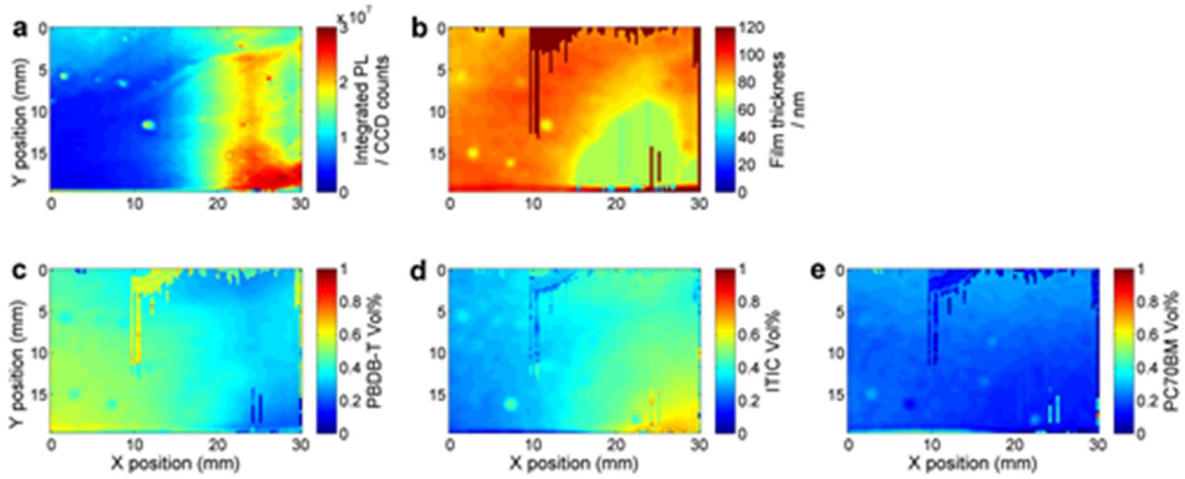


**Figure S9.** Additional data for a PBDB-T:ITIC:$PC_{70}BM$ sample. a) Integrated photoluminescence; b) Raman-deduced thickness, and composition of c) PBDB-T, d) ITIC and e) $PC_{70}BM$.

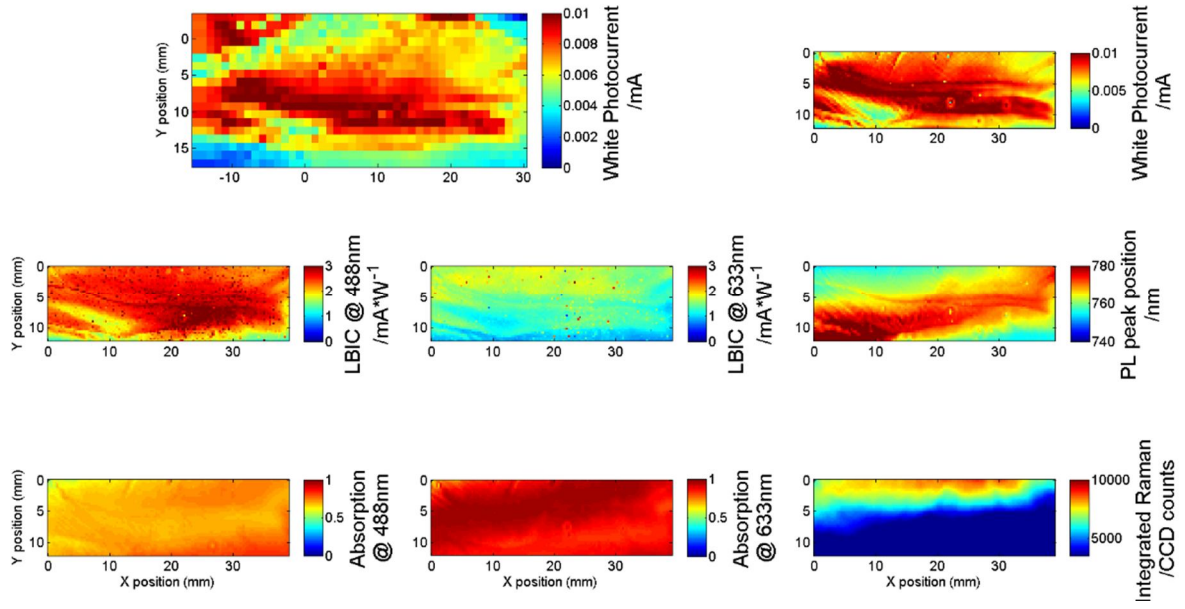


**Figure S10.** Full set of optical characterization maps performed in a sequentially deposited sample of P3HT:O-IDFBR:O-IDTBR, with the donor layer processed as a thickness gradient. a) Coarse photocurrent map obtained with white light; b) higher resolution white light photocurrent map centred at the region of better performance; c) photocurrent map acquired at 488 nm excitation; d) photocurrent map acquired at 633 nm excitation; e) wavelength of the

main photoluminescence peak measured at 633 nm excitation; f) absorption at 488 nm excitation wavelength; g) absorption at 633 nm excitation wavelength; h) integrated Raman scattered intensity at 488 nm excitation.

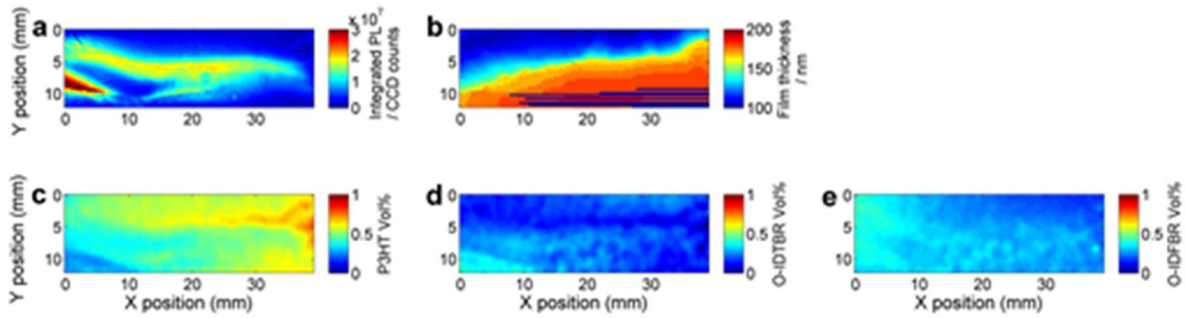


**Figure S11.** Additional data for a P3HT:O-IDFBR:O-IDTBR sample. a) Integrated photoluminescence; b) Raman-deduced thickness, and composition of c) P3HT, d) O-IDTBR and e) O-IDFBR.

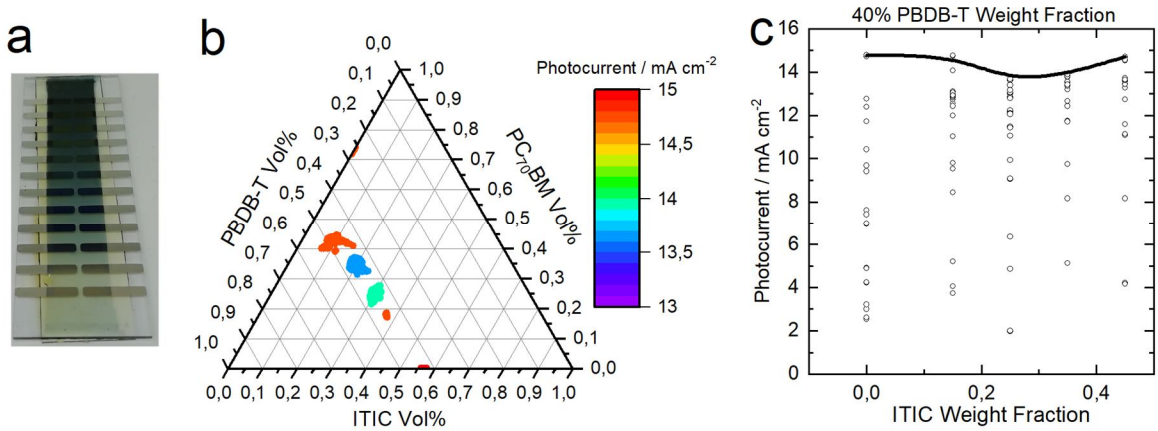


**Figure S12**. a) Optical image of a sample consisting of 24 different devices (12 per side) with the ternary PBDB-T:ITIC:$PC_{70}BM$ blend as active layer, which was deposited as a lateral thickness gradient. b) Representation of the ternary composition diagram of 6 different samples (24 devices each, of different thickness and fixed weight blending ratios), with the highest photocurrent obtained in the sample as colour scale. c) Photocurrent dispersion obtained for all wedge-like samples (keeping fixed PBDB-T loading at 40 wt%) as a function of ITIC wt%.

**Uncertainty in the determination of volumetric composition through Raman spectroscopy**

The raw Raman spectra obtained experimentally in the ternary photovoltaic devices are fitted according to Equation (3) in the main manuscript, which reads

$$I_{R,\mathrm{blend}}(\beta, v_u, \omega, \delta_u) \propto \beta \sum_{u=1}^{3} v_u \sigma_{R,u} I_{\mathrm{ref},u}(\omega + \delta_u) \qquad \text{(S1)}$$

The six free parameters found in a ternary blend ($\beta, v_u, \delta_u$) are generally fitted with large accuracy: for the here analysed ternary blends and at moderate compositions the typical standard deviation (defined with a confidence interval of 95%) of the fitted parameters is < 1% (relative error). In the worst scenario, which includes combinations of materials with large Raman cross-section ratios and blending ratios that are enriched with the most Raman active material, the fitting error can be as high as 10-20% as reported elsewhere (J. Mater. Chem. C, 2017, 5, 7270-7282). This is a consequence of the partial hindering of the characteristic vibrational fingerprints of the low Raman intensity material by the main Raman active component of the blend. Such effect can even be more pronounced if their vibrational signatures are qualitatively similar. Thus, it is important to properly choose the blended materials so as to minimize the fitting error source in the Raman modelling. The ternary blends selected in this work are all compatible in terms of Raman cross-section ratios as well as in terms of vibrational characteristics, thus the fitting error remains well below 5% in all cases.

Therefore, in the here presented case the main error source is attributed to the determination of the Raman cross-section of the materials. As described elsewhere (J. Mater. Chem. C, 2017, 5, 7270-7282), such determination is performed by fabricating films with lateral thickness gradients, then measuring the Raman intensity as a function of thickness and finally modelling and fitting the Raman scattered intensity as a function of the film thickness while using the optical constants of the sample as model inputs. This approach includes several

sources of error including the quantification of the scattered intensity, the modelling of film thickness in ellipsometry as well as the Raman intensity modelling using the experimentally determined optical constants. In our previous works we showed several examples of Raman cross-section determinations together with their standard deviation, including PTB7-Th and $PC_{70}BM$ (Figure 1c in Adv. Electron.Mater. 2018, 4, 1700477) which are used in this paper.

We evaluate the effect that the error of the Raman cross-section determination has on the extracted ternary compositions by randomly adding or subtracting the corresponding standard deviation to the cross-sections and then re-fitting the raw Raman spectra. We repeat this process several times (Figure S13, panels a-e) to gain statistics and then average the datasets to obtain the corresponding relative errors in the loading of each material (Figure 13f). We observe that in the worst scenario the relative error in the composition can exceed 25% (ITIC) whereas it is close to 10% in the most favourable case ($PC_{70}BM$). In average, an error close to 10-20% is expected, matching what we previously observed in binary blends (J. Mater. Chem. C, 2017, 5, 7270-7282). This is in agreement with Raman data taken for homogeneous samples (Figure 5b in the manuscript and Figure S12b).

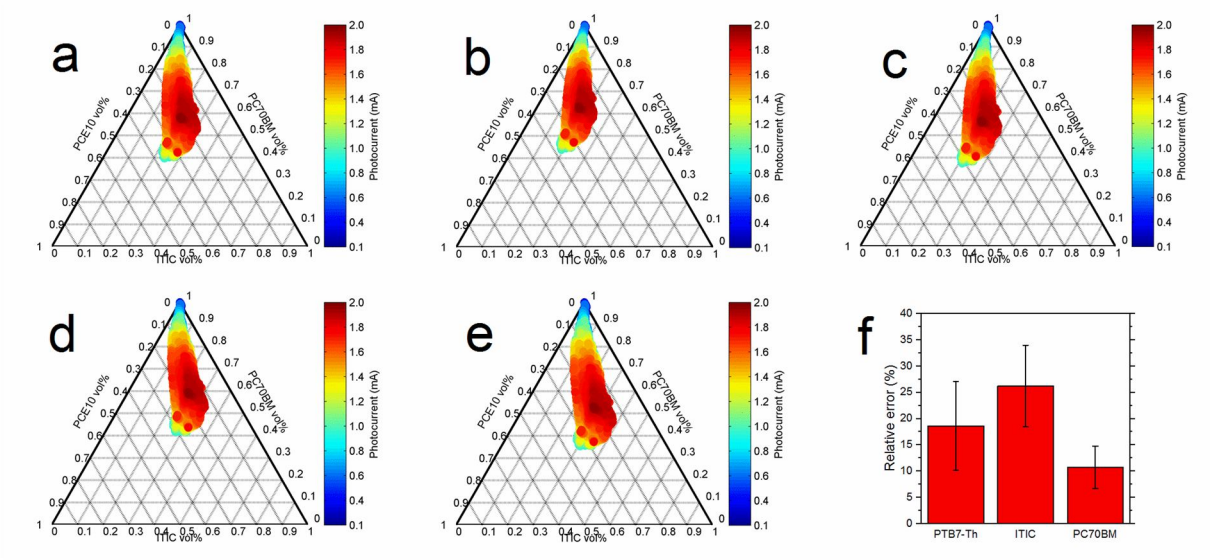


**Figure S13.** Panels a-e represent ternary composition diagrams of the PTB7-Th:ITIC:$PC_{70}BM$ sample analysed in Figure 4 in the main manuscript in which the

corresponding Raman cross-sections have been randomly modified within a standard deviation (either added or subtracted). Panel f shows the average relative error of the composition of each blended material.

# PAPER IV

## Suppressing Co-Crystallization of Halogenated Non-Fullerene Acceptors for Thermally Stable Ternary Solar Cells

Sandra Hultmark, Sri Harish Kumar Paleti, Albert Harillo-Baños, Sara Marina, Ferry Anggoro Ardy Nugroho, Yanfeng Liu, Leif K. E. Ericsson, Ruipeng Li, Jaime Martín, Jonas Bergqvist, Christoph Langhammer, Fengling Zhang, Liyang Yu, Mariano Campoy-Quiles, Ellen Moons, Derya Baran, and Christian Müller. *Advanced Functional Materials*, 30, 1–10

ADVANCED FUNCTIONAL MATERIALS
www.afm-journal.de

# Suppressing Co-Crystallization of Halogenated Non-Fullerene Acceptors for Thermally Stable Ternary Solar Cells

*Sandra Hultmark, Sri Harish Kumar Paleti, Albert Harillo, Sara Marina, Ferry Anggoro Ardy Nugroho, Yanfeng Liu, Leif K. E. Ericsson, Ruipeng Li, Jaime Martín, Jonas Bergqvist, Christoph Langhammer, Fengling Zhang, Liyang Yu, Mariano Campoy-Quiles, Ellen Moons, Derya Baran,* and Christian Müller**

**While photovoltaic blends based on non-fullerene acceptors are touted for their thermal stability, this type of acceptor tends to crystallize, which can result in a gradual decrease in photovoltaic performance and affects the reproducibility of the devices. Two halogenated indacenodithienothiophene-based acceptors that readily co-crystallize upon mixing are studied, which indicates that the use of an acceptor mixture alone does not guarantee the formation of a disordered mixture. The addition of the donor polymer to the acceptor mixture readily suppresses the crystallization, which results in a fine-grained ternary blend with nanometer-sized domains that do not coarsen due to a high $T_g \approx 200$ °C. As a result, annealing at temperatures of up to 170 °C does not markedly affect the photovoltaic performance of ternary devices, in contrast to binary devices that suffer from acceptor crystallization in the active layer. The results indicate that the ternary approach enables the use of high-temperature processing protocols, which are needed for upscaling and high-throughput fabrication of organic solar cells. Further, ternary devices display a stable photovoltaic performance at 130 °C for at least 205 h, which indicates that the use of acceptor mixtures allows to fabricate devices with excellent thermal stability.**

## 1. Introduction

The state-of-the-art power conversion efficiency (PCE) of lab-scale solution-processed organic solar cells is approaching 18%.[1,2] The translation of these record values to large-area modules as well as long-term stability are prerequisites for commercialization. A considerable amount of work has been done to address stability issues related to the device electrodes and interlayers.[3,4] The stability of the bulk-heterojunction active layer, however, requires further development. Bulk heterojunctions are blends of donor and acceptor materials with an intricate nanostructure that provides both efficient charge generation and transport.[5–7] Typically, the optimal blend nanostructure is far away from thermal equilibrium and hence tends to change with time, for example, through phase separation or crystallization, which results in a gradual

S. Hultmark, Prof. C. Müller
Department of Chemistry and Chemical Engineering
Chalmers University of Technology
Göteborg 41296, Sweden
E-mail: christian.muller@chalmers.se

S. H. K. Paleti, Prof. D. Baran
King Abdullah University of Science and Technology (KAUST)
Division of Physical Sciences and Engineering and KAUST Solar Center (KSC)
Thuwal 23955-6900, Saudi Arabia
E-mail: derya.baran@kaust.edu.sa

A. Harillo, Dr. M. Campoy-Quiles
Institut de Ciència de Materials de Barcelona (ICMAB-CSIC)
Campus de la UAB
Bellaterra 08193, Spain

The ORCID identification number(s) for the author(s) of this article can be found under https://doi.org/10.1002/adfm.202005462.

© 2020 The Authors. Published by Wiley-VCH GmbH. This is an open access article under the terms of the Creative Commons Attribution License, which permits use, distribution and reproduction in any medium, provided the original work is properly cited.

**DOI: 10.1002/adfm.202005462**

S. Marina, Dr. J. Martín
POLYMAT and Polymer Science and Technology Department
Faculty of Chemistry
University of the Basque Country UPV/EHU
Paseo Manuel de Lardizabal 3, Donostia-San Sebastián 20018, Spain

S. Marina, Dr. J. Martín
Ikerbasque Basque Foundation for Science
Bilbao 48013, Spain

Dr. F. A. A. Nugroho, Prof. C. Langhammer
Department of Physics
Chalmers University of Technology
Göteborg 41296, Sweden

Y. Liu, Dr. J. Bergqvist, Prof. F. Zhang
Department of Physics
Chemistry and Biology (IFM)
Linköping University
Linköping 58183, Sweden

Dr. L. K. E. Ericsson, Prof. E. Moons
Department of Engineering and Physics
Karlstad University
Karlstad 65188, Sweden

Dr. R. Li
National Synchrotron Light Source II
Brookhaven National Laboratory
New York, NY 11973, USA

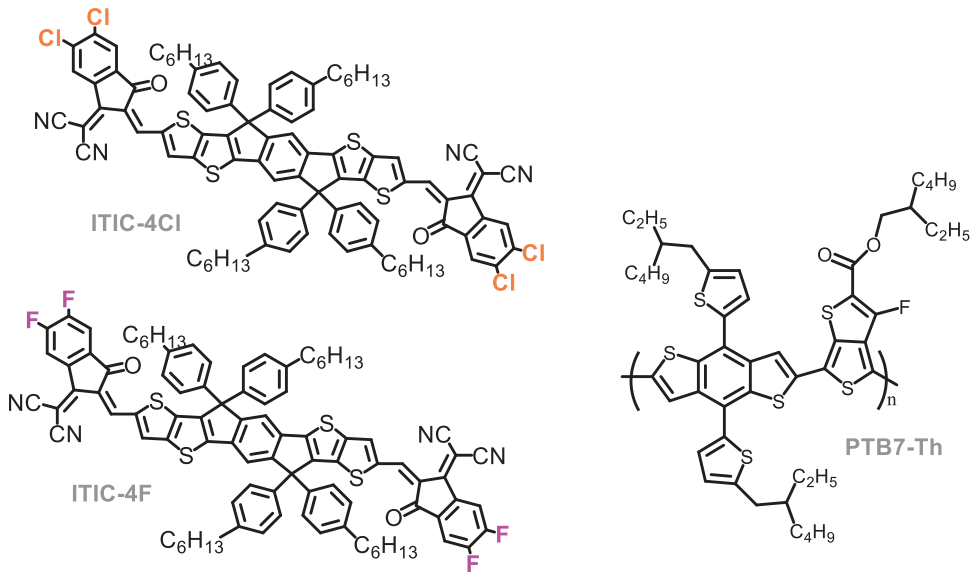


**Figure 1.** Chemical structures of ITIC-4Cl, ITIC-4F and PTB7-Th.

decrease in photovoltaic performance. Many blends are finely mixed and display a single glass transition temperature $T_g$, which represents an upper limit above which the nanostructure rapidly coarsens.[8]

Current understanding of structure–property relationships related to the thermal stability of bulk-heterojunction blends is based on the large body of work on fullerene-based solar cells. Fullerene crystals rapidly form upon heating above the blend $T_g$ and disrupt the nanostructure of the active layer.[9,10] One widely explored strategy to suppress crystallization of the fullerene acceptor involves the use of fullerene mixtures.[11–13]

The superior thermal stability of fullerene mixtures arises due to the increase in entropy upon mixing by $\Delta S_{mix} = -Nk_B \sum_i \phi_i \ln \phi_i$, where $N$ is the number of molecules, $k_B$ the Boltzmann constant, and $\phi_i$ the molar fraction of component $i$.[14] The resulting decrease in the Gibbs free energy of the liquid state, that is, the disordered mixture of several acceptor molecules, reduces the tendency for crystallization. As a result, mixing of several components tends to impede coarsening of the multicomponent (i.e., ternary, quaternary, etc.) blend.

The best performing solar cells are now consistently realized with non-fullerene acceptors, which offer additional advantages over fullerenes such as more cost-effective synthesis, stronger optical absorption, and a higher degree of chemical stability.[15–17] Non-fullerene acceptors such as the acceptor 3,9-bis(2-methylene-(3-(1,1-dicyanomethylene)-indanone))-5,5,11,11-tetrakis(4-hexylphenyl)-dithieno[2,3-d:2′,3′-d′]-s-indaceno[1,2-b:5,6-b′]dithiophene (ITIC) and its many derivatives readily crystallize upon annealing, and hence create a rich blend nanostructure that can only be controlled by complex processing schemes.[18,19] Crystal nucleation of ITIC occurs at temperatures as low as 100 °C despite a very high $T_g \approx 180$ °C, giving rise to nanometer-sized crystallites whose number and size strongly depend on the precise annealing time and temperature.[20] Further, ITIC derivatives can form several different polymorphs, which further complicates their phase behavior.[20–23] The range of temperatures where non-fullerene crystals are prone to form covers the processing conditions that are commonly selected for the roll-to-roll fabrication of organic solar cells. For instance, printing on flexible poly(ethylene terephthalate) (PET) foil is typically done at temperatures up to 140 °C, which ensures rapid evaporation of the processing solvent.[24,25] Besides, the printing of solution processable hole transport layers requires annealing at similar temperatures.[26,27] We argue that considerable gains in terms of device reproducibility could be made if it was possible to process non-fullerene acceptor-based blends at elevated temperatures without the risk of phase separation and acceptor crystallization.[28] Attempts to impede the crystallization of non-fullerene acceptors by mixing of several components has met with limited success due to the complex nanostructure of the resulting ternary blends, where the stoichiometry and processing conditions can display either enhanced or suppressed crystallization.[29] ITIC derivatives experience stronger attractive forces than fullerenes, caused by $\pi$–$\pi$ interactions and, as we will argue below, halogen interactions, which promote crystallization. As a result, mixing of several non-fullerene acceptors, and the associated increase in the entropy of the liquid state $\Delta S_{mix}$, is not a guarantee that crystallization is suppressed.

In this work, we explore the phase behavior of a non-fullerene acceptor binary system based on two ITIC derivatives, ITIC-4F and ITIC-4Cl (see **Figure 1** for chemical structures), which form a complex phase behavior that—in contrast to fullerenes—is governed by both the entropy of mixing as well as positive enthalpic interactions. We find that the two acceptors can co-crystallize, a process which is however suppressed when blended with the benzodithiophene–fluorothienothiophene based donor polymer PTB7-Th (see Figure 1 for chemical

Dr. L. Yu
Key Laboratory of Green Chemistry and Technology of Ministry of Education
College of Chemistry
Sichuan University
Chengdu 610064, China


© 2020 The Authors. Published by Wiley-VCH GmbH

structure). The resulting ternary blend features a fine-grained nanostructure composed of distinct, tens-of-nanometers small domains of the acceptor mixture, intertwined with polymer-rich domains. As a result, the corresponding ternary devices display a stable photovoltaic performance at temperatures approaching the blend $T_g \approx 200$ °C, in contrast to the corresponding binary ones, which suffer from extensive crystallization of the acceptor considerably below 200 °C.

## 2. Results and Discussion

We study the two acceptors ITIC-4F and ITIC-4Cl (see Figure 1 for chemical structures), motivated by their structural similarity, and the halogenation of the indanone groups that flank the indacenodithienothiophene core on either side. Fluorine has a low polarizability due to its small size as well as a high electronegativity, and hence the F···F interactions are thought to be weak compared to those of other halogens, such as Cl···Cl interactions, which are considerably stronger.[30,31] In agreement, solution-processed ITIC-4F appears disordered in contrast to ITIC-4Cl whose X-ray diffractogram features sharp diffractions, which indicate a crystalline solid (**Figure 2**a; Figure S2b, Supporting Information).

Both acceptors display a rich phase behavior. Differential scanning calorimetry (DSC) of ITIC-4F shows a broad endotherm with peak at $T_{endo} \approx 155$ °C (Figure 2b,c), above which X-ray diffractions from polymorph $I_F$ are lost (cf. X-ray diffractogram recorded for material annealed at 160 °C; Figure 2a), indicating that the compound undergoes crystal melting. Above the $T_g \approx 185$ °C (cf. Figure S1a, Supporting Information) re-crystallization occurs and ITIC-4F forms polymorph $II_F$. ITIC-4Cl also displays a $T_{endo} \approx 180$ °C, which we assign to a solid–solid phase transformation from polymorph $I_{Cl}$ to $II_{Cl}$, as indicated by distinct differences in the X-ray diffraction patterns recorded at 160 and 200 °C (Figure 2a). Hence, ITIC-4Cl does not undergo re-crystallization above its $T_g \approx 210$ °C (cf. Figure S1b, Supporting Information), as evidenced by the

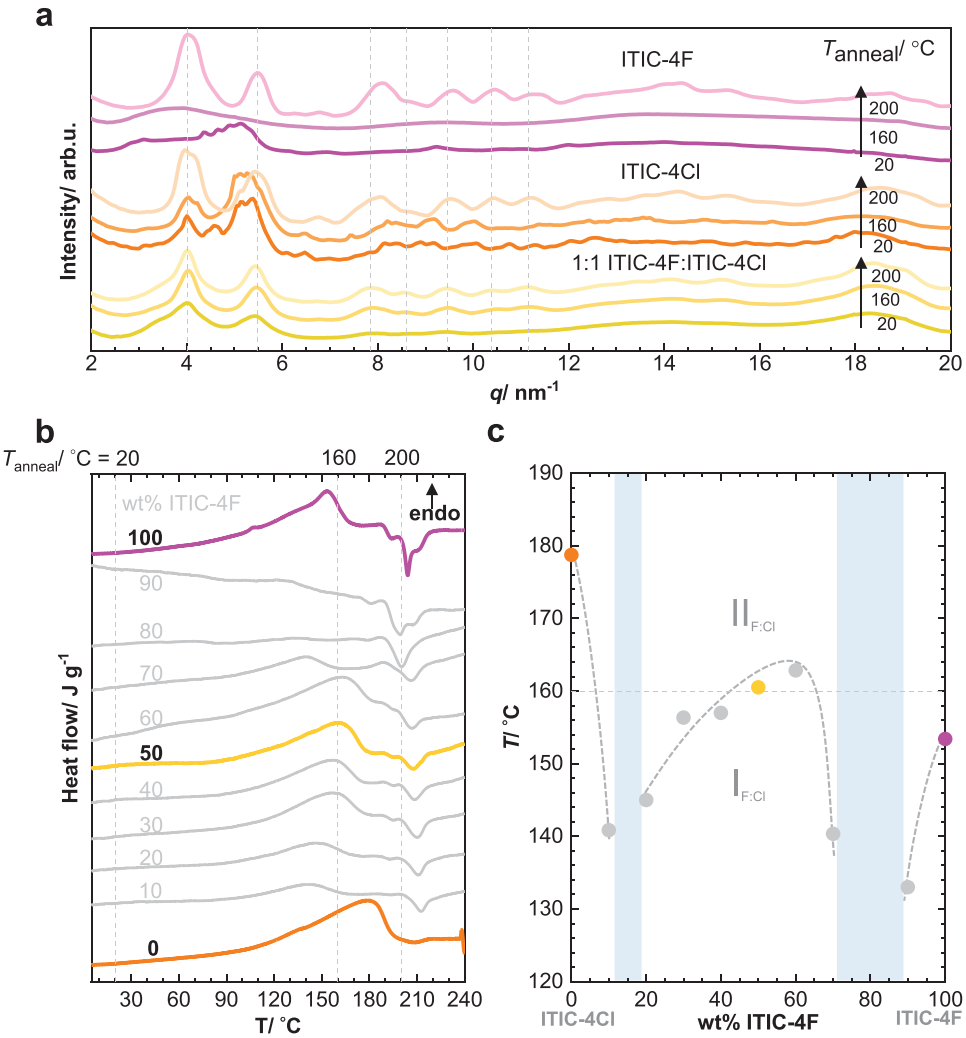


**Figure 2.** a) Radially integrated GIWAXS diffractograms of ITIC-4F, ITIC-4Cl, and 1:1 ITIC-4F:ITIC-4Cl directly after spin-coating, annealing at 160 and 200 °C, dashed lines indicate the peak positions of prominent diffractions observed for 1:1 ITIC-4F:ITIC-4Cl; b) DSC first heating thermograms of ITIC-4F:ITIC-4Cl mixtures; c) Peak temperatures of endothermic transitions corresponding to the solid–solid transition from polymorph $I_{F:Cl}$ to $II_{F:Cl}$ (melting of polymorph $I_F$ in case of ITIC-4F); compositions of mixtures that are mostly disordered are indicated in light blue.


© 2020 The Authors. Published by Wiley-VCH GmbH

absence of an exotherm above this temperature (Figure 2b). The high temperature polymorphs of both acceptors, $II_F$ and $II_{Cl}$, show virtually the same diffraction pattern with distinct peaks at, for example, $q \approx 4.0$, 5.5, and 8.1 $nm^{-1}$ (Figure 2a; Figure S2b, Supporting Information).

The DSC thermograms of ITIC-4F:ITIC-4Cl binary mixtures display both an endotherm and exotherm, with peak at 160 and 210 °C in case of a 1:1 mixture (Figure 2b). The corresponding GIWAXS diffractogram recorded at 200 °C features distinct crystalline diffractions (Figure 2a), which indicates that the endotherm at 160 °C arises due to a solid–solid state transformation and not crystal melting. We therefore argue that binary mixtures of ITIC-4F and ITIC-4Cl show comparable behavior to ITIC-4Cl, that is, a solid-state transformation from $I_{F:Cl}$ to $II_{F:Cl}$ (Figure 2c), but followed by an additional crystallization at 210 °C. The X-ray diffraction pattern of $II_{F:Cl}$ resembles that of the two neat components, albeit with slightly shifted peaks, which is due to the formation of an acceptor co-crystal. We propose that F···Cl interactions occur,[30,31] which enable incorporation of the two acceptors into the same crystal lattice. Acceptor molecules that have not joined a co-crystal will instead form a homogeneous amorphous mixture, driven by the entropy of mixing $\Delta S_{mix}$ as well as, possibly, F···Cl interactions leading to a decrease in enthalpy upon mixing, that is, $\Delta H_{mix} < 0$. Hence, mixtures of ITIC-4Cl and ITIC-4F are thermodynamically stable and will not undergo liquid–liquid phase separation below 200 °C.

We went on to study the phase behavior of the ITIC-4F:ITIC-4Cl mixture when blended with the donor polymer PTB7-Th. We focus on a blend ratio of 1:0.5:0.5 (wt%) PTB7-Th:ITIC-4F:ITIC-4Cl, which also offers the best photovoltaic performance (cf. discussion on device performance below). Diffraction patterns of the as-cast ternary blend, as well as films annealed at 160 °C only feature a broad amorphous halo around $q \approx 17$ $nm^{-1}$ (Figure S2a,b, Supporting Information), which suggests that the presence of the polymer effectively suppresses crystallization of the acceptor mixture (note that PTB7-Th does not crystallize; cf. Figure S2a,b, Supporting Information, and ref. [32]). Annealing at 200 °C ultimately results in crystallization of the acceptor mixture, as evidenced by the appearance of distinct diffraction peaks as well as an exotherm in DSC heating thermograms (cf. Figures S2a and S3, Supporting Information).

Since crystallization of the acceptor mixture in the ternary blend only occurs above 200 °C, we suspected that the ternary blend displays a $T_g$ at a similar temperature. We performed physical aging experiments of the ternary blend using fast scanning calorimetry (FSC) to determine its $T_g$. First, we heated a thin film of the ternary blend to 450 °C to delete the thermal history, followed by annealing (aging) at different temperatures for 30 min. Quenching from 450 to −90 °C gave a reference scan void of crystallization (see the heating thermogram in **Figure 3**a). Reorganization of molecules to a more equilibrated thermodynamic state takes place below the $T_g$ if given enough time. This reorganization results in an endothermic overshoot in a subsequent FSC heating scan. The enthalpy overshoot decreases in magnitude and shifts to higher temperatures as the aging temperature approaches the $T_g$ (Figure 3b), and hence the aging temperature where the enthalpy change $\Delta H$ goes to zero is a measure for the $T_g$.[33] We obtain a value of $T_g \approx 205$ °C for the ternary blend, and 195 and 215 °C for the two binaries PTB7-Th:ITIC-4F and PTB7-Th:ITIC-4Cl, respectively (Figure 3b; Figure S4, Supporting Information). The midpoint of the corresponding step in FSC heating scans indicates

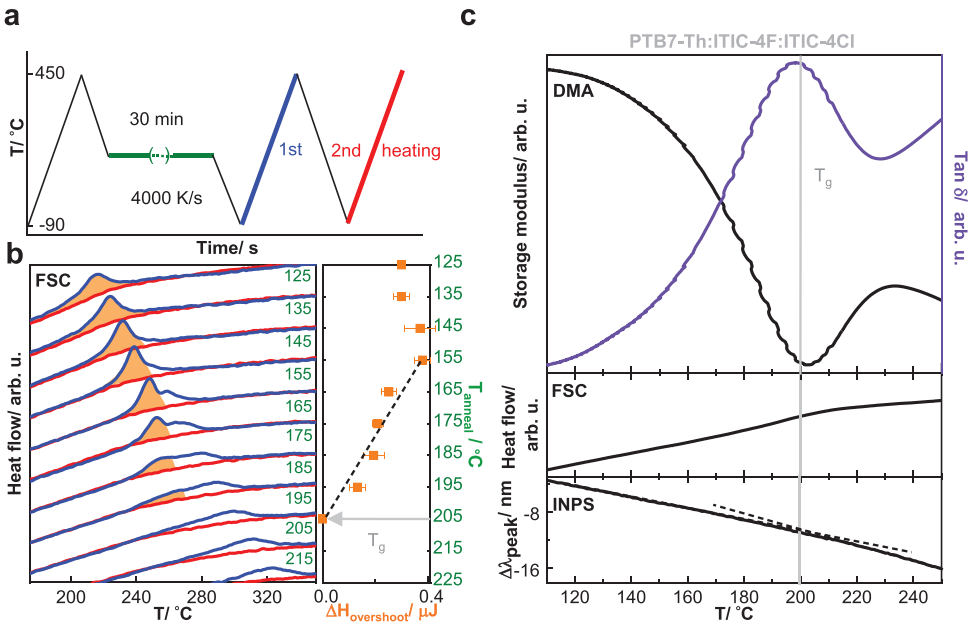


**Figure 3.** a) FSC protocol: the sample is first rapidly heated to 450 °C and then annealed for 30 min at different annealing temperatures $T_{anneal}$ (green), followed by a first (blue) and second heating scan (red), both after quenching to −90 °C; b) FSC heating thermograms of the 1:0.5:0.5 PTB7-Th:ITIC-4F:ITIC-4Cl ternary blend after annealing (blue) and after quenching from 450 to −90 °C (red) with the enthalpy overshoot indicated in orange (left); the temperature where the enthalpy overshoot $\Delta H_{overshoot}$ approaches zero corresponds to the $T_g$ (right); c) DMA thermogram showing the storage modulus and loss tangent tan $\delta$, FSC heating thermogram recorded after quenching the sample, and plasmonic nanospectroscopy, or indirect nanoplasmonic sensing (INPS), of the ternary blend showing the relative shift of the localized surface plasmon resonance peak $\Delta\lambda_{peak}$ with temperature.


© 2020 The Authors. Published by Wiley-VCH GmbH

similar values of 200, 190, and 212 °C for the ternary and the two binary blends, respectively. We were able to confirm the $T_g$ values with dynamic mechanical analysis (DMA), and plasmonic nanospectroscopy (Figure 3c; Table S1, Figure S5, Supporting Information).[34,35] Notably, for the ternary blend, the loss tangent tan $\delta$ from DMA first heating thermograms peaks at 200 °C, and the shift of the plasmonic resonance peak $\Delta\lambda_{peak}$ changes slope at the same temperature, which is in good agreement with our FSC data (Figure 3c).

In a further set of experiments, we compared the tendency of the acceptor to crystallize in binary and ternary blends. Samples were annealed at $T_{anneal}$ = 160 °C for 10 min and 24 h, respectively. The typical crystal size is on the order of a few hundred nanometers, which we explain with diffusion-limited crystallization below the $T_g$, similar to the crystallization behavior of ITIC.[20] Acceptor crystals are clearly visible in optical micrographs and scanning electron microscopy (SEM) images of both binary blends after 10 min (**Figure 4**b; Figure S6, Supporting Information). After 24 h, the crystallites visible in the binary blends have grown in size (Figure S7, Supporting Information). In contrast, no crystals can be observed in the case of the ternary blend at 160 °C after 10 min or 24 h, which indicates that the ternary blend is more thermally stable (Figure 4b).

We used atomic force microscopy based infrared spectroscopy (AFM-IR) to elucidate the make-up of the blend nanostructure in more detail. First, we used AFM-IR to confirm that

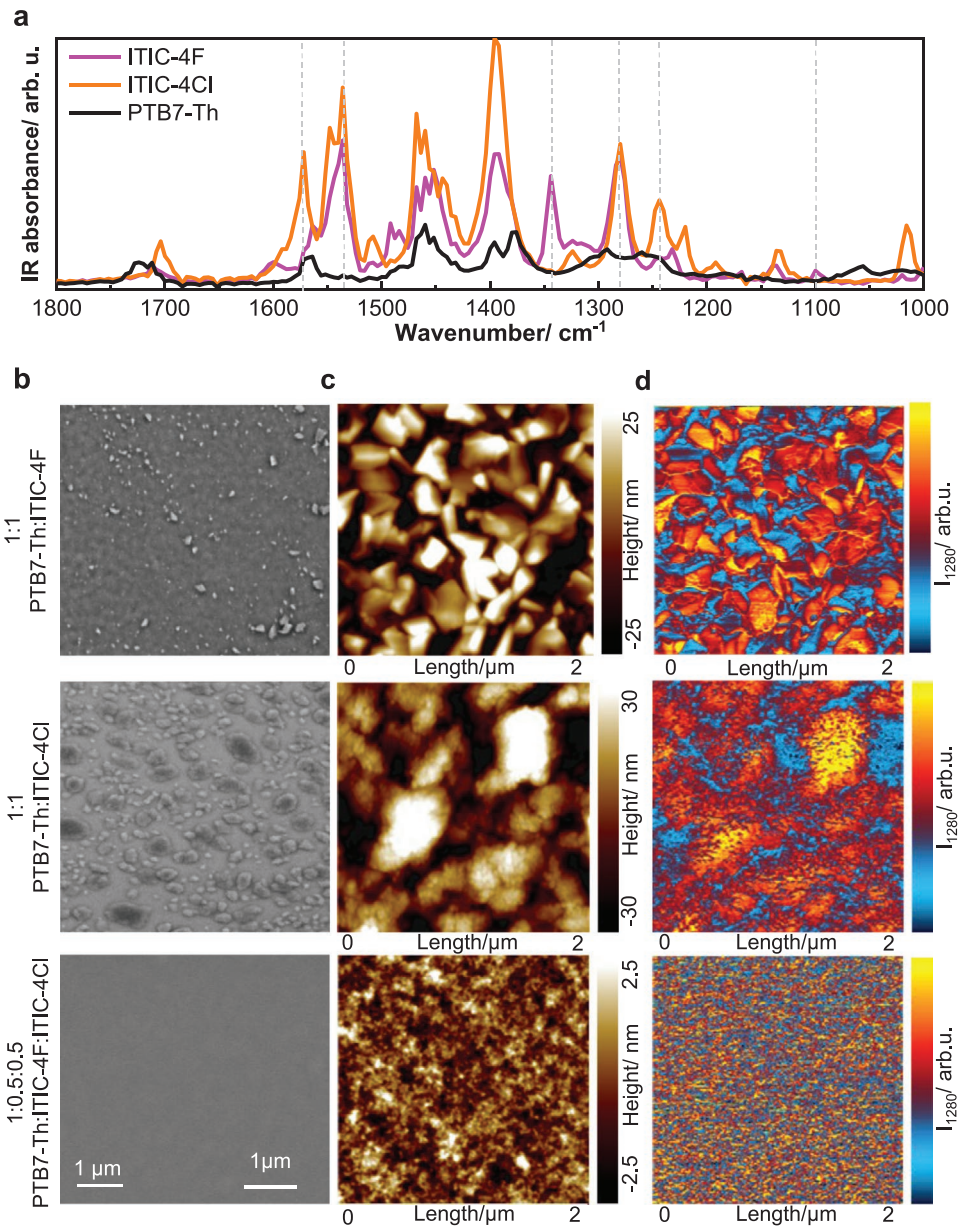


**Figure 4.** a) AFM-IR spectra recorded for neat films of PTB7-Th, ITIC-4F, and ITIC-4Cl with a resolution of 4 $cm^{-1}$ per pt; b) SEM images; c) AFM height images showing the peak-to-valley height difference; and d) AFM-IR images recorded at 1280 $cm^{-1}$ of the binary blend 1:1 PTB7-Th:ITIC-4F (top row), PTB7-Th:ITIC-4Cl (center row), and the ternary blend 1:0.5:0.5 PTB7-Th:ITIC-4F:ITIC-4Cl (bottom); all samples annealed at 160 °C for 10 min.


© 2020 The Authors. Published by Wiley-VCH GmbH

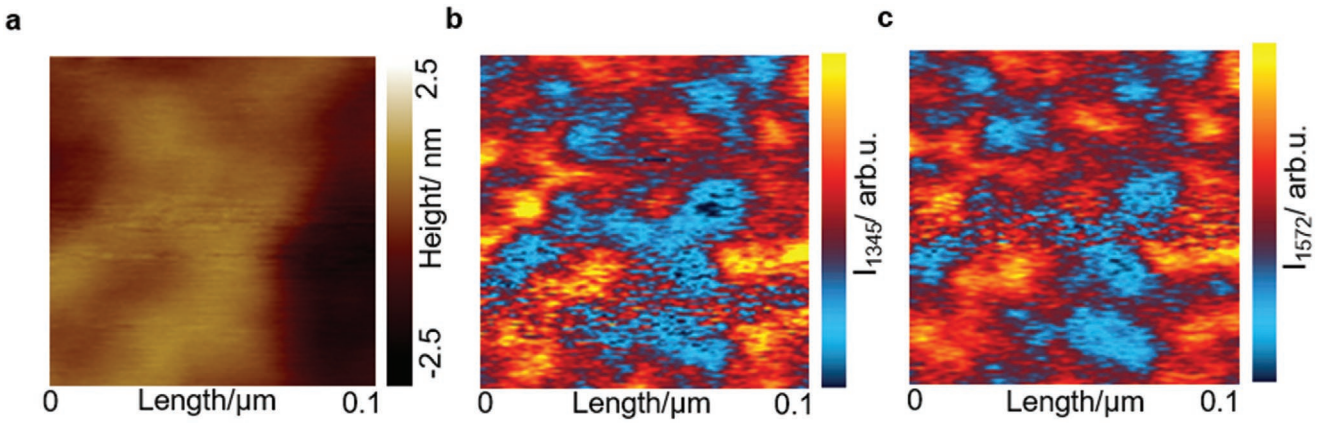


**Figure 5.** The same spot of a 1:0.5:0.5 PTB7-Th:ITIC-4F:ITIC-4Cl ternary film annealed at 160 °C and imaged with a) AFM in height mode; b) AFM-IR recorded at 1345 $cm^{-1}$, where only ITIC-4F absorbs; and c) AFM-IR recorded at 1572 $cm^{-1}$, where ITIC-4Cl absorbs.

the crystals in thin films of the two binaries consist of ITIC-4F and ITIC-4Cl, respectively. IR spectra recorded at areas covered by crystals are dominated by absorption peaks that arise from the two acceptors, for example, peaks at 1280 and 1540 $cm^{-1}$ that we assign to stretching vibrations of C—C or $CH_2$ twisting and C=C bonds, respectively (Figure 4a). Further, the spectra of both ITIC-4F and ITIC-4Cl show peaks that are unique for each material, that is, peaks at 1345 and 1572 $cm^{-1}$, respectively, which we can use to selectively image either material. Mapping of the binary films with AFM-IR or standard AFM in height mode produced images with similar features, that is, those arising from crystals that protrude ≈ 50–60 nm from the film surface and coincide with areas where acceptor specific IR absorption peaks are recorded (Figure 4c,d; Figure S9, Supporting Information). The surface of ternary blend films appears considerably more fine-grained and shows a roughness of only 5 nm. Due to the low surface roughness of ternary blend films we were able to record AFM-IR images at very high magnification. We imaged the same spot in a ternary film annealed at 160 °C with both AFM in height mode (**Figure 5**a), as well as AFM-IR using an IR-laser wavenumber of 1345 $cm^{-1}$, where only ITIC-4F absorbs, or 1572 $cm^{-1}$, where ITIC-4Cl absorbs (Figure 5b,c). The two AFM-IR images reveal 10–30 nm small domains that are similar in shape. We conclude that ITIC-4F and ITIC-4Cl are located in close vicinity to each other and form distinct domains that are uniform in composition, and are intertwined with polymer-rich domains, in agreement with the phase behavior described above (cf. Figure 2c).

We propose that the small size of the ITIC-4F:ITIC-4Cl domains suppresses crystallization of the acceptor mixture due to confinement, that is, nucleation events are rare and hence most of the material is effectively separated from nucleation sites by the surrounding polymer domains. Since the polymer is disordered, and ternary blends display a high degree of photoluminescence (PL) quenching (see discussion below), we argue that the polymer-rich domains nevertheless contain a certain amount of ITIC-4F and ITIC-4Cl, which can be considered as dissolved in the polymer phase. Annealing at 200 °C, that is, at the $T_g$ of the ternary, results in coarsening as evidenced by somewhat larger domains with a size of 20–50 nm (Figure S8, Supporting Information), as well as co-crystallization of the acceptor mixture (cf. Figure S2a, Supporting Information). Coarsening of the ternary blend at 200 °C and above is corroborated by variable-temperature PL and scattering measurements, which show a clear increase in PL intensity with peak at 820 nm (Figure S10a,b, Supporting Information) and

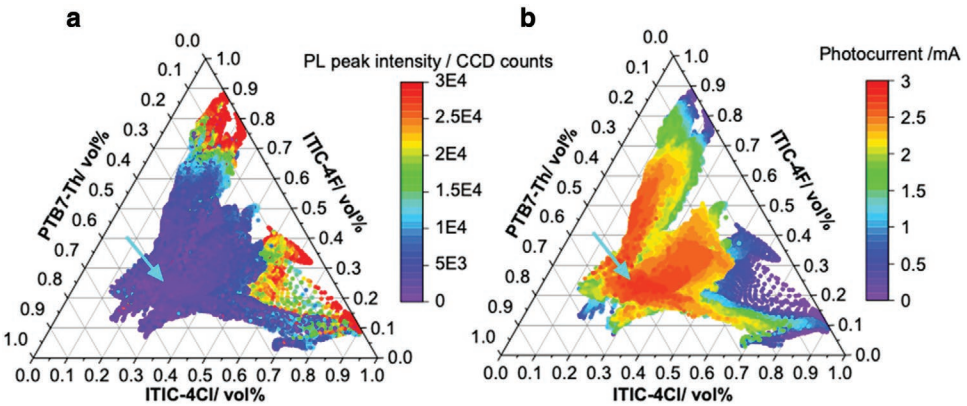


**Figure 6.** Ternary composition diagrams showing a) the photoluminescence intensity, PL; and b) the photocurrent obtained with white light for different compositions of PTB7-Th:ITIC-4F:ITIC-4Cl. The ternary 1:0.5:0.5 PTB7-Th:ITIC-4F:ITIC-4Cl is marked with arrows. The composition in this figure refers to number of molecules per unit volume. We assume that all materials have the same density (1 g $cm^{-3}$).


© 2020 The Authors. Published by Wiley-VCH GmbH

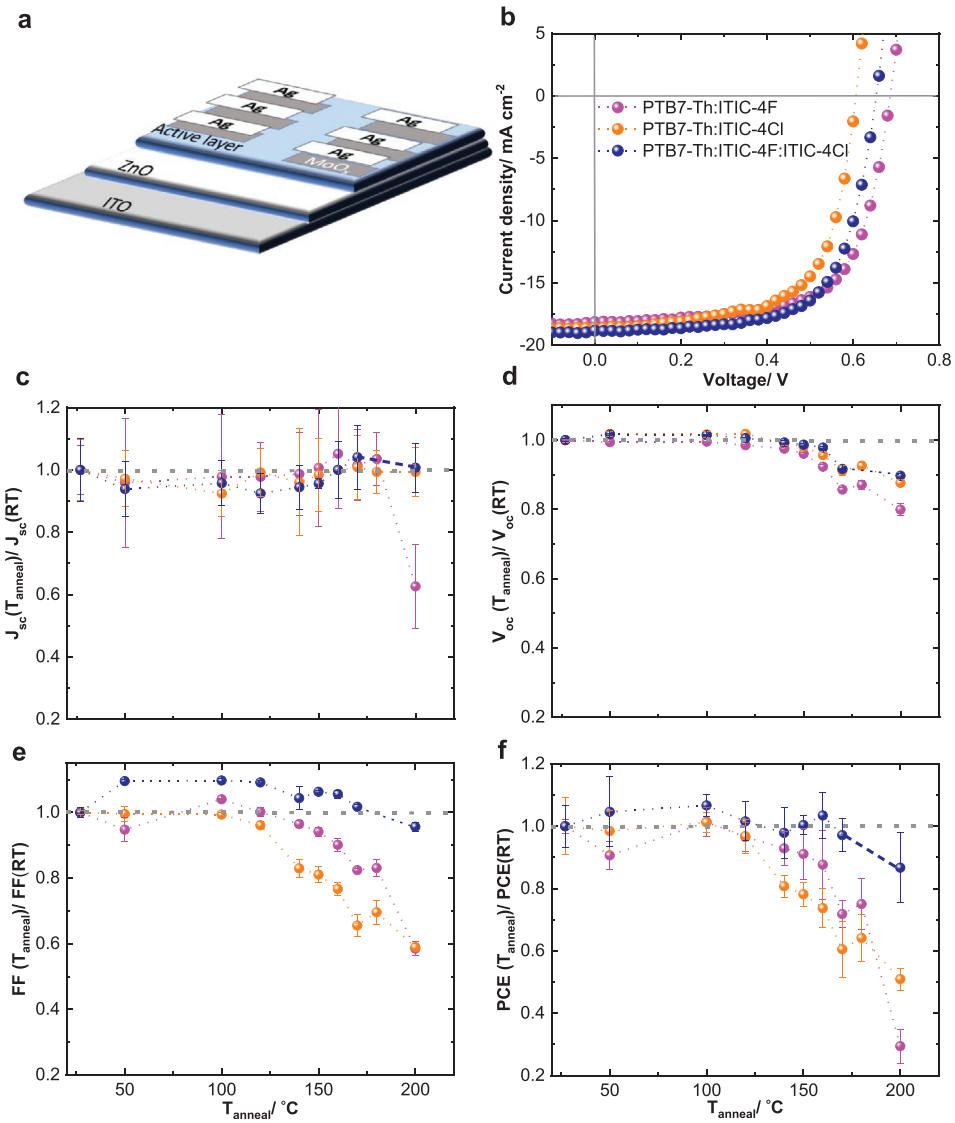


**Figure 7.** a) Photovoltaic device layout, b) Representative current density–voltage (*J*–*V*) characteristics of devices comprising the two binary blends, 1:1 PTB7-Th:ITIC-4F and 1:1 PTB7-Th:ITIC-4Cl, and the 1:0.5:0.5 PTB7-Th:ITIC-4F:ITIC-4Cl ternary blend, c) Short-circuit current density $J_{sc}$, d) Open-circuit voltage $V_{oc}$, e) Fill factor FF and f) Power conversion efficiency PCE of devices comprising active layers annealed for 10 min at temperatures between 25 and 200 °C; data points represent average values of measurements done for up to 6 pixels on the same substrate.

an increase in scattered laser intensity at 200 °C (Figure S10c, Supporting Information), suggesting that donor and acceptor domains become purer.

To determine the likely range of compositions that will display an optimal photovoltaic performance, we used a combinatorial screening method recently described by Harillo-Banos et al. for ternary solar cells.[36] In brief, thin layers of the three components (or mixtures thereof) were sequentially deposited on top of each other, resulting in four samples with different lateral composition gradients that when combined covered approximately 65% of the phase space (see Figure S11, Supporting Information, and Experimental Section for details). We then mapped the local Raman intensity, PL, and photocurrent at all compositions covered by the graded samples to obtain maps of these parameters (**Figure 6**; Figure S12, Supporting Information). Analysis of the Raman spectra was used to determine the local composition.[37] The PL map indicates the highest degree of PL quenching for compositions that are rich in all three components. We propose that for these compositions the highest degree of intermixing of the donor polymer and acceptor mixture is obtained, in agreement with the AFM-IR based analysis of the ternary blend nanostructure (cf. Figure 5). The photocurrent map shows a similar trend with a broad maximum for compositions ranging from 20–60% PTB7-Th (Figure 6b). We argue that the ternary blend displays a high photovoltaic performance across a wide range of compositions. Therefore, position-dependent deviations from the optimal composition, which would no doubt occur


© 2020 The Authors. Published by Wiley-VCH GmbH

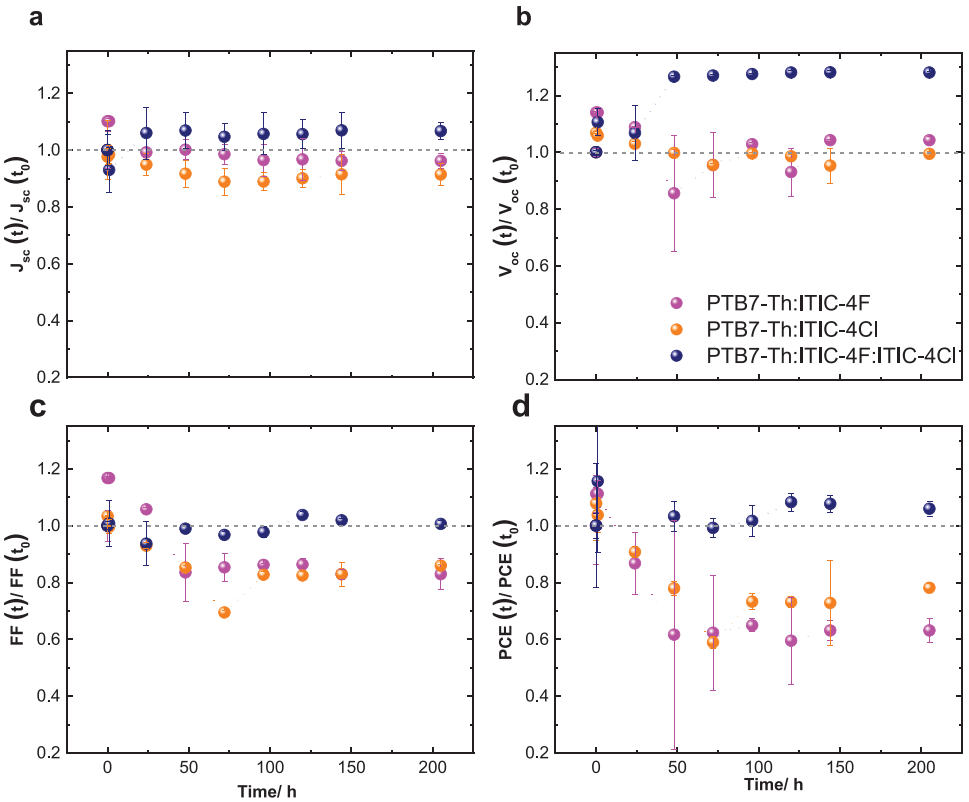


**Figure 8.** a) $J_{sc}$, b) $V_{oc}$, c) FF, and d) PCE of 1:1 PTB7-Th:ITIC-4F and 1:1 PTB7-Th:ITIC-4Cl binary devices, and 1:0.5:0.5 PTB7-Th:ITIC-4F:ITIC-4Cl ternary devices recorded after annealing for up to 205 h at 130 °C; data points represent average values of measurements done for up to 6 pixels on the same substrate.

if large-area device fabrication was attempted, will nevertheless result in solar cells with limited spatial variation in light harvesting efficiency.

In a further set of experiments, we fabricated a series of solar cells with an inverted architecture and an active layer composed of the ternary blend (see Experimental Section for details). We varied the composition of the active layer blend by changing the ratio of ITIC-4F and ITIC-4Cl, while maintaining a constant 1:1 ratio of donor to acceptor materials (Table S2, Supporting Information). These series of devices covered the range of compositions for which our combinatorial screening experiments had revealed the highest photocurrent (cf. Figure 6a). In agreement with our photocurrent map a ternary blend composition of 1:0.5:0.5 (wt%) PTB7-Th:ITIC-4F:ITIC-4Cl showed the best photovoltaic performance with a short-circuit current density $J_{sc} \approx 18.6$ mA cm$^{-2}$, open-circuit voltage $V_{oc} \approx 660$ mV, and fill factor FF ≈ 68%, giving rise to a power conversion efficiency PCE ≈ 8.3% (Table S3, Supporting Information).

We, therefore, studied the thermal stability of the 1:0.5:0.5 ternary devices. We annealed active layers for 10 min at various temperatures up to $T_{anneal} = 200$ °C prior to evaporation of the top $MoO_x$ interlayer and Ag electrode. For comparison, we also fabricated 1:1 binary blend devices and used the same annealing protocol. Binary blend devices show no drop in $J_{sc}$ and $V_{oc}$ up to at least 150 °C (**Figure 7**c,d). However, we observe a drastic drop in FF by as much as 40% for $T_{anneal} > 120$ °C, which we explain by the growth of acceptor crystals that disrupt the blend nanostructure. Overall, annealing of binary blend devices at, for example, $T_{anneal} = 150$ °C results in a drop in PCE by 10% in case of PTB7-Th:ITIC-4F and 20% in case of PTB7-Th:ITIC-4Cl. Ternary blend devices show a markedly different behavior. Neither $J_{sc}$ nor the FF deteriorate up to $T_{anneal} > 170$ °C as a result of suppressed crystallization of the acceptor mixture and hence an unaltered blend nanostructure (Figure 7c,d,e). We note a slight drop in $V_{oc}$ by 10%, which occurs for the two binary blend devices as well as the ternary devices and may result from an adverse effect of annealing on the ZnO bottom interlayer.[38,39] Overall, the ternary blend devices display superior thermal stability as compared to the two binary blend ones, with a stable PCE up to 170 °C by maintaining the same blend nanostructure, which indicates that device fabrication and operation at very high temperatures can be considered.

In a final set of experiments, we studied the thermal stability during longer annealing times of up to 205 h. Binary and ternary devices were annealed at $T_{anneal} = 130$ °C under dark and inert conditions. We chose this temperature to ensure that our annealing protocol does not affect the ZnO interface layer. Binary devices display a notable burn-in during the first 50 h, leading to a drop in PCE by at least one third (**Figure 8**). Strikingly, the addition of third component arrested the burn-in and resulted in a steady PCE in case of ternary devices, which we assign to a more stable nanostructure. The constant photovoltaic performance of ternary devices at 130 °C confirms that the use of an acceptor mixture is a powerful tool to improve the thermal stability of organic solar cells.

 © 2020 The Authors. Published by Wiley-VCH GmbH

## 3. Conclusions

In this study, we have investigated the phase behavior of a binary non-fullerene acceptor mixture, ITIC-4F:ITIC-4Cl, which can undergo co-crystallization. Addition of the donor polymer PTB7-Th results in a ternary blend with a high $T_g \approx 200$ °C. The acceptor mixture phase separates into tens of nanometer-sized domains, intertwined with polymer-rich domains, which effectively suppresses co-crystallization. The resulting non-crystalline ternary blend nanostructure remains unaltered despite annealing at temperatures up to 170 °C, resulting in stable photovoltaic devices. We conclude that the use of ternary blends facilitates fabrication protocols that expose the active layer to a high thermal stress. The combination of a high $T_g$ and suppressed crystallization guarantees a highly reproducible and thermally robust nanostructure, which is of urgent need for upscaling of organic solar cells.

## 4. Experimental Section

*Materials*: PTB7-Th (number-average molecular weight $M_n \approx 19$ kg mol$^{-1}$, polydispersity index PDI = 4.4), ITIC-4F, and ITIC-4Cl were purchased from 1-Materials Inc. and used as received. Chlorobenzene was obtained from Sigma-Aldrich and used as received. All samples were processed from 20 g L$^{-1}$ chlorobenzene solutions. For more information, refer to device fabrication.

*Differential Scanning Calorimetry*: Measurements were done with a DSC2 from Mettler Toledo equipped with a Gas controller GC 200 system at a heating/cooling rate of 10 °C min$^{-1}$. Samples were prepared by drop casting 4 mg of material on a glass slide, followed by transfer to a 40 µL Al crucible.

*Fast Scanning Calorimetry*: Measurements were done with a Flash DSC 1 from Mettler Toledo. A thin film was spin-coated directly on the backside of the sensor. The sample was first heated to 450 °C, followed by aging at different temperatures (60–225 °C) for 30 min; heating/cooling rate 4000 K s$^{-1}$ (see Figure 2a).

*Dynamic Mechanical Analysis*: Measurements were done with a Q800 from TA Instruments from room temperature to 300 °C at a frequency of 1 Hz and a heating rate of 3 °C min$^{-1}$.[20,34] 2.5 cm × 0.5 cm pieces of a plain weave glass fiber mesh with a weight of 25 g m$^{-2}$ (Easycomposites) were cut at an angle of 45°, drop coated, and dried under vacuum at 60 °C for 60 min.

*Indirect Nanoplasmonic Sensing*: Details about the measurement and setup can be found in refs. [20,35].

*Grazing-Incident Wide-Angle X-Ray Scattering*: GIWAXS experiments were conducted on CMS beamline at NSLS II, Brookhaven National Lab. An X-ray of energy of 13.5 keV was directed onto the thin films at an incident angle of 0.15°. The generated diffractograms were collected by a Pilatus 1M detector placed 255 mm away from the sample along the incident X-ray beam.

*Polarized Optical Microscopy*: Images of samples on silicon wafers were taken with a Zeiss Axio Scope A1 optical microscope in cross-polarization and reflection mode.

*Scanning Electron Microscopy*: Imaging was done with a Leo Ultra 55 SEM at 3 kV using a secondary-electron detector at a working distance of ≈10 mm.

*Atomic Force Microscopy-Infrared Spectroscopy*: For local IR characterization, AFM-IR was used. Samples were spin-coated on oxygen plasma cleaned Si-wafers. AFM-IR measurements were performed in Tapping Mode with a Bruker/Anasys Instruments nanoIR3 (France/USA), equipped with an MIR-cat QT 2400 QCL laser from Daylight Solutions (USA). Gold-coated silicon tips were used: PR-EX-TnIR-A (75 kHz, 1–7 N m$^{-1}$).

*Variable-Temperature Photoluminescence Spectroscopy*: Thin films were spin-coated on glass substrates coated with 90 nm Al, placed on a hot plate at ambient atmosphere, and excited with a green laser with peak emission at 530 nm (the spot size was narrowed with a 1 mm aperture). Emission spectra were recorded via an optical fiber from Ocean Optics (diameter 600 µm) with an Ocean Optics QE-Pro spectrometer in kinetic mode and 100 ms integration time during heating at 10 °C min$^{-1}$ from 30 to 260 °C.

*Photoluminescence, Raman and Photocurrent Phase Diagram*: The detailed sample description can be found in ref. [36]. While extracting the current the samples were scanned under a microscope (WITec alpha 300 RA confocal Raman setup). White photocurrent maps were extracted using the setup built-in white light, while excitation at 488 and 633 nm was used to measure the Raman and photoluminescence spectra at each position, respectively. The ternary composition diagram was constructed from the Raman fingerprints of the neat materials as well as the cross-section, refractive index, and extinction coefficient at 488 nm. All measurements were done co-locally to mitigate the spatial dependence.

*Device Fabrication*: Pre-patterned indium tin oxide (ITO) glass substrates were cleaned in an ultrasonic bath with acetone and isopropyl alcohol, dried under nitrogen flow, and treated with oxygen plasma. 20 mg ml$^{-1}$ of each of PTB7-Th, ITIC-4F, and ITIC-4Cl were dissolved in chlorobenzene overnight at 80 °C. The appropriate ratios of each were stirred for couple of hours before spin coating the active layer. No additives were added to evade any possible additive-induced crystallization in the active layer. A ZnO NP interlayer was deposited by spin coating a nanoparticle suspension from Avantama Inc. at 4000 rpm for 40 s, followed by annealing for 10 min at 80 °C in air. Active layers were spin-coated at 2000 rpm inside a glove box, followed by annealing as indicated. Finally, 10 nm $MoO_x$ followed by 100 nm silver were thermally evaporated at $1 \times 10^{-6}$ bar. *I–V* curves were measured using Keithley 2400 source meter and a WaveLabs sinus-70 solar simulator calibrated to 1 sun, AM1.5 G.

*Thermal Stability of Devices*: All thermal stability experiments were conducted inside a glove box. The partial device stack (ITO/ZnO NP/Active layer) was annealed at different temperatures and for different times. The device fabrication was completed by evaporating $MoO_x$ and Ag as mentioned above. The devices were measured under a WaveLabs sinus-70 solar simulator calibrated to 1 sun, AM1.5 G.

## Supporting Information

Supporting Information is available from the Wiley Online Library or from the author.

## Acknowledgements

S.H. and S.H.K.P. contributed equally to this work. The authors acknowledge the King Abdullah University of Science and Technology (KAUST) Office of Sponsored Research (OSR) under OSR-2018-CPF-4106 and the Knut and Alice Wallenberg Foundation through the project "Mastering Morphology for Solution-borne Electronics" (2016.0059) for funding. M.C.-Q. and A.H. acknowledge the European Research Council (ERC) for funding under grant agreement no. 648901. The authors thank MCIU for a Ramón y Cajal contract, Ikerbasque Foundation for the Fellow program (J.M) and grants Ref. PGC2018-094620-A-100, SEV-2015-0496 and PGC2018-095411-B-100. L.Y. thanks the National Nature Science Foundation of China (NSFC 21905185) for financial support. The authors thank the National Synchrotron Light Source II, Brookhaven National Lab (Suffolk, Upton, New York, USA) for beamtime.

## Conflict of Interest

The authors declare no conflict of interest.

 © 2020 The Authors. Published by Wiley-VCH GmbH

## Keywords

co-crystals, glass transition temperatures, non-fullerene acceptors, suppressed crystallization, ternary solar cells

Received: June 29, 2020
Revised: September 23, 2020
Published online:

[1] Y. Cui, H. Yao, J. Zhang, K. Xian, T. Zhang, L. Hong, Y. Wang, Y. Xu, K. Ma, C. An, C. He, Z. Wei, F. Gao, J. Hou, *Adv. Mater.* **2020**, *32*, 1908205.
[2] N. Gasparini, S. H. K. Paleti, J. Bertrandie, G. Cai, G. Zhang, A. Wadsworth, X. Lu, H.-L. Yip, I. McCulloch, D. Baran, *ACS Energy Lett.* **2020**, *5*, 1371.
[3] Y. Jiang, L. Sun, F. Jiang, C. Xie, L. Hu, X. Dong, F. Qin, T. Liu, L. Hu, X. Jiang, Y. Zhou, *Mater. Horiz.* **2019**, *6*, 1438.
[4] I. T. Sachs-Quintana, T. Heumüller, W. R. Mateker, D. E. Orozco, R. Cheacharoen, S. Sweetnam, C. J. Brabec, M. D. McGehee, *Adv. Funct. Mater.* **2014**, *24*, 3978.
[5] M. Schubert, B. A. Collins, H. Mangold, I. A. Howard, W. Schindler, K. Vandewal, S. Roland, J. Behrends, F. Kraffert, R. Steyrleuthner, Z. Chen, K. Fostiropoulos, R. Bittl, A. Salleo, A. Facchetti, F. Laquai, H. W. Ade, D. Neher, *Adv. Funct. Mater.* **2014**, *24*, 4068.
[6] A. Zusan, K. Vandewal, B. Allendorf, N. H. Hansen, J. Pflaum, A. Salleo, V. Dyakonov, C. Deibel, *Adv. Energy Mater.* **2014**, *4*, 1400922.
[7] S. A. Mollinger, B. A. Krajina, R. Noriega, A. Salleo, A. J. Spakowitz, *ACS Macro Lett.* **2015**, *4*, 708.
[8] C. Müller, *Chem. Mater.* **2015**, *27*, 2740.
[9] S. Bertho, G. Janssen, T. J. Cleij, B. Conings, W. Moons, A. Gadisa, J. D'Haen, E. Goovaerts, L. Lutsen, J. Manca, D. Vanderzande, *Sol. Energy Mater. Sol. Cells* **2008**, *92*, 753.
[10] C. Lindqvist, A. Sanz-Velasco, E. Wang, O. Bäcke, S. Gustafsson, E. Olsson, M. R. Andersson, C. Müller, *J. Mater. Chem. A* **2013**, *1*, 7174.
[11] D. Angmo, M. Bjerring, N. C. Nielsen, B. C. Thompson, F. C. Krebs, *J. Mater. Chem. C* **2015**, *3*, 5541.
[12] A. Diaz de Zerio Mendaza, A. Melianas, S. Rossbauer, O. Bäcke, L. Nordstierna, P. Erhart, E. Olsson, T. D. Anthopoulos, O. Inganäs, C. Müller, *Adv. Mater.* **2015**, *27*, 7325.
[13] P. Cheng, C. Yan, Y. Wu, J. Wang, M. Qin, Q. An, J. Cao, L. Huo, F. Zhang, L. Ding, Y. Sun, W. Ma, X. Zhan, *Adv. Mater.* **2016**, *28*, 8021.
[14] A. Diaz de Zerio, C. Müller, *Adv. Energy Mater.* **2018**, *8*, 1702741.
[15] J. Hou, O. Inganäs, R. H. Friend, F. Gao, *Nat. Mater.* **2018**, *17*, 119.
[16] C. Yan, S. Barlow, Z. Wang, H. Yan, A. K. Y. Jen, S. R. Marder, X. Zhan, *Nat. Rev. Mater.* **2018**, *3*, 18003.
[17] A. Wadsworth, M. Moser, A. Marks, M. S. Little, N. Gasparini, C. J. Brabec, D. Baran, I. McCulloch, *Chem. Soc. Rev.* **2019**, *48*, 1596.
[18] J. Xin, X. Meng, X. Xu, Q. Zhu, H. B. Naveed, W. Ma, *Matter* **2019**, *1*, 1316.
[19] Q. Liang, J. Han, C. Song, X. Yu, D.-M. Smilgies, K. Zhao, J. Liu, Y. Han, *J. Mater. Chem. A* **2018**, *6*, 15610.
[20] L. Yu, D. Qian, S. Marina, F. A. A. Nugroho, A. Sharma, S. Hultmark, A. I. Hofmann, R. Kroon, J. Benduhn, D.-M. Smilgies, K. Vandewal, M. R. Andersson, C. Langhammer, J. Martín, F. Gao, C. Müller, *ACS Appl. Mater. Interfaces* **2019**, *11*, 21766.
[21] Z. Fei, F. D. Eisner, X. Jiao, M. Azzouzi, J. A. Röhr, Y. Han, M. Shahid, A. S. R. Chesman, C. D. Easton, C. R. McNeill, T. D. Anthopoulos, J. Nelson, M. Heeney, *Adv. Mater.* **2018**, *30*, 1705209.
[22] S. M. Swick, T. Gebraad, L. Jones, B. Fu, T. J. Aldrich, K. L. Kohlstedt, G. C. Schatz, A. Facchetti, T. J. Marks, *ChemPhysChem* **2019**, *20*, 2608.
[23] W. Köntges, P. Perkhun, J. Kammerer, R. Alkarsifi, U. Würfel, O. Margeat, C. Videlot-Ackermann, J.-J. Simon, R. R. Schröder, J. Ackermann, M. Pfannmöller, *Energy Environ. Sci.* **2020**, *13*, 1259.
[24] M. Jørgensen, K. Norrman, S. A. Gevorgyan, T. Tromholt, B. Andreasen, F. C. Krebs, *Adv. Mater.* **2012**, *24*, 580.
[25] F. C. Krebs, *Sol. Energy Mater. Sol. Cells* **2009**, *93*, 394.
[26] S. Strohm, F. Machui, S. Langner, P. Kubis, N. Gasparini, M. Salvador, I. McCulloch, H. J. Egelhaaf, C. J. Brabec, *Energy Environ. Sci.* **2018**, *11*, 2225.
[27] E. Bihar, D. Corzo, T. C. Hidalgo, D. Rosas-Villalva, K. N. Salama, S. Inal, D. Baran, *Adv. Mater. Technol.* **2020**, *5*, 2000226.
[28] C.-Y. Liao, Y. Chen, C.-C. Lee, G. Wang, N.-W. Teng, C.-H. Lee, W.-L. Li, Y.-K. Chen, C.-H. Li, H.-L. Ho, P. H.-S. Tan, B. Wang, Y.-C. Huang, R. M. Young, M. R. Wasielewski, T. J. Marks, Y.-M. Chang, A. Facchetti, *Joule* **2020**, *4*, 189.
[29] N. Gasparini, A. Salleo, I. McCulloch, D. Baran, *Nat. Rev. Mater.* **2019**, *4*, 229.
[30] G. R. Desiraju, R. Parthasarathy, *J. Am. Chem. Soc.* **1989**, *111*, 8725.
[31] V. R. Hathwar, T. N. G. Row, *Cryst. Growth Des.* **2011**, *11*, 1338.
[32] X. Song, N. Gasparini, L. Ye, H. Yao, J. Hou, H. Ade, D. Baran, *ACS Energy Lett.* **2018**, *3*, 669.
[33] J. Martín, N. Stingelin, D. Cangialosi, *J. Phys. Chem. Lett.* **2018**, *9*, 990.
[34] A. Sharma, X. Pan, J. A. Campbell, M. R. Andersson, D. A. Lewis, *Macromolecules* **2017**, *50*, 3347.
[35] F. A. A. Nugroho, A. Diaz de Zerio Mendaza, C. Lindqvist, T. J. Antosiewicz, C. Müller, C. Langhammer, *Anal. Chem.* **2017**, *89*, 2575.
[36] A. Harillo-Baños, X. Rodríguez-Martínez, M. Campoy-Quiles, *Adv. Energy Mater.* **2020**, *10*, 2070001.
[37] X. Rodríguez-Martínez, M. S. Vezie, X. Shi, I. McCulloch, J. Nelson, A. R. Goñi, M. Campoy-Quiles, *J. Mater. Chem. C* **2017**, *5*, 7270.
[38] A. Sharma, S. E. Watkins, G. Andersson, D. A. Lewis, *Energy Technol.* **2014**, *2*, 462.
[39] C. Jiang, R. R. Lunt, P. M. Duxbury, P. P. Zhang, *RSC Adv.* **2014**, *4*, 3604.

 © 2020 The Authors. Published by Wiley-VCH GmbH

© 2020 Wiley-VCH GmbH

ADVANCED FUNCTIONAL MATERIALS

# Supporting Information

for *Adv. Funct. Mater.*, DOI: 10.1002/adfm.202005462

# Suppressing Co-Crystallization of Halogenated Non-Fullerene Acceptors for Thermally Stable Ternary Solar Cells

*Sandra Hultmark, Sri Harish Kumar Paleti, Albert Harillo, Sara Marina, Ferry Anggoro Ardy Nugroho, Yanfeng Liu, Leif K. E. Ericsson, Ruipeng Li, Jaime Martín, Jonas Bergqvist, Christoph Langhammer, Fengling Zhang, Liyang Yu, Mariano Campoy-Quiles, Ellen Moons, Derya Baran,* and Christian Müller**

# Suppressing Co-crystallization of Halogenated Non-Fullerene Acceptors for Thermally Stable Ternary Solar Cells

Sandra Hultmark, [†] Sri Harish Kumar Paleti,[†] Albert Harillo, Sara Marina, Ferry Anggoro Ardy Nugroho, Yanfeng Liu, Leif Ericsson, Ruipeng Li, Jaime Martín, Jonas Bergqvist, Christoph Langhammer, Fengling Zhang, Liyang Yu, Mariano Campoy-Quiles, Ellen Moons, Derya Baran,* Christian Müller*

[†]these authors contributed equally

Sandra Hultmark, Prof. Christian Müller
Department of Chemistry and Chemical Engineering, Chalmers University of Technology, 41296 Göteborg, Sweden
*christian.muller@chalmers.se

Sri Harish Kumar Paleti, Prof. Derya Baran
King Abdullah University of Science and Technology (KAUST), Division of Physical Sciences & Engineering and KAUST Solar Center (KSC), Thuwal, Saudi Arabia
*derya.baran@kaust.edu.sa

Dr. Leif Ericsson, Prof. Ellen Moons
Department of Physics and Electrical Engineering, Karlstad University, 65188 Karlstad, Sweden

Dr. Liyang Yu
Key Laboratory of Green Chemistry and Technology of Ministry of Education, College of Chemistry, Sichuan University, Chengdu 610064, China

Dr. Ruipeng Li
National Synchrotron Light Source II, Brookhaven National Laboratory, New York 11973, United States; Phone: +86-28-85415506; Email: rli@bnl.gov; Fax: +86-28- 85415506

Albert Harillo, Dr. Mariano Campoy-Quiles
Institut de Ciència de Materials de Barcelona (ICMAB-CSIC), Campus de la UAB, Bellaterra, 08193, Spain

Sara Marina, Dr. Jaime Martín
POLYMAT and Polymer Science and Technology Department, Faculty of Chemistry, University of the Basque Country UPV/EHU, Paseo Manuel de Lardizabal 3, 20018 Donostia-San Sebastián, Spain

Dr. Ferry Anggoro Ardy Nugroho, Prof. Christoph Langhammer
Department of Physics, Chalmers University of Technology, 41296 Göteborg, Sweden

Yanfeng Liu, Dr. Jonas Bergqvist, Prof. Fengling Zhang
Department of Physics, Chemistry and Biology (IFM), Linköping University, 581 83 Linköping, Sweden

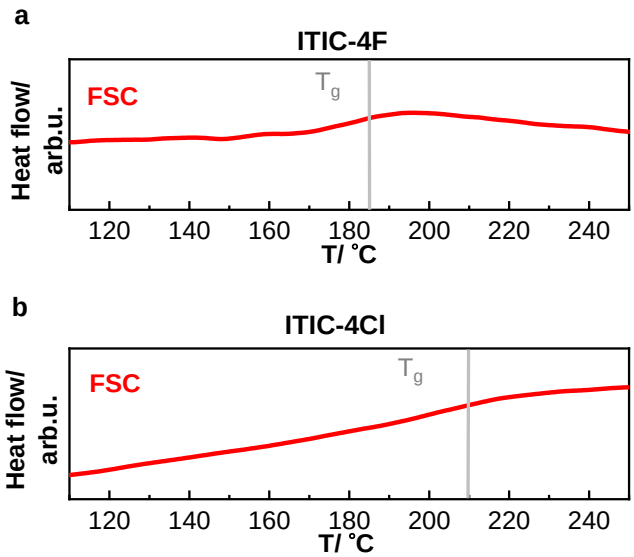


**Figure S1.** FSC heating thermograms of (a) 1:1 PTB7-Th:ITIC-4F and (b) 1:1 PTB7-Th:ITIC-4Cl.

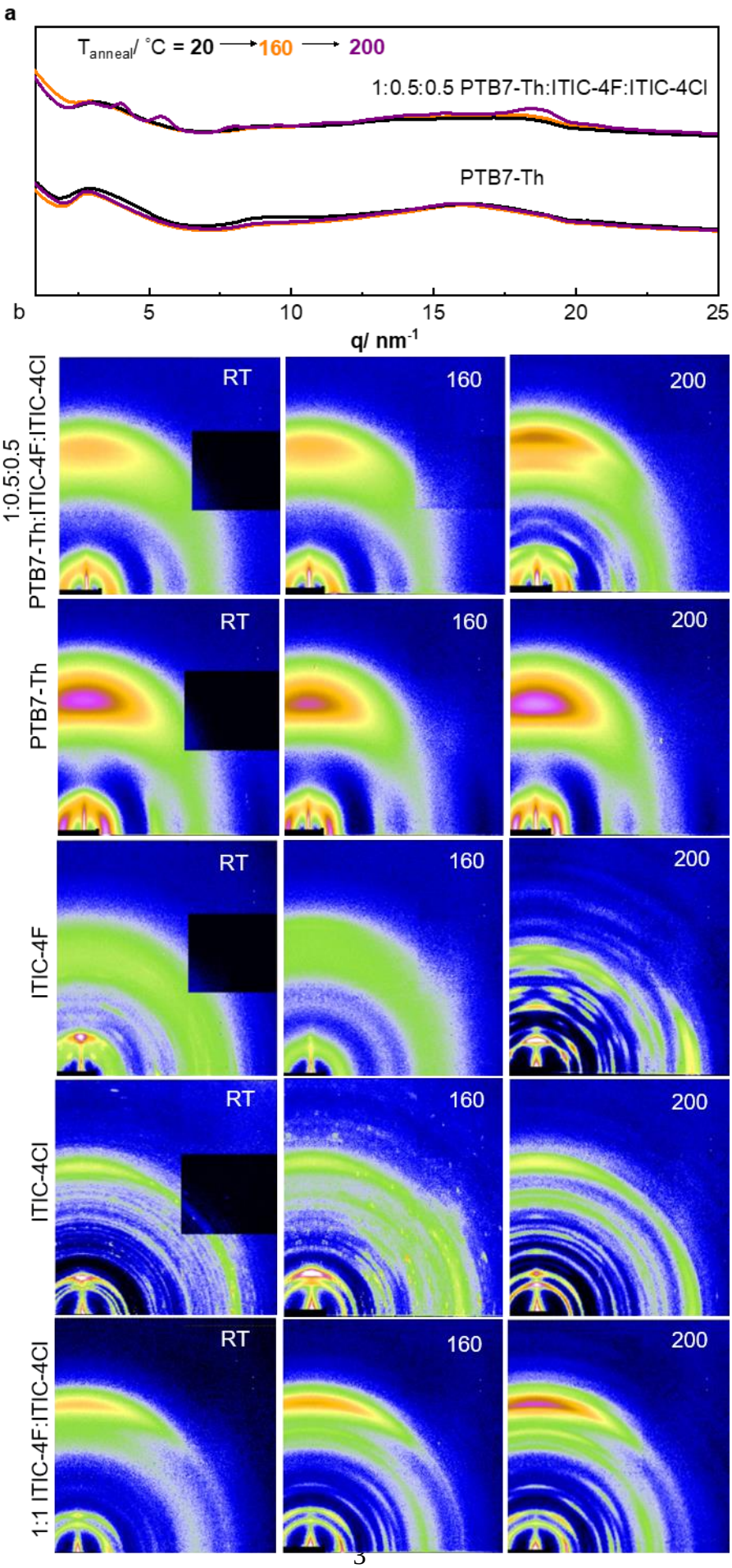
a
$T_{anneal}$/ °C = 20 → 160 → 200
1:0.5:0.5 PTB7-Th:ITIC-4F:ITIC-4Cl
PTB7-Th
b
5
10
15
20
25
q/ nm$^{-1}$
1:0.5:0.5 PTB7-Th:ITIC-4F:ITIC-4Cl
PTB7-Th
ITIC-4F
ITIC-4Cl
1:1 ITIC-4F:ITIC-4Cl
RT
160
200

**Figure S2.** (a) Radially integrated GIWAXS diffractograms of the ternary 1:0.5:0.5 PTB7-Th:ITIC-4F:ITIC-4Cl and pristine PTB7-Th directly after spin-coating (black), annealing at 160 °C (orange) and 200 °C (purple). (b) GIWAXS images of ternary 1:0.5:0.5 PTB7-Th:ITIC-4F:ITIC-4Cl (1st row), PTB7-Th (2nd row), ITIC-4F(3rd row), ITIC-4Cl (4th row) and 1:1 ITIC-4F:ITIC-4Cl (bottom row), directly after spin-coating, annealing at 160 °C and 200 °C.

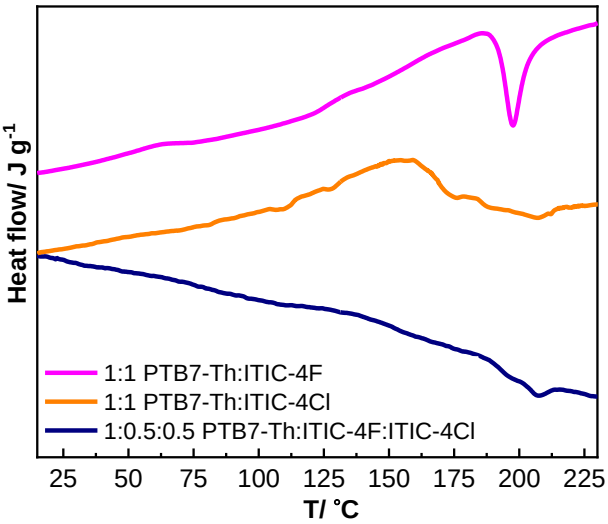


**Figure S3.** (a) DSC heating thermograms for the first heating of the binary blends 1:1 PTB7-Th:ITIC-4F, 1:1 PTB7-Th:ITIC-4Cl and the ternary 1:0.5:0.5 PTB7-Th:ITIC-4F:ITIC-4Cl.

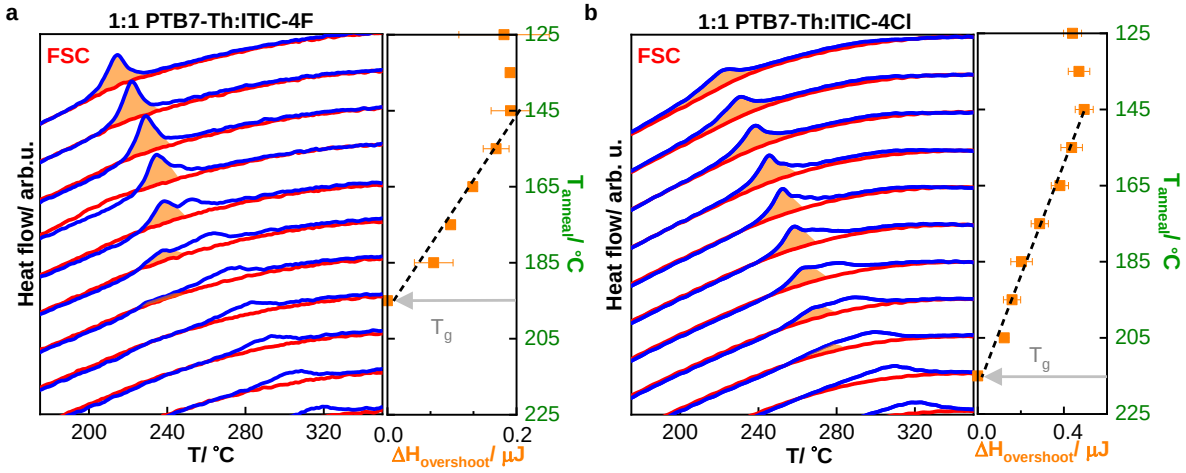


**Figure S4.** FSC heating thermograms after annealing (blue) and after quenching (red), the enthalpy overshoot (orange) against different annealing temperatures show the $T_g$ of (a) 1:1 PTB7-Th:ITIC-4F and (b) 1:1 PTB7-Th:ITIC-4Cl.

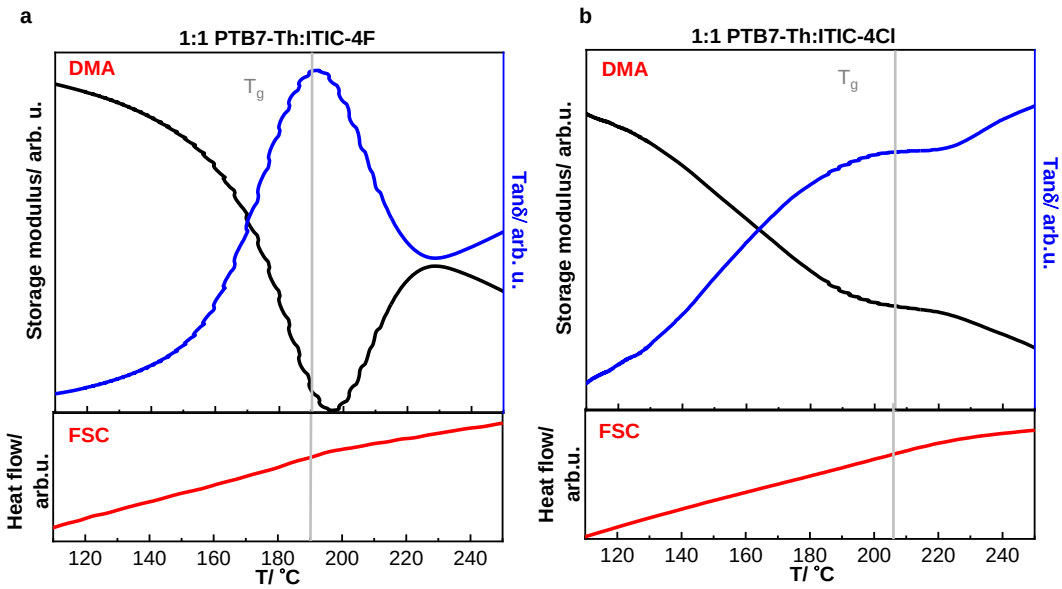


**Figure S5.** DMA heating thermogram showing the storage modulus and loss tangent and plasmonic nanospectroscopy showing the relative shift of the localized surface plasmon resonance peak of (a) 1:1 PTB7-Th:ITIC-4F and (b) 1:1 PTB7-th:ITIC-4Cl.

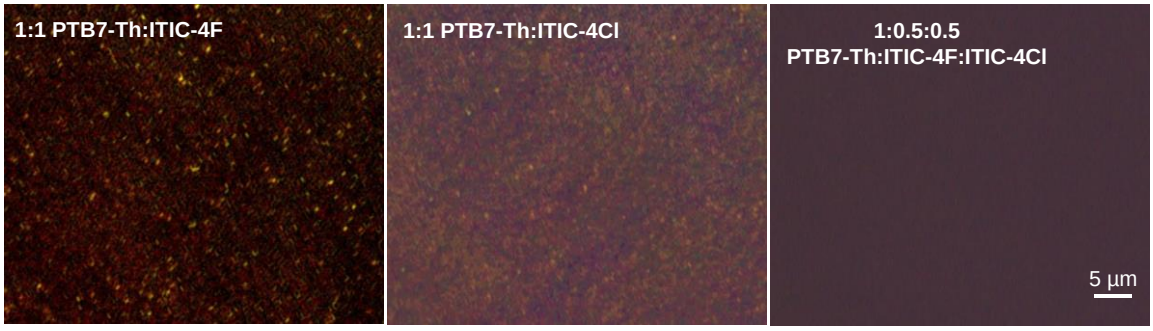


**Figure S6.** (a) Optical microscope images of the binary blends 1:1 PTB7-Th:ITIC-4F, 1:1 PTB7-Th:ITIC-4Cl and the ternary 1:0.5:0.5 PTB7-Th:ITIC-4F:ITIC-4Cl annealed at 160 °C for 10 min.

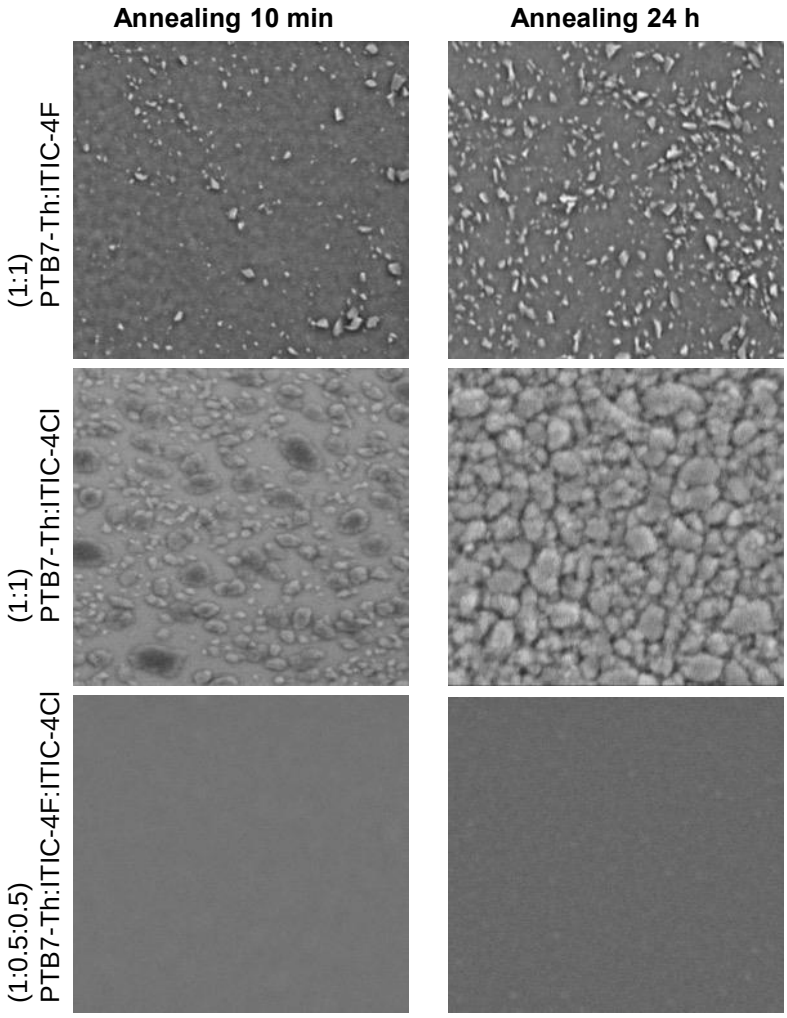


**Figure S7.** SEM images of the binary blend 1:1 PTB7-Th:ITIC-4F, PTB7-Th:ITIC-4Cl and the ternary blend 1:0.5:0.5 PTB7-Th:ITIC-4F:ITIC-4Cl; all samples annealed at 160 °C for 10 min and 24 h.

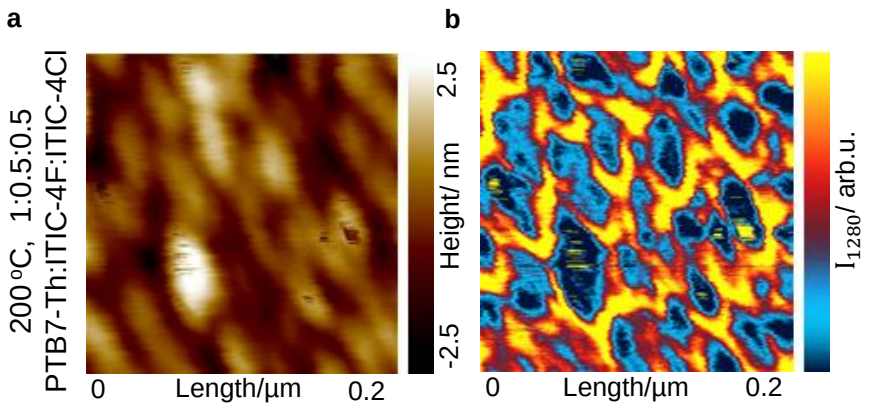


**Figure S8.** (a) AFM height image showing the peak-to-valley height difference; and (b) AFM-IR image recorded at 1280 $cm^{-1}$ the ternary blend 1:0.5:0.5 PTB7-Th:ITIC-4F:ITIC-4Cl; after annealing at 160 °C for 10 min.

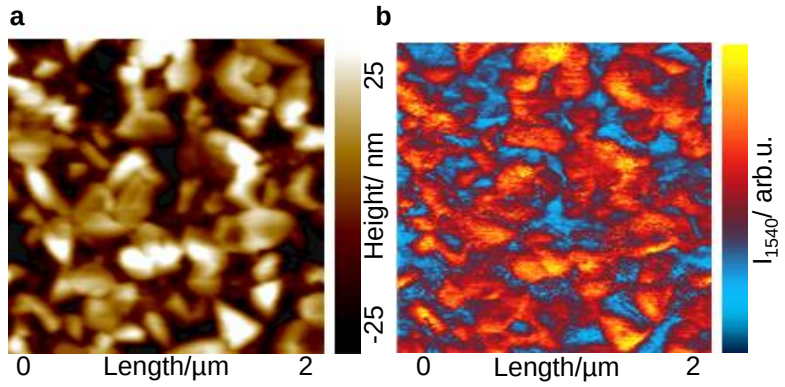


**Figure S9.** (a) AFM height image showing the peak-to-valley height difference; and (b) AFM-IR image recorded at 1540 $cm^{-1}$ of the binary blend 1:1 PTB7-Th:ITIC-4F; after annealing at 160 °C for 10 min.

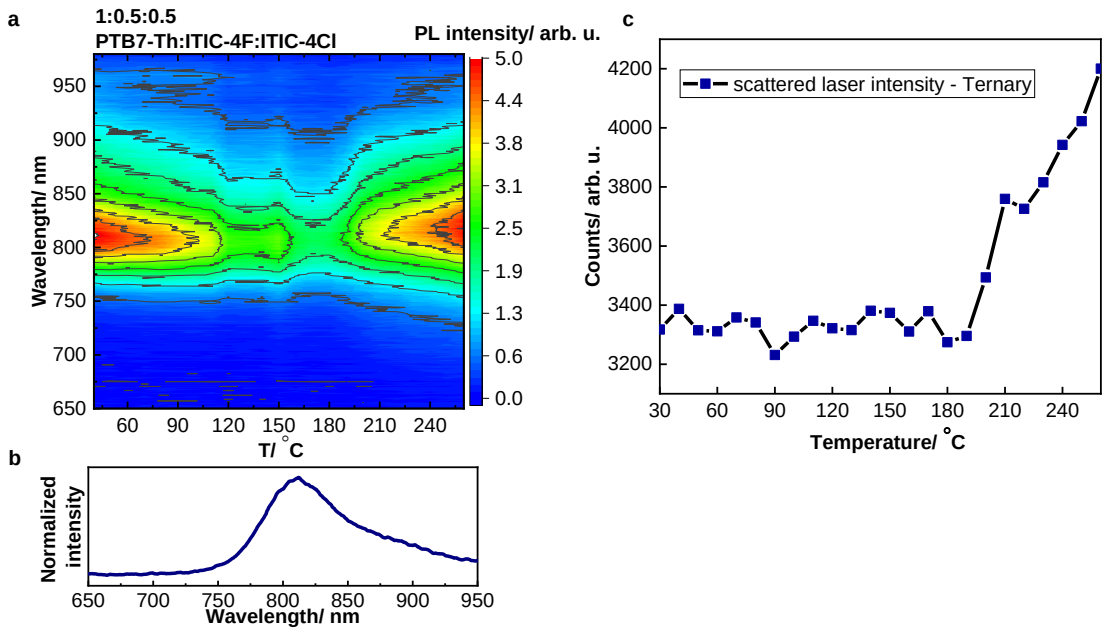


**Figure S10.** (a) The change in photo luminescence intensity as the temperature is increased from 40 °C to 260 °C with a heating rate of 10 °C /min, (b) PL spectra at 40 °C of 1:0.5:0.5 PTB7-Th:ITIC-4F:ITIC-4Cl. (c) The change in scattered laser intensity as the temperature is increased from 30 °C to 260 °C.

Samples for combinatorial screening were fabricated using a triple sequential deposition during blade coating as illustrated in the figure. Solutions of pure (or mixed) materials were prepared in chlorobenzene at a concentration of 15mg/ml. Gradients (for donor polymer layer) were obtained by changing speed from 90 to 10 mm/s during blade coating of the corresponding layer. This results initially in a thickness gradient of the polymer. Then the two acceptor rich solutions were deposited following an oblique trajectory starting from different corners, at constant 30mm/s speed. In order to cover as much as possible of the phase space, four samples were analysed: (i) 1 sample with deposition order shown below from pristine material solutions; (ii) 1 sample in which the two acceptors were deposited in the opposite order as for (i); (iii) 1 sample as (i) but adding 20%w of ITIC-4Cl in the other two solutions (1st and 3rd layers); (iv) 1 sample as (i) but adding 40%w of ITIC-4Cl in the other two solutions (1st and 3rd layers);

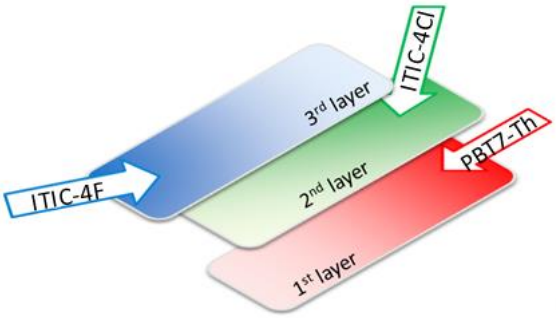


**Figure S11.** Schematics of the blade coating sequence for one sample used in the combinatorial screening method.

Each sample was then imaged by Raman, photoluminescence and white photocurrent techniques. An example of the measurements for sample (i) above is given in Figure S10. These images are combined to produce the figures in the main text.

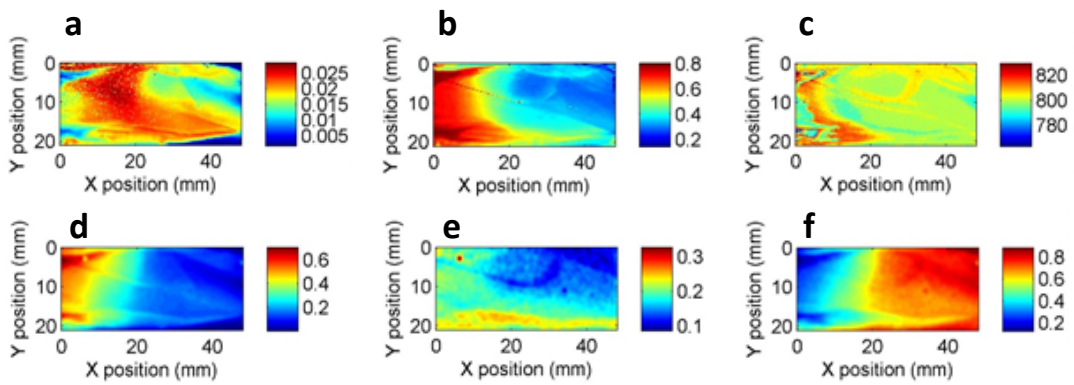


**Figure S12.** Spatial imaging of a ternary system exhibiting a gradient of composition. (a) Photocurrent under white light; (b) absorption at 488nm; (c) Photoluminescence maximum; and Raman deduced local composition of the polymer (d), ITIC-Cl (e), and ITIC-4F (f).

**Table S1.** Glass transition temperatures of PTB7-Th, ITIC-4F, ITIC-4Cl, binary blends 1:1 PTB7-Th:ITIC-4F and 1:1 PTB7-Th:ITIC-4Cl, ternary 1:0.5:0.5 PTB7-Th:ITIC-4F:ITIC-4Cl measured with FSC, DMA and INPS.

| | **PTB7-Th** | **ITIC-4F** | **ITIC-4Cl** | $T_{g,midpoint}^{FSC}$ / °C | $T_{g,\Delta H}^{FSC}$ / °C | $T_{g}^{DMA}$ / °C | $T_{g}^{INPS}$ / °C |
|---|---|---|---|---|---|---|---|
| **PTB7-Th** | 1 | - | - | 123 | - | 120 | 123 |
| **ITIC-4F** | - | 1 | - | 185 | 200 | - | - |
| **ITIC-4Cl** | - | - | 1 | 210 | - | - | - |
| **Binary-F** | 1 | 1 | - | 190 | 195 | 190 | - |
| **Binary-Cl** | 1 | - | 1 | 212 | 215 | 200 | - |
| **Ternary** | 1 | 0.5 | 0.5 | 200 | 205 | 200 | 200 |

**Table S2.** Parameters of the best working devices produced with different active layer compositions.

| **PTBT-Th** | **ITIC-4F** | **ITIC-4Cl** | $J_{sc}$ / mA cm$^{-2}$ | $V_{oc}$ / V | $FF$ / % | $PCE$ / % |
|---|---|---|---|---|---|---|
| 1 | 1 | 0 | 17.8 | 0.67 | 60.7 | 7.2 |
| 1 | 0.9 | 0.1 | 16.6 | 0.67 | 64.6 | 7.2 |
| 1 | 0.75 | 0.25 | 20.6 | 0.66 | 62.0 | 8.4 |
| 1 | 0.5 | 0.5 | 18.8 | 0.66 | 68.0 | 8.5 |
| 1 | 0.25 | 0.75 | 19.3 | 0.64 | 63.6 | 7.8 |
| 1 | 0.1 | 0.9 | 18.7 | 0.62 | 71.2 | 8.3 |
| 1 | 0 | 1 | 21.2 | 0.59 | 67.5 | 8.4 |

**Table S3.** Photovoltaic device parameters averaged for 6 devices on the same substrate.

| | $J_{sc}$ / mA cm$^{-2}$ | $V_{oc}$ / mV | $FF$ / % | $PCE$ / % |
|---|---|---|---|---|
| 1:1 PTB7-Th:ITIC-4F | 17.1 ± 0.6 | 672 ± 2 | 60.6 ± 0.1 | 7.0 ± 0.2 |
| 1:1 PTB7-Th:ITIC-4Cl | 20.3 ± 0.8 | 584 ± 5 | 66.8 ± 0.6 | 8.2 ± 0.2 |
| 1:0.5:0.5 PTB7-Th:ITIC-4F:ITIC-4Cl | 18.6 ± 0.2 | 660 ± 5 | 68.0 ± 0.1 | 8.3 ± 0.2 |